High Temperature Supercapacitors

by

Victoria Jane Black

A Doctoral Thesis

Submitted in partial fulfilment of the requirements for the award of

Doctor of Philosophy of Loughborough University

June 2013

Preface

The work in this thesis was carried out in the Department of Chemistry at Loughborough University under the supervision of Professor Stephen Fletcher. Some of the work reported here has already been published:

1. Fletcher, S., Black, V. J., Kirkpatrick, I., and Varley, T. S. *Quantum design of ionic liquids for extreme chemical inertness, and a new theory of the glass transition*. Journal of Solid State Electrochemistry, 17(2): 327-337 (2013). ISSN: 1432-8488. DOI: 10.1007/s10008-012-1974-2.

Acknowledgements

I would like to thank my supervisor, Professor Stephen Fletcher for the opportunity to obtain a PhD in an interesting field. I would also like to thank him for his continual support, encouragement and words of wisdom. I have learned a lot.

Cheers to everyone that passed through lab F101 over the last three (and a bit!) years for your help and friendship. A special mention goes to Tom, Zee, Iain, Ani, Mei, Laura, Amanda, Sally, Andy, Roger, and Stuart. I would also like to thank my friends outside of the lab: Adelaide, Jenny, Kathryn, Lindsay, Rachel, Yan, Tom and Jordan for planning fun things to do and for helping me to stay sane throughout.

For financial support, I would like to thank Schlumberger and Loughborough University for funding my studentship, and I would like to thank Steve for the financial support during my write up stage.

My final thank you goes to my family: my dad, my brother, my sister, and especially my mum for taking care of me and for being around at stressful times. This thesis is dedicated to you.

Abstract

The scientific objective of this research program was to determine the feasibility of manufacturing an ionic liquid-based supercapacitor that could operate at temperatures up to 220 ^{o}C. A secondary objective was to determine the compatibility of ionic liquids with other cell components (e.g. current collectors) at high temperature and, if required, consider means of mitigating any problems.

The industrial motivation for the present work was to develop a supercapacitor capable of working in the harsh environment of deep offshore boreholes. If successful, this technology would allow down-hole telemetry under conditions of mechanical vibration and high temperature. The obstacles, however, were many. All supercapacitor components had to be stable against thermal decomposition up to $T \geq 220$ °C. Volatile components had to be eliminated. If possible, the finished device should be able to withstand voltages greater than 4 V, in order to maximise the amount of stored energy. The internal resistance should be as low as possible. Side reactions, particularly faradaic reactions, should be eliminated or suppressed. All liquid components should be gelled to minimise leakage in the event of cell damage. Finally, any emergent problems should be identified.

Conventional (room temperature) supercapacitors are a well-developed technology, and have been commercialised by a number of companies such as Maxwell Technologies (USA), NESS Capacitor Company (South Korea), and Cap-XX (Australia). Typically, they contain activated carbon electrodes and sulfuric acid electrolyte. As is well known, these devices exhibit high power densities (1-15 kW kg^{-1}) and low energy densities (1-5 Wh kg^{-1}). They are ideal for applications in which high power surges are required, but are less useful for sustained energy delivery. Their success has led many groups to consider whether they could be improved, either by increasing their energy density, or by increasing their operating temperature (up to 100 ºC). However, even if these goals could be achieved, they would still fall short of requirements.

In the present work, the possibility of increasing the operating temperature of supercapacitors above 100 ºC using ionic liquid electrolytes has been explored. Ionic liquids are combinations of anions and cations that form chemically stable melts at temperatures below ~350 °C. They typically have very low vapour pressures and wide voltage stability windows, implying that

they can be recycled efficiently. Indeed, the dual prospects of long life and enhanced safety explain why ionic liquids are being widely mooted as “green” industrial solvents (i.e. environmentally benign alternatives to organic solvents). The wide voltage window also promises a high energy density, since the stored energy in a supercapacitor increases with the square of the voltage.

A number of factors need to be considered when selecting an ionic liquid for use in a high temperature supercapacitor. These include (1) cost, (2) toxicity, (3) thermal stability, (4) electrochemical stability, (5) liquid range, and (6) hydrophobicity. In order to identify candidate ionic liquids, a large database was compiled summarising their known properties. This suggested that tetra-alkylammonium bis(trifluoromethylsulfonyl)imide compounds (***Figure 1***) were outstanding candidates for initial study. However, there was a lack of information regarding the temperature dependence of their conductivity, a lack of information regarding their electrochemical stability, and the nature and even the number of their phase transitions were unknown. Accordingly, a detailed study of these compounds was initiated.

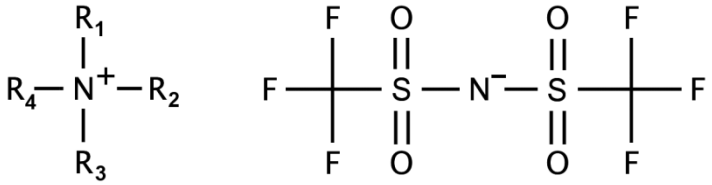

Figure 1 – The generic structural formula of a tetra-alkylammonium bis(trifluoromethylsulfonyl)-imide ionic liquid.

As a first step, the voltage stability windows of ionic liquids containing a variety of tetra-alkylammonium cations were determined, and then the results were interpreted using the quantum theory of electron tunnelling. It was discovered that longer alkyl chains inhibited electron tunnelling and thus conferred improved electrochemical stability. In the next phase of work, a series of long chain tetra-alkylammonium compounds was synthesised and characterised. From these experiments, it became evident that the melting points of ionic liquids could be depressed by incorporating asymmetric cations. As a result of these insights, butyltrimethylammonium bis(trifluoromethylsulfonyl)imide (BTM TFSI) and hexyltriethyl-ammonium bis(trifluoromethyl-sulfonyl)imide (HTE TFSI) were both identified as exceptionally promising ionic liquids for use in supercapacitor devices.

For a particular ionic liquid, another parameter of importance was the temperature dependence of the electrical conductivity. Accordingly, an apparatus was developed for measuring the electrical conductivity to very high precision over the temperature range 20 ºC to 195ºC. The resulting data showed unequivocally that, for the ionic liquids tested, the conductivity was behaving in accordance with the Vogel-Tammann-Fulcher relation,

$$\kappa = A \exp\left(\frac{-B}{\kappa_B (T - T_0)}\right)$$

where κ is the conductivity (S m^{-1}), A and B are unknown constants, κ_B is the Boltzmann constant (1.38062 x 10^{-23} J K^{-1}) and T_0 is the absolute temperature (K) for the onset of conduction. Hence, the ionic liquids under investigation all became much more conducting as the temperature was raised. In addition, thermal analysis revealed that T_0 corresponded with the glass transition temperature of the ionic liquid. This implied that the ionic liquids were behaving as molten glasses at room temperature. In addition, a new theory of the glass transition was developed that provided a model for the parameter B.

As a spin-off from the conductivity studies, miniaturised probes for measuring the conductivity of ionic liquids in small volumes were also developed. This involved the plating of platinum black onto interdigitated gold electrodes that were 200 µm thick and 200 µm apart on alumina substrates. By means of these probes conductivities at elevated temperature (T > 100 ºC) and in volumes less than 3 ml were able to be measured. With appropriate calibration, the results coincided with those obtained using macroscopic commercial electrodes.

The long-term stability of high surface area carbon electrodes was also of experimental interest. In this regard, a series of unique poly(phenol) coatings was developed that could potentially inhibit unwanted electrochemical reactions at the electrode surface. Initial studies were based on a result of Brett et al. [Electroanalysis, 18: 757-762 (2006)] who had previously noted the unwanted polymerisation of the natural product resveratrol (trans-3,5,4'-trihydroxystilbene) on carbon in aqueous solution. For Brett, this was problematic, but in the present work it was a desirable outcome. Unfortunately, resveratrol proved insoluble in ionic liquids. Next, bisphenol A (4,4'-(2,2-propanediyl)diphenol)) was tried as a possible

replacement. Although sucessful, this compound is a suspected endocrine disrupter, which caused it to be rejected also. Finally, after an extensive search, a few non-endocrine disruptive bisphenols were identified which readily polymerised on carbon electrodes in ionic liquid solutions. An attractive feature of these polymerisation reactions was that they were self-limited by the percolation length of the electron in the polymer, which restricted the thickness of the polymer coating to a few nanometers.

Physical immobilisation of ionic liquids was also of interest. Given the high working temperatures, it was necessary to focus on high-surface-area, thermally-stable, ceramic materials to gel them. It was found that fumed silica was a near-ideal choice. A few authors had previously claimed to have successfully gelled ionic liquids using very different amounts of fumed silica, varying from 5% to as much as 50% by weight, and using silica particle sizes ranging from 7 nm to 100 μm. In our hands, it was found that fumed silica having a primary particle size of 7 nm and a BET surface area exceeding 350 $m^2 g^{-1}$ was able to gel ionic liquids when added at the level of only 7.5% by weight.

In practical supercapacitors, porous electrodes are used to increase the rate of interfacial charging. However, the use of highly heterogeneous materials (such as activated carbons) introduces a wide diversity of pore diameters and pore lengths. This, in turn, creates a wide distribution of time constants in the finished product. To model this distribution, a new equivalent circuit has been developed which closely mimics the response of real-world supercapacitors.

Finally, laboratory scale supercapacitors capable of long term operation at 220 ºC (a minimum of 3 weeks) were assembled. These devices incorporated screen printed activated carbon electrodes, an immobilised ionic liquid electrolyte, a polyimide substrate, a glass fibre separator, and a silicone sealant. The ionic liquid electrolytes were of the asymmetric tetraalkylammonium bis(trifluoromethylsulfonyl)imide class, namely butyltrimethyl-ammonium bis(trifluoromethylsulfonyl)imide and hexyltriethylammonium bis(trifluoro-methylsulfonyl)imide. Laboratory experiments revealed that the measured capacitance increased with operating temperature, although the voltage stability window decreased. The technology was also shown to be scalable, which is promising for its use in down-hole telemetry and other real-world applications. The largest supercapacitors assembled in the present work had a capacitance of 20 F.

Contents

Chapter 1 – Introduction to Supercapacitors

1.1 – Chapter overview

This chapter aims to highlight to the reader the motivation for the present work, as well as provide relevant background information on supercapacitors. It includes a review of supercapacitor literature, how their design and properties influence performance, and a summary of the materials under investigation for next generation devices.

1.2 – What are supercapacitors?

Supercapacitors are electrochemical energy storage and delivery systems of high specific power. They are designed for the rapid charge and discharge of electric current. Internally, supercapacitors utilise an interfacial space charge region, and/or localised surface states, to achieve high electrical capacitance. As a rough guide, the capacitance of conventional capacitors used in electronic circuits typically ranges from pico-farads (pF) to micro-farads (μF). By contrast, the capacitance of commercial supercapacitors is usually much larger, in the range farads (F) to kilo-farads (kF) justifying the 'super' prefix[1-2].

In practice, supercapacitors are commonly used in tandem with batteries, due to their ability to meet short term demands for power. One example where this technology is currently being exploited is in hybrid electric vehicles, where supercapacitors are able to store energy during braking and re-use it during acceleration[3]. In this way, supercapacitors are able to bridge the technology gap between low specific power batteries and low specific energy conventional capacitors[4]. Some of the main advantages and disadvantages of supercapacitors are summarised in ***Table 1.1***.

Typically, a supercapacitor consists of an electrolyte solution sandwiched between two polarisable electrodes. The electrodes are physically separated by an inert ion-permeable membrane as illustrated in ***Figure 1.1***.

***Table 1.1 − A summary of the perceived advantages and disadvantages of supercapacitors*[5-6].**

Advantages	
Property	**Overview**
Power density	(1-10 kW kg^{-1}). Able to charge and discharge on time scale of seconds due to fast charging/discharging mechanism, meaning energy can be rapidly extracted. (Batteries > 1 h).
Cycle life	< 10^5 cycles. Highly reversible energy storage involving the charge / discharge of the interfacial capacitance. No faradaic reactions to damage electrode materials.
Operating temperature	Typically –30 ºC to 70 ºC for sulfuric acid electrolytes.
Hybrid friendly	Can be combined with rechargeable batteries for hybrid applications (i.e. electric vehicles).
Disadvantages	
Property	**Overview**
Low energy density	0.05 to 10 Wh kg^{-1}[3].
High self-discharge rate	Higher self-discharge than batteries. Approximately 10–40% per day. Leads to lower voltages.

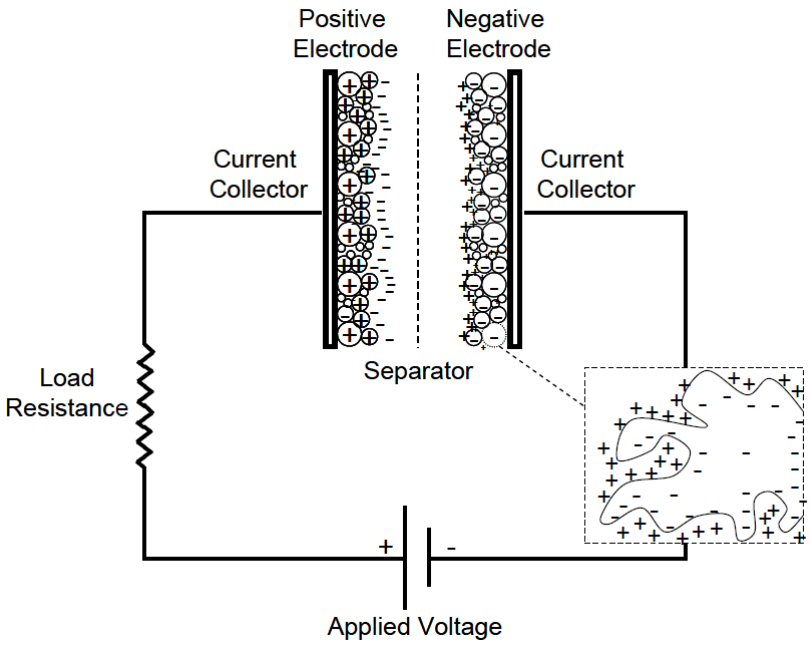

Figure 1.1 − A schematic diagram of supercapacitor components.

Because each electrode/solution interface constitutes a single capacitor, a two-electrode cell may be modelled as two capacitors in series. Therefore, the total capacitance of a supercapacitor cell is given by ***Equation 1.1***,

$$\frac{1}{C_{\text{cell}}} = \frac{1}{C_1} + \frac{1}{C_2}$$

Equation 1.1

where C_1 and C_2 are one-electrode capacitances (F) and C_{cell} is the two-electrode capacitance. Each electrode may be thought of as consisting of a double layer capacitance plus a surface state capacitance. Thus,

$$C_1 = \frac{\varepsilon A}{d} + nC_{ss}$$

Equation 1.2

where ε is the dielectric constant of the double layer region, *A* is the geometric area of the electrode (m^2), and *d* is the width of the space-charge region (m), n is the number of localised states, and C_{ss} is the capacitance (F) of each surface state. A similar formula applies to C_2.

For industrial uses, the challenge in supercapacitor design is to find ways to enhance energy density and power density of the finished device, without compromising the safety or cycle life. ***Equation 1.3*** and ***Equation 1.4*** give the equations for energy and power density and show that *R*, *V* and *C* are the important variables.

The energy stored in a supercapacitor cell is given by ***Equation 1.3***,

$$E = \frac{1}{2} C_{\text{cell}} V_{\text{cell}}^2$$

Equation 1.3

where *E* is the stored energy (J), C_{cell} is the cell capacitance (F), and V_{cell} is the cell voltage (V).

The maximum power delivered into an equivalent series resistance of value R_s is given by ***Equation 1.4***,

$$P_{max} = \frac{V_{\text{cell}}^2}{4R_s}$$

Equation 1.4

where P_{max} is maximum power (W), V_{cell} is the cell voltage (V), and R_s is the equivalent series resistance (Ω).

As both stored energy and maximum power are proportional to the square of the cell voltage, developing electrolyte solutions with wide voltage stability windows is a desirable goal.

1.3 − The history of supercapacitors

The storage of electrical energy on surfaces was achieved in ancient times, by rubbing amber[7]. However, as far as it is known, the effect was never exploited for technological purposes. Modern scientific interest originated in the mid-18th century when systematic investigations began for the first time. It was during this period that one of the earliest charge storage devices, a condenser (or electrostatic capacitor as it is known today) was reported by Musschenbroek[8]. His device consisted of a sealed glass jar which was covered in conducting metal foil on the inner and outer surfaces. The interior was filled with aqueous acidic electrolyte. An electrode was inserted directly into the solution and the inner foil was charged by an external power source. It was shown that despite the inner and outer foils being separated by a non-conducting dielectric (glass), an equal and opposite charge to the inner foil appeared on the outer foil. About the same time, Dean Kleist[9] of Leiden University made a similar device, leading to the historical name of the "Leiden Jar".

Despite the discovery of the Leiden Jar, the actual mechanism of charge storage remained mysterious for another 120 years, until the development of Maxwell's equations in 1861. Maxwell described how electric fields could be generated and how they could be altered by electric charge and electric current[10].

The first supercapacitor was patented was by H. E. Becker of the General Electric Company in 1957 (US Patent 2,800,616)[11]. His patent described the storage of charge in the electrical double layer of two carbon electrodes separated by an aqueous solution, but the device was never commercialised. The Standard Oil Company of Ohio (SOHIO) was the next to contribute to the development of supercapacitors in the late 1960s and early 1970s. They

introduced non-aqueous electrolytes to their devices, and as a result, were able to achieve higher operating voltages (3.4-4.0 V)[12-13]. In 1978, The Nippon Electric Company (NEC) were the first to commercialise a supercapacitor device after licensing the technology from SOHIO. They were also the first to use the phrase 'supercapacitor' in their marketing campaign, in which they promoted the use of supercapacitors for back-up power in consumer electronics. During the following decades, many other manufacturers entered the market as the potential for supercapacitors across a broad range of applications was realised. This led to the production of devices with improved electrical properties and lower unit costs. Some of these developments are summarised in ***Table 1.1***[14].

The market for supercapacitors is currently valued at approximately half a billion dollars[15], and continues to grow at a healthy pace. Leading manufacturers today are Maxwell Technologies (US), NESS Capacitor Company (South Korea), and Okamura Lab (Japan), and Cap-XX (Australia).

Table 1.2 – Advances in supercapacitor technology.

Year	Contributor	Contribution
1957	General Electric Company	First ever example of a double layer capacitor.
1962	Standard Oil of Ohio	First double layer capacitor patented in the form known today using high surface area carbon electrodes.
1978	The Nippon Electric Company	First commercial "supercapacitor."
1982	The Nippon Electric Company	Maxcap capacitor (5.5 V and several farads)
1882	The Pinnacle Research Corporation	First supercapacitor to use transition metal oxides as electrodes. Used for high power military applications such as laser weaponry and missile guidance systems. These devices were not commercialised due to high cost of transition metal oxides.
1985	Panasonic	First button cell supercapacitor produced for solar watches.
1989	ELIT power sources	First asymmetric supercapacitor manufactured. Used for toys and wheelchairs. The positive electrode was nickeloxyhydroxide and the negative electrode was activated carbon.
1993	MP Pulsar	First supercapacitor rated for 24 V and 50 kJ which could be used for train engine starting.
1994	ECOND	First capacitor systems for hybrid electric vehicles.
1996	CSIRO	First supercapacitor with specific energy of 9 Wh kg^{-1}.
1997	ESMA	Showed that busses and trucks could be powered solely off supercapacitors with energy densities >10 Wh kg^{-1} (no batteries or gas engines).
1999	Panasonic	Developed "UpCap" supercapacitors for hybrid electric vehicles (2000 F, 2.3 V) for transport applications and hybrid electric vehicles.
2001	The Nippon Electric Company	Manufactured supercapacitors with organic electrolytes.
2002		Asymmetric supercapacitors developed with specific energy of 16 Wh Kg^{-1}.
2005		Supercapacitors developed for solar lamps and forklifts.
2007	ESMA	Supercapacitors developed for grid energy storage.

1.4 – Next generation of supercapacitors

Next-generation supercapacitors for the mining industry are aiming for operating temperature around 220 ºC. At present, commercially available 'high temperature' supercapacitors are rated for a maximum temperature of 85 °C, with standard operating temperatures around 60 °C. (Maxwell Technology, Cap-XX).

Most "high temperature" work reported in the literature is actually in the range of 40 °C to 90 °C, with only a few reports at the higher end of this temperature range [16-24]. The only work found to date for a supercapacitor operating at temperatures greater than 100 °C is that of Hastak *et al.*[25] who made a supercapacitor that successfully operated in the temperature range 27 °C to 120 °C using activated carbon electrodes and a conducting polymer electrolyte; phosphoric acid doped poly(2,5-benzimidazole).

The ultimate aim of the present work was to develop a supercapacitor that could operate in harsh environmental conditions such as those found down bore-holes. Diminishing stocks of fossil fuel are compelling oil companies to drill deeper underground, where extreme temperatures and pressures are encountered. Such drilling requires specialist telemetry equipment, and this must be powered by a robust source of electrical energy. Consequently, the brief was to develop a supercapacitor adequate to this task.

1.5 – Materials for next-generation supercapacitors

In the present work, the target was to develop a supercapacitor having electrochemical stability over the voltage range ±3 V, and thermal stability over the temperature range 25 ºC to +220 ºC. These were such difficult criteria to meet that the choice of materials was strictly limited. After an extensive search, ionic liquids became the focus for potential electrolytes, activated carbon as the potential electrode material, and polyimide as the potential cell body material. The thermal stability of ionic liquids was confirmed by DSC, which revealed that two ionic liquids butyltrimethylammonium bis(trifluoromethylsulfonyl)imide and hexyltriethylammonium bis(trifluoromethylsulfonyl)imide were of special interest, since they remained stable at T < 350 ºC. Similarly, activated carbon resists pyrolysis at T < 450 ºC. Finally polyimide is stable at T < 400 ºC.

In order to complete a functioning device, several additional components were needed. These included a gelling agent, a separator, and a sealant. As a gelling agent fumed silica was selected, which is stable at T < 1710 ºC. As a separator glass fibre was chosen, which is stable at T < 850 ºC, and as a sealant a high temperature polyimide masking tape (K6339) manufactured by DuPont, which is stable up to 250 ºC (long term), and 300ºC (short term) was chosen. An overview of these materials now follows.

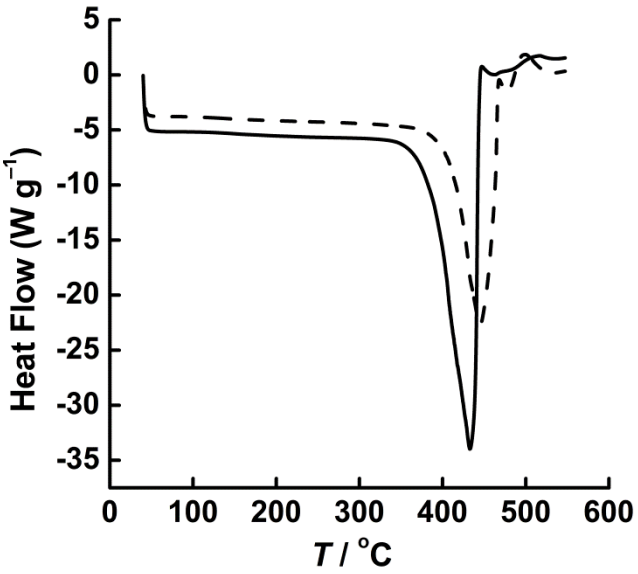

***Figure 1.2 – DSC thermograms showing the thermal decomposition of butyltrimethylammonium bis(trifluoromethyl-sulfonyl)imide (dotted) and hexyltriethylammonium bis(trifluoromethyl-sulfonyl)imide (solid) at T* > 350 ºC.**

1.5.1 − Ionic liquids (electrolyte/solvent)

Ionic liquids are salts that are composed entirely of ions and exist in the liquid state below an arbitrary temperature, usually quoted as 100 ºC[26-28]. While this definition is widely used, there are some ionic liquids that survive indefinitely at temperatures greater than 100 ºC, and these are of special interest in the present work. Therefore, in light of this fact, the definition of ionic liquids is here revised to be "a solvent-free combination of anions and cations that exhibits liquid-like behaviour below 350 °C".

For supercapacitors, it is already known that ionic liquids exhibit wide voltage stability windows (up to 4 V)[29] and negligible vapour pressures. They also have acceptable ionic

conductivities (0.1-10 mS cm^{-1})[30], and show capacitances of the order of 10 µF cm^{-2}[31] at carbon electrodes. It is this combination of properties that makes them attractive solvents for use in energy storage devices. For high temperature devices, they are the only candidate material. Conventional electrolytes, both aqueous and organic, cannot operate at elevated temperatures due to the evaporation of solvent (T > 80 °C in the case of water).

Ionic liquids have a long history. Some materials such as ethanolammonium nitrate $[EtNH_3OH][NO_3]$, m.p. 52 °C, were reported as far back as the 19th century[32], and some intensive studies were carried out. in 1914[33]. In that year, a related ionic liquid ethylammonium nitrate $[EtNH_3][NO_3]$, m.p. 12 °C, was synthesised by Paul Walden. This was made by the neutralisation of ethylamine with concentrated nitric acid. However, while Walden's work left an important legacy, the industrial potential of ionic liquids was still not realised.

Hurley and Wier accidentally discovered what were later to be classified as the 'first generation' of ionic liquids in 1948[34]. During their investigations into cheaper and easier ways to electroplate aluminium they found that if powdered pyridinium halides were added to aluminium chlorides, the resulting reaction produced a clear colourless liquid ($[EtPyBr][AlCl_3]$)[35]. These haloaluminates were studied extensively for their physical and chemical properties and were found to be useful catalysts for organic reactions such as the Friedel Crafts reaction. However, their practicality and use in industrial applications were seveley limited due to their high affinity for moisture and their high reactivity with air[26].

The biggest breakthrough in the history of ionic liquids came with the discovery of the air and moisture stable "second generation", reported by Wilkes and Zaworotho in 1992[36]. Their discovery combined a dialkylimidazolium cation, such as 1-ethyl-3-methylimidazolium, with a weakly co-ordinating anion, such as tetrafluoroborate or hexafluorophosphate. However, even though the resulting ionic liquids were water insensitive, they did slowly absorb water from air. This was undesirable as water changed the chemical and physical properties of the ionic liquids. For example, the tetrafluoroborate anion underwent hydrolysis to toxic and corrosive hydrogen fluoride. As a result, a move towards hydrophobic anions was made[37-39]. Popular choices were bis(trifluoromethylsulfonyl)imide $[(CF_3SO_2)_2N^-]$ and trifluoromethanesulfonate $[CF_3SO_3^-]$. These not only had low reactivity with water but also had enhanced voltage stability and lower toxicity than halogenated anions. The ability of the second generation of ionic liquids to be used on the benchtop, was

the start of an explosion of interest amongst the academic and industrial communities. As well as being the subject of fundamental physical chemistry studies, numerous applications of ionic liquids were realised, especially in the fields of inorganic synthesis[40], lithium batteries[41], solar cells[42], catalysis[43], separation chemistry[44], and sensors[45].

The development of "designer" ionic liquids took off in the early 2000's. These are considered to constitute a "third generation" of ionic liquids. Examples include functionalised cations which exhibit biological activity for pharmaceutical applications.

The scientific literature on ionic liquids has exploded dramatically over the last few decades as ionic liquids have been explored for use in all areas of chemistry. This is illustrated by a plot showing the journal entries to Science Direct containing the phrase "ionic liquids" in their title from the years 1920 to 2010, ***Figure 1.3***. It can be seen that while in the 1920's there were only 41 papers published on ionic liquids, in the decade 2000-2010, a phenomenal 81,576 papers were published on ionic liquids.

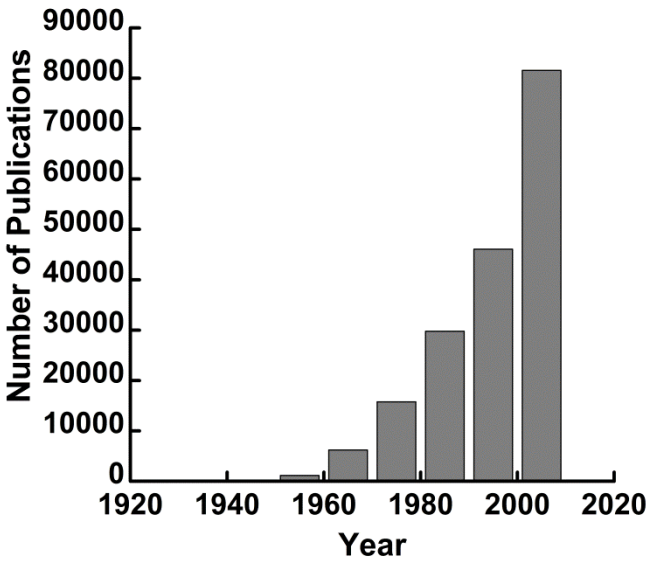

Figure 1.3 – The phenomenal growth in ionic liquid literature since their discovery in 1914.

There are now theoretically 10^{18} potential ionic liquids that can be synthesised based on different anion and cation combinations, with 350 currently commercially available[46]. The most commonly used anions and cations are illustrated in ***Figure 1.5.***

The tailoribility of ionic liquids makes them adaptable and potentially useful in a vast number of applications. In recent times new uses have emerged in energy technologies (such as metal-air batteries[47] and supercapacitors[24,29,48-49], in CO_2 capture[50-53], in polymerization[54], in synthesis of nanoparticles[55-57], in cellulose chemistry[58-60], in extraction of rare earths[61-62], in desulfurization of process streams[63-64], in separation of fission products[65], in heat transfer fluids[66-67] and in lubricants[68-71].

Plechkova and colleagues[72] have predicted that, in the future, ionic liquids will be used in all the fields illustrated in ***Figure 1.4***.

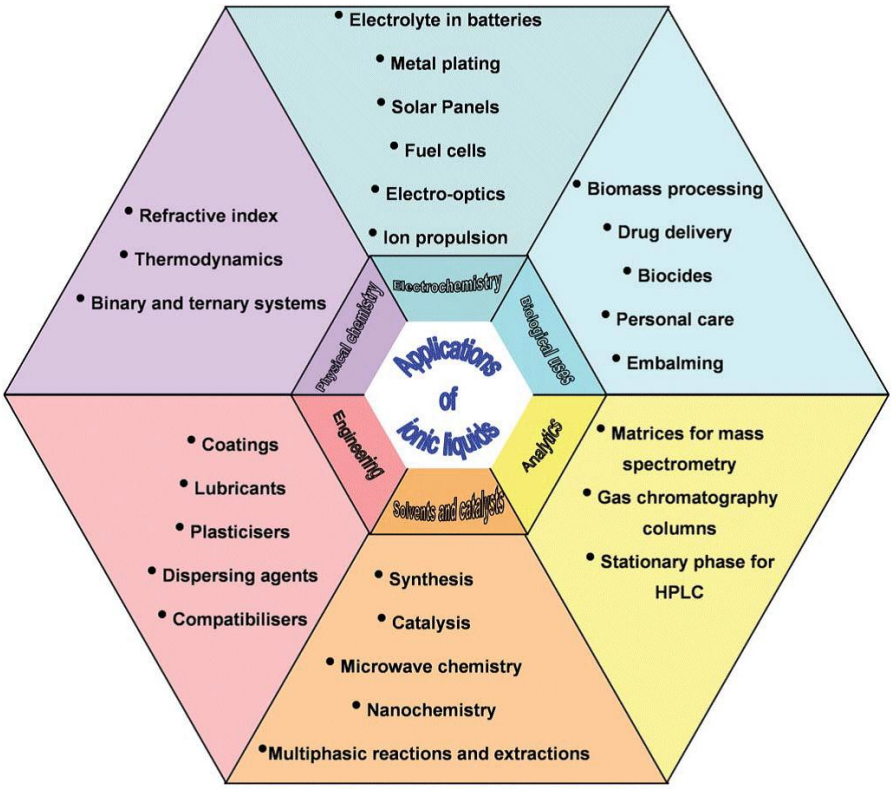

Figure 1.4 − An illustration of the fields in which ionic liquids are predicted to find future applications.

Cations

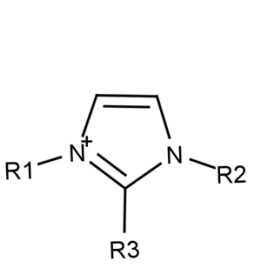

imidazolium

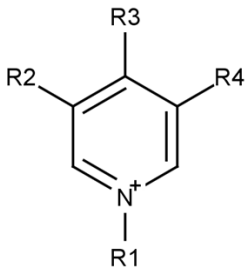

pyridinium

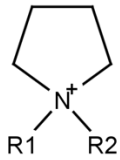

pyrrolidinium

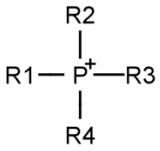

phosphonium

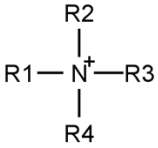

ammonium

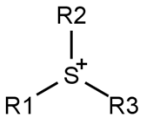

sulfonium

Anions

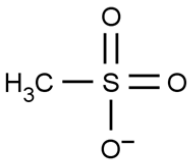

methanesulfonate

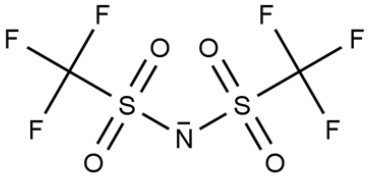

bis(trifluoromethylsulfonyl)imide

PF_6^-

hexafluorophosphate

BF_4^-

tetrafluoroborate

X^-

halide

Figure 1.5 – Structural formulae of common anions and cations of ionic liquids.

As the range of ionic liquids available is so vast, choosing the most suitable candidate for a high temperature supercapacitor is difficult. A number of criteria need to be considered, including voltage stability, conductivity, viscosity, melting point and thermal stability. Each of these factors will now be considered in turn.

Voltage stability

The voltage stability window of a solvent indicates the range of potentials over which the solvent is stable, without undergoing faradaic decomposition. In the case of ionic liquids, it is necessary to consider the electrochemical stability of the cation at negative potentials, and the electrochemical stability of the anion at positive potentials. A typical measurement of a voltage stability window is illustrated in ***Figure 1.6***.

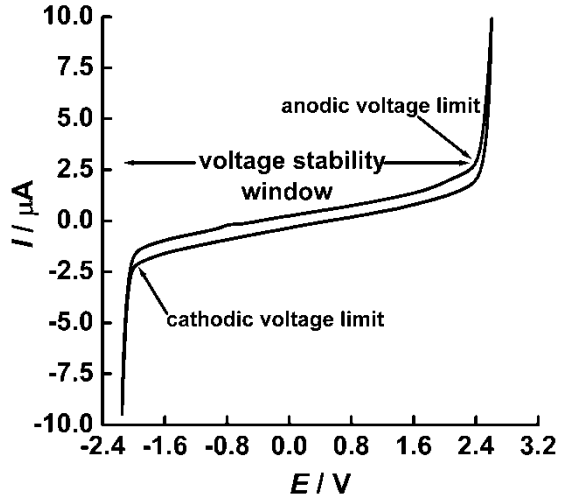

Figure 1.6 − An illustration of the voltage stability window of an ionic liquid on a glassy carbon electrode.

An advantage of wide voltage stability windows is that they correlate with high energy density and high power density of the functioning supercapacitor. Interestingly, Gonçalves and co-workers have reported that 1-butyl-3-methylimidazolium tetrafluoroborate and 1-butyl-3-methylimidazolium pentafluorophosphate are electrochemically stable over a 7 V

voltage window[30], one of the highest values recorded to date. These windows are much wider than those achieveable by aqueous systems, since the latter are limited by the decomposition voltage of water (~1.23 V)[26]. Similarly, ionic liquids are much more stable than common non-aqueous systems.

Trulove and Mantz[38] have tabulated the stabilities of many anions and cations, and report them in the following order.

Cation stability:

Tetra-alkyl ammonium > sulfonium > imidazolium > pyrazolium > pyridinium

Anion stability:

TFSI/triflate > BF_4^-/PF_6^- > chloroaluminates > halides

Accordingly, tetraalkylammonium TFSI compounds were selected as the starting materials. The hydrophobicity of these compounds was also beneficial as it helped to minimise trace levels of water. The key to synthesizing hydrophobic ionic liquids is to suppress hydrogen bonding between water molecules and anions.

Conductivity and viscosity

It has long been recognized that a reciprocal relation exists between ionic conduction and liquid viscosity. The origin of the reciprocity lies in the fact that the motion of an ion through a stationary liquid may also be viewed as the flow of a liquid around a stationary ion. This kinetic equivalence underpins the classical Stokes-Einstein relation, and explains why the activation energy for ionic conduction is the same as the activation energy for viscous flow.

Viscosity measures the resistance of a liquid to macroscopic flow. Ionic liquids typically have viscosities in the range 10-500 mPa·s[49] (depending on the size, shape, charge, and molar mass of the ions) whereas the viscosity of water is 1.0 mPa·s. This correlates with lower conductivity for ionic liquids (0.1-10 mS cm^{-1}[49] *vs.* 500-700 mS cm^{-1} for water), because the product of viscosity and conductivity is approximately constant (Walden's Rule). Low conductivity is undesirable for supercapacitor electrolytes because it creates a high internal

resistance in the finished cell. High viscosity is also undesirable because it inhibits wetting of porous electrodes. One way to decrease the viscosity of ionic liquids is to add inert solvents such as nitrobenzene[73] or acetonitrile[74], but this approach is not environmentally friendly, and diminishes the accessible temperature range. Fortunately, the viscosity of ionic liquids can be decreased by increasing their temperature, which is advantageous when designing high temperature supercapacitors. The conductivity is also enhanced. For example, Arbizzani *et al.*[75] compared the conductivity values of three pyrrolidinium ionic liquids at 20 °C and 60 °C and found that in all cases the conductivity was more than double at the higher temperature.

Table 1.3 – Conductivity at 20 °C ***vs. 60*** °C ***for three pyrrolidinium based ionic liquids.***

Ionic liquid	**σ / mS cm^{-1}**	
	20 °C	**60 °C**
N-butyl-*N*-methylpyrrolidinium bis(trifluoromethanesulfonyl)imide	2.6	6.0
N-butyl-*N*-methylpyrrolidinium trifluoromethanesulfonate	2.0	5.5
N-methoxyethyl-*N*-methyl pyrrolidinium bis(trifluoromethane-sulfonyl)imide	3.8	8.4

In the scientific literature two disparate approaches have been taken towards quantifying the conductivity and viscosity of ionic liquids. The classical approach, based on the theory of electrolyte solutions, is to assume that the ionic conductivity obeys the Arrhenius equation as a function of temperature, *viz*.

$$\kappa = \kappa_0 \exp\left(\frac{-E_a}{RT}\right)$$

Equation 1.5

Here, κ is the conductivity (S m^{-1}), E_a is the activation energy (J mol^{-1}) for electrical conduction, R is the universal gas constant (8.315 J K^{-1} mol^{-1}) and T is the temperature (K).

An alternative approach, which is purely empirical, is to assume that the ionic conductivity obeys the Vogel-Tammann-Fulcher equation as a function of temperature, *viz.*

$$\kappa = \kappa_0 \exp\left(\frac{-B}{k_B(T - T_0)}\right)$$

Equation 1.6

Here, κ is the conductivity (S m^{-1}), κ_0 is the conductivity at infinitely high temperature, B is a fitting parameter (K), and T_0 is the absolute temperature (K) for the onset of conduction. Although the Vogel-Tammann-Fulcher equation lacks theoretical support, it has great utility as a fitting function because it is able to interpolate data in systems where the Arrhenius equation fails. Overall, however, the literature relating to these two approaches is confusing, and no consensus has been reached regarding which is preferable. Indeed, some authors such as Jarosik *et al.*[76] even state that the choice of relationship depends on the temperature range of measurements, e.g. Arrhenius at room temperature and Vogel-Tammann-Fulcher at low temperature. This is inherently unlikely, and one of the goals of the present work was to obtain experimental data over a wide enough range of temperatures in order to decide this issue.

Melting point and thermal stability

Ionic compounds are usually high melting point solids. It is understood that the melting point of an ionic compound correlates with its lattice energy, which is dependent on the size, charge and electrostatic interactions between the component ions. Large ions with a small charge are the most unstable in crystalline form and require less energy to disrupt the crystal lattice than small, highly charged ions. This explains why standard inorganic salts such as sodium bromide and sodium chloride (small and highly charged with a stable lattice) have high melting points, 747 °C and 801 °C respectively, whereas ionic liquids such as tetrabutyl ammonium bromide (with a much larger cation and weaker electrostatic lattice forces) have much lower melting points, 104 °C[75].

It is possible to prepare salts having low melting points by decreasing the symmetry between the ion pairs. By contrast, symmetrical species from more tightly packed crystalline structures and require much greater energy to break down. Sun *et al.*[77] and Matsumoto *et al.*[78] have shown this to also be the case for ionic liquids. Sun *et al.* investigated the influence of cation symmetry on the melting point of tetraalkylammonium salts and Matsumoto *et al.* showed that by reducing the symmetry of the anion (from bis(trifluoromethylsulfonyl)imide to 2,2,2-

trifluoro-*N*-(trifluoromethylsulfonyl)-acetamide), the melting point of the ionic liquid could be reduced to room temperature.

For high temperature operations ($T \geq 200$ °C) , the thermal stabily of a solvent is an important property to consider. Due to the volatility and flammability of organic solvents and the evaporation of water at high temperatures, neither aqueous nor organic based solvents are appropriate. Ionic liquids, however, are non-flammable and thermally stable up to temperatures of, and in some cases exceeding, 400 °C[27,79]. For example, 1-ethyl-3-methyl-imidazolium tetrafluoroborate, 1-butyl-3-methyl-imidazolium tetrafluoroborate and 1,2-dimethyl-3-propyl imidazolium bis(trifluoromethylsulfonyl)imide are thermally stable up to 445, 423, and 457 °C respectively[80]. Interestingly, according to Singh and colleagues[26], it is the nature of the anion that determines the thermal stability of an ionic liquid and chosing non-fluorinated anions would likely decrease the thermal decomposition temperature of the ionic liquid.

1.5.2 − Activated carbon (electrode material)

Activated carbon is a highly porous form of carbon. It is an extremely attractive material for supercapacitor electrodes because as well as having a large internal surface for capacitance, it has all the beneficial properties of pure carbon such as temperature stability, corrosion resistance, low cost, and good electrical conductivity.

Activated carbon is synthesised from precursor materials such as coconut shells, wood or polymers. These are firstly carbonised *via* pyrolysis to form chars, before being "activated" by physical or chemical methods[81]. Physical activation of carbon typically involves high temperature treatment (700 ºC - 1100 ºC) under CO_2, whereas chemical activation typically involves treatment with concentrated solutions of dehydrating agents such as H_2SO_4 or KOH at 400 ºC - 800 ºC[81]. During the activation process, pores are widened by burning out less-organised carbon, and chemical functionalities are formed on the carbon surface. The parameters of the activation process such as temperature, time, gaseous environment and choice of activating agent can be varied to control the properties of the activated carbon[81].

A schematic illustrating the surface functionalities on carbon is given in ***Figure 1.7***.

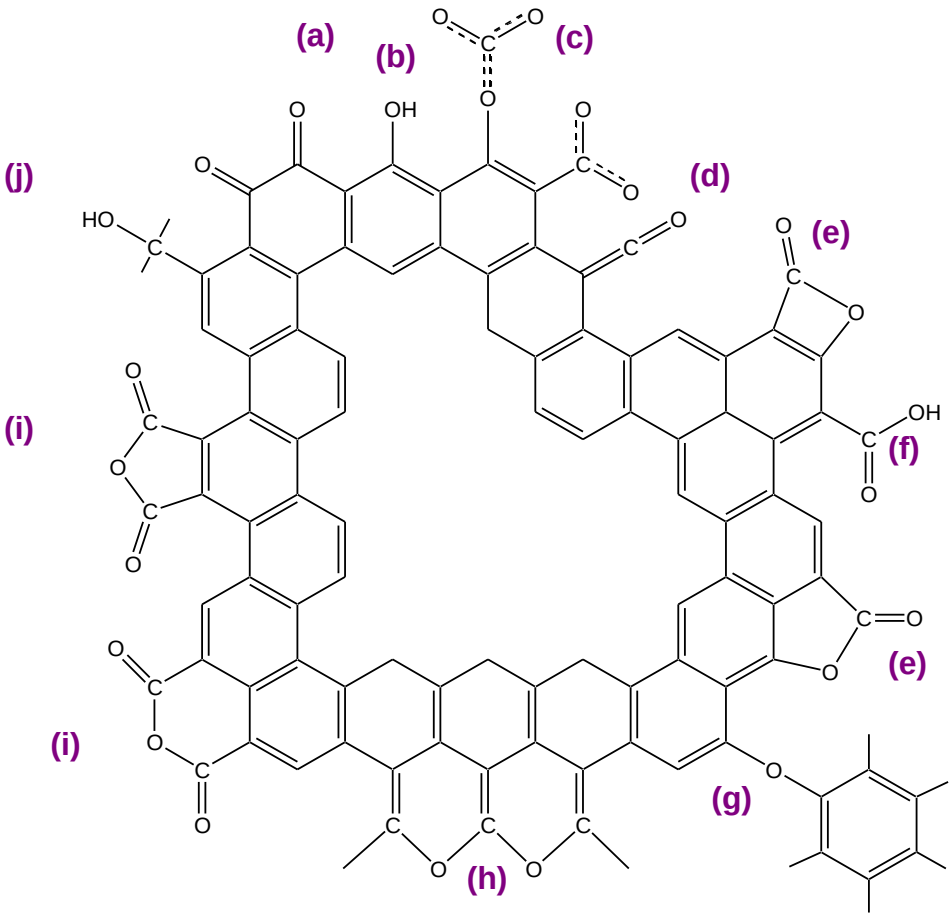

Figure 1.7 – The oxygen functionalities on carbon surfaces; (a) quinone, (b) phenol, (c) carboxyl carbonates, (d) ketene, (e) lactone, (f) carboxylic acid, (g) ether bridge, (h) cyclic ethers, (i) cyclic anhydride, (j) alcohol. All of these have been identified by IR spectroscopy.

The total surface area or BET surface area for activated carbon is in the region of 1000 – 3000 m^2 g^{-1}, which is divided into approximately 1000 m^2 g^{-1} of micropores (< 1 nm, IUPAC), 10-100 m^2 g^{-1} of mesopores (1-25 nm, IUPAC), and 1 m^2 g^{-1} of macropores (> 25 nm, IUPAC). It is often assumed that materials with greater surface areas will have greater capacitances but it should be noted that this is only applicable if all of the surface area is accessible, for example if the size of the interconnecting pores is large enough for the electrolyte ions to penetrate. Therefore, research tailoring electrode pore size for optimum performance with an electrolyte is beneficial in terms of improving supercapacitor performance. Similarly, it is also important to ensure that the porosity does not decrease the mechanical strength of the electrode. The specific capacitance of a variety of branded activated carbons in tetraethylammonium tetrafluoroborate were investigated by Centeno *et al.* and values were shown to be in the region of 50-160 F g^{-1}[48].

A computer generated model of activated carbon, obtained by Petersen *et al.*[82] using the reverse Monte Carlo method is given in ***Figure 1.8.*** It shows the presence of graphene planes containing mainly sp^2 bonded carbons, just as there are in graphite, but shows that the interplanar spacing is severely disrupted by sp^3 bonded carbons. These sp^3 sites increase the stiffness of the carbon but damages its conductivity.

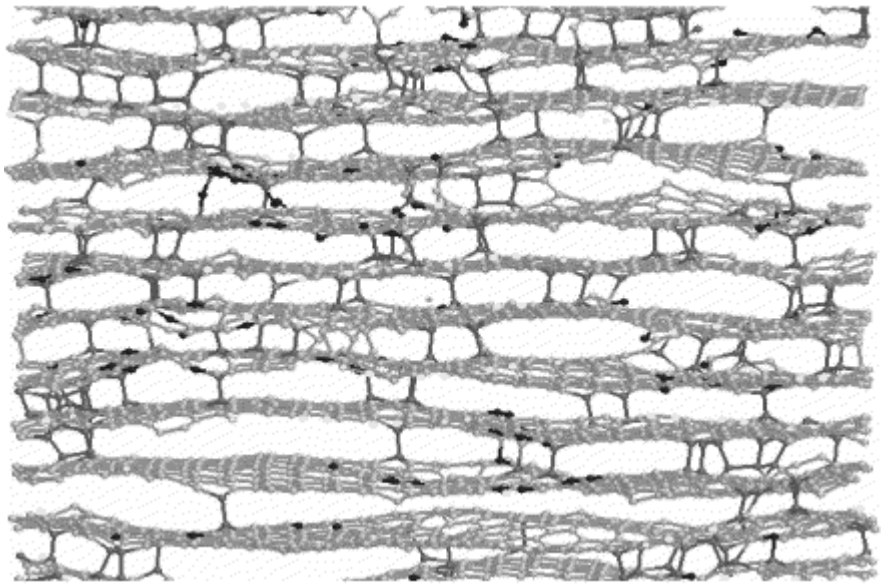

Figure 1.8 − A computer generated image of activated carbon, illustrating the typical pore size distribution.

1.5.3 − Polyimide (cell material and sealant)

Polyimides are a class of thermally stable polymers (T > 400 ºC) based on stiff aromatic backbones. Their high performance properties, such as thermal stability, electrical insulation, chemical resistance, and high mechanical strength has resulted in their use across a variety of fields including electronics, optical films, spacecraft, and in this thesis, supercapacitors. The first aromatic polyimide was reported by Bogert *et al.* in1908[83]. In the 1950s workers at Dupont[84] developed the first high molecular weight polyimides and pioneered a two-step process for their synthesis. The two step poly(amic acid) process is still the primary method used today. It involves reacting a dianhydride with a diamine at ambient conditions in a dipolar aprotic solvent such as *N*,*N*-dimethylacetamide or *N*-methylpyrrolidinone to yield the corresponding poly(amic acid). The poly(amic acid) is then cyclised into the final polyimide

at high temperature (200-300 ºC). Kapton™ (poly(4,4'-oxydiphenylene-pyromellitimide) is the most developed polyimide. It had a temperature stability range of −269 ºC to 400 ºC and is synthesised *via* a pyromellitic dianhydride monomer and 4,4´-oxydianiline. The reaction scheme for the synthesis is shown in ***Figure 1.9***[85].

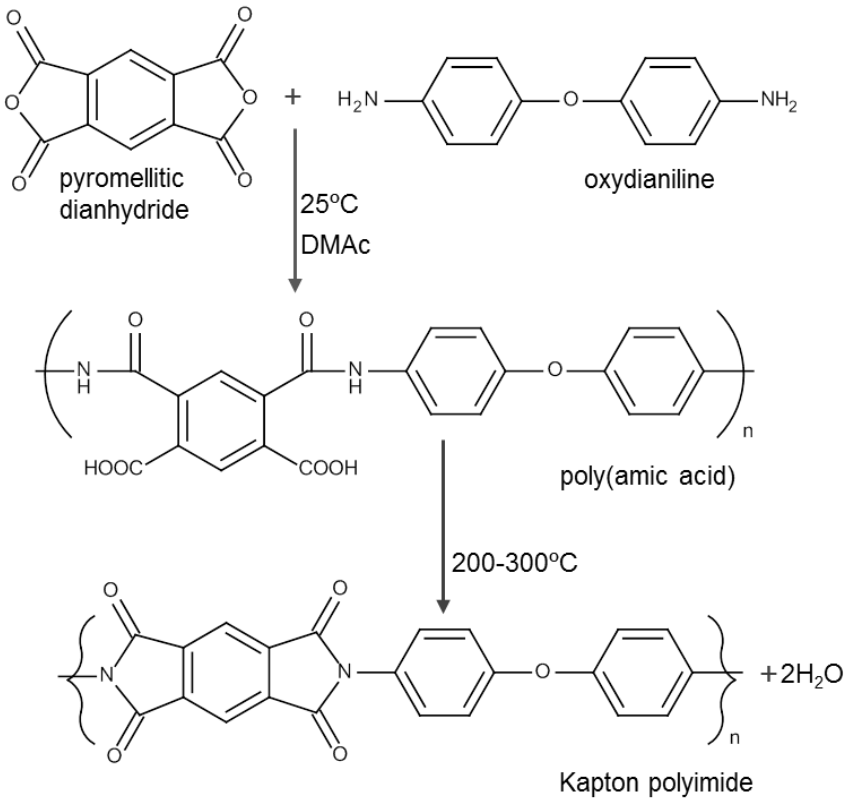

Scheme 1.1 – The reaction scheme for the formation of Kapton polyimide used in this thesis. DMAc is an abbreviation for N,N-dimethylacetamide.

1.5.4 − Fumed silica (gelling agent)

Fumed silica is an exceptionally pure form of amorphous silicon dioxide formed by the flame hydrolysis of volatile chlorosilanes in an oxyhydrogen flame at 1800 ºC[86].

$$SiCl_4 + 2H_20 \rightarrow SiO_2 + 4HCl \qquad \textbf{Equation 1.7}$$

The reaction produces microscopic droplets of amorphous silica which collide and fuse to form branched, chain-like aggregates in an extended three-dimensional structure. These aggregates typically consist of chains which are 10-30 spheres long (0.1-0.2 μm). As the reaction cools below the fusion temperature of silica (1710 ºC), further collisions result in reversible mechanical entanglement or agglomeration[86]. The hydrophilic nature of fumed silica produced *via* this method arises from the hydroxyl groups that adhere to the surface during its formation. It is thought that approximately 3.5-4.5 hydroxyl groups exist per square milli-micron of silica surface[86]. Hydrophobic fumed silica can be created by reacting hydrophilic fumed silica with reactive silanes such as chlorosilane or hexamethyldisilane, which give it water repelling properties[87].

Fumed silica has a low bulk density but an extremely high surface area (50–600 $m^2 g^{-1}$) and confers viscosity increasing behaviour when added to liquids[86,88]. As a result of this, fumed silica is commonly used as a non-toxic thickening agent in industrial products such as paints, coatings, and printing inks.

1.5.5 – Glass fibre (cell separator)

Glass fibre finds uses in many areas, including reinforcement, filtration, and insulation[89]. Bulk properties of glass fibre include good high electrical insulation, low moisture absorption, high strength to weight ratio, heat resistance, and chemical inertness. It is stable up to temperatures of 850 °C.

Glass fibre is synthesised in three steps. To begin, glass is melted in a furnace at *T*~1500 °C to form a uniformly viscous molten glass (0.4-0.5 P). The molten glass then undergoes a process called “fiberisation” where it is extruded through a platinum alloy tray called a “bushing”. The bushing contains several thousand orifices, with diameters of 0.793-3.175 mm[90] creating continuous fibres of the same size as they are drawn through. While the glass is still viscous, further extrusion produces filaments with finer diameters (3-20μm) after which the fibres are cooled. The individual fibres may then be treated by chemical and physical methods (‘sizing’) to tailor their properties, for example to increase their compatability with resins or their adhesion ability, before being combined into multi-fibre strands. The multi-fibre strands are then used to create a range of glass fibre products such as matt, cloth and paper.

Commercial glass fibres are denoted by a letter prefix. These are listed in ***Table 1.4***[89].

Table 1.4 − Properties of commercial glass fibres.

Commercial name	Letter designation	Property / Characteristic
E-glass	E (electrical)	Low electrical conductivity
S-glass	S (strength)	High strength
C-glass	C (chemical)	High chemical durability
M-glass	M (modulus)	High stiffness
A-glass	A (alkali)	High alkali or soda lime glass
D-glass	D (dielectric)	Low dielectric constant

1.6 – Areas for investigation

The primary scientific objective for this thesis was to design, construct and test a high temperature supercapacitor capable of operation over the temperature range 20 ºC to 220 ºC. A secondary objective was to determine the compatibility of ionic liquids with other cell components at high temperature and, if required, consider mitigating any problems. In addition to the main objectives, several other research areas were explored as key to optimising the performance.

As previously mentioned, ionic liquids are particularly attractive solvents for supercapacitors due to their wide voltage windows, which correlate with enhanced energy storage and power delivery as shown in ***Equation 1.3***. As a result, it was clear that it would be advantageous to identify the properties of ionic liquids that correlate with enhanced voltage stability. This would allow ionic liquids to be designed with larger energy storage capabilities than previously reported. Additionally, it would also be useful to be able to measure the conductivity ionic liquids with extremely high precision. The internal resistance of a supercapacitor is directly affected by the electrical conductivity of the solvent medium, and these measurements would also allow the precise relationship between conductivity and temperature to be determined, a relationship currently debated in the literature. However, due to the price of ionic liquids it would also be better, in terms of cost, to be able to measure their conductivity in a low sample volume (a few mls). Designing a miniature conductivity probe would make this possible.

Finally, for carbon electrodes, there are two mechanisms contributing to energy storage; electrochemical double layer capacitance (as a result of potential driven charge separation at the electrode|electrolyte interface) and pseudocapacitance (resulting from faradaic, charge transfer reactions into surface states). However, any additional faradic processes are unwanted as they may produce products that interfere with the operation of the device. Consequently, it would be beneficial to find a way of selectively inhibiting such faradaic reactions at the electrode surface whilst maintaining electrode capacitance.

1.7 – References

[1] Chen, C., Zhao, D. & Wang, X. *Influence of addition of tantalum oxide on electrochemical capacitor performance of molybdenum nitride*. Materials Chemistry and Physics, 97: 156-161 (2006).

[2] Zhang, Y., Gui, Y., Wu, X., Feng, H., Zhang, A. & Wang, L. *Preparation of nanostructures NiO and their electrochemical capacitive behaviours*. International Journal of Hydrogen Energy, 34: 2467-2470 (2009).

[3] Hall, P. J. & Bain, E. J. *Energy-storage technologies and electricity generation*. Energy Policy, 36: 4352-4355 (2008).

[4] Haas, O. & Cairns, E. Journal of Electrochemical Energy Storage (RSC Annual Reports). Section C, 95: pp 163-197 (1999).

[5] Zhang, Y., Feng, H., Wu, X., Wang, L., Zhang, A., Xia, T., Dong, H., Li, X. & Zhang, L. *Progress of electrochemical capacitor electrode materials: A review*. International Journal of Hydrogen Energy, 34: 4889-4899 (2009).

[6] Conway, B. *Electrochemical Supercapacitors, Scientific Fundamentals and Technological Applications.* Kluwer Academic / Plenum Publishers, New York, Chapter 2, pp11-31 (1999).

[7] Conway, B. E. *Electrochemical Supercapacitors. Scientific Fundamentals and Technological Applications*. Kluwer academic / Plenum publishers, New York, Chapter 1, pp1-9 (1999).

[8] van Musschenbroek, P (translated by P. Massuet). *Essai de Physique*, 1: (1739).

[9] Edwin J. Houston. *Electricity in Every-day Life*. P. F. Collier & Son, California, (1905).

[10] Maxwell, James Clerk. "*XXV. On physical lines of force*." The London, Edinburgh, and Dublin Philosophical Magazine and Journal of Science, 21**(**139): 161-175 (1861).

[11] Becker, H. E, US Patent 2,800,616 (to General Electric Company.), "*Low Voltage Electrolytic Capacitor*" (July 23, 1957).

[12] Rightmire, R. A, US Patent 3,288,641 (to SOHIO), "*Electrical Energy Storage Apparatus*" (Nov 29, 1966).

[13] Boos, D. L, US Patent 3,536,963 (to SOHIO), "*Electrolytic Capacitor Having Carbon Paste Electrodes*" (Oct 27, 1970).

[14] http://prezi.com/f8ukvhgprl_v/supercapacitor-technology-forecast/ (last accessed 25th November 2012).

[15] Saiki, Y. *New EDLC Developments for Portable Consumer Applications after 25 Years in the Business*," Proc Advanced Capacitor World Summit 2004, Washington DC, (July 14-16, 2004).

[16] Hung, K., Masarapu, C., Tsehao, Ko. & Wei, B. *Wide-temperature range operation supercapacitors from nanostructured activated carbon fabric.* Journal of Power Sources, 193: 944-949 (2009).

[17] Masarapu, C., Feng, H., Kai, Z., Hung, H. & Wei, B. *Effect of Temperature on the Capacitance of Carbon Nanotube Supercapacitors.* ACS Nano, 3(8): 2199-2206 (2009).

[18] Lin, R., Taberna, P. L. Fantini, S., Presser, V., Perez, C. R., Malbosc, F., Rupesinghe, N. L. Teo, K. B. K. Gogotsi Y. & Simon, P. *Capacitive Energy Storage from 50 to 100 C Using an Ionic Liquid Electrolyte.* Journal of Physical Chemistry Letters, 2: 2396-2401 (2011).

[19] Largeot, C., Taberna, P. L. Gogotsi, Y. & Simona, P. *Microporous Carbon-Based Electrical Double Layer Capacitor Operating at High Temperature in Ionic Liquid Electrolyte.* Electrochemical and Solid-State Letters, 14(12): 174-176 (2011).

[20] Kotz, R., Hahn, M. & Gallay, R. *Temperature behavior and impedance fundamentals of supercapacitors.* Journal of Power Sources, 154: 550-555 (2006).

[21] Liu, W., Yan, X., Langa, J. & Xuea, Q. *Effects of concentration and temperature of EMIMBF4/acetonitrile electrolyte on the supercapacitive behavior of graphene nanosheets.* Journal of Materials Chemistry, 22: 8853-8861 (2012).

[22] Xu, B., Wu, F., Chen, R., Cao, G., Chen, S. &, Yang, Y. *Mesoporous activated carbon fiber as electrode material for high-performance electrochemical double layer capacitors with ionic liquid electrolyte*. Journal of Power Sources, 195: 2118-2124 (2010).

[23] Anouti, M., Timperman, L., el Hilali, M., Boisset, A. & Galiano, H. *Sulfonium Bis(trifluorosulfonimide) Plastic Crystal Ionic Liquid as an Electrolyte at Elevated Temperature for High-Energy Supercapacitors.* Journal of Physical Chemistry. C, 116: 9412-9418 (2012).

[24] Balducci, A., Dugas, R., Taberna, P. L., Simon, P., Plée, D., Mastragostino, M. & Passerini, S. *High temperature carbon–carbon supercapacitor using ionic liquid as electrolyte*. Journal of Power Sources, 165(2): 922-927 (2007).

[25] Hastak, R. S., Sivaraman, P., Potphode, D. D., Shashidhara, K. & Samui, B. *All solid supercapacitor based on activated carbon and poly [2,5-benzimidazole] for high temperature application*. Electrochimica Acta, 59: 296-303 (2012).

[26] Singh, G. & Kumar, A. *Ionic liquids: Physico-chemical, solvent properties and their applications in chemical processes*. Indian Journal of Chemistry A, 47: pp 495-503 (2008).

[27] Endres, F. & Zein El Abedin, S. *Air and water stable ionic liquids in physical chemistry.* Physical Chemistry Chemical Physics, 8: 2101-2116 (2006).

[28] Chemfiles Enabling Technologies: Ionic Liquids. Published by Sigma-Aldrich Co, 5(6): 2 (2005).

[29] Izmailova, M. Y., Rychagov, Y., Den'shchikoc, K. K., Vol'fkovich, Y. M., Lozinskaya, E. I. & Shaplov, A. S. *Electrochemical Supercapacitor with Electrolyte Based on an Ionic Liquid.* Russian Journal of Electrochemistry, 48: pp 1014-1015 (2009).

[30] Suarez, P. A. Z., Consorti, C. S., de Souza, R. F., Dupont. J. & Goncąlves, R. S. *Electrochemical behaviour of vitreous glass carbon and platinum electrodes in the ionic liquid 1-n-butyl-3-methylimidazolium trifluoroacetate.* Journal of the Brazilian Chemical Society, 13(1): 106-109 (2002).

[31] Galiński, M., Lewandowski. A. & Stępniak, I. *Ionic liquids as electrolytes*. Electrochimica Acta, 51: 5567-5580 (2006).

[32] Siegmund, G. & Weiner, J. *Ueber einige Abkömmlinge des Propylamins*. Berichte der deutschen chemischen Gesellschaft, 21(2): 2669-2679 (1888).

[33] Walden, P. Bull. Russian Academy of Sciences, St. Petersburg, 1800 (1914).

[34] Wier, T. P. Jr. & Hurley, F. H. Journal of the Electrochemical Society, 98(5): 203-206 (1951).

[35] Wier, T. P. Jr. & Hurley, F. H. US Patent 4,446,349 (1948).

[36] Wilkes, J. S. & Zaworotko, M. J. *Air and water stable 1-ethyl-3-methylimidazolium based ionic liquids*. Journal of the Chemical Society, Chemical Communications, 13: 965-967 (1992).

[37] Bohnote, P., Dias, A. P., Papageorgiou, N., Kalyanasundaram, K. & Gräzel, M. *Hydrophobic highly conductivityy ambient temperature molten salts*. Inorganic Chemistry, 35(5): 1168-1178 (1996).

[38] Trulove, P. C., De Long, H. C., Stafford, G. R. & Deki, S. *Molten Salts XII*, The Electrochemical Society Proceedings Series, Pennington, New Jersey, USA, 99(41): 473-484 (1998).

[39] MacFarlane, D. R., Meakin, P., Sun, J., Amini, N. & Forsyth, M. *Pyrrolidinium imides: a new family of molten salts and conductive plastic crystal phases*. Journal of Physical Chemistry V, 103(20): 4164-4170 (1990).

[40] Wasserscheid, P. & Welton, T. *Ionic Liquids in Syntheses*, Wiley-VCH; Weinheim, Germany (2003).

[41] Sun, X. & Dai, S. *Electrochemical investigations of ionic liquids with vinylene carbonate for applications in rechargeable lithium ion batteries*. Electrochimica Acta, 55: pp 4618-4626 (2010).

[42] Pang, Y., Li, X., Shi, G, Wang, F. & Jin, L. *Electrochromic properties of poly(3-chlorothiophene) film electrodeposited on a nanoporous TiO_2 surface via a room*

temperature ionic liquid and its application in an electrochromic device. Thin Solid Films, 516: pp 6512-6516 (2002).

[43] Zhao, D., Wu, M., Kou, Y. & Min, E. *Ionic liquids: applications in catalysis*. Catalysis Today, 74: 157-189 (2002).

[44] Pereiro, A. B. & Rodriguez, A. *Application of the ionic liquid Ammoeng 102 for aromatic/aliphatic hydrocarbon separation*. The Journal of Chemical Thermodynamics, 41(8): pp 951-956 (2009).

[45] Wei, D. & Ivaska, A. *Applications of ionic liquids in electrochemical sensors*. Analytica Chimica Acta, 607: 126-135 (2008).

[46] Koel, M. *Ionic Liquids in chemical analysis*, In: Analytical Chemistry Series, 1st Edition. CRC Press, Taylor & Francis Group, USA (2009).

[47] Kuboki T., Okuyama T., Ohsaki T. & Takami N. *Lithium-air batteries using hydrophobic room temperature ionic liquid electrolyte*. Journal of Power Sources, 146: 766–769 (2005).

[48] Pandey, G. P., Kumar, Y. & Hashimi, S. A. *Ionic liquid incorporated polymer electrolytes for supercapacitor application*. Indian Journal of Chemistry, 49(A): 743-751 (2010).

[49] Frackowiak, E. *Supercapacitors Based on Carbon Materials and Ionic Liquids.* Journal of the Brazilian Chemical Society, 17: 1074-1082 (2006).

[50] Brennecke, J. F. & Gurkan, B. E. *Ionic Liquids for CO_2 Capture and Emission Reduction*. Journal of Physical Chemistry Letters, 1: 3459-3464 (2010).

[51] Hasib-ur-Rahman, M., Siaj, M. & Larachi, F. *Ionic liquids for CO_2 capture-development and progress*. Chemical Engineering and Processing. Chemical Engineering and Processing: Process Intensification, 49: 313-322 (2010).

[52] Karadas, F., Atilhan, M. & Aparicio. S. *Review on the Use of Ionic Liquids (ILs) as Alternative Fluids for CO_2 and Natural Gas Sweetening*. Energy & Fuels, 24: 5817-5828 (2010).

[53] Zhang, X., Zhang, X., Dong, H., Zhao, Z., Zhang, S. & Huang, Y. *Carbon capture with ionic liquids, overview and progress*. Energy & Environmental Science, 5: 6668-6681 (2012).

[54] Kowsari, E. *Advanced Applications of Ionic Liquids in Polymer Science* in *Ionic Liquids: Applications and Perspectives*. Edited by Kokorin, A (Pub InTech, Rijeka, Croatia) Chapter 1: pp3-27 (2011).

[55] Mudring, V. A., Alammar, T., Bäcker, T. & Richter, K. *Nanoparticle Synthesis in Ionic Liquids* in Ionic Liquids: From Knowledge to Application. ACS Symposium Series, Vol 1030. Edited by Plechkova, N. V., Rogers, R. D. & Seddon, K. R. (pub by American Chemical Socety) Chapter 12: pp177–188 (2009).

[56] Nan, A. & Lievscher, J. *Ionic Liquids as Advantageous Solvents for the Preparation of Nanostructres,* in Applications of Ionic Liquids in Science & Technology. Edited by Handy, S. Chapter 23: pp549-564 (2011).

[57] Tsuda, T., Imanishi, A., Torimoto, T. & Kuwabata, S. *Nanoparticle preparation in Room-Temperature Ionic Liquids under Vacuum Condition in Ionic Liquids: Theory, Properties, New Approaches*. Edited by Kokorin, A, (pub. InTech, Rijeka, Croatia) Chapter 23: pp549-564 (2011).

[58] Pinkert, A., Marsh, K. N., Pang, S. & Staiger, M. P. *Ionic liquids and their interaction with cellulose*. Chemical Reviews, 109: 6712–6728 (2009).

[59] Wang, H., Gurau, G. & Rogers, R. D. *Ionic liquid processing of cellulose*. Chemical Society Reviews, 41(4): 1519-1537 (2012).

[60] Gibril M. E. *Current Status of Applications of Ionic Liquids for Cellulose Dissolution and Modifications: Review*. International Journal of Engineering, Science & Technology (IJEST), 4(7): 3556-3571 (2012).

[61] Liu, Y., Chen, Ji. & Li, D. *Applications and Perspective of Ionic Liquids on Rare Earths Green Separation* in In Separation Science & Technology, 47(2): 223-232 (2009).

[62] Gluklov, L. M., Greish, A. A. & Kustov, L. M. *Electrodeposition of Rare Earth Metals Y, Gd, Yb in Ionic Liquids*. Russian Journal of Physical Chemistry, 84(1): 104-108 (2009).

[63] Eßer, J., Wasserscheid, P. & Jess, A. *Deep desulfurization of Oil Refinary Streams by Extraction with Ionic Liquids*. Green Chemistry, 6: 316-322 (2004).

[64] Zhang, S. & Zhang, Z. C. *Novel properties of ionic liquids in selective sulfur removal from fuels at room temperature*. Green Chemistry, 4: 376-379 (2002).

[65] Luo, H., Dai, S., Bonnesen, P. V. & Buchanan AC. *Separation of Fission Products Based on Room-Temperature Ionic Liquids*. Nuclear Waste Management: Accomplishments of the Environmental Management Science Program. ACS Symposium Series Volume 943. Edited by Wang P, W. & Zachry, T. Chapter 8, pp 146–160 (2006).

[66] Van Valkenburg, M. E. V., Vaughn, R. L., Williams, M. & Wilkes, J. S. *Thermochemistry of ionic liquid heat-transfer fluids.* Thermochimica Acta. 425(1-2): 181–188 (2005).

[67] Liu, H., Maginn, E., Visser, A. E., Bridges, N. J. & Fox, E. B. *Thermal and Transport Properties of Six Ionic Liquids: An Experimental and Molecular Dynamics Study*. 51(21): 7242–7254 (2012).

[68] Palacio, M. & Bhushan, B. *A Review of Ionic Liquids for Green Molecular Lubrication in Nanotechnology*. Tribology Letters, 40(2): 247-268 (2010).

[69] Bermúdez, M. D., Jiménez, A. E., Sanes, J. & Carrión, F. J. *Ionic Liquids as Advanced Lubricant Fluids*. Molecules, 14: 2888-2908 (2009).

[70] Doerr, N., Gebeshuber, I. C., Holzer, D., Wazenboeck, H. D., Ecker, A., Pauschitz, A. & Franek, F. *Evaluation of Ionic Liquids as Lubricants*. Journal of Microengineering and Nanoelectronics, 1(1): 29-34 (2010).

[71] Zhou, F., Liang, Y., Lui, W. *Ionic liquids lubricants designed for engineering applications*. Chemical Society Reviews, 38(9): 2590-2599 (2009).

[72] Plechkova, N. V. & Seddon, K. R. *Applications of ionic liquids in the chemical industry.* Chemical Society Reviews, 37: 123-150 (2008).

[73] Kumar, A. *Surface Tension, Viscosity, Vapour Pressure, Density, and Sound Velocity for a Sysyem Miscible Continuosly from a Pure Fused Electrolyte to a Nonaqeous Liquid with a Low Dielectric Constant: Anisole with Tetra-n-butylammonium Pictate*. Journal of the American Chemical Society, 115: 9243-9248 (1993).

[74] McEwen, A. B., Ngo, H. L., LeCompte, K. & Goldman, J. L. *Electrochemical Properties of Imidazolium Salt Electrolytes for Electrochemical Capacitor Applications*. Journal of the Electrochemical Society, 146: 1687-1695 (1999).

[75] Arbizzani, C., Biso, M., Cericola, D., Lazzari, M., Soavi, F. & Mastragostino, M. *Safe, high-energy supercapacitors based on solvent-free ionic liquid electrolytes*. Journal of Power Sources, 185: 1575-1579 (2008).

[76] Jarosik, A., Krajewski, R., Lewandowski, A. & Radzimski, P. *Conductivity of ionic liquids in mixtures.* Journal of Molecular Liquids, 123: 43-50 (2006).

[77] Sun, J., Forsyth, M. & MacFarlane, D. R. *Room-Temperature Molten Salts Based on the Quaternary Ammonium Ion.* Journal of Physical Chemistry B, 102(44): 8858-8864 (1998).

[78] Matsumoto, H., Kageyama, H. & Myazaki, Y. *Room temperature ionic liquids based on small aliphatic ammonium cations and asymmetric amide anions*. Chemistry Communications, pp 1726-1727 (2002).

[79] Ngo, H., LeCompte, K., Hargens, L. & McEwen A. B. *Thermal properties of imidazolium ionic liquids*. Thermochimica Acta, 357-358: 97-102 (2000).

[80] Van Valkenburg, M. E., Vaughan, R. L., Williams, M. & Wilkes, J. S. 15th Symposium on Thermophysical Properties (2003).

[81] Pandolfo., A. G. & Hollenkemp, A. F. *Carbon properties and their role in supercapacitors*. Journal of Power Sources, 157: pp 11-27 (2006).

[82] Petersen, T., Yarovsky, I., Snook, I., Mcculloch, D. G., & Opletal, G. Structural analysis of carbonaceous solids using an adapted reverse Monte Carlo algorithm. Carbon, 41: 2403-2411 (2003).

[83] Bogert, T. M. & Renshaw, R. R. Journal of the American Chemical Society. 30: 1140 (1908).

[84] Sroog, C. E., Endrey, A. L., Abramo, S. V., Berr, C. E., Edward, W. M. & Olivier, K.L. Journal of Polymer Sciences, Part A, 3: 1373 (1965).

[85] Takekoshi, T., Polyimides- Fundamentals and Applications, Edited by Ghosh, M. K. & Mittal, K. L. Marcel Dekker, New York, Chapter 2 (1996).

[86]http://www.sigmaaldrich.com/etc/medialib/docs/Aldrich/Product_Information_Sheet/s5130pis.Par.0001.File.tmp/s5130pis.pdf (last accessed 24th November 2012).

[87]http://www.powerchemical.net/library/public/fumed_silica/SiSiB_Fumed_Silica.pdf (last accessed 24th November 2012).

[88] http://www.azom.com/article.aspx?ArticleID=1386 (last accessed 24th November 2012).

[89] Wallenberg, F. T., Watson, J. C. & Li, H. *Glass Fibers*, ASM Handbook, American Technical Publishers, 21: (2001).

[90] Loewenstein, K. L. *The Manufacturing Technology of Continuous Glass Fibers*, 3rd Edition (revised), Elsevier, Amsterdam (1993).

Chapter 2 – Experimental Techniques

The main experimental techniques that have been used in this thesis are:

- Cyclic voltammetry
- Conductivity
- Impedance spectroscopy
- Scanning electron microscopy
- Differential scanning calorimetry
- Screen printing

The following chapter aims to give an overview of these techniques. Relevant theory and methods of analysis are also provided where appropriate.

2.1 – Cyclic voltammetry

Cyclic voltammetry is a very popular electrochemical technique that measures current *I* (A) as a function of applied potential *E* (V). Current is a measure of the rate of flow of charge in a complete circuit and applied potential difference is a measure of the energy carried by the charged species, and can be thought of as '*electrical pressure'*. Cyclic voltammetry allows information to be gained from the system under study. For example, it allows the determination of thermodynamic parameters, such as the formal redox potentials of electroactive species, and kinetic parameters, such as rate constants[1].

Cyclic voltammetry principally operates with a three electrode set up, a working electrode, W, a reference half-cell, R, and a counter electrode, C, which are all controlled by a potentiostat. The working electrode is the interface under study, the counter electrode passes the same current as the working electrode to complete the circuit, and the reference half-cell provides a stable reference potential against which all applied potentials to the working electrode surface are measured.

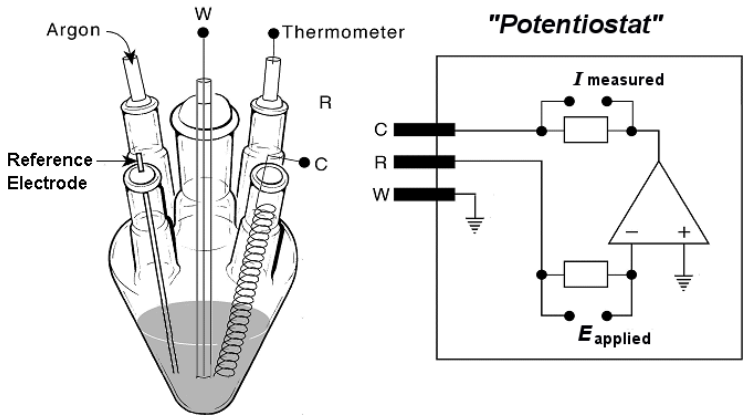

Figure 2.1 – An illustration of a three-electrode set up for an electrochemical cell (left). A schematic diagram of a potentiostat (right).

Stable reference electrodes are non-polarisable so that the electrode maintains a fixed potential even in the presence of small currents[2]. There are numerous reference half-cells available, however, electrode potentials should, by convention, be reported against a standard hydrogen electrode (SHE)[3], an arbitrary zero reference. Nonetheless, it has become common practice to report applied potentials against the reference half-cell used experimentally. Ives and Janz[4] have tabulated the reference potentials of a variety of reference half-cells. The properties of the reference half-cells used in this thesis are given in ***Table 2.1*** with the SHE included for comparison.

Table 2.1 – Reference potentials of common reference half-cells in aqueous solutions at 25 ºC.

Reference half-cell	Half-cell equation	Reference potential / V
$H_2\|H^+$ (SHE)	$2H^+_{(aq)} + 2e^-_{(metal)} \leftrightarrows H_{2(gas)}$	0.0000
Ag|AgCl, $KCl_{(saturated)}$	$AgCl_{(s)} + e^-_{(metal)} \leftrightarrows Ag^0_{(s)} + Cl^-_{(aq)}$	0.197
$Hg\|Hg_2Cl_2$, $KCl_{(saturated)}$ (SCE)	$Hg_2Cl_{2(s)} + 2e^-_{(metal)} \leftrightarrows Hg^0_{(s)} + 2Cl^-_{(aq)}$	0.2412
Fc^+/Fc	$Fc^+_{(aq)} + e^-_{(metal)} \leftrightarrows Fc_{(aq)}$	0.64

In cyclic voltammetry, a potential difference is applied between the working and reference electrodes and 'swept' between two values linearly with time. The total current, a combination of faradaic and non-faradaic currents, is then recorded[5]. Faradaic currents arise

due to redox reactions at the electrode surface, while non-faradaic currents arise from a variety of sources, such as charging of the double layer.

A schematic diagram illustrating the principle of linear sweep and cyclic voltammetry is shown in ***Figure 2.2***. Linear sweep voltammetry involves a potential sweep in a single direction from one potential E_1 to another E_2. The scan direction can be in the positive or negative direction. In linear sweep voltammetry the linear sweep is terminated at the second potential E_2, but, in cyclic voltammetry the sweep direction is reversed, and the potential is swept to a third potential E_3. E_3 can be either the start potential $E_{3(i)}$ or some other potential $E_{3(ii)}$. At E_3, the scan may be terminated to record a single cycle or reversed again to record multiple cycles. The rate at which the potential is swept is fixed and defined as the scan rate $\frac{dE}{dt} = \nu$ (V s^{-1}).

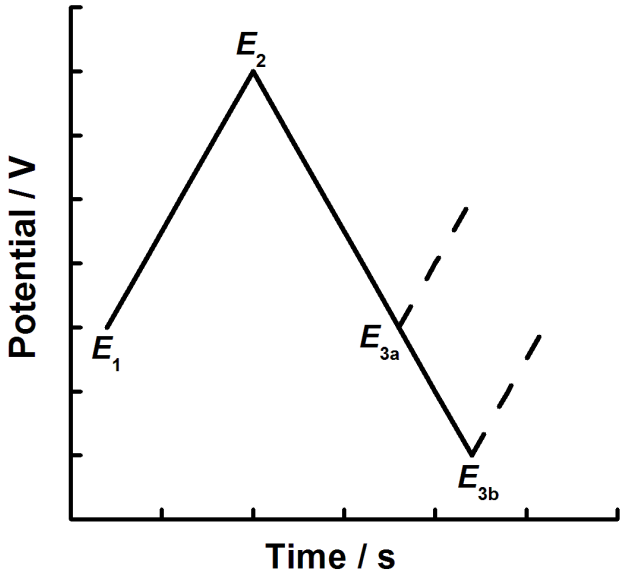

Figure 2.2 – Schematic diagram illustrating the principle of linear sweep and cyclic voltammetry.

2.1.1 – Faradaic processes: Voltammetric response for electrochemically reversible systems

A generic electron transfer reaction is shown in ***Equation 2.1***.

$$O + ne^- \leftrightarrows R \qquad \textit{Equation 2.1}$$

The corresponding voltammetric response shown in ***Figure 2.3***.

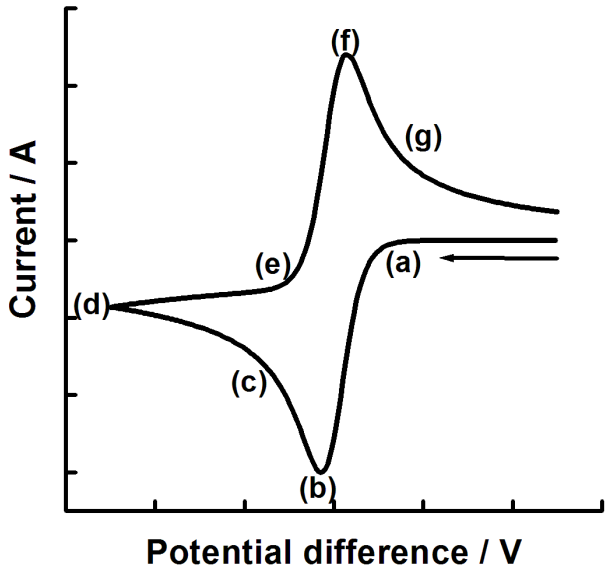

Figure 2.3 – A cyclic voltammogram illustrating a reversible electrode reaction.

At the start of the scan, the electrolyte solution initially contains only the oxidised species O, in uniform concentration at the electrode surface and in the bulk solution. As the applied potential is swept negative, cathodic current from non-faradaic reactions, i.e. capacitative charging is measured. When a potential negative enough for the electrochemical reduction of O is reached, a rapid increase in the cathodic current is observed as O is converted to R (a). A peak in the current I_p is observed at a peak potential E_p (b) when the surface concentration of O at the electrode becomes effectively zero and the concentration gradient starts to decrease. The current response is now purely reliant on the mass transport of the O to the surface, resulting in a non-steady state diffusion controlled response. Diffusion control is characterised by a decay in the measured current proportional to $t^{-\frac{1}{2}}$ (c)[5]. When the scan is then inverted (d), the forward electron transfer slows down and R, which is now in high concentrations at the electrode surface is oxidised back to O. Some of R present at the electrode surface is oxidised even before the formal oxidation potential is reached. This oxidation of R is signalled by a rapid increase in the anodic current (e) and a peak shaped current response is again observed (this time in the positive direction), (f).

Electrode reactions are divided into three different categories, reversible, irreversible and those in between (quasi-reversible). A concise discussion follows for each case.

Faradaic processes: reversible reactions

Under standard conditions, the concentrations of the oxidised species c_{O} and the reduced species c_{R} are unity. In that case the (heterogeneous) rate constant for electron transfer k_{f} (m s^{-1}) may be expressed in the form

$$k_{\mathrm{f}} = k_{\mathrm{f}}^{0} \exp\left(\frac{-\beta F(E - E^{0})}{RT}\right)$$

Equation 2.2

where k_{f}^{0} (m s^{-1}) is known as the *standard rate constant*. The latter is the value of k_{f} at the potential $E = E^{0}$ (i.e. at the standard potential). By definition,

$$k_{\mathrm{f}}^{0} = k_{\mathrm{b}}^{0} = k^{0}$$

Equation 2.3

Somewhat arbitrarily, but by a long-established electrochemical convention, a system exhibiting

$$k^{0} > 10^{-4} \text{ m s}^{-1}$$

Equation 2.4

is said to be ***electrochemically reversible***[6]. As the potential E is varied, such a system shows a very rapid variation of reaction rate (electrical current) in the vicinity of E^{0}.

In addition to this criterion, the following diagnostic tests can be applied to a cyclic voltammogram to confirm an electron transfer process is reversible (at 298 K)[1].

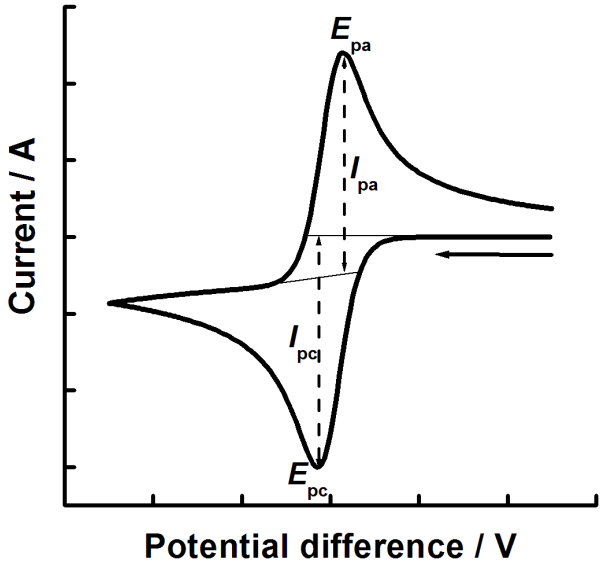

Figure 2.4 – A cyclic voltammogram illustrating a reversible electrode reaction. E_p is peak potential, I_p is peak current, a is anodic and c is cathodic.

1. The voltage separation ΔE_p between the current peaks for the oxidation $E_{pa}$and reduction processes E_{pc} is 57.2 mV for a one electron reaction

$$\Delta E_p = E_{pa} - E_{pc} = 0.0572\ V \qquad \textbf{Equation 2.5}$$

2. The ratio of the peak currents I_{pa} and I_{pc} is equal to one:

$$\left|\frac{I_{pa}}{I_{pc}}\right| = 1$$

Equation 2.6

3. The peak currents $I_{p,a} and\ I_{p,c}$ are proportional to the square root of the scan rate ν and that a plot $I_p\ vs\ \sqrt{\nu}$ is linear and passes through the origin.

$$I_p \propto \sqrt{\nu} \qquad \textbf{Equation 2.7}$$

4. The position of the peak potential is constant and independent of scan rate.

The peak current I_p for a reversible reaction is the result of a number of contributing factors described by the Randles[7-8]-Ševčík[9], ***Equation 2.8***,

$$I_p = 0.4463\, n\mathrm{F}AC\sqrt{\frac{n\mathrm{F}\nu D}{\mathrm{R}T}}$$

Equation 2.8

where n is the number of electrons transferred in the redox reaction, A is the accessible area of the electrode (cm^2), C is the concentration of the reactant (mol cm^{-3}), F is Faraday's constant (96,485.3365 C mol^{-1}), ν is the scan rate (V s^{-1}), D is the diffusion coefficient (cm^2 s^{-1}), R is the universal gas constant (8.3145 J K mol^{-1}), and T is the temperature (K). From a plot of I_p *vs.* $\sqrt{\nu}$ it is possible to determine various physical parameters such as n, A, C and D.

Faradaic processes: irreversible systems

In an irreversible reaction, the electrode reaction cannot be reversed due to slow reaction kinetics between the redox species and the working electrode. A system exhibiting

$$k^0 < 10^{-6}\ \mathrm{m\ s^{-1}}$$ ***Equation 2.9***

is said to be ***electrochemically irreversible***[6]. As the potential E is varied, such a system shows a very slow variation of reaction rate (electrical current) in the vicinity of E^0.

In irreversible systems, a large overpotential (η) is required before the redox reaction has the activation energy needed to occur. This causes a peak shift to the right (more positive potentials) for oxidation reactions or to the left (more negative potentials) for reduction reactions. The retarding effects of the kinetics also causes a shallower peak than in a reversible system. In a totally irreversible system, no reverse peak is observed. A typical cyclic voltammogram for an irreversible system is given in ***Figure 2.5***.

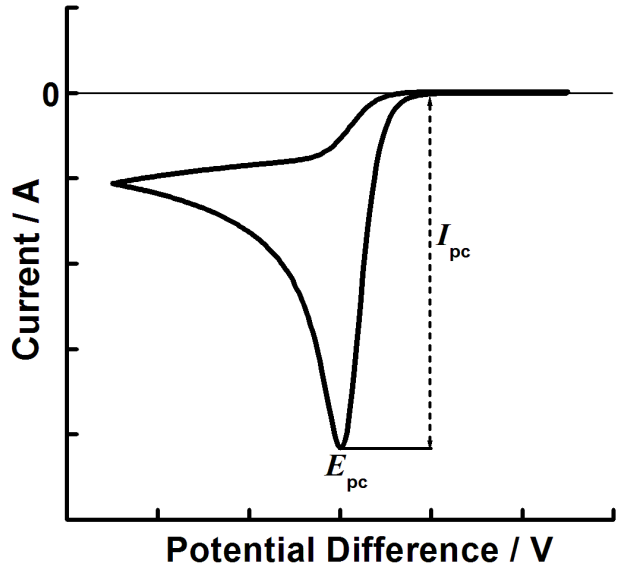

Figure 2.5 – A cyclic voltammogram illustrating an irreversible electrode reaction. E_p is peak potential, I_p is peak current, a is anodic and c is cathodic.

The following diagnostic tests can be applied to a cyclic voltammogram to confirm an electron transfer process is totally irreversible (at 298 K)[1].

1. No reverse peak

2. The peak current I_{pc} is proportional to the square root of the scan rate ν and that a plot $I_{pc}\ vs\ \sqrt{\nu}$ is linear and passes through the origin.

$$I_{pc} \propto \sqrt{\nu} \qquad \textbf{Equation 2.10}$$

3. The peak potential $E_{p,c}$ will shift 30 mV with every decade increase in scan rate ν.

4. The peak potential $E_{p,c}$ and the half-peak potential will differ by 48 mV.

For an irreversible system, the Randles[7-8]-Ševčík[9] equation takes the following form,

$$I_p = 0.496\, n\sqrt{\alpha n}\mathrm{F}AC\sqrt{\frac{n\mathrm{F}\nu D}{\mathrm{R}T}}$$

Equation 2.11

where α is the transfer coefficient.

Quasi reversible systems exhibit behaviour intermediate between reversible and irreversible reactions, i.e. the standard rate constant falls between the limits 10^{-4} and 10^{-6} m s^{-1}[6]. They will not meet all of the listed criteria for reversible or irreversible cases.

2.1.2 – Non-faradaic processes

Non-faradaic (capacitive) current does not arise from redox reactions. It arises from charge separation at the electrode|solution (supercapacitor) or electrode-electrode (capacitor) interface. The electrode-solution interface has been shown to behave like a capacitor and many elaborations of this model have been proposed[10-13]. However, unlike a simple capacitor, the interfacial capacitance depends on the applied potential. An example of a non-faradaic (capacitance current) is given in ***Figure 2.6***.

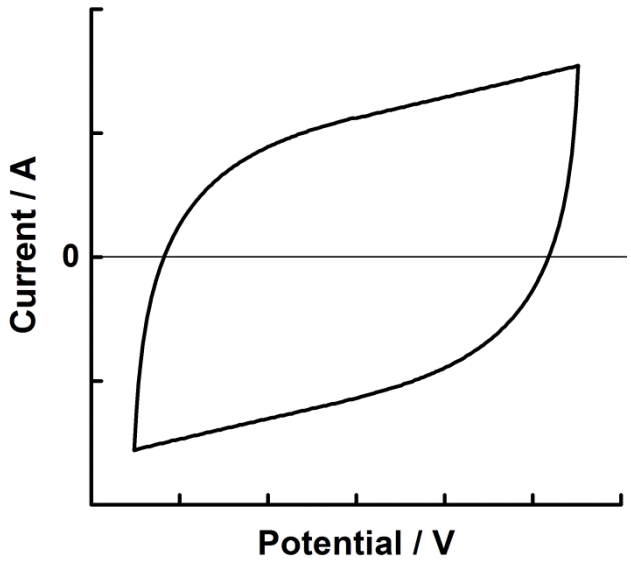

Figure 2.6 – A typical cyclic voltammogram arising from non-faradaic processes.

2.1.3 – Determining experimental parameters from cyclic voltammetry

Much information on faradaic and non-faradaic processes can be derived from the analysis of cyclic voltammetry. Here, some examples are given.

Tafel slopes

The current-voltage curve for a single electron transfer (not under diffusional control) is given by the Butler-Volmer equation.

$$I = I_0 \left\{ -\exp\left(\frac{-\beta_f F\eta}{RT}\right) + \exp\left(\frac{\beta_b F\eta}{RT}\right) \right\}$$

Equation 2.12

Where I is the current (A), I_0 is the exchange current, β_f and β_b are symmetry factors for the forwards and backwards reactions respectively, and η is the overpotential (V). Note for a reduction process $\beta_f = \alpha$ and $\beta_b = (1-\alpha)$, and $\eta = E - E^0$. All other constants have previously been defined.

Rearrangement of the Tafel equation[14] into modern format produces.

$$\log|I| = a + b\eta \qquad \textbf{Equation 2.13}$$

A plot of overpotential η versus the logarithm of the modulus current is called a Tafel Plot. The linear region of this plot, which is observed at high overpotentials (> 0.1 V), is called a Tafel Slope. b is the gradient of the Tafel slope and a is the exchange current. Such plots allow comparison of experimental and theoretical values and can aid in determining a reaction mechanism. An example of a Tafel plot for an oxidation and reduction is given in ***Figure 2.7***.

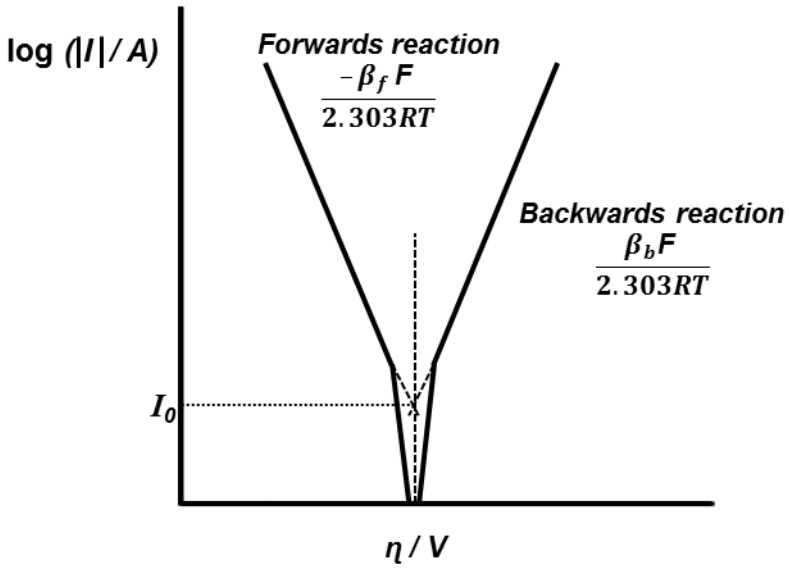

Figure 2.7 – An illustration of the Tafel slopes for a one electron reversible reaction. In this case, the forwards reaction is the cathodic Tafel slope and the backwards reaction is the anodic Tafel slope.

Fletcher[15] has calculated theoretical Tafel slope values for various reaction schemes, ***Table 2.2***. In the table E indicates an electrochemical step, C indicates a chemical step, D indicates a dimerization step, and a circumflex accent (^) indicates a rate-determining step. Δ is a small correction factor equal to $F\eta/2\lambda$, where F if the Faraday constant, η is the over potential, and λ is the reorganisation energy.

Fletcher and Varley[16] have listed the criteria needed to obtain accurate and precise Tafel slope values. These are:

1. No ligand substitution in the inner sphere of the reactant species.
2. A single reactant species (no significant speciation).
3. A high concentration of reactant species.
4. Data collection over more than two orders of magnitude.
5. A low faradaic background current (no parallel reactions).
6. Minimal mains interference (or suitable digital filtering thereof).
7. Minimal IR drop (minimal ohmic distortions).
8. A high concentration of supporting electrolyte
9. no significant reactant adsorption.

10. Minimal capacitive charging currents.
11. Enough data to provide 95% confidence in any derived parameter.

Table 2.2 – Tafel slopes for multistep electrochemical reactions.

Reaction scheme	**Tafel slope *b* / mV decade^{-1}**
$\hat{C}E$	∞
$\hat{C}ED$	∞
$\hat{E}$	$120/(1-\Delta)$
$\hat{E}E$	$120/(1-\Delta)$
$\hat{E}EE$	$120/(1-\Delta)$
$\hat{E}C$	$120/(1-\Delta)$
$\hat{E}CE$	$120/(1-\Delta)$
$C\hat{E}$	$120/(1-\Delta)$
$C\hat{E}D$	$120/(1-\Delta)$
$E\hat{C}$	60 exactly
$E\hat{C}E$	60 exactly
$E\hat{E}$	$40/(1-\Delta/3)$
$E\hat{E}E$	$40/(1-\Delta/3)$
$EC\hat{E}$	$40/(1-\Delta/3)$
$EE\hat{C}$	30 exactly
$CE\hat{D}$	30 exactly
$EE\hat{E}$	$24/(1-\Delta/5)$
$EEE\hat{C}$	20 exactly

Capacitance values

Capacitance C (F) can be calculated by rearranging ***Equation 2.14***,

$$I = C\frac{dE}{dt}$$

Equation 2.14

where I is the current (A) and $\frac{dE}{dt}$ is the scan rate ν (V s^{-1}), giving:

$$C = \frac{I}{\nu}$$

Equation 2.15

To cancel out any offset in the capacitance curve, the current I may be calculated from the amplitude of the hysteresis as shown in ***Figure 2.8***.

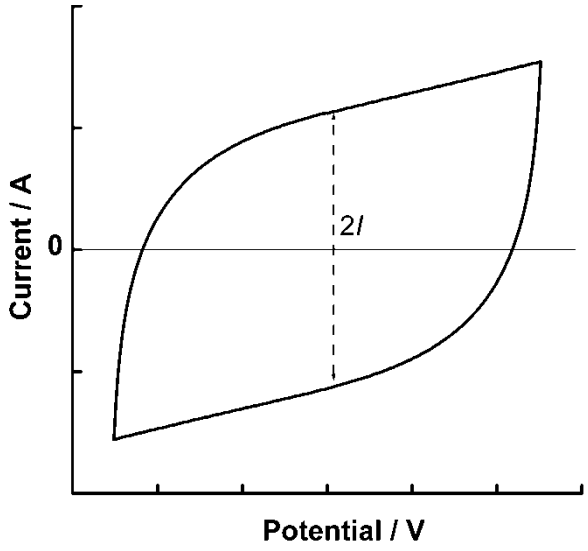

Figure 2.8 – The amplitude of the hysteresis has been used throughout this thesis to measure capacitance.

Time constants

All electronic circuits suffer from time delays between input and output signals. This phenomenon, characterised be a time constant, τ (s), represents the response time of the circuit. Energy storage systems exhibit time constants for their charging and discharging behaviour. The magnitude of the time constant τ (s) is determined by the product of the capacitance C (F), and resistance R (Ω).

$$\tau = RC \qquad \textbf{\textit{Equation 2.16}}$$

When performing cyclic voltammetry, a non-faradaic system behaves has a capacitor and resistor in series (***Figure 2.9***). This is evident from the shape of the voltammogram in ***Figure 2.10***.

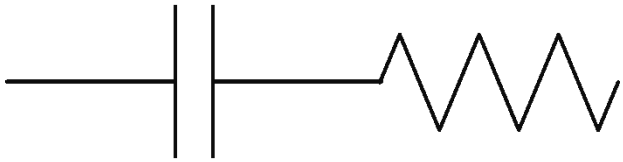

Figure 2.9 – The RC equivalent of a non-faradaic system.

An non-faradaic system exhibiting pure capacitance behaviour would produce a CV with a rectangular shape. However, the presence of a finite resistance in the cell slows down the charging and discharging process, producing rounded corners at the switching potentials. This effect is accentuated as the resistance increases.

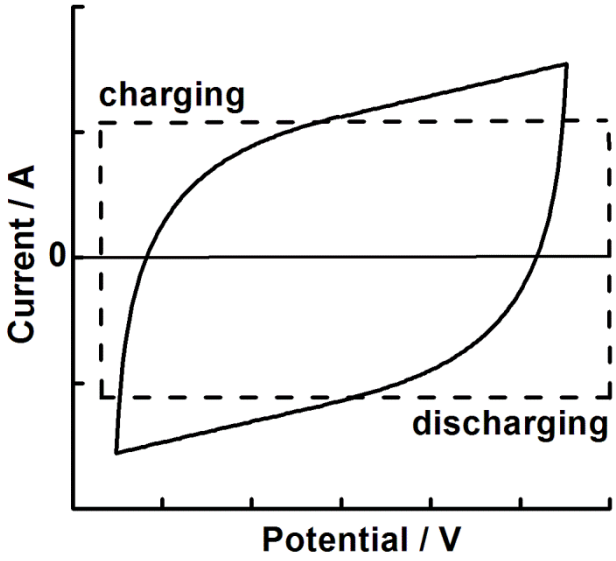

Figure 2.10 – A cyclic voltammogram illustrating the effect of the RC time constant τ on charging and discharging. The dotted line represents a short τ. The solid line represents a long τ.

It is possible to calculate the time constant for the system by analysing the "*curved corners*" using the following equation,

$$I_t = I_0 \exp\left(-\frac{t}{\tau}\right)$$

Equation 2.17

where t is the time (s), I_t is the current (A) at time t, I_0 is the initial current (A), and τ is the time constant.

By plotting the natural logarithm of the current *vs*. time, τ^{-1} is given by the slope. This is the simplest approach used to determine time constants of electrochemical systems. More complex models are possible and these are discussed in the relevant chapters.

2.2 – Conductivity

The ability of a solution to "carry a current" and form a complete electrical circuit is quantified by its conductivity. Current flow in liquids differs from that of solids, as electrons

are not able to move freely through the liquid phase. Instead, electrical charge is carried by the migration of ions.

When new materials (e.g. ionic liquids) are to be considered for use in physical devices or as replacements for existing solvent systems, their fundamental properties need to be explored and quantified. One such property, relevant to electrochemical applications, is the ability of the material to conduct electricity. Conductivity can be measured in a variety of ways, of which the most common are bridge methods and a.c. impedance methods. The latter were well suited to the experiments in this thesis. A schematic depicting the fundamental experimental setup, and a commercial probe, is illustrated in ***Figure 2.11***.

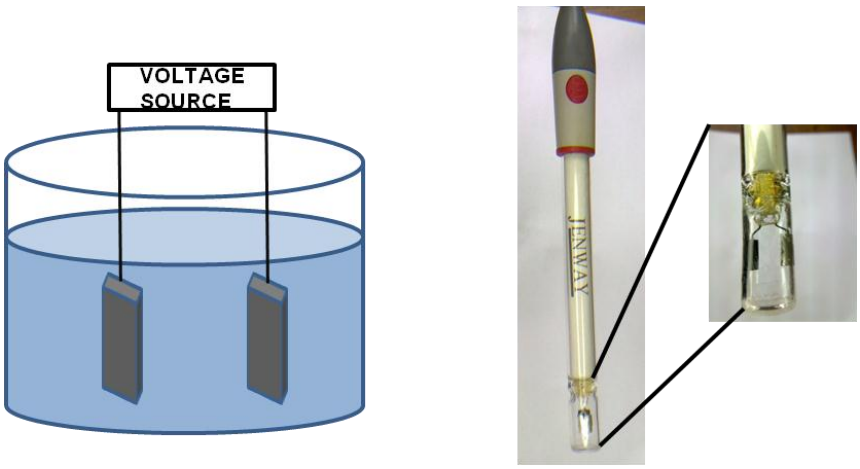

Figure 2.11 – A Schematic illustrating the cell set-up for conductivity measurement (left), and a commercial Jenway 027-013 conductivity probe (right).

In essence, conductivity measurements are recorded using two metal plates of a fixed geometry, inserted into the solution under investigation. In commercial conductivity probes, such as the Jenway 027-013 (pictured) the electrodes are made of platinised platinum for enhanced surface area, and encased in a glass surround to avoid fringe field effects. The chosen glass has a low coefficient of thermal expansion so that the cell dimensions do not change with changing temperature.

Figure 2.12 (right) shows the equivalent circuit that arises when a conductivity probe is placed in a solution. R_{sol} is the resistance of the solution, and Z_L and Z_R are the impedances

of the left and right electrodes respectively. The goal of the electrical measurements is to eliminate Z_L and Z_R from the final measurement so that only R_{sol} is measured.

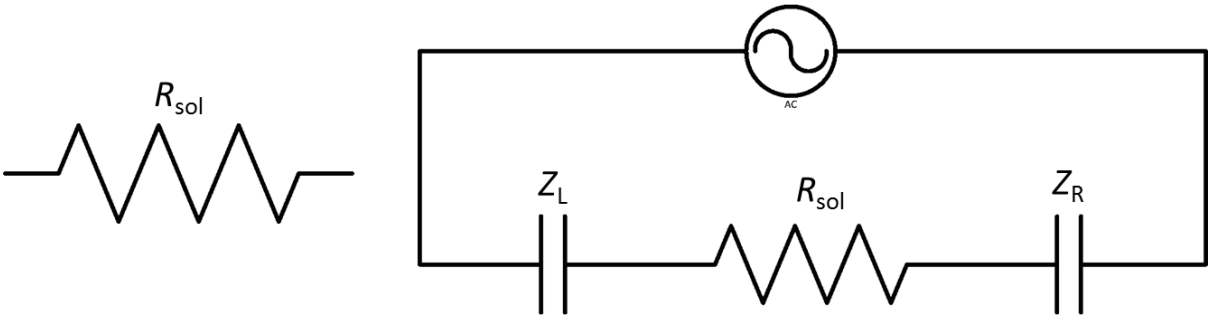

Figure 2.12 – Idealised equivalent circuit of a conductivity solution before (left) and after (right) electrodes are inserted.

The impedance of a resistor Z_R is defined as

$$Z_R = R \qquad \textbf{Equation 2.18}$$

where R is the resistance of the solution. The impedance of a capacitor Z_C is defined as

$$Z_C = \frac{1}{j\omega C}$$

Equation 2.19

where C is the interfacial capacitance (F), j is the square root of minus one, and $\omega = 2\pi f$, where f is the angular frequency of the applied potential (radians s^{-1}). Therefore, as can be seen from ***Equation 2.19***, Z_C can be minimised by two processes, (1) increasing the capacitance of the electrodes, and (2) increasing the measurement frequency. Thus,

$$Z_L \rightarrow 0 \text{ as } f \rightarrow \infty \text{ or as } C \rightarrow \infty$$

$$Z_R \rightarrow 0 \text{ as } f \rightarrow \infty \text{ or as } C \rightarrow \infty$$

The ability of AC impedance bridges to vary the measuring frequency is a big advantage over traditional DC conductivity bridges, such as the Wheatstone Bridge, which adopt a fixed frequency (usually 1 kHz) for all measurements, regardless of solution. ***Figure 2.13*** shows a typical impedance plot in the complex plane for a commercial conductivity probe. The semicircle is due to the presence of stray capacitance, C_{stray}, across the solution resistance, R_{sol}, as illustrated in ***Figure 2.14***.

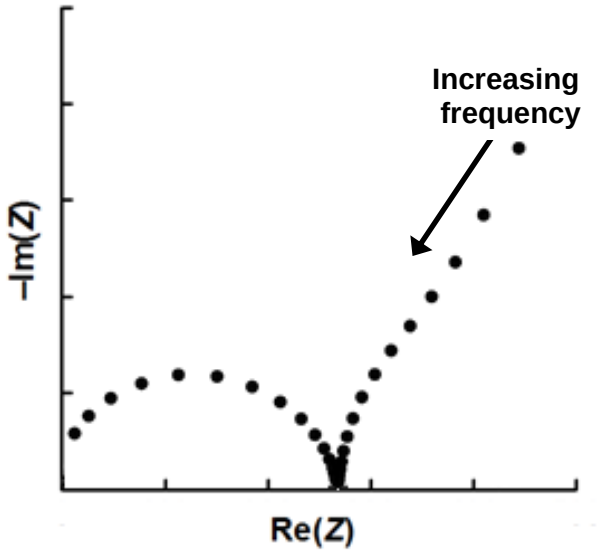

Figure 2.13 – A typical impedance plot in the complex plane for a commercial conductivity probe. The deep local minimum indicates an optimum measuring frequency where the measured impedance is the resistance of the solution.

An optimum frequency can be identified as the point where the deep local minimum is observed. At this point, the phase angle of the total impedance is zero, and the system behaves as a pure resistor.

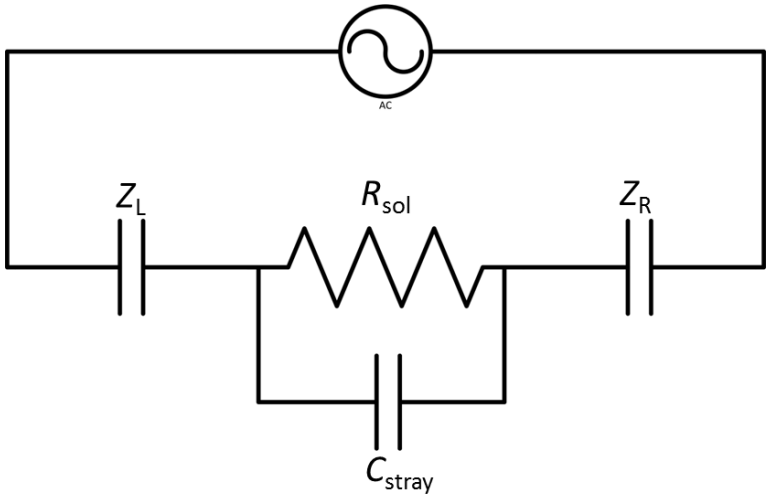

Figure 2.14 – More realistic equivalent circuit of a conductivity solution including stray capacitance (C_{stray}).

2.2.1 - Impedance bridge circuits

To obtain high precision conductivity data, an impedance bridge is commonly adopted. A schematic diagram for an impedance bridge is given in ***Figure 2.15***.

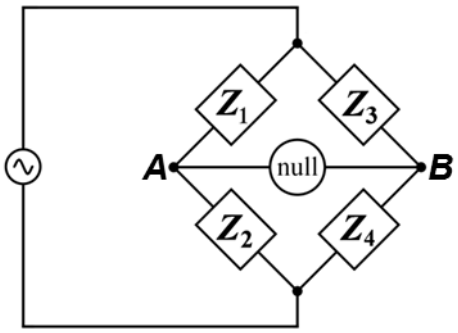

Figure 2.15 – A schematic diagram illustrating the set-up for an impedance bridge circuit.

An impedance bridge consists of four impedances, arranged in two parallel pairs. Z_1 and Z_2 have known impedance values, Z_3 is the unknown impedance, i.e. the impedance of the solution that is being measured, and Z_4 is adjustable. The impedances are connected by a null

detector. When the ratio of impedances Z_2 and Z_1 is equal to the ratio of Z_3 and Z_4, no current flows between point A and B and the system is said to be balanced, i.e.

$$\frac{Z_1}{Z_2} = \frac{Z_3}{Z_4}$$

Equation 2.20

When the system is balanced, Z_3 can be calculated as

$$Z_3 = \frac{Z_1}{Z_2} Z_4$$

Equation 2.21

When the system is unbalanced, i.e.

$$\frac{Z_1}{Z_2} \neq \frac{Z_3}{Z_4}$$

Equation 2.22

the direction of the resulting current flow provides feedback as to whether Z_4 is too high or too low. If Z_4 is too high, the impedance of Z_4 is decreased. Similarly, if the impedance of Z_4 is too low, the impedance of Z_4 is increased. Adjustments are continuously made until there is no current flow through the null detector. In an AC impedance bridge both the impedance magnitude $|Z|$ and phase angle θ must be properly matched at the balance point.

One of the main sources of error with impedance bridges is the presence of "stray capacitances" between adjacent circuit elements. It is particularly problematic at high frequencies (> 10 kHz). Stray capacitance can be observed in ***Figure 2.13***, after the deep local minimum, and gives rise to semi-circular data in the complex plane.

2.2.2 – Determining conductivity from resistance output

After taking the aforementioned steps to ensure that the measured impedance is outputting the correct solution resistance values, the electrical conductivity κ (S m^{-1}) of the solution can then be calculated according to ***Equation 2.23***,

$$\kappa = G\,K$$ ***Equation 2.23***

where G (S), is the conductance, the reciprocal of electrical resistance, R (Ω),

$$G = \frac{1}{R}$$

Equation 2.24

and K (m^{-1}) is the cell constant of the measuring cell. The latter is defined as,

$$K = \frac{l}{A}$$

Equation 2.25

where A is the cross sectional area of an electrode (m^2) and l is the the inter-electrode gap (m).

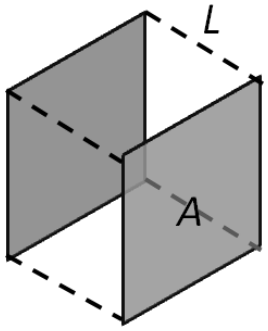

Figure 2.16 – A schematic diagram illustrating the dimensions of a conductivity cell. A is the cross sectional area of the electrodes (m^2) and l is the distance between the electrodes (m).

It is standard practise to calculate K by calibrating against a system such as 0.01 M aqueous potassium chloride with a known specific conductivity of 1413 µS cm^{-1}(25 °C)[17].

Note that electrical conductivity κ (S m^{-1}) is the reciprocal of electrical resistivity ρ (Ω.m)

$$\kappa = \frac{1}{\rho}$$

Equation 2.26

and that resistance R (Ω) and electrical resistivity are connected according to the following relationship

$$R = \rho K$$ ***Equation 2.27***

2.3 - Scanning electron microscopy

Scanning Electron Microscopy, (SEM) is a useful technique for obtaining high resolution, high magnification images. A photograph of the SEM apparatus used in this thesis is shown in ***Figure 2.17***.

Figure 2.17 − The FEG-SEM instrumentation used in this thesis. Model: Carl Zeiss (Leo) 1530 VP.

In an SEM, high energy electrons are fired from an emission gun at the top of a miscroscope. The electrons are then focused into a fine electron beam, which is scanned continuously across the surface of the sample. The high energy electrons interact both elastically (conserving kinetic energy) and inelastically (not conserving kinetic energy) with the sample, resulting in the production of various types of radiation, such as secondary electrons, characteristic x-rays, and backstattered x-rays. The electrons are then detected by a scintillation detector, amplified, and an image is constructed on a cathode ray tube which scans in synchronisation with the electrode beam. The process takes place in a vacuum to prevent collisions between electrons and air molecules. An example of a high resolution SEM image is given in ***Figure 2.18.***

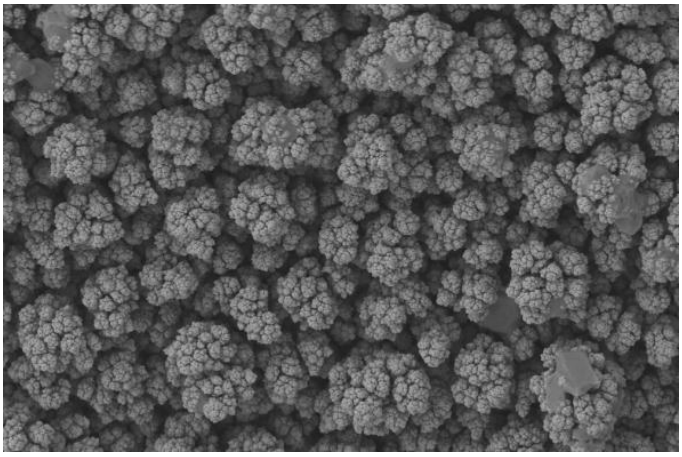

Figure 2.18 – An SEM image of a platinised platinum electrode.

2.4 – Differential scanning calorimetry

A differential scanning calorimeter (DSC) is a device that monitors the heat flow associated with phase transitions and chemical reactions, as a function of temperature. A schematic illustrating the design of a conventional DSC is given in ***Figure 2.19***. The diagram shows two identical metal pans, S and R inside a furnace. S contains the sample under test, and R contains an inert reference (often an empty pan). Below both pans there is a heater and temperature sensor. Gas vents are also present to allow testing under different atmospheric conditions.

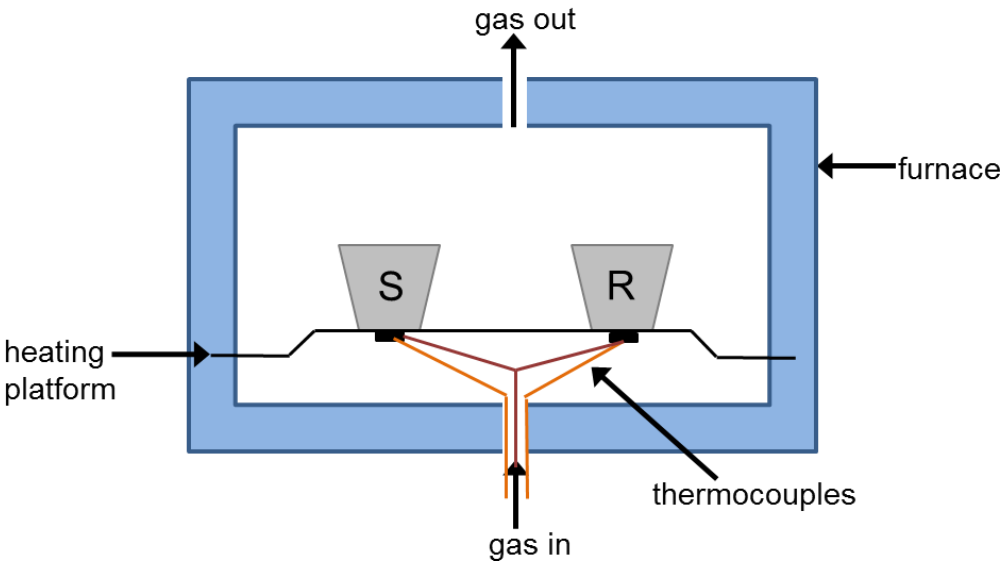

Figure 2.19 – A schematic diagram of a differential scanning calorimeter.

A photograph of an aluminium sample pan is given in ***Figure 2.20***. A 10 pence coin has been used for size reference.

Figure 2.20 – A photograph of an aluminium sample pan (right).

The heat flow (W g^{-1}) to and from the sample is measured relative to the inert reference, in addition to the mass. The heat flow will be zero in the absence of thermally initiated phase changes. However, when S undergoes a thermally initiated phase change, the rate of change

of heating/cooling is affected and the heat flow to the reference must change to maintain a zero temperature difference between the two.

Heat flow (W g^{-1}) to S and R is recorded as a function of programmed furnace temperature (K). A DSC thermogram showing some of the possible transitions measureable by DSC are given in ***Figure 2.21***.

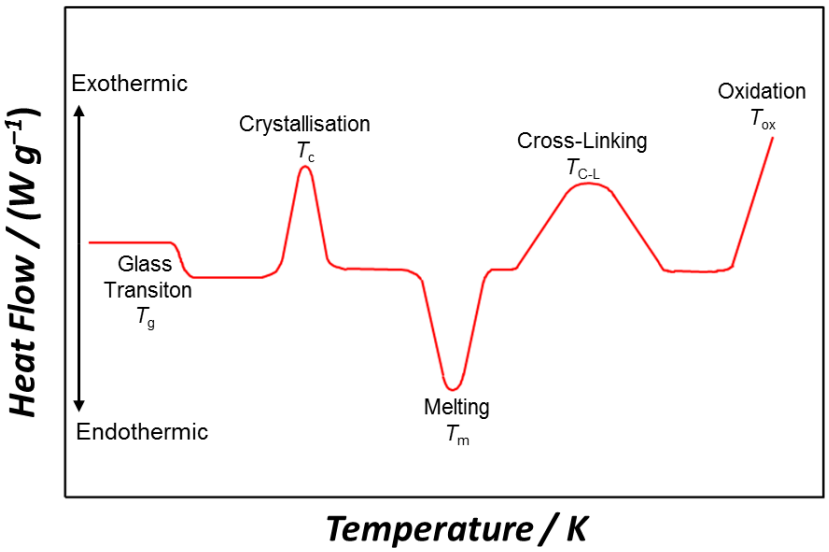

Figure 2.21 – A DSC thermogram illustrating transitions observed in DSC.
Image derived from: Sun, J., Forsyth, M. & MacFarlane, D. R. *Room-Temperature Molten Salts Based on the Quaternary Ammonium Ion*. Journal of Physical Chemistry B. 102: 8858-8864 (1998).

It can be seen that melting points, T_m, and glass transitions, T_g, are endothermic processes and crystallisation, T_c, oxidation, T_{ox}, and cross linking, T_{C-L} are exothermic processes. It should be noted that the recorded signals are proportional to the amount of heat necessary to change sample temperature by given amount, and the approximate equivalence of the areas under T_c and T_m peaks indicates the total enthalpies of the transitions (ΔH).

2.4.1 – Assignment of transition temperatures.

For phase changes where a peak is observed, the transition temperature is taken as the temperature at maximum heat flow, i.e. the peak. For phase changes where a peak is not observed, for example at T_g, the transition temperature is given as the intersect between the

tangent and co-tangent of the step in the baseline (T_2, ***Figure 2.22***). This ensures that the measured transition temperature is consistent, regardless of whether it is measured during a heating or cooling cycle.

The onset temperature of T_g (T_1) is also measured in this thesis. It was important to measure T_1 when establishing the relationship between temperature and conductivity. This is because T_1 is the critical temperature at which the amorphous glass gains enough thermal momentum to unfreeze the degrees of freedom required for conductivity. An illustration of T_1 and T_2 are given in ***Figure 2.22***.

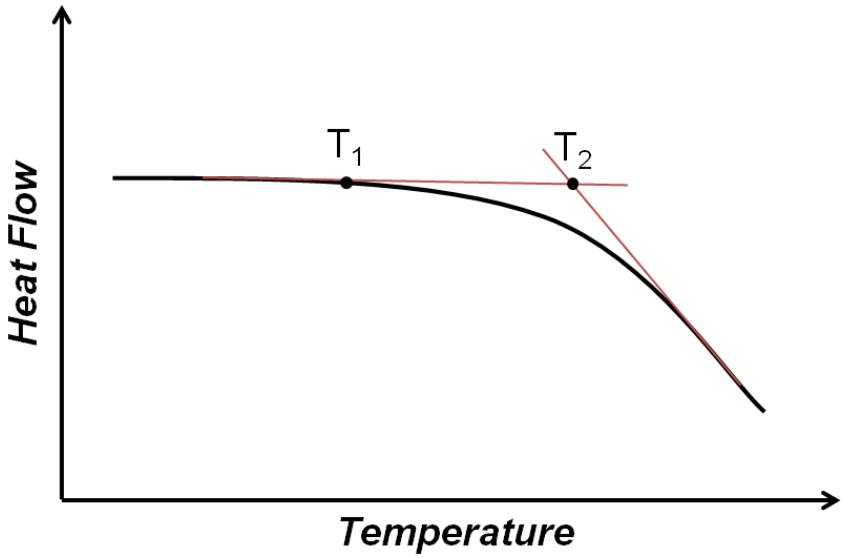

Figure 2.22 – An illustration of T_1 and T_2 obtained from a DSC thermogram.

2.5 – Screen-printing

Screen-printing is a type of stencilling technique that can reproducibly manufacture large numbers of test electrodes with controlled electrode area, thickness and composition permitting the statistical analysis of experimental data.

The screens used in screen-printing contain a mesh mask which defines the image to be printed and controls how much ink is deposited. An example of a screen secured into a screen printer is given in ***Figure 2.23***.

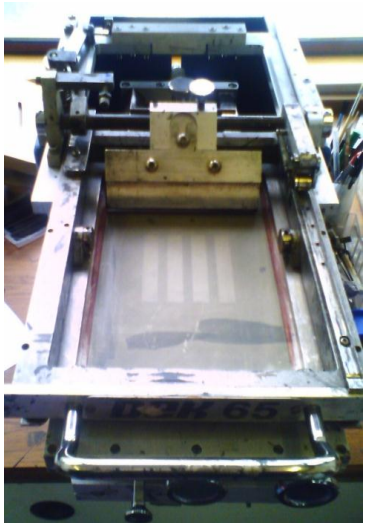

Figure 2.23 – A screen secured into a manual screen printer.

The principle of screen printing is straightforward. Firstly, the substrate to be printed upon is secured onto the substrate holder. Secondly, the chosen screen is secured 1-2 mm above the substrate and ink is applied to the screen. Finally, to print the image, the ink is pushed through the negative image of the screen using a doctor blade which transfers the ink onto the substrate below and prints a positive image. A schematic representation of the screen-printing process is given in ***Figure 2.24***.

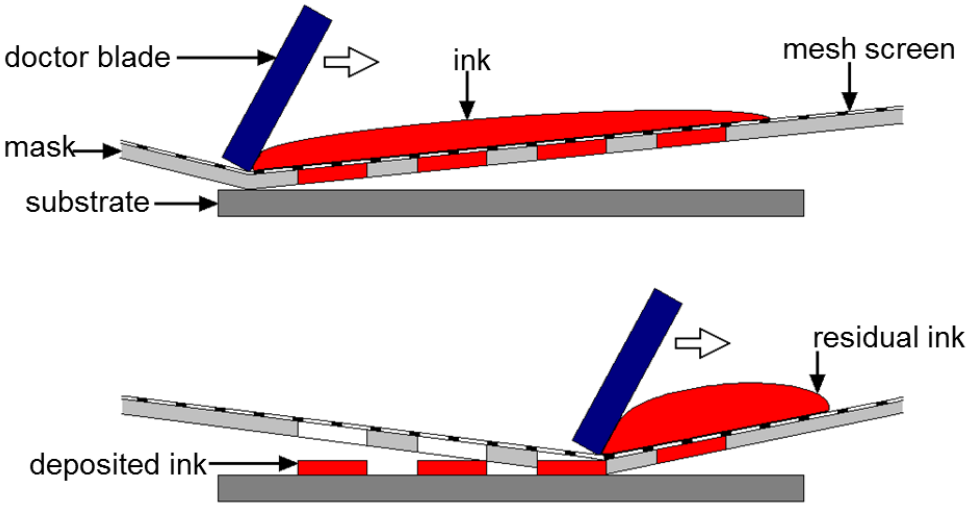

Figure 2.24 – A schematic diagram illustrating the screen printing process showing how ink is transferred from the screen on to the substrate using a doctor blade.

An SEM image obtained for a screen printed electrode is given in ***Figure 2.25***. The electrode substrate is glass and the three screen printed layers are silver, smooth carbon, and activated carbon.

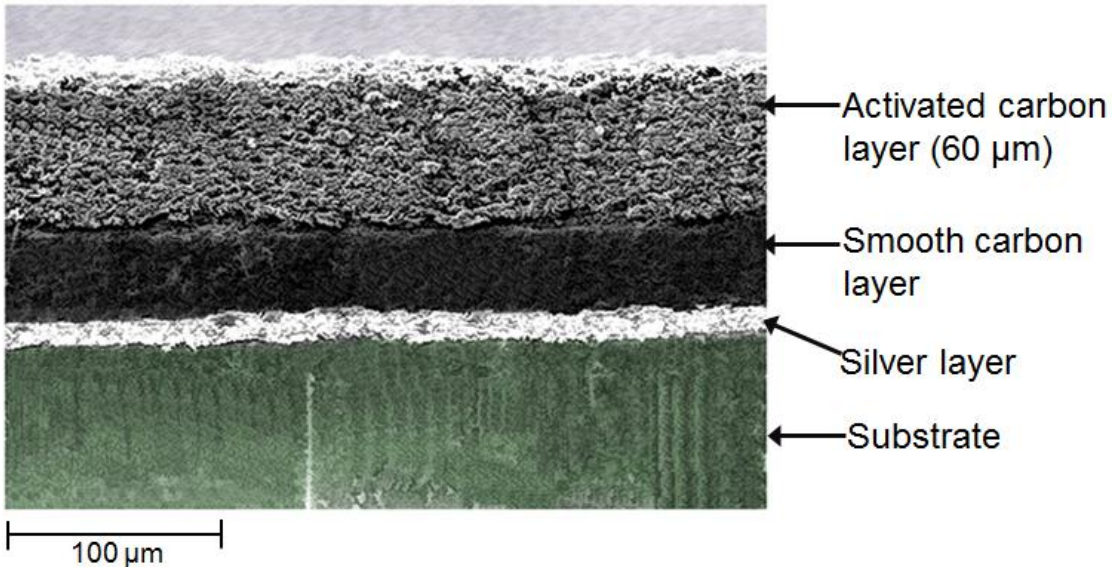

Figure 2.25 – An SEM image of a screen printed electrode.

2.6 – References

[1] Southampton Electrochemistry Group. *Instrumental Methods in Electrochemistry*. Ellis Horward Limited, Chicester, West Sussex, Chapter 6, pp178-228 (1990).

[2] Bard, A. J. & Faulkner, L. R. *Electrochemical Methods Fundamentals and Applications*, 2nd Edition, Wiley, New York, Chapter 1, pp1-43 (2001).

[3] Compton, R. G. Banks, C. E. *Understanding Voltammetry*. World Scientific, Singapore, Chapter 1, pp1-32 (2007).

[4] Ives, D. J. G. & Janz, G. J. *Reference Electrodes, Theory and Practice*. Academic Press, New York, (1961).

[5] Brett, C. M. & Brett, A. M. O. *Electrochemistry Principles, Methods and Applications*, Oxford Science Publications, New York, Chapter 9, pp174-197 (1993).

[6] Gosser, D. K. Jr. *Cyclic Voltammetry: Simultation and Analysis of Reaction Mechanisms*, Wiley-VCH Inc, New York, pp27-71 (1993).

[7] Randles, J. E. B. *A Cathode Ray Polarograph*. Transactions of the Faraday Society. 44: 322-327 (1948).

[8] Randles, J. E. B. *A Cathode Ray Polarograph.2. The Current Voltage Curves*. Transactions of the Faraday Society, 44: 327-338, (1948).

[9] Cited in Nichloson, R. S. & Shain, I. *Theory of Stationary Electrode Polarography – Single Scan Plus Cyclis Methods Applied to Reversible Irreversible and Kinetic Systems*. Analytical Chemistry, 36: p706 (1964).

[10] Stern, O. Zeitschrift für Elektrochemie, 30: 508 (1924).

[11] Gouy, G. Journal of Physics, 9: 475 (1910).

[12] Chapman, D. L. Philisophical Magazine, 25: 475 (1913).

[13] Helmholtz, H. Poggendorff's Biographisch-Literarisches Handwörterbuch, LXXXIX, 211 (1853).

[14] Tafel, J., Schmitz, K., Naremann, B. & Emmert, B. Zeitschrift fur Physikalische Chemie-International, 50: 641-712 (1905).

[15] Fletcher, S. *Tafel Slopes from First Principles*. Journal of Solid State Electrochemistry, 13: 537-549 (2009).

[16] Fletcher, S. & Varley, T. S. *Beyond the Butler-Volmer Equation. Curved Tafel Slopes from Steady-State Current-Voltage Curves*. Physical Chemistry, Chemical Physics, 13: 5359-5364 (2011).

[17] Robinson, R. A. & Stokes, R. H. *Electrolyte Solutions*, 2nd Edition (Revised), Butterworths, London, Appendix 6.2: pp465 (1965).

Chapter 3 – Experimental Details

In this chapter, the equipment, consumables and software used to complete the work in this thesis is presented.

3.1 Apparatus

3.1.1 – Instrumentation and Equipment

- Voltammetric experiments were carried out using an AutoLab PGSTAT 20 or a μ-Autolab 70282 (type II) potentiostat (both Metrohm-Autolab, Eco-Chemie, Utrecht, The Netherlands). The operating software was General Purpose Electrochemical System (GPES), version 4.9 (Eco-Chemie Utrecht, The Netherlands). No *IR* compensation or noise filters were applied.
- Supercapacitors were charged using a Concept Series HY3003-3 D.C. bench top power supply (Digimess Instruments, Derby, UK).
- DSC measurements were carried out using a Q-1000 Diffential Scanning Calorimeter (TA Instruments, Elstree, UK). Data analysis of themograms was conducted using Universal Analysis 2000, version 4.3, (TA instruments Elstree, UK).
- SEM images were obtained using a high resolution (1 nm) field emission gun scanning microscope or an FEGSEM. The model was a Carl Zeiss (Leo) 1530 VP, with VP standing for variable pressure.
- Solution resistance and impedance measurements were carried out using a Wayne-Kerr Precision Component Analyser, model 6430A (Wayne-Kerr Electronics, Chichester, UK). The operating software was written in Microsoft Visual Basic, version 6.0.
- High temperature conductivity and voltammetric experiments were carried out using a F25-ME thermostatted heated oil bath with external circulation (Julabo Labortechnik GmbH, Seelbach, Germany). The bath oil was Thermal H20S (Julabo, Labortechnik, Seelbach, Germany). The operating software was EasyTemp, version 3.20, (Julabo Labortechnik GmbH, Seelbach, Germany).

- Temperature was measured using a Pt-100 probe attached to a P755-Log digital thermometer (both DOSTMANN Electronic, Wertheim, Germany). The operating software was DE-Graph, version 1.3.3 (DOSTMANN Electronic, Wertheim, Germany).
- Conductivity measurements were obtained using a Jenway 027-013 commercial conductivity probe (Bibby Scientific Limited, Stone, Staffordshire, UK).
- The operational temperature of supercapacitors was controlled by placing the devices into a MTF 10/25/130 single zone horizontal tube furnace (Carbolite, Hope Valley, UK). Screen printed inks were cured in a Midi/4/SS laboratory oven (GenLab, Cheshire, UK).
- Sonication was performed in a FB15047 sonic bath (Fisher Scientific, Loughborough, UK)
- Weighing was performed using a NA114 analytical sealed digital balance (Oertling Ltd, Thermal Scientific, UK)
- A 0800501 (0-25 mm) micrometer (Preisser UK Ltd, Surrey, UK) was used for measuring material thickness.
- Ball milling was undertaken using a Pulverisette 7 planetary ball mill using an agate pot and three agate balls (FRISCH, Idar-Oberstein, Germany).

3.1.2 – Electrodes

Electrochemical experiments were carried out in a two-electrode or a three-electrode set-up. In a three-electrode set up, there was an individual reference half-cell, a counter electrode and a working electrode. In a two electrode set-up, the electrodes were identical in mass and composition, one electrode acted as both the counter and reference half-cell and the other as the working electrode. Specific details for each set-up are given below.

Counter electrodes

Counter electrodes were made in-house. Platinum gauze mesh was chosen due to its large surface area, its inertness, and its ease of preparation. To prepare the counter electrodes, a 4 cm^2 platinum gauze mesh (Aldrich, 99.9%, 52 mesh, CAS: 7440-06-4) was spot welded onto platinum wire, which was then attached to copper wire and sealed in a glass tube using a

graduated glass seal to ensure no copper was exposed. The platinum could be flame-annealed before use.

Reference half-cells

A Saturated Calomel Electrode (SCE) was used as the reference half-cell for aqueous systems unless otherwise stated. The SCE consists of mercurous chloride (Hg_2Cl_2, "calomel"), in contact with mercury metal, immersed in a saturated solution of potsassium chloride (KCl). The KCl solution ensures that the concentration of the chloride anion remains constant. Contact with the cell solution is made through a porous glass frit. The SCE cannot be used in non-aqueous solutions without introducing a large liquid-junction potential.

Half-cell equation:

$$Hg_2Cl_{2(s)} + 2e^- \rightleftharpoons 2Hg_{(l)} + 2Cl^-_{(saturated)}$$

To avoid a large liquid-junction potential, a silver-silver chloride (Ag|AgCl) pseudo-reference electrode was used in non-aqueous systems, unless otherwise stated. The reference potential exhibited by a pseudo-reference is strictly dependent on the composition of the solution in which it is immersed. However, among a homogolous series of ionic liquids, we found the potential to be remarkably stable. The half-cell can be represented as:

$$Ag_{(s)} \mid AgCl_{(s)} \mid X^-$$

where X^- represents the anion of the ionic liquid in which the Ag|AgCl reference electrode is immersed, typically bis(trifluoromethylsulfonyl)imide.

Half-cell equation:

$$AgCl_{(s)} + e^- \rightleftharpoons Ag^0_{(s)} + Cl^-/X^-_{(soln)}$$

The potential difference between two Ag|AgCl reference electrodes in two different ionic liquids was checked by forming cells with liquid junctions. A stable cell potential was then obtained and found to be < 4 mV in all cases.

Preparation of Ag|AgCl pseudo-reference half-cell

Ag|AgCl pseudo-reference half-cells were prepared in-house before use. High purity Ag wire (Johnson-Matthey, Stoke-on-Trent, UK (99.99%)), d = 1 mm, l = 10 cm) was sanded with emery paper and rinsed with water. The Ag wire was then immersed in a solution of 0.5 M NaCl and plated with chloride ions at +0.8 V *vs.* a SCE reference half cell (60 s). A typical Ag|AgCl voltammogram is shown below:

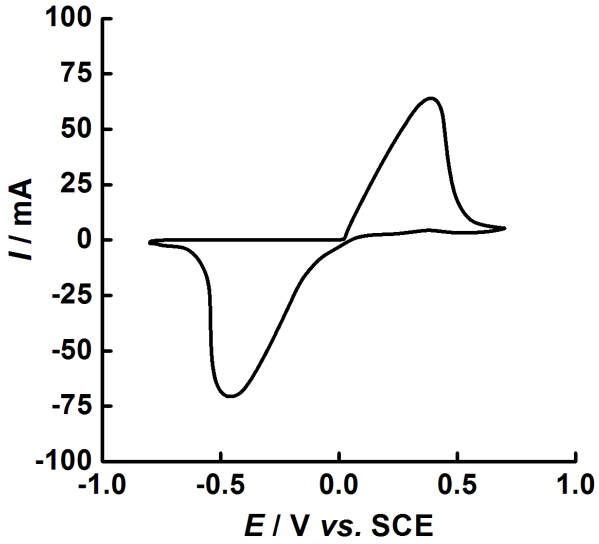

Figure 3.1 – Voltammetry of Ag wire in NaCl (0.5 M). The potential was held at –0.5 V for 10 s vs. SCE before being cycled from –0.5 V to +0.8 V to –0.5 V at 20 mV s^{-1}. During the second cycle the potential was held at +0.8 V for 60 s to allow the Ag wire to be coated with AgCl before disconnecting the Ag|AgCl wire from the cell. The counter electrode was platinum gauze. Shown above is the first potential cycle.

Once the Ag|AgCl half-cell was prepared, its potential was compared to a commercial Ag|AgCl half-cell (Bio Analytical Systems Inc, Warwickshire, UK). Ideally, there should be no potential difference between the two half-cells, and no differences greater than 3 mV were recorded.

Working electrodes

For room temperature electrochemistry, the following electrodes were used:

- A glassy carbon disc electrode (d = 3.0 mm, Bioanalytical Systems Inc, Warwickshire, UK).
- A platinum disc electrode (d = 1.6 mm Bioanalytical Systems Inc, Warwickshire, UK).
- A gold disc electrode (d = 1.6 mm Bioanalytical Systems Inc, Warwickshire, UK).
- Gold wire (d = 0.4 mm, E401-3, Agar Scientific, Essex, UK).
- Platinum wire (d = 0.4 mm, E404-5, Agar Scientific, Essex, UK).
- A Random Assembly of carbon Microelectrodes (RAM™ electrode, CSIRO, Melbourne, Australia). Further details of these electrodes are contained within the subsequent section.
- Stainless steel circular plates (d = 30 mm grade 316, LaserMaster, Cornwall, UK).

All disc electrodes were supplied as rods press fitted into an insulating polymer surrounds.

For high temperature electrochemistry *(T* > 25 °C*)*, the following electrodes were used:

- A glassy carbon disc electrode set into a glass filled Teflon shroud (d = 3.0 mm Metrohm, Herisau, Switzerland)

The RAM electrode

The RAM electrode consists of *circa* 800 active microdiscs (d = 7 µm) distributed randomly within one square centimetre of working surface, set in an epoxy resin surround. The number of microdiscs was confirmed using the method of Fletcher and Horne[1].

RAM electrodes were particularly valuable in systems where *IR* drop was distorting experimental results, for example when calculating Tafel slopes.

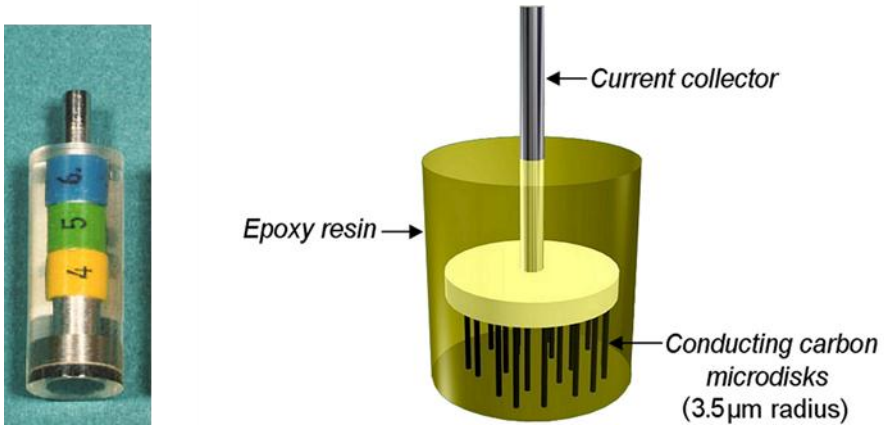

Figure 3.2 – A photograph of a RAM electrode (left) and a 3D image of a RAM™ electrode (right).

Electrode cleaning

Electrodes were cleaned before each experiment and also between runs. Polishable electrodes (disc electrodes and RAM electrodes), were polished using 0.3 µm alumina powder (6000242 Alpha Alumina Powder, Kemet, Greensville, USA) and a 40-7218 Buehler polishing cloth with adhesive backing (Microcloth®, Buehler, Coventry, UK) for at least 30 seconds. The electrodes were then washed in a 50/50 mix of water and concentrated nitric acid to remove adventitious adsorbates, then sonicated in triply distilled water. Non-polishable electrodes (wires, sheets and meshes) were flame treated (T > 500°C) and washed in concentrated nitric acid followed by triply distilled water. When wire electrodes could not be flamed due to low melting points, they were polished with Emery paper (162-3553, 3M, Loughborough UK), washed in a 50/50 mix of water/concentrated nitric acid and dried.

When using electrodes in non-aqueous systems, electrodes were dried in a pressurised stream of pure nitrogen gas until all residual water had been removed prior to use.

3.2 – Computer software

Analysis and manipulation of collected data was carried out using Microsoft Office Excel (2010). Graphs were plotted using OriginLab, version 6.1 (2001). Circuit diagrams were drawn using Microsoft Office Visio (2010). MarvinSketch, version 5.3 (2010) was used for

drawing 2D chemical structures and MarvinSpace, version 5.3 (2010) was used for modelling chemical structures in 3D. Jasc Paint Shop Pro, version 7, was used for image formatting.

3.3 – Glassware

Electrochemical cells and test tubes for room temperature experiments were purchased from Fisher Scientific, Loughborough, UK. Jacketed electrochemical cells for high temperature voltammetry were purchased from Soham Scientific, Cambridgeshire, UK. All other custom-made glassware was produced by John Spray (Glass blower, Loughborough University, UK).

3.4 – Consumables

All chemicals were used as supplied, unless otherwise stated.

- All ionic liquids were purchased from or custom synthesised by Iolitec (Ionic Liquid Technologies, GmbH, Heilbronn, Germany, with the exception of 1-ethyl-3-methylimidazolium bis(trifluoromethylsulfonyl)imide (CAS: 174899-82-2) which was supplied by Schlumberger (Stonehouse, Gloucester, UK). All ionic liquids were dried at 130 ºC (t > 1 h) prior to use.
- Nitric acid (CAS: 7697-37-2), sodium chloride (CAS: 7647-14-5), potassium chloride (CAS: 7447-40-7), and self-indicating silica gel (CAS: 7631-86-9, orange to colourless) were all purchased from Fisher-Scientific (Loughborough, UK).
- Propylene carbonate (CAS: 108-32-7), hydrophilic fumed silica (S5130, CAS: 112945-52-5), self-inidicating silica gel (orange, CAS: 112926-00-8), resveratrol (CAS: 501-36-0), bisphenol A (CAS: 1478-61-1), 4,4´-(hexafluoroisopropylidene)diphenol (CAS: 1478-61-1), 4,4´(1,4-phenylene-diisopropylidenebisphenol, and 4,4´-sulfonyldiphenol (CAS: 80-09-1) were all purchased from Sigma-Aldrich, (Dorset, UK).
- Glass frit (flux system 23901) was kindly donated by Johnson-Matthey Colour Technologies, (Stoke on Trent, UK).
- Silver Ink (E1660) was purchased from Ercon, (Wareham, USA).
- Smooth carbon ink (CHSN8032) was purchased from SunChemical, (Norton, UK).
- Activated carbon powder (DLC SUPRA 30) was kindly donated by Norit, (Cambuslang, UK).

- Fumed silica (R821S AEROSIL®, CAS: 272-697-1) was purchased from Evonik industries, (Essen, Germany).
- Fumed silica (S5130, CAS: 112945-52-5) was purchased from Sigma Aldrich (Dorset, UK).
- Kapton adhesive polyimide tape (K6339, 125 µm) and Kapton (500 HN, 85 µm) polyimide film were products of DuPont, and purchased from Katco Ltd (Hemel Hempstead, UK).
- Copper tape (542-5369), PTFE coated wire (526-7955), and tin/copper solder (185-0058) were purchased from RS Electronics, (Nottinghamshire, UK).
- Glass fibre (VP35, 0.3 mm) was purchased from The Glass Fabric Company (Leicestershire, UK).
- All water was obtained from a Millipore Milli-Q gradient A10 water filter (18.2 MΩ internal measurement) and was triply filtered.
- Nitrogen gas was supplied in a BOC cyclinder (The Linde Group, UK), and fed through a silica drying trap prior to use.

3.5 – References

[1] Fletcher, S. & Horne, M. D. *Random assemblies of microelectrodes (RAM™ electrodes) for electrochemical studies*. Electrochemistry Communications, 1: 502-512 (1999).

Chapter 4 – Electron Tunnelling in Ionic Liquids

4.1 – Introduction

In order for an ionic liquid to be a successful electrolyte for an electrochemical system, it must be stable over a wide voltage range. The voltage stability window can be defined as the potential region over which electron tunnelling does not occur. However, at extreme positive and negative potentials, the anions and cations will inevitably be subjected to electrochemical oxidation and reduction, by the tunnelling of electrons. Recent theoretical work by S. Fletcher (unpublished) suggested that the probability of electron tunnelling to ions in solution might be diminished by surrounding the ion with alkyl groups, conferring increased chemical inertness.

In the present work, a homologous series of novel symmetrical tetraalkylammonium ionic liquids were custom synthesised to explore this possibility. The quaternary cations consisted of four symmetrical alkyl groups, with each in the series containing one more alkyl group than the last. Bis(trifluoromethylsulfonyl)imide, a stable, water-repelling (hydrophobic) anion, was the anion in all cases. The ionic liquids were scanned voltammetrically in order to determine their stability at cathodic potentials. The goal was to determine whether long-chain tetraalkylammonium cations really could diminish the tunnelling probability.

4.2 – Theory of electron transfer

Electron transfer is a type of quantum transition, in which an electron delocalises from one stationary state, and localises in another stationary state, thereby inducing a change in the occupation number of both states[1]. It can be used to explain how redox reactions occur.

The modern theory of electron transfer emerged out of wave mechanics, as formulated by Erwin Schrödinger in 1926[2]. The Schrödinger model assumes that the electron is a wave, and then locates regions of space where the wave is most likely to be found. These regions are called orbitals. Since orbitals exist in three-dimensional space, it always requires three coordinates to describe them. Due to the complexity of the governing equations of the Schrödinger model, approximate methods of solution needed to be developed. One of these,

known as time-dependent perturbation theory, was published by Paul Dirac in 1927[3]. Dirac's ideas were then introduced into electrochemistry by Ronald Gurney in 1931[4].

Gurney provided an elegant picture of how electron transfer events actually occur. An electron initially resides in an orbital of a chemical species (the donor). Nearby, an empty orbital exists inside a second chemical species (the acceptor). Due to random fluctuations of the electrostatic potential energy of both species, the energies of both states are momentarily equalized, at which point the electron crosses from one orbital to the other.

If electron transfer changes the size of an ion (as it often does) then it follows that some energy must be supplied to expand or contract the associated solvation shell. This idea was missed by the early researchers, but it was noticed by Randles in 1952, and it led to the first kinetic theory of electron transfer based on molecular properties[5]. Shortly thereafter, Marcus pointed out that the surrounding solvent should also be considered, since it must adjust to the electron transfer event [6-7]. Finally, in 2007, Fletcher pointed out that counter ions were also exerting an important influence[8].

The speed at which an electron transfers from one state to another depends on the extent of "symmetry allowed" orbital overlap between the donor and acceptor orbitals. When such overlap occurs, an electron will "tunnel" from the highest occupied molecular orbital (HOMO) of the donor atom, D, to the lowest unoccupied molecular orbital (LUMO) of the acceptor atom, A, provided that the energies match. The extent to which the orbitals overlap is termed the overlap integral (S_{DA}), where ψ_D and ψ_A are wave functions of the donor and acceptor orbitals.

$$S_{DA} = \langle \psi_D | \psi_A \rangle \qquad \textbf{\textit{Equation 4.1}}$$

Providing the orbitals are Slater-type[9] then

$$S_{DA} \approx Ax^B \exp(-Cx) \qquad \textbf{\textit{Equation 4.2}}$$

where x is the inter-nuclear separation between donor and acceptor orbitals and A and C are numerical constants. It can be seen that the overlap integral decays sharply with donor-acceptor distance.

Fletcher 2010[1] developed an expression to show how the rate of electron transfer (k_{et}) is affected by the overlap integral (S_{DA}), ***Equation 4.3***, where k_{et} is the rate constant for electron transfer, ħ is the reduced Planck constant (1.054 x 10^{-34} J s), H' is a constant related to the electronic coupling matrix element between a single electron donor and a single electron acceptor, λ is the reorganization energy, k_B is the Boltzmann constant (1.38 x 10^{-23}), T is absolute temperature, and ΔG^0 is the difference in Gibbs energy between the acceptor and the product. From this equation it is apparent that as the overlap integral increases or decreases, so would the rate constant.

$$k_{et} = \frac{2\pi}{\hbar}|H'|^2 S_{DA}^2 \frac{1}{\sqrt{4\pi\lambda k_B T}} \exp\left(\frac{-(\lambda + \Delta G^0)^2}{4\lambda k_B T}\right)$$

Equation 4.3

The relationship between the inter-nuclear distance of the donor and acceptor atoms (x) and the rate constant is strongly exponential, ***Equation 4.2***. The probability of electron tunnelling (i.e. the rate of electron transfer) decreases dramatically with distance, falling by a factor of nearly a million between 0.23 nm and 1.23 nm, which may be taken as a practical maximum distance for electron tunnelling. This is illustrated in ***Figure 4.1***.

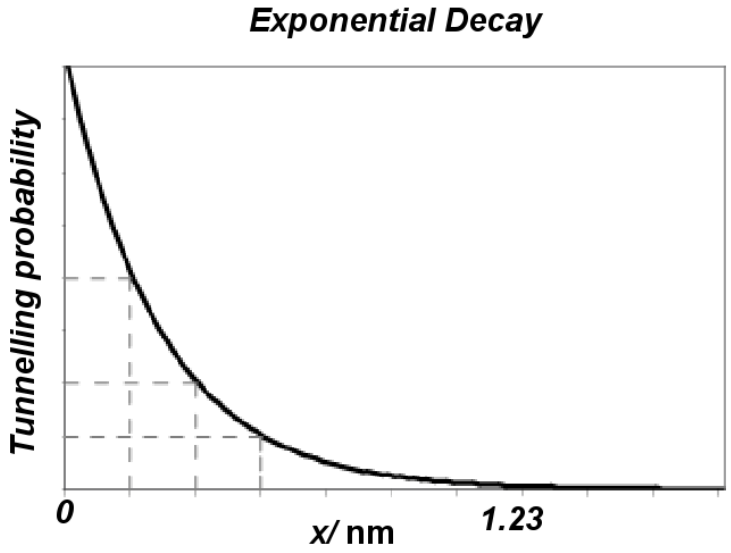

Figure 4.1 – The relationship between the inter-nuclear distance (x) of a donor and an acceptor molecule or atom, and the tunnelling probably of an electron.

Using quantum theory, it can therefore be predicted that the further the acceptor orbital of the cation is from the donor orbital of the electrode, then the harder it will be for an electron to tunnel into it, and the more negative the potential will need to be before the cation can be reduced. Hence, by adding long chain alkyl groups on to the cation for shielding, the inertness of the cation should be improved

4.3 – Experimental demonstration of electron tunnelling in ionic liquids

The homologous series of tetraalkylammnonium ionic liquids used for the experimental demonstration of electron tunnelling consisted of a quaternary ammonium cation, and a bistrifluoromethylsulfonyl)imide anion. The structural formulas for the four ionic liquids are given in ***Figure 4.2***. The ionic liquids were identical, apart from the symmetrically increasing alkyl chain lengths on the quaternary ammonium cation. Thus, the investigation into whether a bigger cation would confer enhanced chemical inertness could be explored. The ionic radii for the four cations are given in ***Table 4.1*** and a 3D simulation in ***Figure 4.6***.

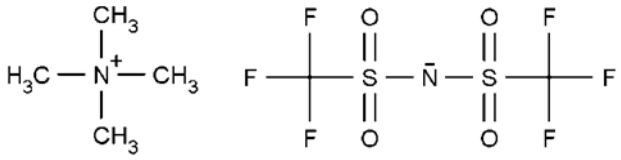

Figure 4.2 – Structural formula of tetramethylammonium bis(trifluoromethylsulfonyl)imide.

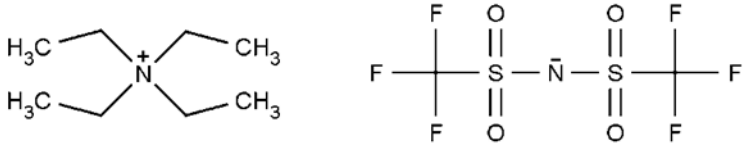

Figure 4.3 – Structural formula of tetraethylammonium bis(trifluoromethylsulfonyl)imide.

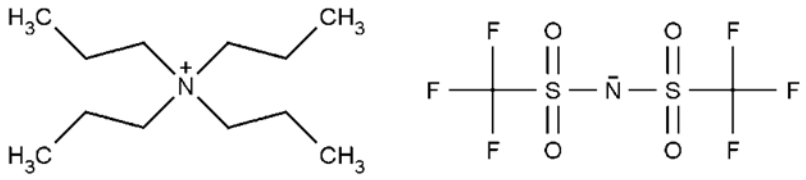

Figure 4.4 – Structural formula of tetrapropylammonium bis(trifluoromethylsulfonyl)imide.

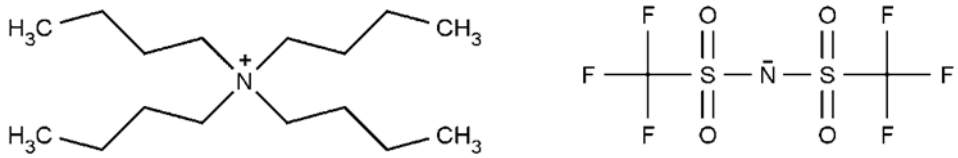

Figure 4.5 – Structural formula of tetrabutylammonium bis(trifluoromethylsulfonyl)imide.

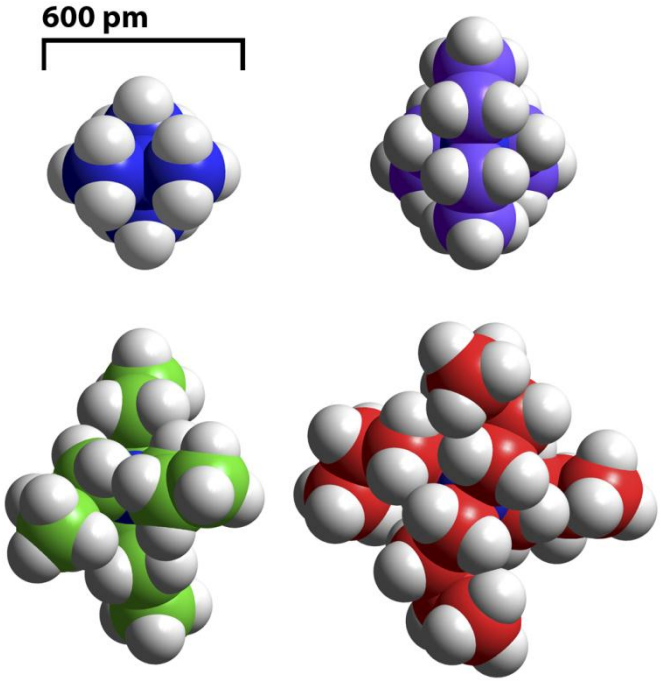

Figure 4.6 – 3D images for tetramethylammonium (blue), tetraethylammonium (purple), tetrapropylammonium (green), tetrabutylammonium (red) cations. Radii calculated using Stewart's semi-empirical (PM3) method[10].

Table 4.1 – Melting points (ºC) and ionic radii (pm) of quaternary ammonium cations.

Name	***Empirical formula***	***Melting point / °C[11]***	***Ionic radius of cation / pm***
Tetra**methyl**ammonium bis(trifluoromethylsulfonyl)imide	$[(CH_3)_4N+][(SO_2CF_3)_2N-]$	133	292
Tetra**ethyl**ammonium bis(trifluoromethylsulfonyl)imide	$[(C_2H_5)_4N+][(SO_2CF_3)_2N-]$	109	347
Tetra**propyl**ammonium bis(trifluoromethylsulfonyl)imide	$[(C_3H_7)_4N+][(SO_2CF_3)_2N-]$	105	390
Tetra**butyl**ammonium bis(trifluoromethylsulfonyl)imide	$[(C_4H_9)_4N+][(SO_2CF_3)_2N-]$	96	424

From ***Table 4.1***, it can be seen that the tetraalkylammonium ionic liquids used in the present work were solids at room temperature, due to the ease of co-crystallization of quaternary ammonium cations and the bis(trifluoromethylsulfonyl)imide anions. Symmetrical cations have a tightly packed crystalline structure with a high lattice enthalpy and therefore exhibit high melting points as a result. In order for useful comparisons to be made, the voltammetry of all compounds had to be carried out in the liquid state, which meant that the ambient temperature had to be above that of the highest melting compound. 140 °C was selected.

It was important to check that the Ag|AgCl reference electrode was giving the same reference potential in all four ionic liquids. One method for doing this was to use an internal standard, such as ferrocene. However, due to contamination worries, this method was discarded. An alternative method was to measure the cell potential directly between two reference half-cells. To this end, two Ag|AgCl wires were prepared, one in tetramethylammonium bis(trifluoromethylsulfonyl)imide and one in tetrabutylammonium bis(trifluoromethyl-sulfonyl)imide, both at 140 °C. The ionic liquids were connected in a cell by a liquid junction. The difference was an acceptable 4 mV showing that the reference systems potential did not vary significantly between ionic liquids.

The voltammetry of the four custom-synthesised ionic liquids was carried out in a thermostat-controlled electrochemical cell at 140 °C. The start potential was 0.0 V and the potential was scanned in a negative direction until the cation was seen to decompose. The potential was held at 0.0 V *vs.* Ag|AgCl wire for 10 s prior to scanning at 100 mV s^{-1}. The counter electrode was platinum gauze and the working electrode was a glassy carbon disc press-fitted

into a glass-filled Teflon shroud. Before each measurement the electrodes were polished and dried in a stream of dry nitrogen to remove any traces of water. Multiple replicates of all measurements were made to ensure reproducibility. The voltammetry for each of the four ionic liquids tested is shown in ***Figure 4.9*** (and in greater detail in ***Figure 4.10)***.

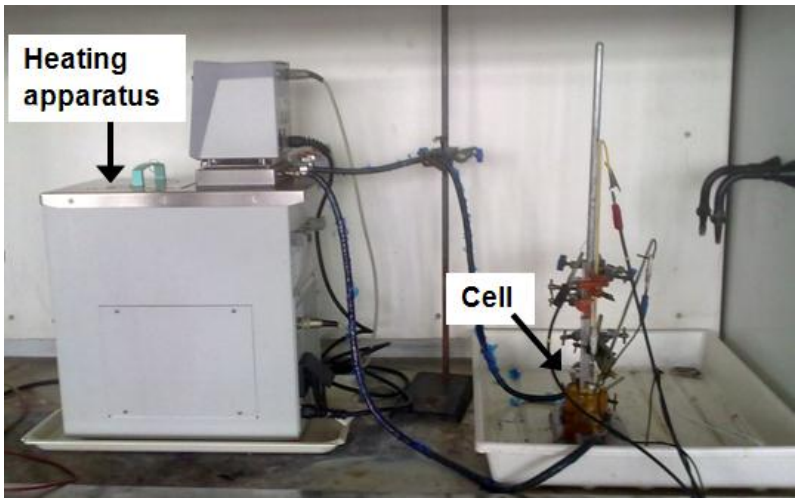

Figure 4.7 – Experimental setup for the voltammetry of ionic liquids at 140 °C.

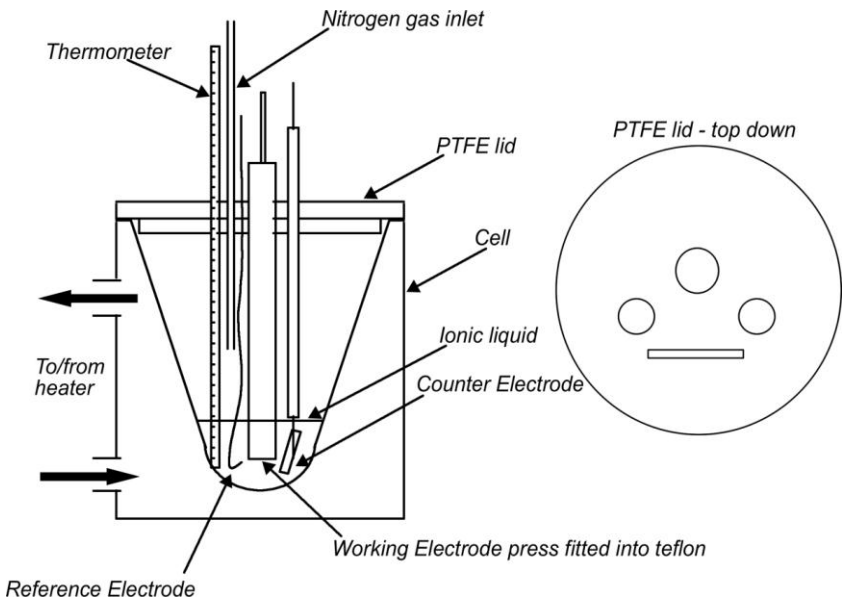

Figure 4.8 – Schematic diagram of cell for high temperature voltammetry.

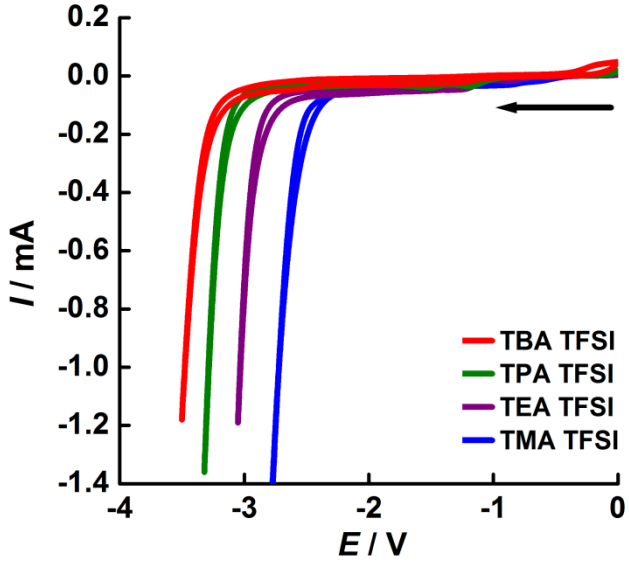

Figure 4.9 – Cyclic voltammograms (superimposed) showing the cathodic reduction of four symmetrical quaternary ammonium cations at 100 mV s^{-1} and 140 ºC. From right to left the ions were; tetramethylammonium, tetraethylammonium, tetrapropylammonium, and tetrabutyl-ammonium. In all cases the anion was bis(trifluoromethylsulfonyl)imide. The working electrode was a glassy carbon disc electrode (d = 3.0 mm) press-fitted into a glass-filled Teflon shroud. The potential was held at 0.0 V for 10 s vs. Ag\|AgCl before being swept in the negative direction. The scan was reversed at ~1.2 mA.

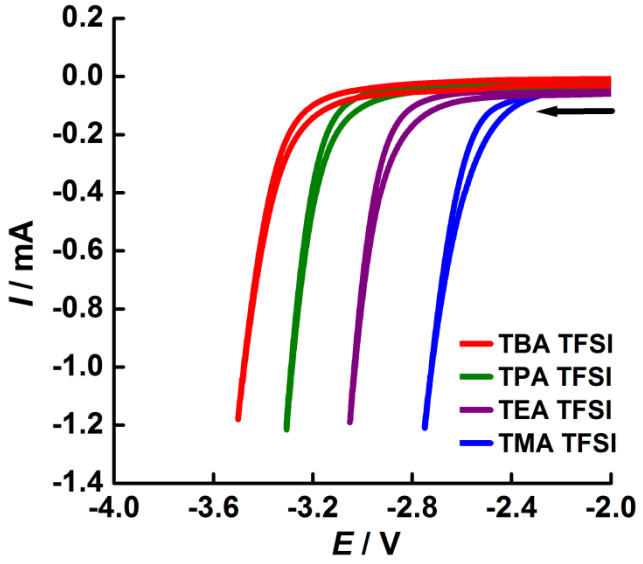

Figure 4.10 – An enlargement of Figure 4.9, showing the cathodic reduction region for the four tetraalkyl ammonium ionic ions. It is clear that the tetrabutylammonium ion (red) has the widest (most negative) potential window.

The result shows that the tetramethylammonium cation is reduced at the least negative potential, followed by the tetraethylammonium cation, then the tetrapropylammonium cation and finally the tetrabutylmmonium cation, which is reduced at the most negative potential and shows an outstanding resistance towards electron tunnelling.

This result is in agreement with quantum electron transfer theory which predicts that as the size of the cations increases, from tetramethylammonium to tetrabutylammonium, the distance that the electron has to tunnel (from the Fermi energy of the electrode to the lowest unoccupied molecular orbital (LUMO) on the central nitrogen atom) increases. As this distance increases, the rate constant for electron transfer decreases, which in turn decreases the electron "tunnelling" probability. This is why a more negative reduction potential is observed for cations with longer alkyl chains.

TBA > TPA > TEA > TMA

The difference between the reduction potential of the tetramethylammonium cation and the tetrabutylammonium cation is about 0.8 V. This is significant as it means that the voltage window (and hence energy stored by a supercapacitor) can be increased simply by reducing the probability that electron transfer will occur.

From the recorded CV data, further analysis was performed. ***Figure 4.11*** shows the Tafel plots for the reduction of each of the tetraalkylammonium ions studied. For reasons that are not clear, the expected Tafel slope of 120 mV per decade for an irreversible, one-electron reduction is not observed in these ionic liquids. Instead, the Tafel slopes do not conform to any standard mechanism and vary from 248 mV $decade^{-1}$ in the case of tetrapropylammonium bis(trifluoromethylsulfonyl)imide up to 333 mV $decade^{-1}$ in the case of tetramethylammonium bis(trifluoromethylsulfonyl)imide.

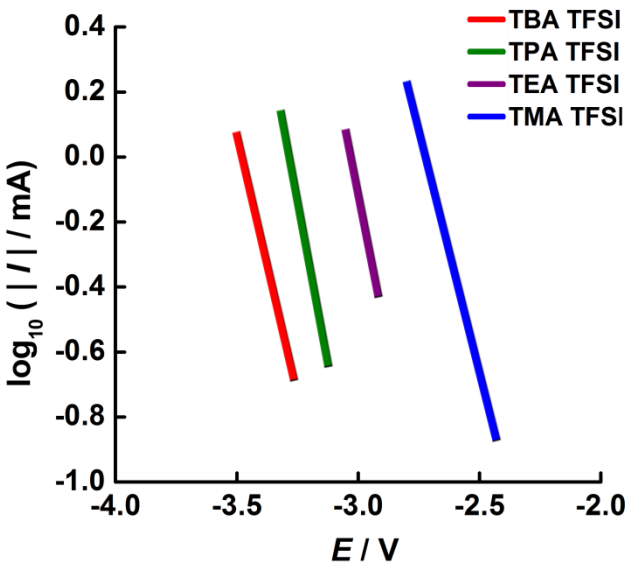

Figure 4.11 – Tafel slopes for the four studied tetraalkylammonium bis(trifluoromethylsulfonyl)-imide ionic liquids. From left to right the cations are tetramethylammonium, tetraethylammonium, tetrpropylammonium, and tetrabutylammonium. Plots based on voltammetric data displayed in Figure 4.10. (Approximately 200 data points per Tafel slope).

Table 4.2 –The Tafel slopes for the studied tetraalkylammonium ionic liquids.

Ionic Liquid	Empirical formula	Tafel slope (mV decade^{-1})
Tetramethylammonium bis(trifluoromethylsulfonyl)imide	$[(CH_3)_4N+][(SO_2CF_3)_2N-]$	333
Tetraethylammonium bis(trifluoromethylsulfonyl)imide	$[(C_2H_5)_4N+][(SO_2CF_3)_2N-]$	258
Tetrapropylammonium bis(trifluoromethylsulfonyl)imide	$[(C_3H_7)_4N+][(SO_2CF_3)_2N-]$	248
Tetrabutylammonium bis(trifluoromethylsulfonyl)imide	$[(C_4H_9)_4N+][(SO_2CF_3)_2N-]$	305

Extrapolation of the Tafel slopes to the potential $E = -3.0$ V allows the rate of electron tunnelling into the various tetraalkylammonium ions to be directly compared, and plotted as a function of ionic radius (***Figure 4.12***). It can be seen that the rate of electron tunnelling decays exponentially with ionic radius. A single exponential function is sufficient to fit the

data with a best-fit quantum tunnelling decay constant of 18 nm^{-1}. The distance dependence of electron tunnelling has been investigated by various authors, especially in biological systems such as proteins and DNA[12-18]. Moser *et al*. reported the quantum tunnelling decay constant for inter-protein electron transfer in biological systems to be 14 nm^{-1}[19-20]. The distance dependence of electron tunnelling has also been studied in self-assembled monolayers by means of conducting probe atomic force microscopy[21]. The decay constant for the alkanethiol layers was found to be approximately 10 nm^{-1}. This picometer scale of electron tunnelling has recently been confirmed by theoretical electron tunnelling models, which probe the transmission probability for electrons tunnelling between states of an atom on a metal surface and the tip of a scanning tunnelling microscope[22].

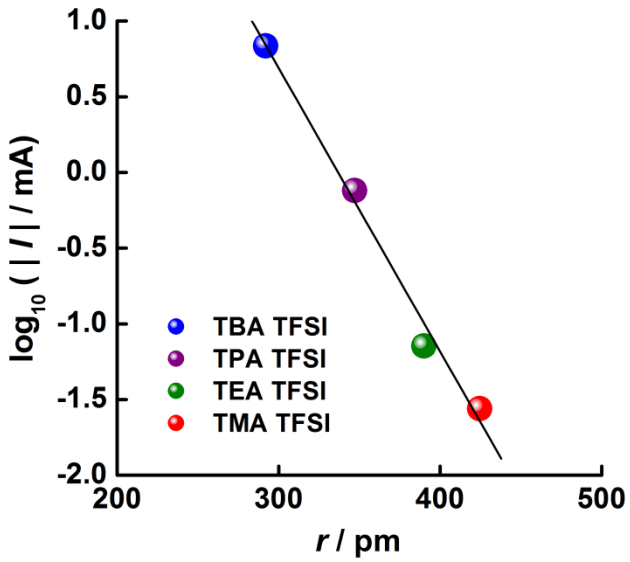

Figure 4.12 – Electron tunnelling probability as a function of ionic radius for the series of symmetrical tetraalkylammonium ions. From left to right the cations are, tetramethylammonium (blue), tetraethylammonium (purple), tetrpropylammonium (green), and tetrabutylammonium (red). Current, I / (mA) was determined from the extrapolation of the Tafel plots in Figure 4.11 to – 3.0 V. The plot shows that the rate of electron tunnelling is quickest in tetramethylammonium bis(trifluoromethylsulfonyl)imide ionic liquid.

The obtained results suggest that a general theory for the stability of ionic liquids is now available, based on the application of quantum theory. Cations with larger alkyl chains have an increased ionic radius. As a result, the electron must tunnel a greater distance to reach the

nitrogen centre and reduce the cation. This causes a decrease in the rate constant for electron transfer and a decrease in the electron tunnelling probability for larger cations. This is why larger cations reduce at more negative potentials than smaller cations.

4.4 – Using quantum theory to design improved ionic liquids

The maximum energy stored by a supercapacitor is proportional to the square of the voltage window, ***Equation 4.4***.

$$E = \frac{1}{2}CV^2 \qquad \textbf{\textit{Equation 4.4}}$$

As a result, by increasing the voltage stability window of an electrolyte, the energy stored by the supercapacitor can be increased dramatically.

As discussed in ***Section 4.3***, quantum theory predicts (and experiments show) that the electron tunnelling probability decreases in the presence of long alkyl chains on the nitrogen atom. Nevertheless, despite the remarkable inertness of tetrabutylammonium TFSI, its melting point is 96 °C. This is far too high for a supercapacitor which is required to operate at both room temperature and high temperature.

The next task was to see whether an ionic liquid could be found that possessed quantum inertness at room temperature. As noted by Welton[23], "There is no reliable way to predict the precise melting point of organic salts, and identification of new room-temperature ionic liquids is a somewhat hit and miss affair." It is widely known that symmetrical compounds have increased melting points due to their increased lattice enthalpy. As a result the search was accelerated by the knowledge that decreasing the symmetry of a component ion would likely decrease the melting point of the ionic liquid[24]. A move towards asymmetric cations was indicated. Accordingly, a range of ionic liquids with bis(trifluoromethylsulfonyl)imide anions and asymmetric tetraalkylammonium cations was screened by DSC and it was found that butyltrimethylammonium bis(trifluoromethylsulfonyl)imide (m.p. 19 °C) and hexyl-triethylammonium bis(trifluoromethylsulfonyl)imide (m.p. 20 °C) were liquids at room temperature. The structural formulas of these two ionic liquids, along with some important physical properties are given in ***Figures 4.13 to 4.15*** and in ***Table 4.3***.

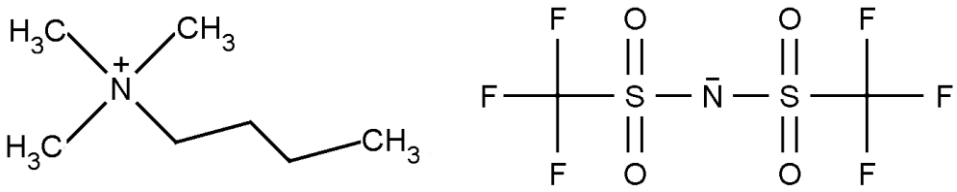

Figure 4.13 – Structural formula of butyltrimethylammonium bis(trifluoromethylsulfonyl)imide.

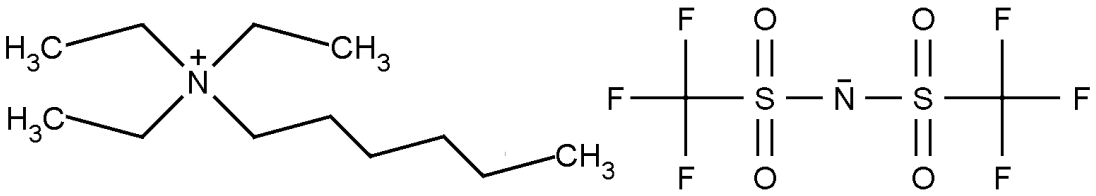

Figure 4.14 – Structural formula of hexyltriethylammonium bis(trifluoromethylsulfonyl)imide.

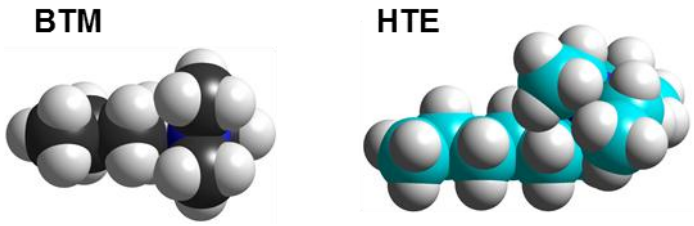

Figure 4.15 – 3D images of left) a butyltrimethylammonium cation (BTM) and right) a hexyltriethylammonium cation (HTE).

Table 4.3 – Physical properties of butyltrimethylammonium bis(trifluoromethylsulfonyl)imide and hexyltriethylammonium bis(trifluoromethylsulfonyl)imide.

Property	**Butyltrimethylammonium bis(trifluoromethylsulfonyl)imide[25]**	**Hexyltriethylammonium bis(trifluoromethylsulfonyl)imide[11]**
Melting point	+19 °C	+20 °C
Glass transition temperature	–74 °C	–81 °C
Viscosity	77 mPa s (30°C)	167 mPa s (25°C)
Conductivity	2.6×10^{-3} S cm^{-1} (30°C)	6.7×10^{-4} S cm^{-1} (25°C)
Molar Conductivity	0.74 S cm^2 mol^{-1} (30°C)	0.25 S cm^2 mol^{-1} (25°C)
Density	1.39 g cm^{-3} (30°C)	1.27 g cm^{-3} (20°C)
Cation radius	347 pm	403 pm

To assess whether these compounds could be used as quantum-inert ionic liquids at room temperature, the electrochemical stability windows of the two suggested ionic liquids were recorded at 25 °C. The cathodic and anodic scans were recorded separately. For butyltrimethylammonium bis(trifluoromethylsulfonyl)imide the start potential was –0.6 V and for hexyltrimethlyammonium bis(trifluoromethylsulfonyl)imide the start potential was –0.1 V. When recording the oxidation scan, the potential was scanned in the positive direction until the observed anodic current reached 0.2 mA. When recording the reduction scan, the potential was scanned in the negative direction until the cathodic current reached 0.2 mA. The scan rate was 100 mV s^{-1}. Prior to scanning, the start potential was held for 30 s *vs.* an Ag|AgCl wire. The counter electrode was platinum gauze and the working electrode was a glassy carbon disc press-fitted into a glass-filled Teflon shroud. Before each measurement the electrodes were polished and dried in a stream of dry nitrogen to remove any traces of water. Multiple replicates of all measurements were made to ensure reproducibility.

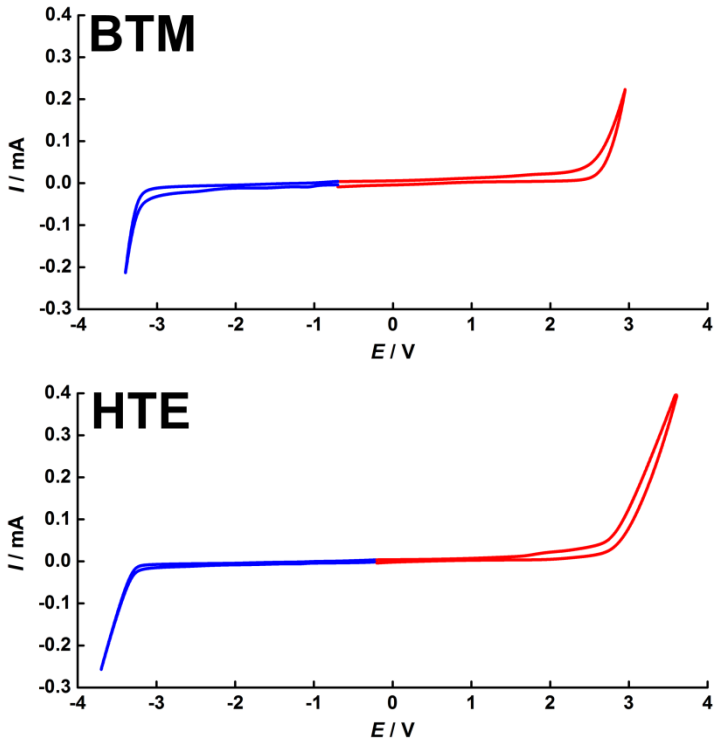

Figure 4.16 – Cyclic voltammograms illustrating the voltage stability window of butyltrimethylammonium bis(trifluoromethylsulfonyl)imide (BTM) and hexyltriethylammonium bis(trifluoromethylsulfonyl)imide (HTE). The working electrode was a glassy carbon disc (d = 3.0 mm) press fitted into a glass-filled Teflon shroud. The reference electrode was a freshly prepared all solid state Ag\|AgCl wire, and the counter electrode was platinum gauze (A = 4.0 cm^2). In all cases, the ionic liquids were driven to decomposition (determined by generation of > 0.2 mA current). The slightly flatter response of the HTE voltammogram can be attributed to greater solution resistance (~2.5 times).

The voltage stability windows of butyltrimethylammonium bis(trifluoromethylsulfonyl)imide and hexyltriethylammonium bis(trifluoromethylsulfonyl)imide are both greater than 5 V and are among the widest yet reported. This means that twenty five times more energy can be stored in a supercapacitor using hexyltriethylammonium bis(trifluoromethylsulfonyl)imide than for an electrolyte with a 1 V voltage stability window (e.g. aqueous systems). The potential limits of room-temperature ionic liquids, and the associated electrochemical windows, have been reported for over a decade, and a compilation of data has been made by O'Mahony *et al.*[26]. The latter authors found that, only in super-dry conditions, the voltage stability window can approach 6 V since the presence of water can significantly damage the results. Nevertheless, the best values exceed those of the leading organic solvent/electrolyte combinations (such as acetonitrile/0.1 M tetrabutylammonium tetrafluoroborate) which have

windows of only 4V. The highest voltage stability window reported to date in the literature for an ionic liquid is 6.35 V, measured for 1-n-butyl-3-methylimidazolium pentafluoro-phosphate on vitreous carbon[27].

As quantum theory predicts, the hexyltriethylammonium cation has a larger voltage window than the butyltrimethylammonium cation. This is because the alkyl groups are larger Similarly, the hexyltriethylammonium cation reduces at a potential more negative than the tetraethylammonium cation. The results are shown in ***Figure 4.17***.

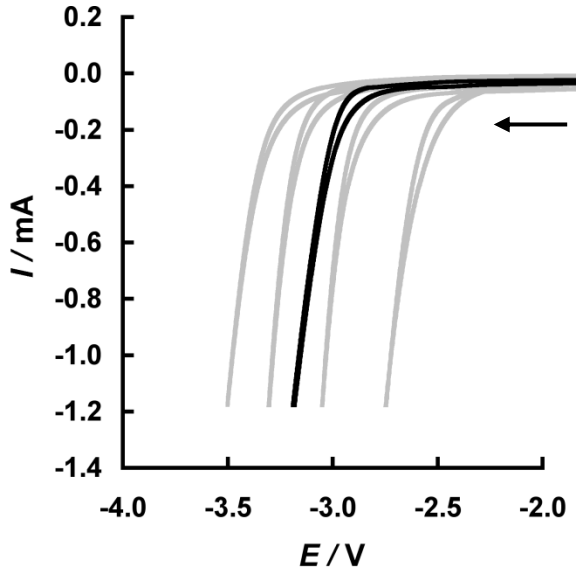

Figure 4.17 – Cyclic voltammograms showing the cathodic reduction of hexyltriethylammonium bis(trifluoromethylsulfonyl) imide (black) at 100 mV s^{-1} (140 °C). The cathodic reduction for these four ionic liquids are superimposed onto Figure 4.10 (grey, from right to left the ions were; tetramethylammonium, tetraethylammonium, tetrapropylammonium, and tetrabutylammonium). In all cases the anion was bis(trifluoromethylsulfonyl)imide. The working electrode was a glassy carbon disc electrode (d = 3.0 mm) press-fitted into a glass-filled Teflon shroud. The potential was held at 0.0 V for 10 s vs. Ag|AgCl before being swept in the negative direction.

4.5 – Conclusion

The design rules for ionic liquids have emerged very slowly but great strides have been taken over the past ten years. In the present work, a contribution has been made by showing that quantum theory can be used to predict the performance of ionic liquids at extreme potentials.

It has also been demonstrated that the reduction potentials of tetraalkylammonium cations are strongly affected by the chain length of the alkyl substituents. By Tafel analysis of experimental results, it was discovered that the rate of electron transfer decayed exponentially with increasing ionic radius. This result was fully consistent with quantum tunnelling theory. Additionally, it was shown that if asymmetric tetraalkylammonium cations were used, then chemical inertness could be extended to room temperature. Since wide voltage windows imply increased energy storage, this work provides a new and exciting route to improved supercapacitor performance.

As a result of this work, a Provisional United States Patent Application has been filed (IS12.2724-US-PSP) highlighting the use of asymmetrical tetraalkylammonium ionic liquids in supercapacitors. In particular, butyltrimethylammonium bis(trifluoromethylsulfonyl)imide and hexyltriethylammonium bis(trifluoromethylsulfonyl)imide have been identified as exceptional candidates for supercapacitor devices.

4.6 – References

[1] Fletcher, S. *The theory of electron transfer*. Journal of Solid State Electrochemistry, 14: 705-739 (2010).

[2] Schrödinger, E. *Quantisierung als Eigenwertproblem*. Annalen der Physik (Leipzig), 79: 361-376 (1926).

[3] Dirac, P. A. M. *The Physical Interpretation of the Quantum Dynamics*. Proceedings of the Royal Society (London), A113: 621-641 (1927).

[4] Gurney, R.W. *The Quantum Mechanics of Electrolysis*. Proceedings of the Royal Society (London), A134: 137-154 (1931)

[5] Randles, J. E. B. *Kinetics of Rapid Electrode Reactions. Part 2. Rate Constants and Activation Energies of Electrode Reactions*. Transactions of the Faraday Society, 48: 828-832 (1952).

[6] Marcus, R. A. *On the Theory of Oxidation Reduction Reactions Involving Electron Transfer (I)*. Journal of Chemical Physics, 24: 966-978 (1956).

[7] Marcus, R. A. *Electrostatic Free Energy and Other Properties of States Having Nonequilibrium Polarization (I)*. Journal of Chemical Physics, 24: 979-989 (1956).

[8] Fletcher S. *A Non-Marcus Model for Electrostatic Fluctuations in Long Range Electron Transfer*. Journal of Solid State Electrochemistry, 11: 965-969 (2007).

[9] Slater, J. C. *Atomic Shielding Constants*. Journal of Physical Reviews, 36: 57-64 (1930).

[10] Stewart, J. J. P. *Optimization of Parameters for Semi-empirical Methods (I). Method.* Journal of Computational Chemistry, 10: 209-220 (2010).

[11] Sun, J., Forsyth, M. & MacFarlane, D. R. *Room-Temperature Molten Salts Based on the Quaternary Ammonium Ion*. Journal of Physical Chemistry B, 102: 8858-8864 (1998).

[12] Winkler, J. R, & Gray, H. B. Chemical Reviews (Washington, DC), 92: 369-379 (1992).

[13] Gray, H. B. & Winkler, J. R. In: *Electron Transfer in Chemistry*. Edited by Balzani, V. Weinheim, Germany: Wiley; 3: pp. 3-23 (2001).

[14] Lewis, F. D. In: *Electron Transfer in Chemistry*. Edited by Balzani, V. Weinheim, Germany: Wiley; 3: pp 105-175 (2001).

[15] Jordan, P., Fromme, P., Witt, H. T., Klukas, O., Seanger, W. & Krauss, N. Nature (London), 411: 909-917 (2001).

[16] De Cola, L. & Belser, P. *In: Electron Transfer in Chemistry*. Balzani V, Editor. Weinheim, Germany: Wiley; 5: pp. 97-136 (2001).

[17] Chen, J., Reed, M. A. Rawlett, A. M. & Tour, J. M. Science, 286: 1550-1552 (1999).

[18] Donhauser , Z. J, Mantooth, B. A, Kelly, K. F., Bumm, L. A., Monnell, J. D, Stapleton J. J, Price, D. W. Jr., Rawlett, A. M., Allara, D. L., Tour, J. M. & Weiss, P. S. Science, 292: 2302-2307 (2001).

[19] Moser, C. C., Keske, J. M., Warncke, K., Farid, R. S. & Dutton, P. L. *Nature of Biological Electron-Transfer*, Nature, 355: 796-802 (1992).

[20] Moser, C. C., Page, C. C., Farid, R. S. & Dutton, P. L. *Nature of Biological Electron-Transfer*. Nature, 355: 796-802 (1992).

[21] Wold, D. J., Rainer, H. Rampi, H. A. & Frisbie. D. *Distance dependence of electron tunneling through self-assembled monolayers measured by conducting probe atomic force microscopy: Unsaturated versus saturated molecular junctions*. Journal of Physical Chemistry B, 106: 2813-2816 (2002).

[22] Palotás, Krisztián., Gábor Mándi. & László Szunyogh, L. *Orbital-dependent electron tunneling within the atom superposition approach: Theory and application to W (110)*. Physical Reviews B, 86(23): 235-415 (2012).

[23] Welton, T., *Room Temperature Ionic Liquids: Solvents for Synthesis and Catalysis. Chemical Reviews*, 99: 2071-2083 (1999).

[24] Holbrey, J. D. & Rogers, R. D. *Physiochemical Properties of Ionic Liquids: Melting Points and Phase Diagrams*. *Ionic Liquids in Synthesis*, 1(3): pp57-71. Edited by Wasserscheid P. & Welton, T. Wiley-VCH, Weinhein, (2008).

[25] Tokuda, H., Tsuzuki, S., Hasan, M. A. B., Hayamizu, S. K & Watanabe, M. J. *How Ionic are Room-Temperature Ionic Liquids? An Indicator of the Physichemical Properties*. Journal of Physical Chemistry B, 110: 19593-19600 (2006).

[26] O'Mahony, A. M. Silvester, D. S. Aldous, L. Hardacre, C. & Compton, R. G. *Effect of water on the electrochemical window and potential limits of room-temperature ionic liquids*. Journal of Chemical & Engineering Data, 53: 2884-2891 (2008).

[27] Suarez, P. A. Z, Selbach, V. M. EL Dullius, J., Einloft, S., Piatnicki, C., Azambuja, D. S. de Souza, R. F. & Dupont, J. *Enlarged electrochemical window in dialkyl-imidazolium cation based room-temperature air and water-stable molten salts*. Electrochimica Acta, 42(16): 2533-2535 (1997).

Chapter 5 – Passivation of Carbon Electrodes in Ionic Liquids

5.1 – Introduction

Faradaic reactions are charge transfer reactions that occur at the electrode|solution interface[1]. Whilst reversible faradaic reactions add to measured capacitance, they are also undesirable in supercapacitors, as they generally cause material degradation. Even when the main components of an electrolyte are faradaically inert, faradaic reactions may still occur as a result of impurities in the solvent or as a result of solvent decomposition. Therefore, eliminating such reactions is a priority in the development of practical devices.

In the present work, a search was initiated to find compounds, such as phenol derivatives, whose electrochemical reactions might form blocking films on the electrode surface. An important criterion for an electrode blocking film was that it should be thin enough to maintain electrode capacitance, but thick enough to "switch off" the tunnelling of electrons into redox species in the solution (> 1.23 nm).

5.2 – Theory for electrode blocking films

In interfacial electrochemistry, electron transfer typically takes place by quantum tunnelling of an electron from an energy state near the Fermi energy of the electrode into an unoccupied orbital of a reactant molecule. In ***Chapter 3***, ***section 3.2***, it was shown that the probability of electron tunnelling decreases exponentially with separation distance between the donor and acceptor orbitals, ***Equation 5.1***, where S_{DA} is the orbital overlap integral, and x is the internuclear distance between the donor and acceptor molecules, and A and C are constants.

$$S_{DA} \approx A\exp(-Cx) \qquad \textbf{\textit{Equation 5.1}}$$

The maximum distance for the electron tunnelling is approximately 1.23 nm. Beyond this distance, the probability of electron tunnelling is insignificant. Therefore, in order for an electrode to be faradaically inert, the deposited film needs to be at least 1.23 nm thick.

5.3 – The search for electrode blocking molecules

It has long been known that phenols polymerise at positive potentials (approx +0.5 V *vs.* SCE) to yield partially blocking films[2-6]. Accordingly, an extensive literature search was carried out among derivatives of phenol (especially the polyhydroxy phenols) to identify candidates for fully blocking films. To avoid quinone formation, focussed was placed on compounds having only one hydroxy substituent, or compounds having two hydroxy substituents *meta* to each other (which cannot oxidise to form quinones).

The electrochemical oxidation (and subsequent polymerisation) of phenols proceeds *via* the generation of free radicals[7-8]. The precise mechanism for the reaction is debated in the literature[2-9], but it is generally agreed that the first stage involves the one electron oxidation of the phenol molecule to produce a resonance stabilised phenoxy radical, (***Scheme 5.1)*** The phenate anion, being charged, is soluble in water; but the phenoxy radical, being uncharged is insoluble. As a result, phenoxy radicals accumulate at the electrode surface.

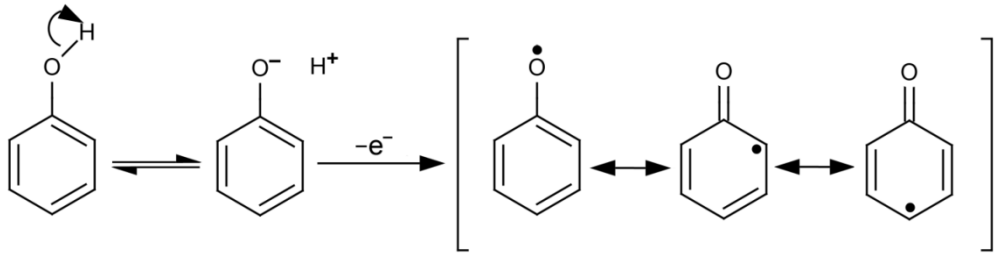

Scheme 5.1

The phenoxy radicals then polymerise by pathways such as those shown in ***Scheme 5.2***. Hydrogen elimination favours the formation of aromatic rings in the product.

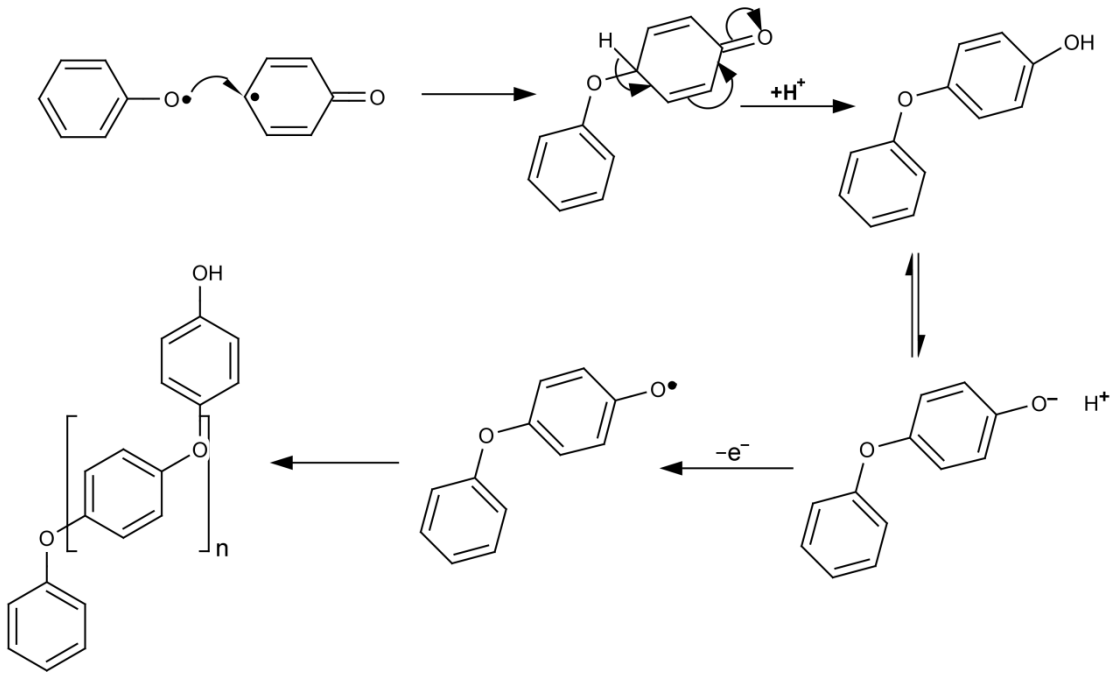

Scheme 5.2

During the literature search, a compound first studied by Brett and co-workers (2006)[10] was identified as a starting point. This compound was 3,5,4′-trihydroxy-*trans*-stilbene (*trans*-resveratrol). Resveratrol is an organic metabolite, present in several families of plants, produced in response to injury, fungal infection and UV radiation[10-11]. It can be found in a variety of foodstuffs including grapes, cranberries and peanuts[12-13]. It is a powerful antioxidant and some health benefits have been claimed[14]. The structure of *trans*-resveratrol is shown in ***Figure 5.1***. In their publication, Brett and co-workers were principally interested in the analytical determination of *trans*–resveratrol, but they did note that it formed insulating thin poly(*trans*-resveratrol) films on electrode surfaces in water. For Brett *et al*, this was a liability, but here it was an asset.

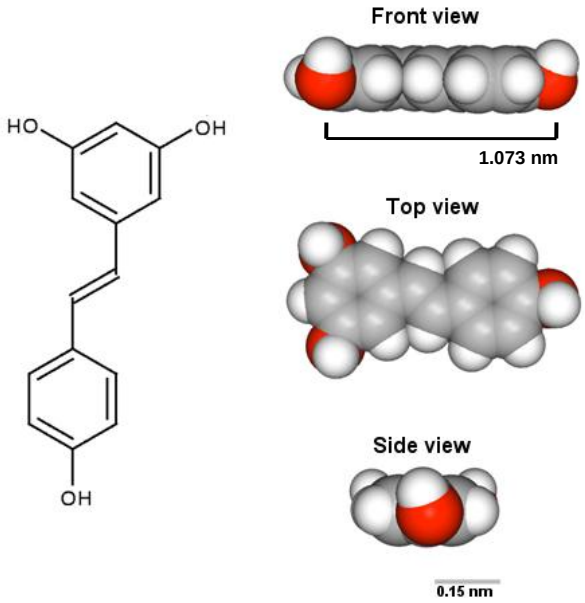

Figure 5.1 – Structural formula and orthographic projection of a trans–resveratrol monomer ($C_4H_{12}O_2$). The scale bar indicates the distance between the terminal oxygens, calculated in HyperChem.

Initial work was carried out to see whether the work of Brett[10] could be repeated and to assess the robustness of the blocking films. Preliminary experiments were carried out using both glassy carbon and RAM working electrodes. This was because, if the phenoxy radical had been even moderately soluble in solution, then it would have escaped from the surface of the RAM electrode, and passivation would not have occurred. In fact, despite the powerful hemispherical flux away from the surface of each micro-electrode in the RAM, very few phenate radicals escaped.

An electrochemical cell was assembled containing the deposition solution promoted by Brett et al[10]: *trans*–resveratrol (10 mmol dm^{-3}) in ethanol (2 ml) added to 5 ml of 10 mmol dm^{-3} acetic acid. The working electrode was either a glassy carbon disc electrode or a RAM electrode. The counter electrode was platinum gauze. The potential was held at 0.0 V *vs.* SCE before being cycled at 20 mV s^{-1} from 0.0 V to +1.0 V to 0.0 V for 2 scans. The onset of deposition current was observed at approximately 0.5 V.

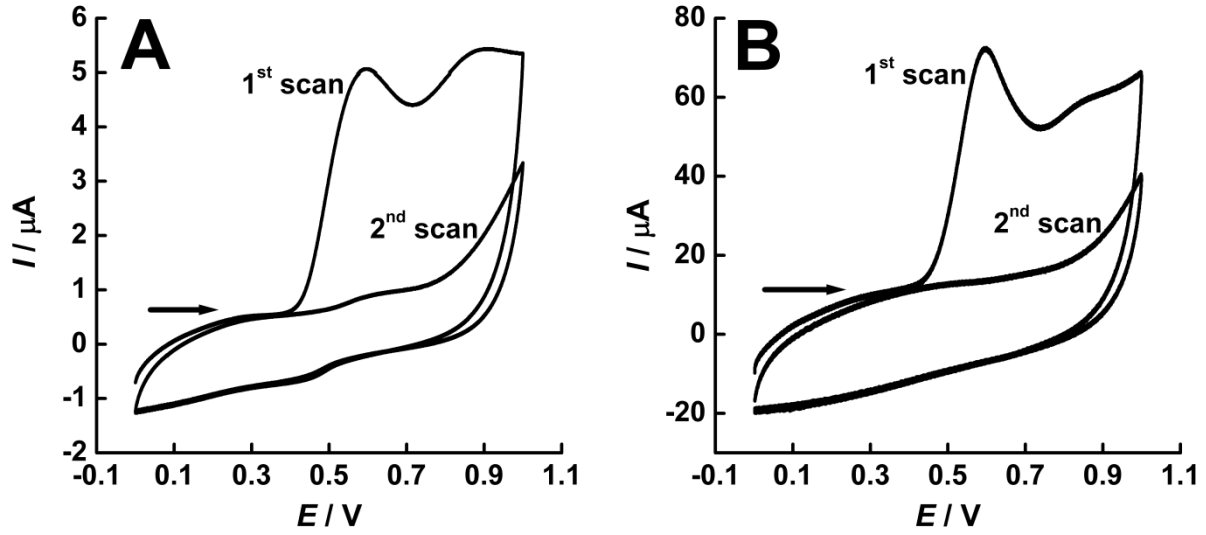

Figure 5.2 – Voltammetry of trans-resveratrol on A) a glassy carbon disc electrode (r = 1.5 mm), areal density of charge circa 1.4 mC cm^{2}, film thickness circa 4.02 nm, and on B) a random assembly of 770 carbon fibre micro disc electrodes (RAM™ electrode), 6,000 data points per cycle, 5 point moving average, areal density of charge circa 3.8 mC cm^{-2}, film thickness circa 11.0 nm . The reference electrode was SCE, the counter electrode was platinum gauze (A = 4.0 cm^{2}). The solution was prepared by adding 0.5 ml of 10 mM trans-resveratrol in ethanol to 5 ml of 10 mM acetic acid. Upper curve is the first scan. Lower curve is the second scan. The potential was held at 0.0 V vs. SCE for 10 s before cycling between 0.0 V and +1.0 V, at 20 mV s^{-1}.

It is evident that polymeric thin films of *trans*–resveratrol were deposited from the solution onto the glassy carbon electrode. The same result was obtained on the random assemblies of carbon fibre micro-discs, as evidenced by the elimination of the resveratrol anodic oxidation current after a single voltammetric scan, ***Figure 5.2***. After this success, it was decided to investigate the ability of the poly(*trans*-resveratrol) films to inhibit redox reactions occurring at the electrode surface. The chosen redox active species for testing were potassium hexacyanoferrate(III), potassium hexachloroiridate(III), and bis(η^5–cyclopentadienyl)iron(II) termed ferrocene. The structures of these compounds are given in ***Figure 5.3***.

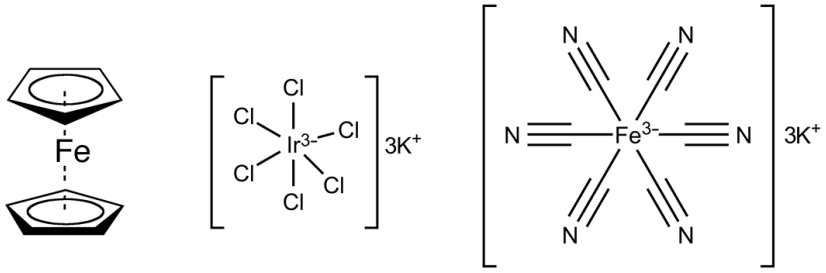

Figure 5.3 – Structural formulae of ferrocene (left), potassium(III) hexachloroiridate (middle), and potassium(III) hexacyanoferrate (right).

Two cells were set up in parallel. One cell contained the deposition solution, namely *trans*–resveratrol (10 mmol dm^{-3}) in ethanol (2 ml) added to 5 ml of 10 mmol dm^{-3} acetic acid. The other cell contained the redox active species under test. The redox active species potassium(III) hexacyanoferrate and potassium(III) hexachloroiridate (both 1 mM) were dissolved in supporting electrolyte, (KNO, 0.5 M), and ferrocene (1 mM) was dissolved in the ionic liquid butyltrimethylammonium bis(trifluoromethylsulfonyl)imide. The cyclic voltammetry of the redox active species was initially recorded over the following potential ranges: Potassium(III) hexacyanoferrate (–0.2 V to +0.8 V), potassium(III) hexachloroiridate (0.0 V to +1.0 V), and ferrocene (0.0 V to +0.5 V). Next, the working electrode was removed from the redox active solution, cleaned, and immersed into the deposition solution. Here, a film of poly(*trans*-resveratrol) was deposited by the aforementioned method. The electrode was subsequently re-immersed into the redox active solution and the cyclic voltammetry re-recorded under the same conditions. The experiment was undertaken on both a glassy carbon and a RAM electrode. In all cases, the scan rate was 20 mV s^{-1}, and the cell was conditioned at the start potential for 10 s. The reference electrode was SCE in aqueous systems and Ag|AgCl in the ionic liquid. The counter electrode was platinum gauze in all cases.

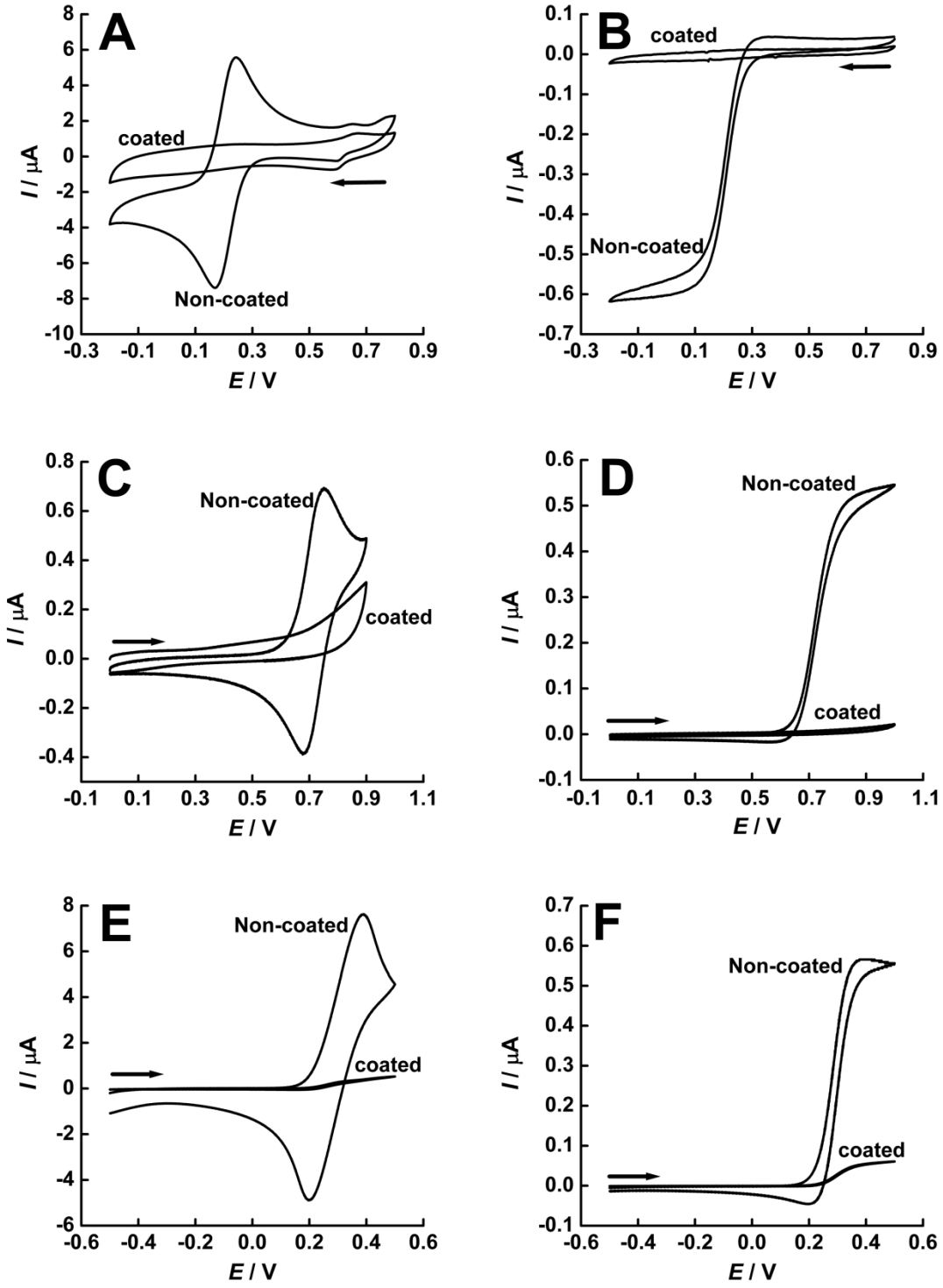

Figure 5.4 – Voltammetry of redox active species on a glassy carbon macro electrode (left) and on a RAM array of micro-electrodes (right) before and after the deposition of poly(trans-resveratrol) films. For A and B, the test solution was aqueous potassium hexacyanoferrate(III) in 0.5 M KNO_3. For C and D, the test solution was aqueous potassium hexachloroiridate(III) in 0.5 M KNO_3, and for E and F the test solution was ferrocene dissolved in butyltrimethylammonium bis(trifluoromethylsulfonyl)imide. The redox species was present in each case at 1 mM concentration. The scan rate in each case was 20 mV s^{-1}. Lower curve, in absence of poly(trans-resveratrol) film. Upper curve, in presence of poly(trans-resveratrol) film.

Phenomenally, although less than five nanometres in thickness, these polymeric films are also capable of inhibiting the redox electrochemistry of potassium hexacyanoferrate(III), potassium hexachloroiridate(III) and bis(η^5–cyclopentadienyl)iron(II) after a single potential scan. The films also demonstrated good mechanical resistance, and were only removable by vigorous electrode polishing.

However, while it has been demonstrated that poly(*trans*-resveratrol) films can inhibit the ferrocene redox reaction in butyltrimethylammonium bis(trifluoromethylsulfonyl)imide when deposited externally, one major draw-back of using *trans*-resveratrol is that it cannot be directly deposited *in-situ* due to its poor solubility in hydrophobic ionic liquids.

5.4 – Electrode blocking deposits in ionic liquids

Although *trans*-resveratrol is useful for forming electrode-blocking films in aqueous systems, it is insoluble in ionic liquids. This means that, for use in an ionic-liquid based supercapacitor, the blocking film must be applied in a separate aqueous step and then thoroughly dried before use. To avoid this complication, a search was undertaken for commercially available compounds that might be soluble in ionic liquids but yield insoluble poly(phenol) films when oxidized on carbon electrodes. One class of compounds that were identified was the *bisphenols*. These typically have two hydroxyphenyl functionalities separated by a bridging moiety. The first compound of this type that was tested was 4,4'-(2,2-propanediyl)diphenol, better known as bisphenol A (see ***Figure 5.5***).

Bisphenol A is made by condensing two molecules of phenol with one of acetone, and is a well-known precursor of polycarbonate plastics and epoxy resins[15]. Unlike resveratrol, bisphenol A dissolves readily in ionic liquids, possibly because it has one less hydroxy group, and hence is less hydrogen bonded. Whatever the reason, a series of experiments was devised to see whether an electropolymerised film of bisphenol A could be formed on a carbon electrode in an ionic liquid, and, if so, whether this film could inhibit an unwanted faradaic reaction. The findings of these experiments follow.

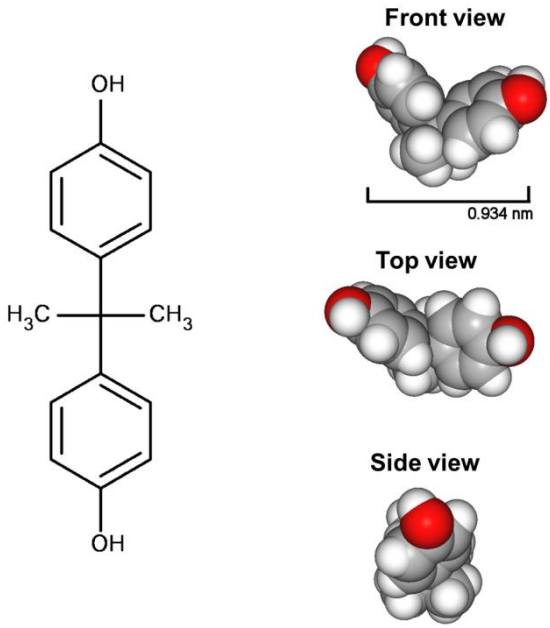

Figure 5.5 – Structural formula and orthographic projection of bisphenol A (4,4'-(2,2-Propanediyl)diphenol). The scale bar indicates the distance between the terminal oxygens, calculated in HyperChem.

Butyltrimethylammonium bis(trifluoromethylsulfonyl)imide was saturated with Bisphenol A (0.2 M). The potential was cycled at 20 mV s^{-1} from 0.0 V to +1.5 V to 0.0 V for five cycles following electrode conditioning for 30 s at 0.0 V *vs*. Ag|AgCl. The counter electrode was platinum gauze. The working electrode was a RAM.

The *in-situ* polymerisation of poly(bisphenol A) was successful in this ionic liquid. Next, in order to determine if the poly(bisphenol A) was able to block faradaic reactions, the electrode response of a standard redox active species (ferrocene) in the ionic liquid before and after the addition of bisphenol A was monitored. The aim was to see whether the poly(bisphenol A) film was capable of inhibiting the ferrocene reaction *in-situ*.

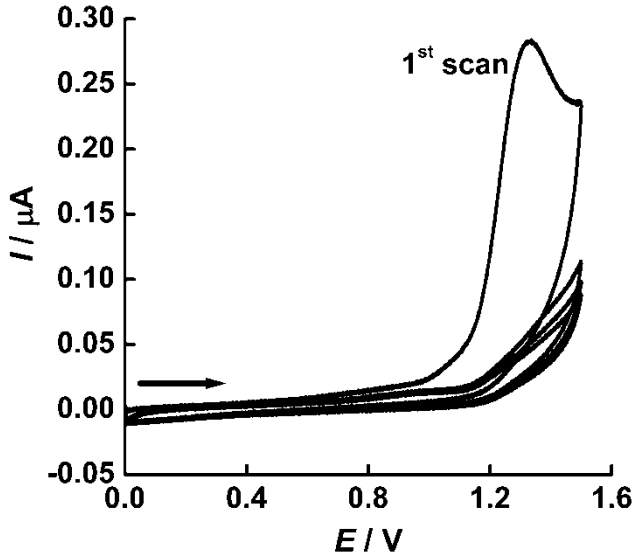

Figure 5.6 – Cyclic voltammetry indicating the ready polymerisation of Bisphenol A (saturated) in butyl–trimethylammonium bis(trifluoromethylsulfonyl)imide ionic liquid. The working electrode was a random assembly of 770 carbon fibre micro disc electrodes (RAM™ electrode) and the counter electrode was platinum gauze (A = 4.0 cm^2). The potential was held for 30 s at 0.0 V vs. Ag\|AgCl before cycling between 0.0 V and +1.5 V at 20 mV s^{-1}. The charge passed was circa 10 mC cm^{-2}. Upper curve, first scan, lower curves, scans two to five.

Cyclic voltammograms of ferrocene (10 mM) in butyltrimethylammonium bis(trifluoro–methylsulfonyl)imide were recorded on both a glassy carbon working electrode, and on a RAM working electrode. The potential was cycled from –0.5 V to +0.5 V at 20 mV $s^{-1.}$ Bisphenol A (saturated) was then added to the ionic liquid and the voltammetry recorded on both working electrodes over the potential range –0.5 V to +1.7 V to –0.5 V at 20 mV s^{-1}. Before all scans, the start potential was held for 120 s *vs.* Ag|AgCl. The counter electrode was platinum gauze. It can be seen that the polymerisation of bisphenol A in butyltrimethylammonium bis(trifluoromethylsulfonyl)imide is self-limiting, with the electrode passivating after a few voltammetric cycles. This was evidenced by the drop in anodic current corresponding to the oxidation of bisphenol A.

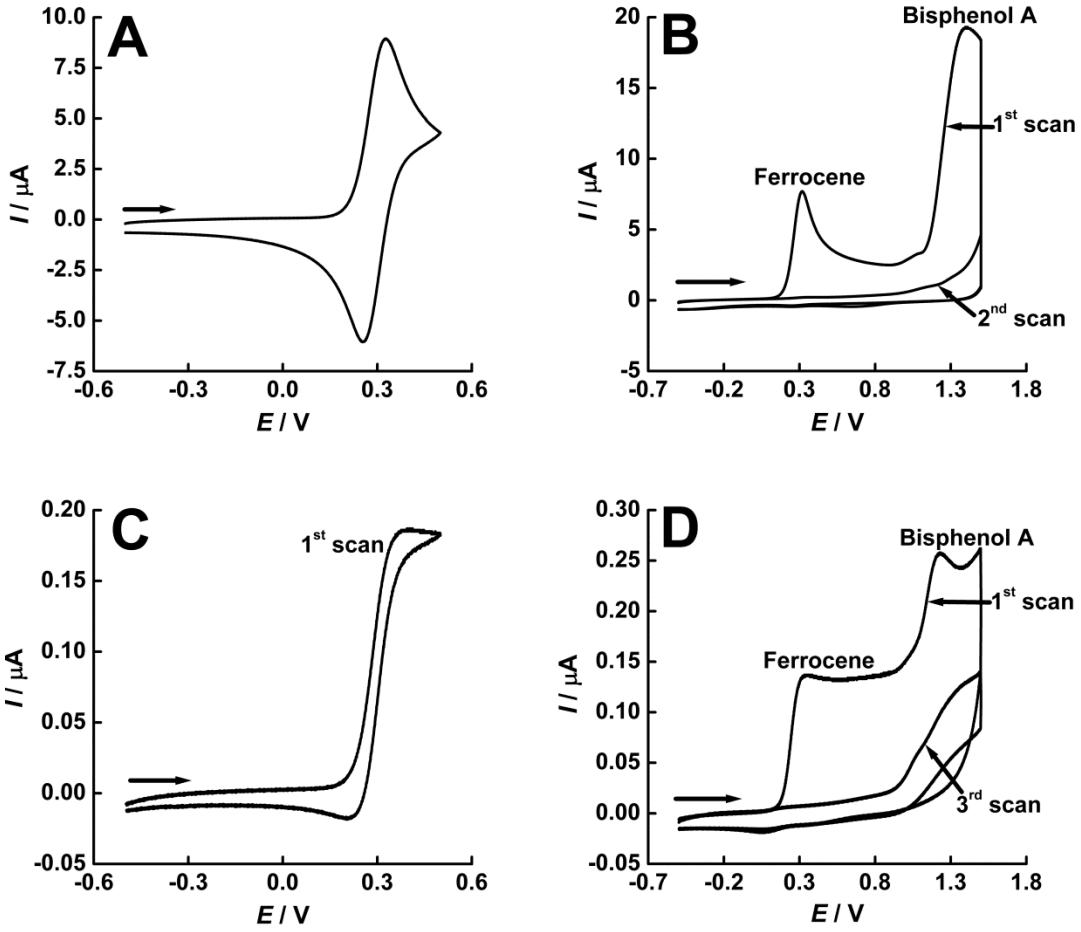

Figure 5.7 – A and C show the cyclic voltammograms of ferrocene (10 mM) in butyltrimethylammonium bis(trifluormethylsulfonyl) imide (–0.5 V to +0.5 V) B and D show the cyclic voltammetry of ferrocene (10 mM) and the in-situ polymerisation of bisphenol A (saturated, –0.5 V to +1.5 V). In A and B the working electrode was a glassy carbon disc electrode (r = 1.5 mm). In C and D the working electrode was a random assembly of 770 carbon fibre micro disc electrodes (RAM™ electrode). The counter electrode was platinum gauze (A = 4.0 cm^2) and the reference electrode was an Ag\|AgCl wire. The potential was held at –0.5 V vs. Ag\|AgCl for 120 s prior to cycling. The scan rate was 20 mV s^{-1}.

5.5 – Bisphenol A: An endocrine disrupter?

Polycarbonates made from bisphenol A are among the most widely synthesised chemicals in the world. They have no competition from other plastic materials in terms of transparency, durability, thermal stability and cost[16]. Annually, it is estimated that a 10^9 kg of bisphenol A are produced for the polycarbonate industry. Another major use is in epoxy resins, which are widely used to line food and drink containers to prevent corrosion[16].

In recent years, sporadic reports have appeared in the media suggesting that bisphenol A might be an endocrine disrupter, together with the suggestion that it should not be used in the manufacture of consumer products[17]. Endocrine disrupters affect male and female reproduction and have been linked to cancer, neuroendocrinology problems, thyroid dysfunction, obesity and metabolic disorders. It has been postulated that bisphenol A might compete with [^{3}H]–17β–estradiol (***Figure 5.8)*** for binding to estrogen receptors, and thus might interfere with the estrogen signalling pathway[18]. Indeed, some British scientists have attributed the sexual disruption of male fish over the last 20 years to this cause [19].

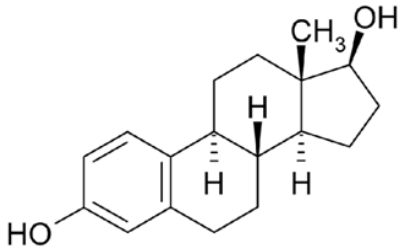

Figure 5.8 – The structural formula of [3H]–17β–estradiol.

In the present work, the electrode surface is blocked with poly(bisphenol A), not the monomer, and so there should be very little chance of exposure to the monomer. Nevertheless, the controversy surrounding bisphenol A prompted a search for possible replacements. Among the tested compounds were 4,4'-(1,1,1,3,3,3-hexafluoro-2,2-propanediyl)diphenol (bisphenol AF), 4,4'-sulfonyldiphenol, (bisphenol S) and 4,4'-(1,4-phenylenedi-2,2-propanediyl)diphenol (bisphenol P). Their structural formulas are shown in ***Figure 5.9***, ***Figure 5.10***, and ***Figure 5.11***.

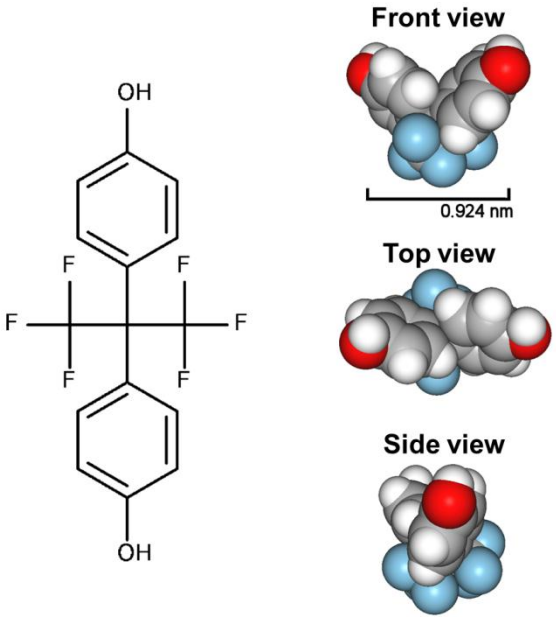

Figure 5.9 – Structural formula and orthographic projection of bisphenol AF. The systematic name of bisphenol AF is 4,4'-(1,1,1,3,3,3-Hexafluoro-2,2-propanediyl)diphenol. The scale bar indicates the distance between the terminal oxygens, calculated in HyperChem.

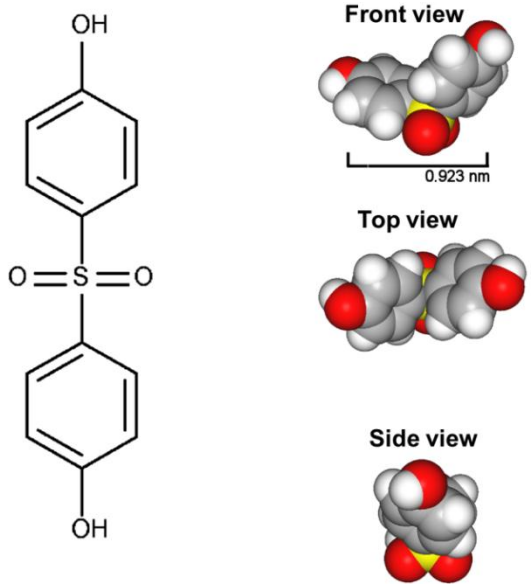

Figure 5.10 – Structural formula and orthographic projection of bisphenol S. The systematic name of bisphenol S is 4,4'-Sulfonyldiphenol. The scale bar indicates the distance between the terminal oxygens, calculated in HyperChem.

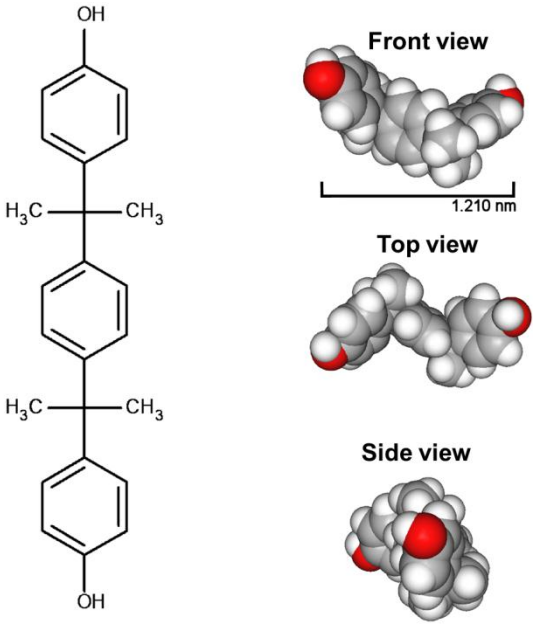

Figure 5.11 – Structural formula and orthographic projection of bisphenol P. The systematic name of bisphenol P is 4,4'-(1,4-Phenylenedi-2,2-propanediyl)diphenol. The scale bar indicates the distance between the terminal oxygens, calculated in HyperChem.

All three compounds, plus bisphenol A, dissolved in butyltrimethylammonium bis(trifluoromethylsulfonyl)imide. To determine their solubilities, four sample tubes, each containing 1 ml of butyltrimethylammonium bis(trifluoromethylsulfonyl)imide were prepared, and then the compounds were added in 10 mM increments. The results are listed in ***Table 5.1***.

Table 5.1 – Solubilities of selected bisphenols in BTM-TFSI.

Phenol monomer		
Common name	**Systematic name**	**Point of saturation / M**
Bisphenol A	4,4'-(2,2-Propanediyl)diphenol	0.2
Bisphenol AF	4,4'-(1,1,1,3,3,3-Hexafluoro-2,2-propanediyl)diphenol	0.5
Bisphenol S	4,4'-Sulfonyldiphenol	0.5
Bisphenol P	4,4'-(1,4-Phenylenedi-2,2-propanediyl)diphenol	0.5

5.6 – Assessing the poly(phenols) passivation capability

In order to test whether the selected compounds were able to polymerise in ionic liquids, cyclic voltammetry was recorded over the range 0.0 V to +2.0 V versus Ag|AgCl and the anodic current was recorded. Scanning to +2.0 V was found to achieve the best passivating film based on extensive trials. When investigating the ability of the polymerised phenol derivatives to inhibit faradaic reactions, the ferrocene/ferrocinium redox reaction was used as the test standard.

Four electrochemical cells were assembled, each containing 2 ml of butyltrimethyl-ammonium bis(trifluoromethylsulfonyl)imide saturated with one of the four phenol derivatives. Cyclic voltammetry of each saturated solution was then recorded at a glassy carbon disc electrode. Initially, the potential was held at 0.0 V *vs.* Ag|AgCl wire for 30 s before being cycled between 0.0 V and +2.0 V at 20 mV s^{-1}. Five cycles were recorded. The counter electrode was platinum gauze. The results are shown in ***Figure 5.12***. It can be seen that one voltammetric scan was sufficient to passivate the electrode. This is a testimony to the extraordinary electrical resistance of the poly(bisphenol) films.

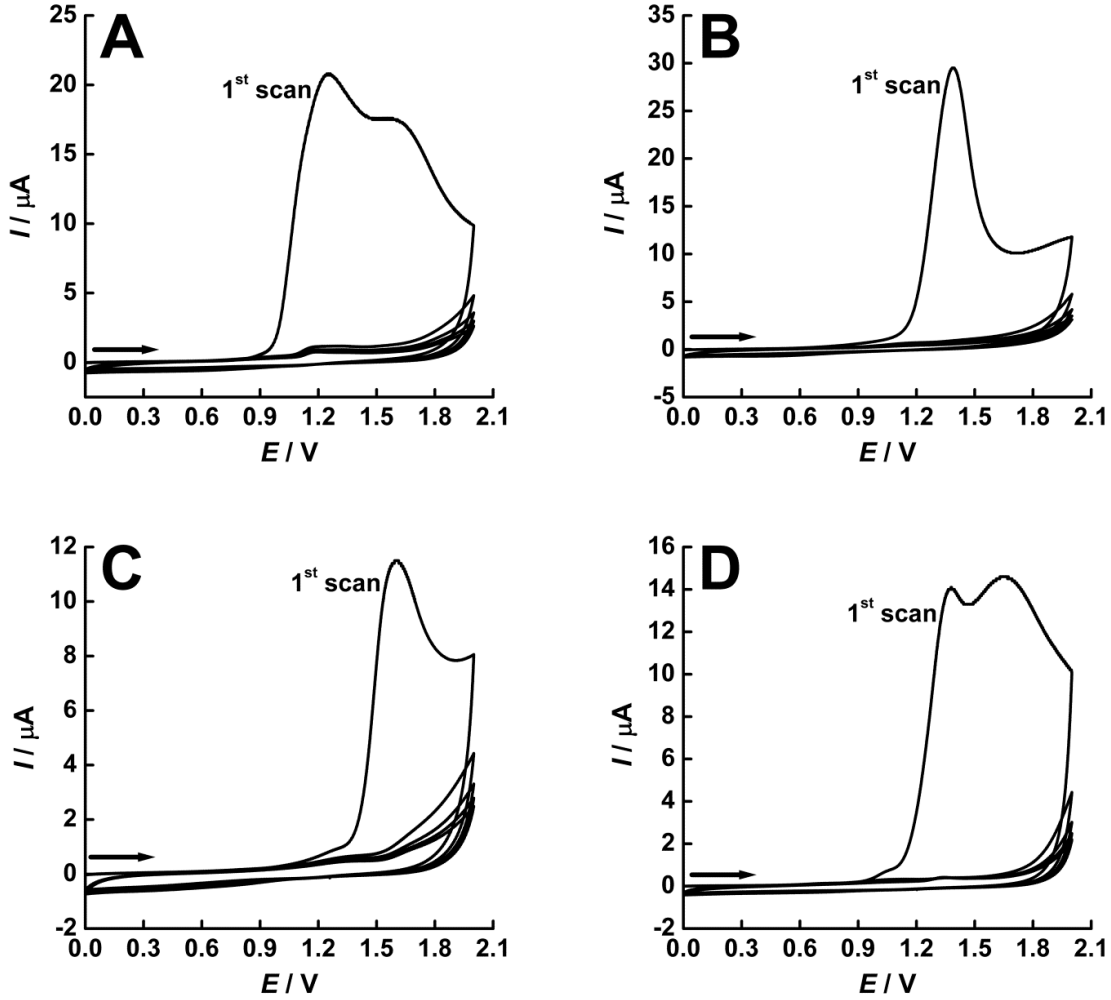

Figure 5.12 – Cyclic voltammetry displaying the polymerisation of A) bisphenol A (0.2 M), areal density of charge circa 10.5 mC cm^{-2}, film thickness circa 30.6 nm B) bisphenol AF (0.5 M), areal density of charge circa 8.4 mC cm^{-2}, film thickness circa 24.6 nm C) bisphenol S (0.5 M), areal density of charge circa 3.4 mC cm^{-2}, film thickness circa 10.0 nm and D) bisphenol P (0.5 M) areal density of charge circa 7.0 mC cm^{-2}, film thickness circa 20.5 nm, on a glassy carbon disc electrode (d = 3 mm) in butyltrimethylammonium bis(trifluoromethylsulfonyl)imide (2 ml). The potential was held at 0.0 V vs. Ag\|AgCl wire for 30 s before cycling from 0.0 V to +2.0 V to 0.0 V at 20 mV s^{-1} for 5 cycles. The counter electrode was platinum gauze (A = 4.0 cm^2).

Next, the ability of poly(bisphenol) films to block faradaic reactions was studied. In four standard electrochemical cells, ferrocene (10 mM) was dissolved in butyl trimethylammonium bis(trifluoromethylsulfonyl)imide (2 ml) and the cyclic voltammetry recorded between 0.0 V to +0.5 V. To each of the four cells, one of the four phenol–based monomers was added (saturated). The voltammetry was then repeated extending the potential limits from 0.0 V to +2.0 V to allow the monomer to polymerise. The potential was held at

+2.0 V for 1000 s to ensure that polymerisation was complete. A second scan was then recorded to assess the ability of the passivated electrode to block the ferrocene/ferrocinium redox reaction. Finally, voltammetry was repeated over the initial potential range 0.0 V to 0.0 V to focus on the potential range of the ferrocene reaction. In each case, the working electrode was glassy carbon disc electrode, and the counter electrode platinum gauze. For each scan the starting potential was held for 30 s before cycling.

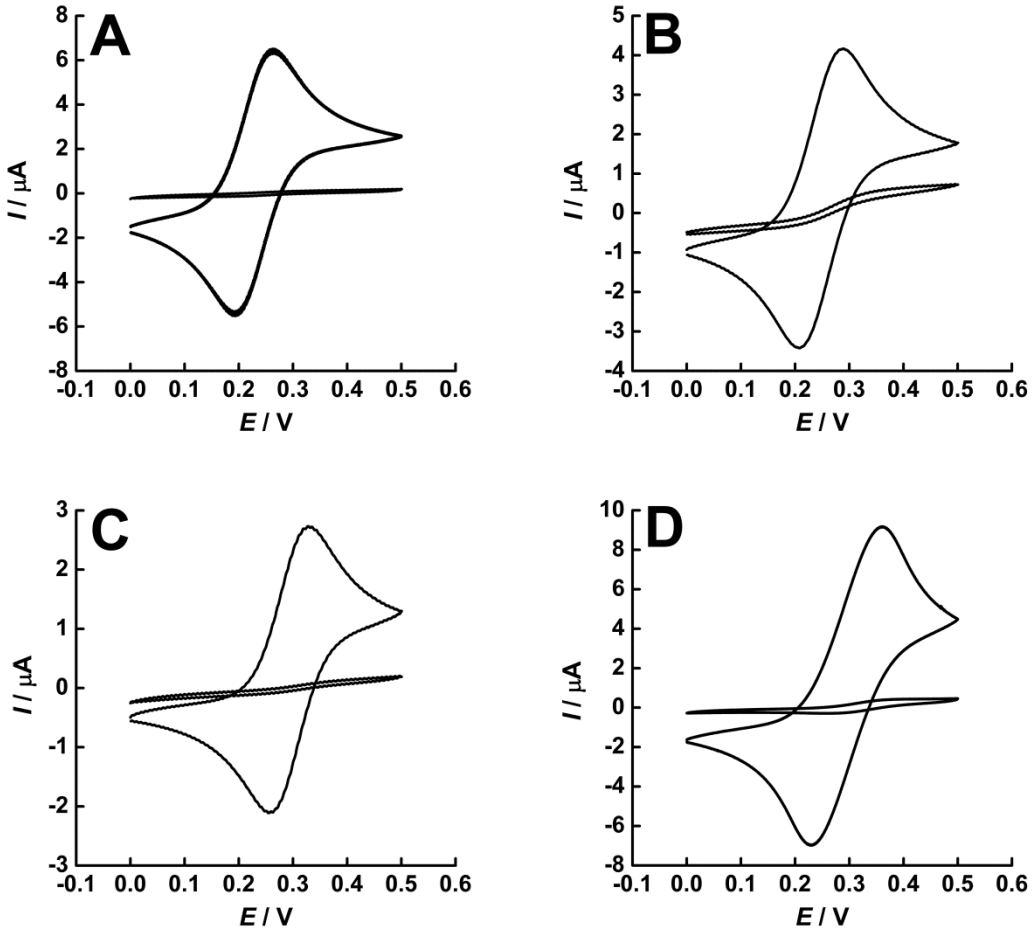

Figure 5.13 – Cyclic voltammograms showing the in-situ inhibition of the ferrocene peak (10 mM) at 25 ºC before and after the surface polymerisation of A) bisphenol A (0.2 M), B) bisphenol AF (0.5 M) , C) bisphenol S (0.5 M) , and D) bisphenol S (0.5 M) in butyltrimethylammonium bis(trifluoromethylsulfonyl)imide. The working electrode was a glassy carbon disc electrode (d = 3 mm). The potential was held at 0.0 V vs. Ag\|AgCl wire for 30 s before cycling from 0.0 V to +0.5 V to 0.0 V at 20 mV s^{-1} for two cycles. Shown above are the second scans. The counter electrode was platinum gauze (A = 4.0 cm^2).

The ability of poly(phenols) to passivate a carbon surface in the presence of a redox active species in ionic liquids has been shown for the first time. From the above results, it is apparent that poly(bisphenol A) produces the most effective passivating film against the ferrocene/ferrocinium redox couple. However, all four of the phenol-based compounds trialled were able to successfully block faradaic redox reactions *in-situ* in ionic liquids.

5.7 – Temperature stability of electrode blocking films

In order for passivating films to be considered for use in high temperature supercapacitors, it was necessary for their effectiveness at high temperature to be tested. There were two possible routes to try.

1. Application of coating at room temperature before transfer into hot ionic liquid.
2. Application of coating in hot ionic liquids.

The first method allowed electrodes to be passivated in a cell external to that of the working supercapacitor. However, the thermal shock of transferring the electrode into a hot ionic liquid generally damaged the integrity of the film. Preliminary results for the second method, applying the coating at high temperature, are given.

Ferrocene (10 mM) was dissolved in butyltrimethylammonium bis(trifluoromethylsulfonyl) imide (2 ml). The voltammetry of ferrocene was then recorded over the range –0.3 V to 0.5 V to –0.3 V at 20 mV s^{-1}. Bisphenol A (0.5 M) was then added to the cell and 5 potential cycles completed in the ionic liquid from –0.0 V to +2.0 V to –0.0 V at 20 mV s^{-1} to coat the electrode. After coating scans, the voltammetry of ferrocene was again recorded under the same conditions. This process was recorded at 25 °C, 50 °C, 100 °C and 150 °C in a thermostatically controlled electrochemical cell. The potential was held at the start potential *vs*. Ag|AgCl wire for 30 s before commencing cycling. The counter electrode was platinum gauze and the working electrode was a glassy carbon disc press-fitted into a glass-filled Teflon shroud.

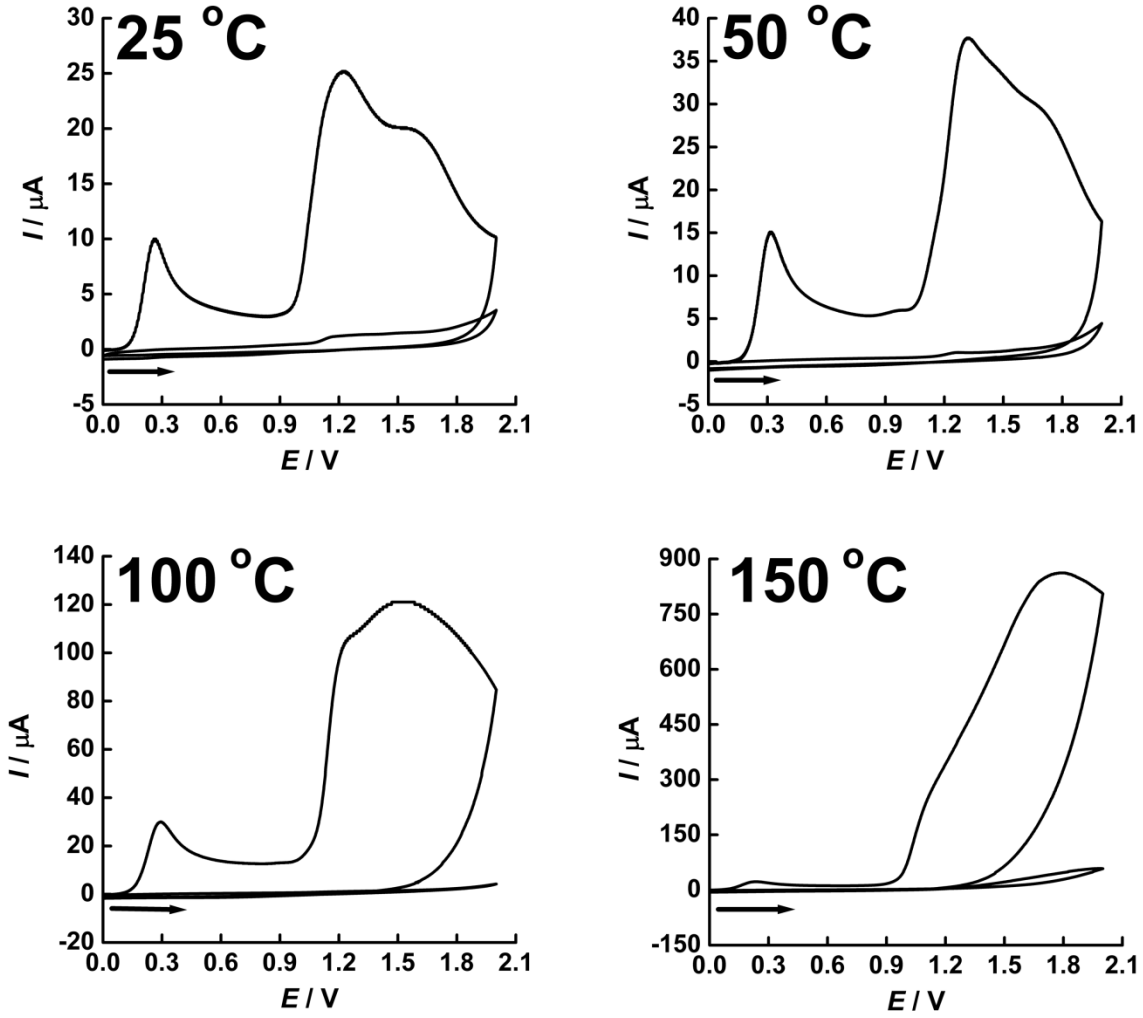

Figure 5.14 – Cyclic voltammograms showing the in-situ polymerisation of bisphenol A (0.5 M) and its ability to inhibit the ferrocene reaction (10 mM) in butyltrimethylammonium bis(trifluoro methylsulfonyl)imide (2 ml) at 25 ºC, 50 ºC, 100 ºC, 150 ºC. The working electrode was a glassy carbon disc electrode press fitted into a glass filled Teflon shroud (d = 3 mm). The potential was held at 0.0 V vs. Ag\|AgCl wire for 30 s before cycling from 0.0 V to +2.0 V to 0.0 V at 20 mV s^{-1} for 5 cycles. The counter electrode was platinum gauze mesh (A = 4.0 cm^2). Shown above are the first and fifth scans.

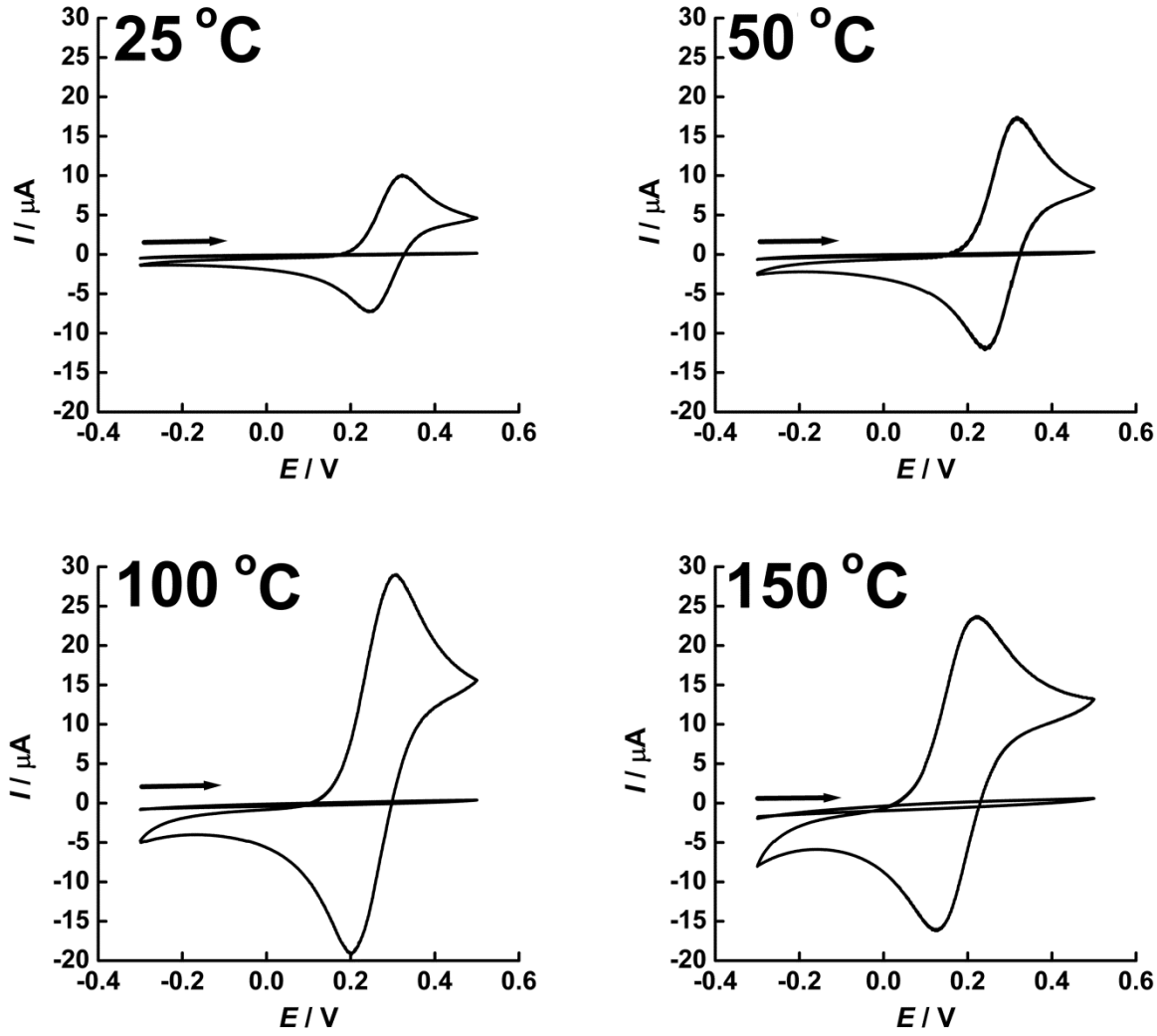

Figure 5.15 – Cyclic voltammograms showing the in-situ inhibition of the ferrocene reaction (10 mM) at 25 ºC, 50 ºC, 100 ºC, 150 ºC before and after the surface polymerisation of bisphenol A (0.5 M) in butyltrimethylammonium bis(trifluoromethylsulfonyl)imide. The potential was held at –0.5 V vs. Ag\|AgCl for 30 s before being cycled from –0.3 V to +0.5 V to –0.3 V at 20 mV s^{-1} for two scans. Shown above are the before and after coating scans. The working electrode was a glassy carbon disc electrode press fitted in to a glass filled Teflon shroud (d = 3.0 mm). The counter electrode was platinum gauze (A = 4.0 cm^2).

The results show that the passivation of glassy carbon electrodes by poly(bisphenol A) is effective up to 150 °C. This was a remarkable result given the thinness (nanometer dimensions) of the films. However, above 150 °C the voltammetry became difficult to reproduce, and the solution changed colour from orange to brown which corresponded with the literature melting point of ferrocene 173-174 °C. This indicated that ferrocene not only melts at ~174 °C but also decomposes. This discovery was a real hindrance to high

temperature testing, and in order for high temperature work to be continued, a redox active compound that is not only soluble in ionic liquids, but also stable beyond 250 °C needs to be identified. A suitable compound would also need to oxidize at a less negative potential than the phenol based monomers (+2.0 V).

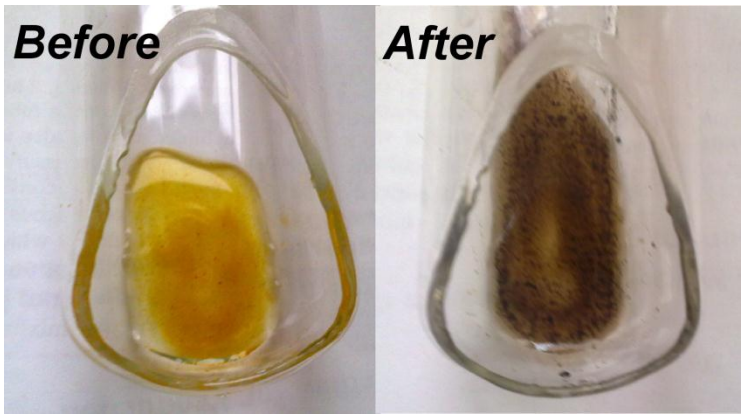

Figure 5.16 – The decomposition of ferrocene in butyltrimethylammonium bis(trifluoro-methylsulfonyl)imide after thermal treatment at 200 °C (30 min).

5.8 – The unusual behaviour of ferrocene in ionic liquid

Whilst recording the cyclic voltammetry of ferrocene in ionic liquid, an unusual effect was observed: the peak current for the oxidation of ferrocene did not decrease with cycle number. Instead, the peak current I_p remained consistently high, with very little difference between cycles (***Figure 5.17*** and ***Figure 5.18***). This unexpected steady state behaviour suggested that some of the reaction product (ferrocinium ion) was trapped at the electrode surface, and therefore inhibiting the diffusion of the reaction product away from the electrode surface. To confirm this hypothesis, the glassy carbon working electrode was replaced by a RAM electrode (an assembly of micro-electrodes, that normally does not show back reactions due to ferrocinium ions) and the cyclic voltammetry was again recorded. The appearance of a small reverse peak strengthened the conviction that some reaction product was sticking to the electrode. To see if this effect was unique to butyltrimethylammonium bis(trifluoromethyl-sulfonyl)imide, the reaction was also carried out in a different ionic liquid (1-ethyl-3-methylimidazolium triflate) and the same phenomenon was observed.

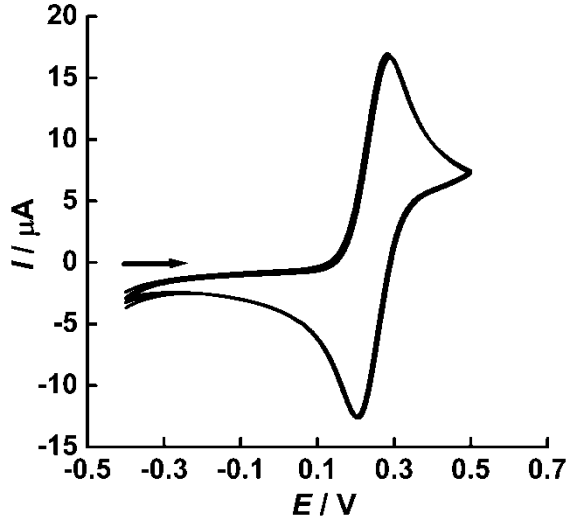

Figure 5.17 – The voltammetric behaviour ferrocene (10 mM) in butyltrimethylammonium bis(trifluoromethylsulfonyl)imide (2 ml). Voltammetry recorded on a glassy carbon disc electrode press fitted into a glass filled Teflon shroud (d = 3.0 mm). The potential was held at –0.4 V vs Ag|AgCl wire for 30 s before cycling from –0.4 V to +0.5 V to –0.4 V at 20 mV s^{-1} for 3 cycles. The counter electrode was platinum gauze (A = 4.0 cm^2). Shown above are the first 3 cycles.

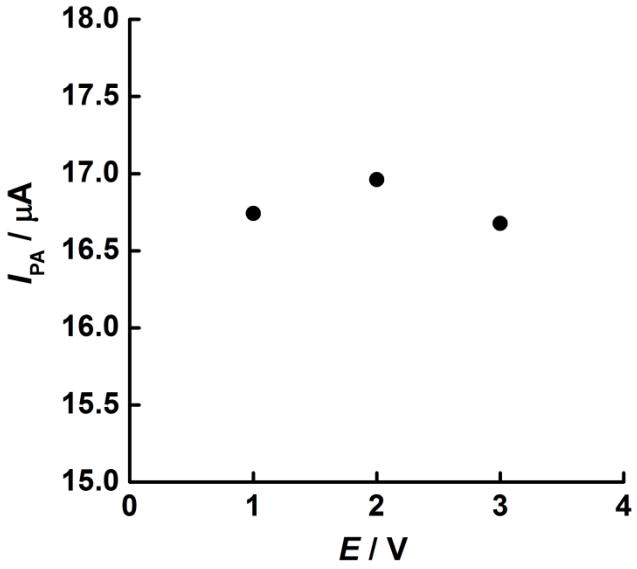

Figure 5.18 – A scatter diagram showing the non-decrease of peak current (I_P) as a function of cycle number for ferrocene (10 mM) in butyltrimethylammonium bis(trifluoromethyl sulfonyl)imide (2 ml). Data were recorded on a glassy carbon disc electrode press fitted into a glass filled Teflon shroud (d = 3.0 mm). The potential was held at –0.4 V vs. Ag|AgCl wire for 30 s before cycling from –0.4 V to +0.5 V to –0.4 V at 20 mV s^{-1} for 3 cycles. The counter electrode was platinum gauze (A = 4.0 cm^2). Shown is the peak current for the first 3 cycles.

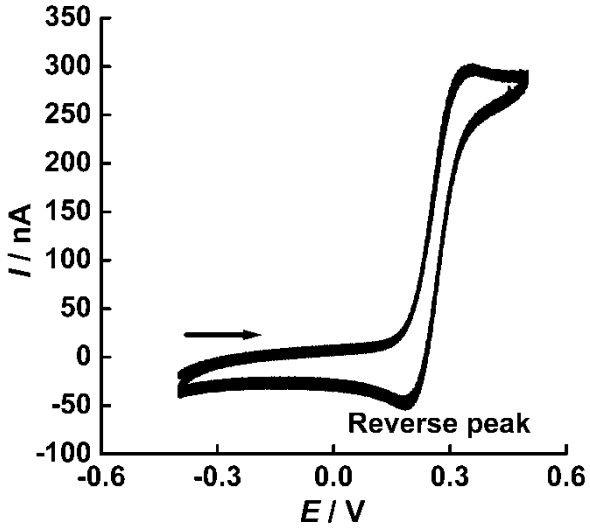

Figure 5.19 – The voltammetric behaviour of ferrocene (10 mM) in butyltrimethylammonium bis(trifluoromethylsulfonyl)imide (2 ml). Voltammetry recorded on a RAM electrode. The potential was held at –0.4 V vs. Ag\|AgCl wire for 30 s before cycling from –0.4 V to +0.5 V to –0.4 V at 20 mV s^{-1} for 3 cycles. The counter electrode was platinum gauze (A = 4.0 cm^2). Shown above are the first 3 cycles. The presence of a reverse peak (indicated) suggests that some of the ferrocinium ion is trapped at the electrode surface.

5.9 – The reaction of ferrocene with bisphenol AF in ionic liquid

Whilst screening the four bisphenol compounds for their ability to passivate carbon electrodes in ionic liquids, it was noted that the peak current of the test compound ferrocene decreased over time following the addition of 4,4´-(1,1,1,3,3,3,-Hexafluoro-2,2-propanediyl)diphenol (bisphenol AF). In order to confirm this observation, an experiment was set up to monitor the reaction over time using a RAM electrode.

10 mM ferrocene was added to 2 ml butyltrimethylammonium bis(trifluoromethylsulfonyl)-imide (2 ml) and the voltammetry was recorded over the range –0.4 V to +0.5 to –0.4 V. The passivating compound, bisphenol AF, was then added to the cell and 14 cycles were recorded over the same range. The electrode was then polished and more cycles were recorded over a 24 h period to enable the reaction progress to be monitored. For all experiments, the working electrode was a RAM, the reference electrode was an Ag\|AgCl wire, and the counter electrode was a platinum gauze electrode. All scans were recorded at 25 °C following 30 seconds conditioning at –0.4 V *vs*. the reference electrode. All scans were recorded at 20 mV s^{-1}.

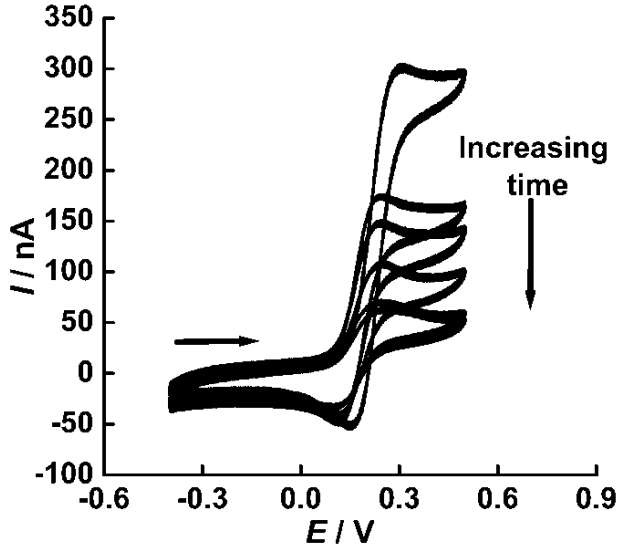

Figure 5.20 – Voltammograms showing the decrease of ferrocene concentration (10 mM) in butyltrimethylammonium bis(trifluoromethylsulfonyl)imide following the addition bisphenol AF (0.5 M) over 24 h. Voltammetry was recorded on RAM™ electrode. The potential was held at –0.4 V vs. Ag|AgCl wire for 30 s before recording a cycle from –0.4 V to +0.5 V to –0.4 V at 20 mV s^{-1}. Time intervals were 0, 24, 144, 264, 324 and 1344 minutes. The counter electrode was platinum gauze (A = 4.0 cm^2).

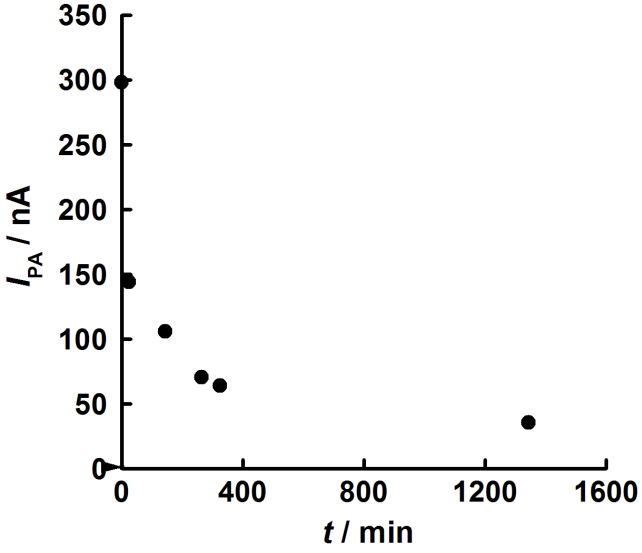

Figure 5.21 – A scatter plot of peak anodic current (nA) vs. time (min) for the oxidation of ferrocene (initially 10 mM) in butyltrimethylammonium bis(trifluoromethylsulfonyl)imide (2 ml) following the addition 4,4'-(hexafluoroisopropylidene)diphenol (0.5 M). Voltammetry recorded on a RAM electrode. The potential was held at –0.4 V vs. Ag|AgCl wire for 30 s before recording a cycle from –0.4 V to +0.5 V to –0.4 V at 20 mV s^{-1} at time intervals of 0, 24, 144, 264, 324 and 1344 minutes. The counter electrode was platinum gauze (A = 4.0 cm^2).

The decrease in ferrocene concentration over time suggests that the bisphenol AF is reacting with ferrocene by an unknown mechanism. If this compound was to be considered as a passivating monomer for an electrode blocking film, a less reactive test compound would need to be sourced.

5.10 – Conclusion

It has been demonstrated that the polymerisation of four soluble phenols into insoluble poly(phenols) *in-situ* can inhibit unwanted faradaic reactions in ionic liquids when deposited onto the electrode surface using an electrochemical, potential cycling technique. In particular, it was shown that poly(phenols) prevented electron tunnelling from the carbon electrode to redox active species in solution, whilst maintaining capacitance. This was a very useful result, because it provides a potential new method to prevent unwanted side reactions in working supercapacitors up to 150 ºC. This technology has potential in other technological areas such as in corrosion prevention.

5.11 – References

[1] Conway, B. *Electrochemical Supercapacitors. Scientific Fundamentals and Technological Applications*. Kluwer Academic/Plenum Publishers (New York), Chapter 2, pp 11-22 (1999).

[2] Y. Miao., Chen, J., Wu, X. *Using electropolymerized non-conducting polymers to develop enzyme amperometric biosensors*. Tends in Biotechnology, 22(5): p227-231 (2004).

[3] Fleischmann, M., Hill, I. R., Mengoli, G., & Musiani, M. *A Raman spectroscopic investigation of the electropolymerization of phenol on silver electrodes*. Electrochimica Acta, 28(11): 1545-1553 (1983).

[4] Xavier, J. L. N. Ortega., Ferreira1, J. Z., Bernardes A. M. & Pérez–Herranz, V. *An electrochemical Study of Phenol Oxidation in Acidic Medium*. International Journal of Electrochemical Science, 6: 622-636 (2011).

[5] Panizza, M. & Cerisola, G. *Influence of anode material on the electrochemical oxidation of 2-napthol*. Part 1. Cyclic voltammetry and potential step experiments. Electrochemica Acta, 48: 3491-3497 (2003).

[6] Zanta, C. L. P. S. & Andrade, J. F. C. *Electrochemical behaviour of olefins: oxidation at ritheniu-titanium dioxide and iridium-titanium dioxide coated electrodes*. Journal of Applied Electrochemistry, 30: 467-474 (2000).

[7] Tahar, B. N., Abdelhédi, R. & Savall, A. *Electrochemical polymerisation of phenol in aqueous solution on a Ta/PbO_2 anode.* Journal of applied Electrochemistry, 30(5): 663-669 (2009).

[8] Odian, G. G. *Principles of Polymerisation.* Wiley (New Jersey), Fourth Edition, Chapter 2, pp 40-185 (2004).

[9] Kobayashi, S., Higashimura, H. *Oxidative polymerization of phenols revisited*. Progress in Polymer Science, 28: 1015-1048 (2003).

[10] Corduneanu, O., Janeiro, P. & Brett, A. M. O. *On the Electrochemical Oxidation of Resveratrol*. Electroanalysis, 18, 757-762 (2006).

[11] Langcake, P. & Pyrce, R. J. *Distribution of resveratrol oligomers in plants.* Phytochemistry, 16: 1193-1196 (1977).

[12] Wang, Y., Cantana, F., Yang, Y. Roderick, R. & Van Breemen, R. B. *An LC–MS method for analysing total resveratrol in grape juice, cranberry juice, and in wine*. Journal of Agricultural Food Chemistry, 50: 431-435 (2002).

[13] Counet, C., Callemien, D. & Colin, S. *Chocolate and cocoa: new sources of trans–resveratrol and trans–piceid*. Food Chemistry, 98: 649-657 (2006).

[14] Savouret, J. F. & Quesne, M. *Resveratrol and cancer: a review*. Biomedicine and Pharmacotherapy, 56: 84-87 (2002).

[15] Kuramitz, H, Nakata, Y. Kawasaki, M. & Tanaka, S. *Electrochemical oxidation of bisphenol A. Application to the removal of bisphenol A using carbon fiber electrode*. Chemposphere, 45: 37-43 (2001).

[16] *BPA: friend or foe*, Chemistry World, 46-49 (December 2012).

[17] Doerge, D. R., Vanlandingham., Twaddle, N. C. & Delcos, K. *Lactational transfer of bisphenol A in Sprague–Dawley rats*. Toxicology Letters, 199: 372-376 (2010).

[18] Kuiper, G. G., Lemmen, J. G., Carlsson, B., Corton, J. C., Safe, S. H., van der Saag, P. T., van der Burg, B. & Gustafsson, J.A. *Interaction of estrogenic chemicals and phytoestrogens with estrogen receptor beta*. Endocrinology, 139: 4252-4263 (1998).

[19] *An end to endocrine disrupters*, Chemistry World, 51-56 (April 2006).

Chapter 6 – Temperature Dependence of Conductivity in Ionic Liquids

6.1 – Introduction

An important characteristic of ionic liquids is their electrical conductivity. Experimentally, the electrical conductivity is found to be a strong function of temperature, increasing rapidly as the temperature is raised. However, the theory of conductivity of ionic liquids is non-standard because the measured conductivity does not obey the Arrhenius equation. In the present chapter, some very high precision measurements are reported for the conductivity of two hydrophobic ionic liquids over the temperature range 20 ºC to 195 ºC. It is shown that the experimental data can be fitted by the Vogel-Tammann-Fulcher equation to "six nines" accuracy.

Up till now, the Vogel-Tammann-Fulcher[1-3] equation has been regarded as a purely empirical equation. Here, the Vogel-Tammann-Fulcher equation is derived from first principles, and it shows that the temperature at which the conductivity collapses to zero (T_0) coincides with the glass transition temperature (T_g) of the ionic liquid. This derivation (the work of Professor Stephen Fletcher) is based on the assumption that mobile conducting species are trapped in the glassy state until the glass transition temperature is exceeded. Although some previous authors have conjectured that T_0 might coincide with T_g, the fact that the Vogel-Tammann-Fulcher equation has three adjustable parameters has prevented a decisive analysis. Frustratingly, the flexibility of the Vogel-Tammann-Fulcher equation in fitting conventional experimental data has meant that the error bars in estimating T_0 have been far too large. To overcome this problem, the conductivity of several ionic liquids have been measured to very high precision using an AC impedance technique (the Wayne-Kerr Precision Component Analyser method). Simultaneously the temperature has been measured using a platinum resistance thermometer. In each experiment, more than 40,000 data points were acquired over forty-eight hours of measurement. The net result is the estimation of T_0 to an unprecedented level of accuracy (±5 K).

6.2 – Derivation of the Vogel-Tammann-Fulcher equation

6.2.1 – The Boltzmann equation

In statistical thermodynamics, the Boltzmann equation[4] relates the thermodynamic entropy S_{total} of a system and its environment to a statistical quantity w, which represents the total number of microstates that can be accessed by the system within one macrostate.

$$S_{\text{total}} = k_{\text{B}} \ln(w) \qquad \textbf{\textit{Equation 6.1}}$$

Here k_{B} is the Boltzmann constant (1.38062 x 10^{-23} J K^{-1}). The "microstates" include all possible modes of energy storage and all possible arrangements of all particles in space.

The use of the symbol *w* derives from the German *wahrscheinlichkeit* meaning "probability", although the term is better rendered into English as the "multiplicity of microstates". Alternatively, the quantity *w* (which is typically an extremely large number) may be regarded as the *statistical weight* of a given "macrostate".

Now consider two different macrostates which are labelled 1 and 2. From the Boltzmann equation it follows that

$$S_{\text{total}(1)} = k_{\text{B}} \ln(w_1) \qquad \textbf{\textit{Equation 6.2}}$$

and

$$S_{\text{total}(2)} = k_{\text{B}} \ln(w_2) \qquad \textbf{\textit{Equation 6.3}}$$

If macrostate 1 converts spontaneously into macrostate 2, where $S_{\text{total}(2)} > S_{\text{total}(1)}$, then the increase in total entropy is

$$S_{\text{total}(2)} - S_{\text{total}(1)} = k_{\text{B}} \ln(\frac{w_2}{w_1})$$

Equation 6.4

Or, with an obvious change of notation,

$$\Delta S_{21} = k_{\text{B}} \ln(\frac{w_2}{w_1})$$

Equation 6.5

This equation reveals that the difference in total entropy between two macrostates is proportional to the logarithm of the ratio of their statistic weights. Inverting the equation now yields.

6.2.2 – The inverted Boltzmann equation

$$w_2 = w_1 \exp\left(\frac{\Delta S_{21}}{k_\mathrm{B}}\right)$$

Equation 6.6

This equation is important because it forms the basis of *transition state theory*[5-8], in which the rate of a reaction is assumed to be proportional to the statistical weight of its transition state $w_2^{\ddagger}$.

In real-world experiments, a given macrostate can usually be divided into two parts, (i) a "system" which is closed to matter, and (ii) a "heat bath" which allows the temperature and pressure of the system to be controlled by the experimenter. In such experiments, the inverted Boltzmann equation may be expanded into the form

$$w_2 = w_1 \exp\left(\frac{\Delta S_{\mathrm{bath}}}{k_\mathrm{B}} + \frac{\Delta S_{\mathrm{sys}}}{k_\mathrm{B}}\right)$$

Equation 6.7

It is emphasised that, in determining the statistical weight of a macrostate, the entropy of the heat bath is just as important as the entropy of the system itself.

6.2.3 – The heat bath

For a heat bath maintained at constant temperature T_{bath} and pressure P_{bath} the standard thermodynamic equation is

$$\Delta U_{\mathrm{bath}} = T_{\mathrm{bath}}\Delta S_{\mathrm{bath}} - P_{\mathrm{bath}}\Delta V_{\mathrm{bath}} \qquad \textbf{\textit{Equation 6.8}}$$

However, since the system and the heat bath together form an isolated system, it follows that

$$\Delta U_{\text{bath}} = -\Delta U_{\text{sys}} \qquad \textit{Equation 6.9}$$

and

$$\Delta V_{\text{bath}} = -\Delta V_{\text{sys}} \qquad \textit{Equation 6.10}$$

Combining these results, the internal energy change of a system inside a heat bath may be written in the revised form:

$$\Delta U_{\text{sys}} = -T_{\text{bath}}\Delta S_{\text{bath}} - P_{\text{bath}}\Delta V_{\text{sys}} \qquad \textit{Equation 6.11}$$

Likewise, the entropy change inside the heat bath may be written in the form:

$$\Delta S_{\text{bath}} = \frac{-\Delta U_{\text{sys}} - P_{\text{bath}}\Delta V_{\text{sys}}}{T_{\text{bath}}}$$

Equation 6.12

6.2.4 – Returning to the inverted Boltzmann equation

The above expression for ΔS_{bath} can now be inserted back into the inverted Boltzmann equation to yield

$$w_2 = w_1 \exp\left(\frac{-\Delta U_{\text{sys}} - P_{\text{bath}}\Delta V_{\text{sys}}}{k_{\text{B}}T_{\text{bath}}} + \frac{\Delta S_{\text{sys}}}{k_{\text{B}}}\right)$$

Equation 6.13

or

$$w_2 = w_1 \exp\left(\frac{-\Delta U_{\text{sys}} - P_{\text{bath}}\Delta V_{\text{sys}} + T_{\text{bath}}\Delta S_{\text{sys}}}{k_{\text{B}}T_{\text{bath}}}\right)$$

Equation 6.14

This equation looks rather clumsy, but actually at constant temperature and pressure of the heat bath, it takes the elegant form

$$w_2 = w_1 \exp\left(\frac{-\Delta G_{\text{sys}}}{k_{\text{B}} T_{\text{bath}}}\right)$$

Equation 6.15

where $T = T_{\text{bath}}$ and $P = P_{\text{bath}}$. (The proof is given below.)

It follows from this analysis that the smaller the Gibbs energy of a given macrostate, the greater the statistical weight that it has, and therefore the more likely it is to occur. This insight explains why closed systems spontaneously decrease their Gibbs energy at constant temperature and pressure. Finally, it is interesting to juxtapose the final result with the original Boltzmann formula:

$$w_2 = w_1 \exp\left(\frac{\Delta S_{21}}{k_{\text{B}}}\right)$$

Equation 6.16

Comparing terms yields

$$\Delta G_{\text{sys}} = -T_{\text{bath}} \Delta S_{21} \qquad \textit{Equation 6.17}$$

Here ΔS_{21} is simply the total entropy change (system + surroundings) involved in passing from one macrostate to another.

6.2.5 – Supporting Proof: The connection between ΔG and ΔU

By definition,

$$G = U - TS + PV \qquad \textit{Equation 6.18}$$

In general, therefore,

$$\Delta G = \Delta U - T\Delta S - S\Delta T + P\Delta V + V\Delta P \qquad \textit{Equation 6.19}$$

If T and P are constants then $\Delta T = 0$ and $\Delta P = 0$. This implies

$$\Delta G = \Delta U - T\Delta S + P\Delta V \qquad (\text{const.}\, T\ \&\ P)$$

Equation 6.20

or $$-\Delta U - P\Delta V + T\Delta S = -\Delta G \qquad (\text{const.}\, T\ \&\ P)$$

Equation 6.21

Thus, $$-\Delta U_{\text{sys}} - P_{\text{bath}}\Delta V_{\text{sys}} + T_{\text{bath}}\Delta S_{\text{sys}} = -\Delta G_{\text{sys}} \qquad (\text{const.}\, T_{\text{bath}}\ \&\ P_{\text{bath}})$$

Equation 6.22

Equation 6.15 follows.

6.2.6 – Transition state theory

It has been shown that, at constant temperature and pressure, the statistical weight of a macrostate in equilibrium with a heat bath is given by the equation

$$w_2 = w_1 \exp\left(\frac{-\Delta G_{\text{sys}}}{k_{\text{B}} T_{\text{bath}}}\right)$$

Equation 6.23

If it is assumed that that the rate of a thermally activated reaction is proportional to the statistical weight of its transition state ("Transition State Theory") then the textbook result is obtained.

$$\kappa_2 = \kappa_1 \exp\left(\frac{-\Delta G^{\ddagger}_{\text{sys}}}{k_{\text{B}} T_{\text{bath}}}\right)$$

Equation 6.24

Here κ_2 is the rate constant for the reaction and $\Delta G^{\ddagger}_{\text{sys}}$ is the Gibbs energy change needed to reach the transition state from the reactant state (the "activation energy"). This theory is valid if the transition state is in thermodynamic equilibrium with the reactants, and the temperature

is the *absolute* temperature. It should also be emphasised that the temperature is not that of the system, but that of the heat bath with which the system is in equilibrium, a fact often omitted from textbooks.

An important question in reaction rate theory is how κ_2 depends on temperature: for "simple" systems it is often assumed without proof that $\Delta G^{\ddagger}_{\mathrm{sys}}$ is constant over a range of temperatures. In the case of glasses, however, this is certainly incorrect. This is because plots of $\log(\text{conductivity})$ *versus* $-1/T$ are curved. To deal with the case of glasses, it is necessary to consider what happens at the glass transition temperature T_g. At temperatures below T_g the conduction of ions occurs with negligible rate. By contrast, at temperatures above T_g, the conduction of ions has a finite rate. This suggests that the activation energy for conduction should be expressed as the *difference* in Gibbs energy between the system at (T, P) and the system at (T_g, P_g), where the Gibbs energy at (T_g, P_g) is acting as a threshold energy. Accordingly, let us call this new activation energy χ. Then

$$\chi = G_{\mathrm{sys}(T,P)} - G_{\mathrm{sys}(T\mathrm{g},P\mathrm{g})} \qquad \textbf{\textit{Equation 6.25}}$$

Now recalling the result

$$\Delta G_{\mathrm{sys}} = -T_{\mathrm{bath}} \Delta S_{\mathrm{total}} \qquad \textbf{\textit{Equation 6.26}}$$

the following is immediately obtained

$$\Delta\chi = -(T - T_{\mathrm{g}})\Delta S_{\mathrm{total}} \qquad (\text{const. } P) \qquad \textbf{\textit{Equation 6.27}}$$

and rearranging yields

$$\Delta S_{\mathrm{total}} = \frac{-\Delta\chi}{(T - T_{\mathrm{g}})} \qquad (\text{const. } P)$$

Equation 6.28

Inserting this back into the inverted Boltzmann expression yields

$$w_2 = w_1 \exp\left(\frac{-\Delta\chi}{k_\mathrm{B}(T - T_\mathrm{g})}\right)$$

Equation 6.29

or, in the case of conductivity,

$$\kappa_2 = \kappa_1 \exp\left(\frac{-\Delta\chi^\ddagger}{k_\mathrm{B}(T - T_\mathrm{g})}\right)$$

Equation 6.29

It can be seen that this equation has the same form as the Vogel-Tammann-Fulcher expression

$$\kappa = A \exp\left(\frac{-B}{k_\mathrm{B}(T - T_0)}\right)$$

Equation 6.30

where κ is the conductivity (S m^{-1}), and A, B, and T_0 are unknown constants. Further, the new derivation suggests that the constant A is κ_1, the constant B is $\Delta\chi^\ddagger$, and the constant T_0 is the glass transition temperature T_g. Experimental confirmation of the latter is presented below. The new derivation also suggests that the "activation energy" $\Delta\chi$ is a measure of the amount by which the Gibbs energy of the system exceeds a particular threshold value. A suitable model of $\Delta\chi$ will also be described.

6.2.7 – A new theory of activation energy in glasses

Over the past half century, various forms of the Vogel-Tammann-Fulcher equation have been applied to the conductivity (and viscosity) of softened glasses, and in 2006 the equation was applied to the conductivity of some ionic liquids by Vila *et al.*[9]. However, despite its widespread adoption, no consensus has been reached regarding a microscopic model of the activation energy. Various models have been proposed, of varying degrees of complexity, but none has achieved universal acceptance. Well-known examples include the free volume

model of Cohen and Turnbull[10], and the configurational entropy model of Adam and Gibbs[11]. In the free volume model, it is assumed that the activation energy arises from the work to form small voids in the softened glass. In the configurational entropy model, it is assumed that the activation energy depends inversely on the number of structural configurations available to the softened glass. In the present work a radically different model for the activation energy is proposed. It is suggested that activation energy arises from the change in Gibbs energy required to detach the mobile species from its glass matrix,

$$\Delta\chi^{\ddagger} \approx \Delta\left(G - G_{\mathrm{g}}\right) \qquad \textbf{\textit{Equation 6.31}}$$

Further progress can now be made on the basis of this model. Our reasoning may be summarized as follows.

(i) The rate-determining step for ionic conduction is the detachment of mobile species from the glass matrix.

(ii) The same rate-determining step is responsible for the onset of viscous flow at $(T_{\mathrm{g}}, P_{\mathrm{g}})$.

(iii) The system exhibits a "late" transition state (the Hammond Postulate[12]) as evidenced by the fact that the glass-to-liquid transition is always *endothermic*.

(iv) The existence of a "late" transition state implies that the change in Gibbs energy is due to the work of detachment of mobile species.

(v) For weakly cohesive glasses, the work of detachment is principally the energy needed to create N new degrees of freedom of the mobile species at $(T_{\mathrm{g}}, P_{\mathrm{g}})$.

(vii) By the equipartition of energy, the energy needed to create one new degree of freedom of the mobile species at $(T_{\mathrm{g}}, P_{\mathrm{g}})$ is simply $k_{\mathrm{B}}T_{\mathrm{g}}/2$.

Combining propositions (i)-(vii), the activation energy for ionic conduction is

$$\Delta\chi^{*} \approx p + N\frac{k_{\mathrm{B}}T_{\mathrm{g}}}{2}$$

Equation 6.32

where p is the energy of cohesion. Further, if the constituent ions of the glass are weakly associated, then $p \ll N(k_{\mathrm{B}}T_{\mathrm{g}}/2)$, and

$$\kappa \approx \kappa_{\infty} \exp\left(\frac{N}{2}\,\frac{T_{\mathrm{g}}}{T_{\mathrm{g}} - T}\right)$$

Equation 6.33

In this weak-cohesion limit, plots of $\ln(\kappa)$ *versus* $T_{\mathrm{g}}/\left(T_{\mathrm{g}} - T\right)$ should yield straight lines having slopes $N/2$ and intercepts $\ln(\kappa_{\infty})$.

Interestingly, ***Equation 6.33*** corresponds precisely to an empirical equation of Angell[13], *viz.*

$$\kappa \approx \kappa_{\infty} \exp\left(\frac{DT_{\mathrm{g}}}{T_{\mathrm{g}} - T}\right)$$

Equation 6.34

where D is an unknown constant, sometimes referred to as the "fragility" of the glass. Based on the present work, the constant D can be identified as $N/2$, where N is the number of new degrees of freedom that are created by the detachment of the mobile species from the glass matrix. This analysis also indicates that the wide applicability of Angell's Equation (***Equation 6.11***) ultimately derives from the wide applicability of the Equipartition Principle.

Elementary geometric considerations suggest a universal minimum value of 6 for the parameter N. This is predicted in the case of a non-associated, non-linear, polyatomic mobile species having three translational degrees of freedom and just three rotational degrees of freedom. Although the quaternary ammonium ions used in the present work actually approach this value, their N values are slightly higher, in the range 6–8, most likely because the charged nature of the ions causes some inter-ionic (cohesive) association. It may be noted, however, that a value of precisely 6 has been reported in the case of o-terphenyl[14], which has been described by Debenedetti and Stillinger as "the canonical fragile glass-former"[15].

In summary, a new model of the glass transition has been developed, and a new equation for the conductivity of ionic liquids has been derived. This latter equation has many similarities with the (purely empirical) Vogel-Tammann-Fulcher equation, and, indeed, can be regarded as a derivation of it.

6.3 – Experimental

The three-parameter Vogel-Tammann-Fulcher equation is commonly used to interpolate plots of conductivity *versus* temperature data. However, for a given data set, it is generally difficult to estimate the parameters (A, B, T_0) with high accuracy, for several reasons: (1) there may not be enough data, (2) the sample space of the data (temperature range) may be too small, (3) there may be systematic or random errors in the data, and (4) there may be inadequate computer time for the curve fitting procedure to converge. In the present work, these difficulties have been successfully overcome, as is now described.

6.3.1 – Apparatus

The experimental apparatus for measuring the conductivity of ionic liquids over a wide temperature range is shown in ***Figure 6.1***. Before the temperature dependence of conductivity in ionic liquids could be explored, it was necessary to determine the cell constant for the cell, and to select the optimum measurement frequency and temperature programme for data collection. These matters are discussed in ***Section 6.3.3***, ***Section 6.3.4 and Appendix 6A***.

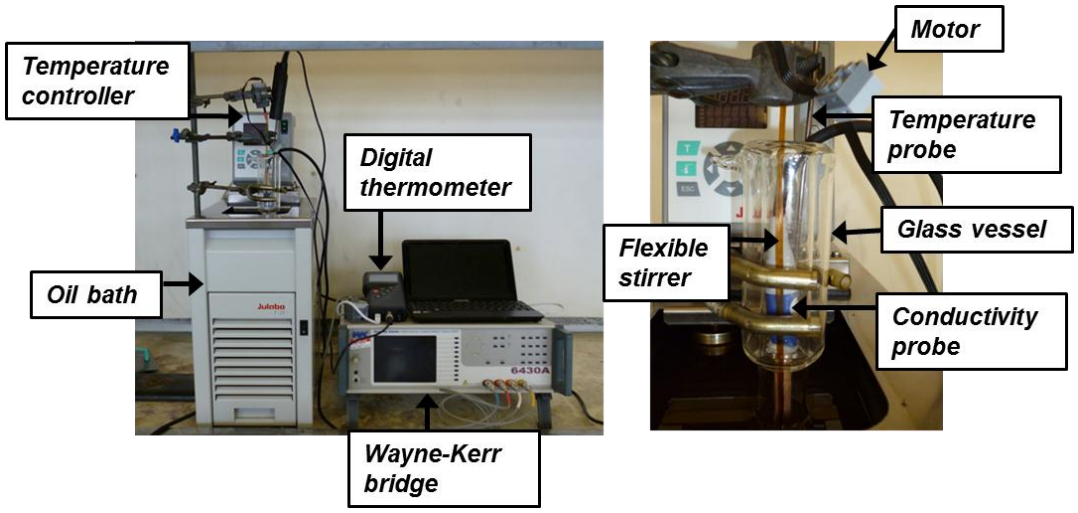

Figure 6.1 – Experimental apparatus for high-precision conductivity measurements in ionic liquids over the temperature range 20 ºC to 195 ºC.

6.3.2 – Experimental details

Conductivity, frequency, and calibration measurements were all carried out in the same thin-walled pyrex cell. This had a jacketed top to prevent thermal losses. Conductivity was measured *via* a 027-013 platinised platinum conductivity probe (Jenway). A Pt-100 platinum resistance probe and a flexible glass fibre stirrer were also inserted directly into the ionic liquid. The pyrex cell was submerged in an F25-ME commercial oil bath (Julabo). Prior to each run, all ionic liquids were held at 130 ºC for 24 h to allow any residual water to evaporate. Following this treatment, a positive pressure of dry nitrogen gas was maintained over the cell to prevent water or oxygen from entering the ionic liquid. The temperature of the oil bath was externally programmed *via* an RS232 interface and EasyTemp software (Julabo). Typically, the temperature was cycled at 0.1 ºC min^{-1} from 20 °C to 200 °C, resulting in approximately 50,000 data points per run. All scans were repeated multiple times to ensure the absence of hysteresis in the measurements. The temperature was logged with a precision of $\pm$0.01 ºC, exceeding the notional accuracy of $\pm$0.03 ºC. Capacitance (C / F), impedance (Z / Ω) and phase angle (θ / degrees) measurements were made every two seconds using a Wayne-Kerr Precision Component Analyser (6430A), and the data were transferred to a computer *via* a GPIB interface using software written in-house by Dr Iain Kirkpatrick (Loughborough University). Resistance values (R / Ω) were computed from the formula $Z_R(1 + \tan^2\theta)$. Conductivity data were recorded at 10 kHz.

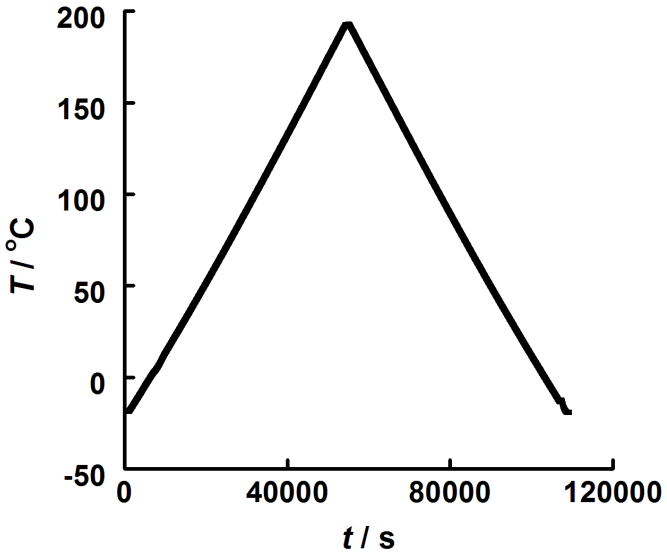

Figure 6.2 – A typical heating profile used for data collection. In this example, the temperature was increased from –15 ºC to 195 ºC at a speed of 0.25 ºC min^{-1}.

6.3.3 – Determination of cell constant (*K*)

The cell constant for the conductivity probe was determined using 0.01 M KCl (aq) with a known conductivity at 25 °C of 1413 μS cm^{-1}[16]. To derive the cell constant, the temperature was maintained at 25 °C, and conductance values were logged every 10 s over a period of 1 h. An average conductance value was then computed. The cell constant (K / cm^{-1}) was calculated as

$$K = \frac{1413\ (\mu S\ cm^{-1})}{\text{Average measured conductance } (\mu S)}$$

Equation 6.35

The cell constant was re-established before each experiment started, and again after each experiment was completed.

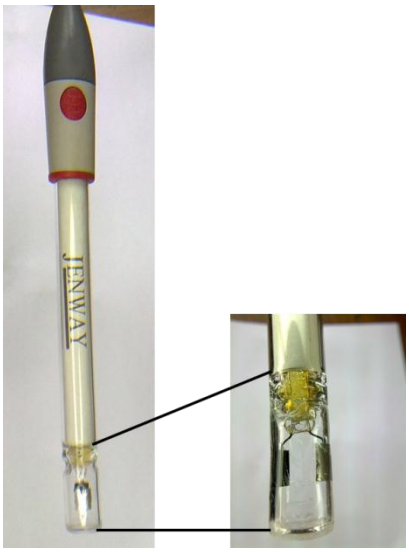

Figure 6.3 – A Jenway 027-013 conductivity cell.

6.3.4 – Choosing the measurement frequency

Commercial conductivity probes operate at a single arbitrary frequency, typically in the range 1–3 kHz. However, the optimum frequency for the measurement of conductance is actually the one at which the complex impedance behaves as a pure resistor, and this varies from cell-

to-cell and from solution-to-solution. At this special frequency, the phase angle should of course be zero.

In order to locate the optimum frequency for the cell design, the impedance (Z_{real}), capacitance, and phase angle of all the ionic liquids were measured over the frequency range 20 Hz to 500 kHz. After the data were collected, the frequency at which the phase angle was a minimum was identified. As an example, ***Figure 6.4*** shows the frequency dependence of the phase angle for butyltrimethylammonium bis(trifluoromethylsulfonyl)imide measured using platinised platinum electrodes. It can be seen that the phase angle is <2° near 10 kHz. Indeed, the optimum frequency was found to be close to 10 kHz for all the ionic liquids that were studied, with phase angles consistently <3°, and so 10 kHz was chosen as the standard. Most importantly, stable resistance and capacitance values were also observed around 10 kHz, as illustrated by ***Figure 6.5*** and ***Figure 6.6***, providing further justification for this choice. At frequencies above 20 kHz, sharp increases in phase angle occurred in all ionic liquids, which is attributed to stray capacitance. Data for other ionic liquids are presented in ***Appendix 6B***.

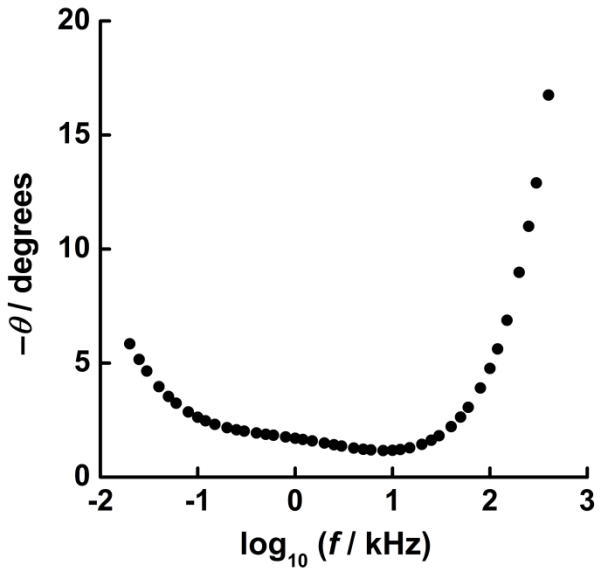

Figure 6.4 – A plot of phase angle (θ / degrees) versus log_{10} frequency, (f / kHz) for butyltrimethyl-ammonium bis(trifluoromethylsulfonyl)imide at 25°C, measured using a Jenway 027-013 platinised platinum conductivity probe. Data shown over a 20 Hz to 500 kHz frequency range and recorded using a Wayne-Kerr Precision Component Analyser (6430A). The minimum phase angle occurs near 10 kHz.

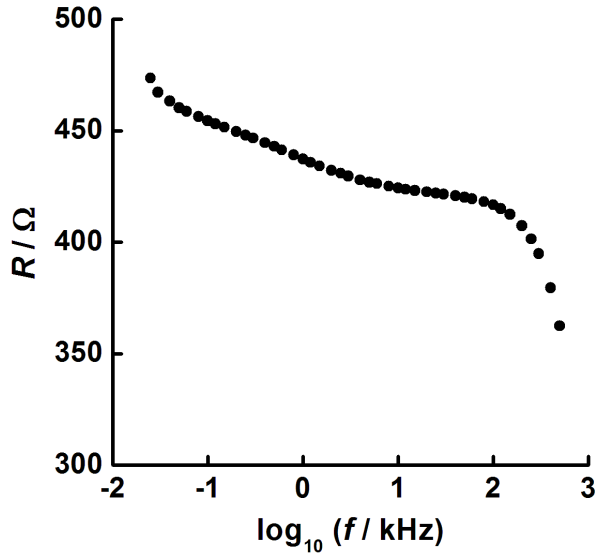

Figure 6.5 – A plot of resistance (R / Ω) versus log_{10} frequency,(f/kHz) for butyltrimethyl-ammonium bis(trifluoromethylsulfonyl)imide at 25ºC measured using a Jenway 027-013 platinised platinum conductivity probe. Data shown over a 20 Hz to 500 kHz frequency range and recorded using a Wayne-Kerr Precision Component Analyser (6430A). The resistance is stable with frequency at 10 kHz. $R = Z_{real}(1 + tan^2\theta)$.

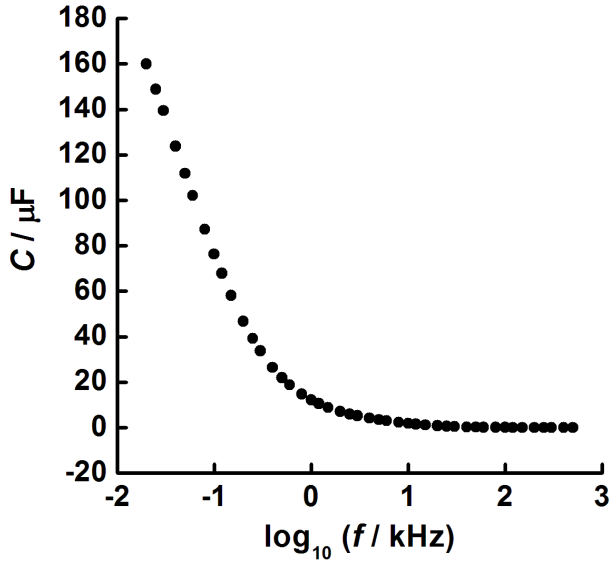

Figure 6.6 – A plot of log_{10} frequency (f / kHz) versus capacitance (C / mF) for butyltrimethyl-ammonium bis(trifluoromethylsulfonyl)imide at 25ºC measured using a Jenway 027-013 platinised platinum conductivity probe. Data shown over a 20 Hz to 500 kHz frequency range and recorded using a Wayne-Kerr Precision Component Analyser (6430A). The capacitance is stable with frequency at 10 kHz.

Confirmatory evidence that 10 kHz was the correct choice for conductivity measurements was provided by impedance plots in the complex plane, as shown in ***Figure 6.7***. A deep local minimum is observed at 10 kHz indicating pure resistive behaviour at that point. The presence of a hemisphere in the complex plane at higher frequencies, which terminates at the origin, is a proof that stray capacitance exists between the platinum electrodes. This capacitance provides a parallel current pathway between the electrodes at frequencies >10 kHz.

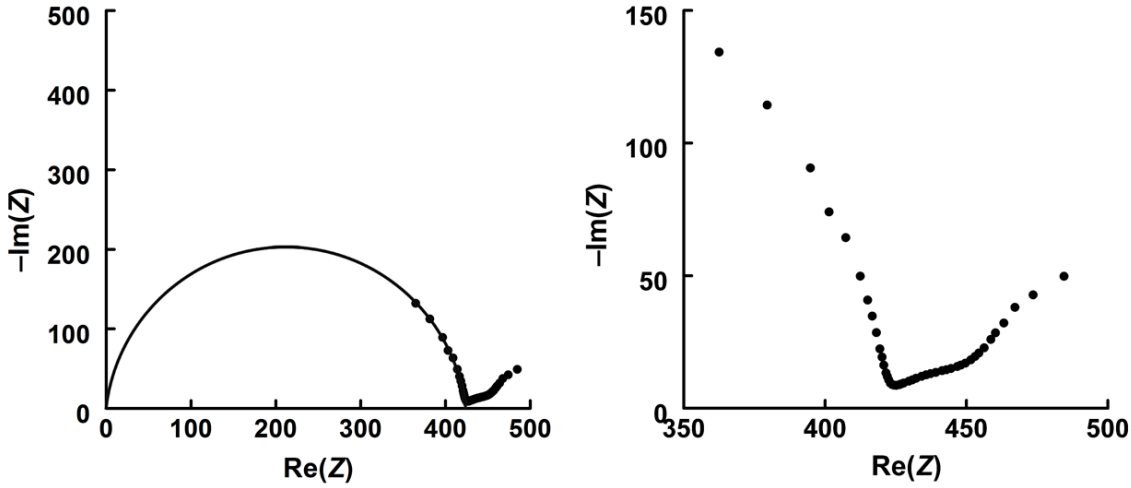

Figure 6.7 – An impedance plot in the complex plane for a Jenway 027-013 platinised platinum conductivity probe in butyltrimethylammonium bis(trifluoromentylsulfonyl)imide at 25 ºC. The local minimum is observed at 424 Ω (10 kHz). Data shown over a 20 Hz to 500 kHz frequency range and recorded using a Wayne-Kerr Precision Component Analyser (6430A). Image on the right is an expansion of the image on the left over the frequency range 350 to 500 kHz.

6.3.5 – Measurements at high temperatures

Because conductivity measurements needed to be performed up to 195 °C, it was necessary to confirm that the optimum frequency of 10 kHz remained unchanged throughout the whole temperature range. The temperature and frequency dependences of the phase angle are shown in ***Figure 6.8***. It can be seen that the phase angle remained below 5° at 10 kHz, at all temperatures.

Figure 6.9 shows plots of conductivity *vs.* temperature for the heating and cooling cycles of the "quantum inert" ionic liquids butyltrimethylammonium bis(trifluoromethylsulfonyl)imide

and hexyltriethylammonium bis(trifluoromethylsulfonyl)imide over the temperature range 20 ºC to 190 ºC (293.15 K to 463.15 K). Evidently, at the temperature scan rate used (0.1 ºC min^{-1}), any thermal hysteresis was negligible, indicating a high degree of thermal stability of both the apparatus and the ionic liquids. By this method it was possible to carry out very high precision electrical conductivity measurements over the range +20 ºC to +190 ºC.

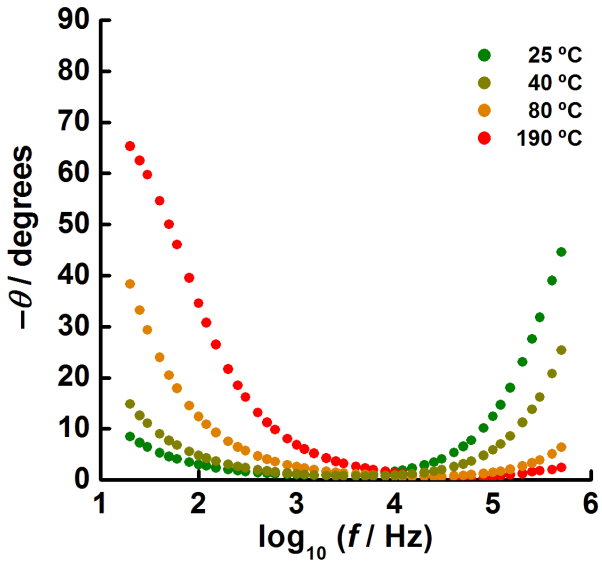

Figure 6.8 – An impedance plot in the complex plane for a a Jenway 027-013 platinised platinum conductivity probe in butyltrimethylammonium bis(trifluoromentylsulfonyl)imide at 25ºC, 40ºC, 80ºC, and 190ºC. The local minimum is observed at 422 Ω (10 kHz). Data shown over a 20 Hz to 500 kHz frequency range and recorded using a Wayne-Kerr Precision Component Analyser (6430A).

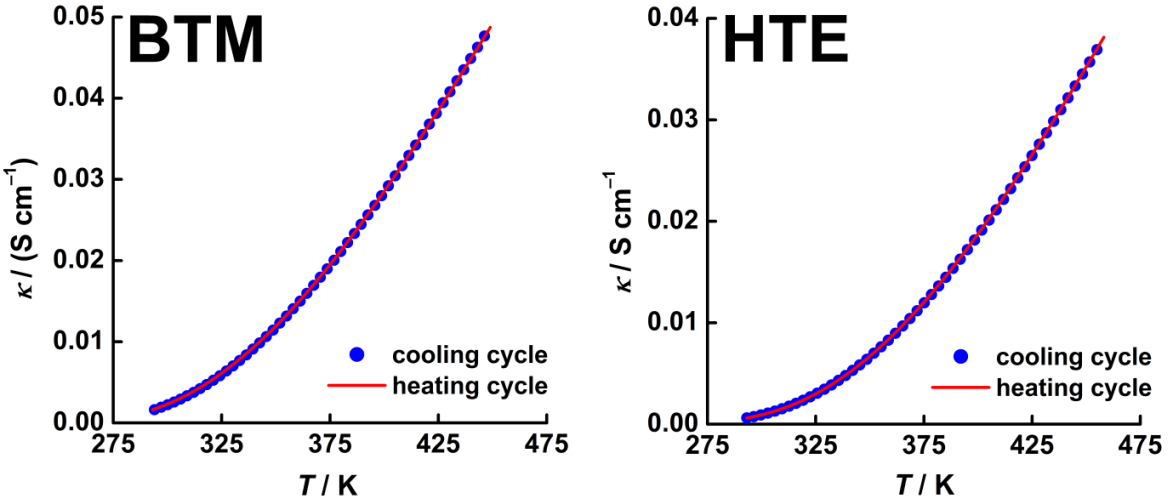

Figure 6.9 – Plots of conductivity (κ/S cm^{-1}) versus temperature (T/K) for (left) butyltrimethylammonium bis(trifluoromethylsulfonyl)imide (BTM) and (right) hexyltriethylammonium bis(trifluoromethylsulfonyl)imide (HTE) over the temperature range 20 ºC to 190 ºC (293.15 K to 463.15 K) at 0.1 ºC min^{-1}. Both the heating and cooling cycles are shown. There is no thermal hysteresis. Approximately 40,000 data points obtained for both cycles. However, for clarity, only 50 data points are displayed for the cooling cycle.

6.3.6 – Data analysis

The scientific literature on the temperature dependence of conductivity in aqueous solutions typically assumes a thermally activated process obeying the Arrhenius Law[7-19].

$$\kappa = \kappa_{\infty} \exp\left(\frac{-E_a}{RT}\right)$$

Equation 6.36

Here κ is the conductivity (S m^{-1}), κ_{∞} is the conductivity at infinite temperature (S m^{-1}), E_a is the activation energy for electrical conduction (J mol^{-1}), R is the universal gas constant (8.315 J K^{-1} mol^{-1}), and T is the absolute temperature (K). However, for all the tetraalkylammonium ionic liquids that were tested, a plot of ln(κ) vs 1/T does not yield a straight line (see the example in ***Figure 6.10***). This curvature strongly implies that the relationship between conductivity and temperature in ionic liquids is non-Arrhenius in origin.

Finding an explanation for the non-Arrhenius behaviour of chemical systems has long been problematic. One popular idea is that the phenomenon is caused by the existence of *distributions* of activation energies inside the system under study, implying the existence of a vast number of different reaction pathways. However, physical evidence for this is completely lacking, and no such phenomena are observed in ordinary liquids.

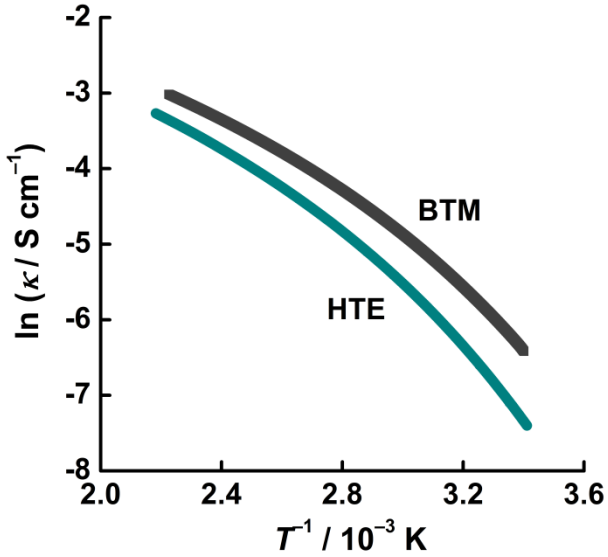

Figure 6.10 – An plot of ln conductivity (κ/S cm^{-1}) versus 1/(temperature, 10^{-3}K) for hexyltriethylammonium bis(trifluoromethylsulfonyl)imide (HTE) and butyltrimethylammonium bis(trifluoromethylsulfonyl)imide (BTM) over the temperature range 20 ºC to 190 ºC (293.15 K to 463.15 K). The plot reveals striking non-Arrhenius behaviour. (~40,000 data points).

A much better equation for the curve-fitting of conductivity *versus* temperature plots is the Vogel-Tammann-Fulcher equation (VTF). The VTF equation has the generic form

$$\kappa = A \exp\left(\frac{-B}{k_{\mathrm{B}}(T - T_0)}\right)$$

Equation 6.37

where κ is the conductivity (S m^{-1}), and A, B, and T_0 are adjustable parameters. However, this equation presumes the existence of a critical temperature T_0 below which the

conductivity collapses to zero, and the physical origin of such a temperature has not so far been explained. In order to investigate the physical origin of T_0 very precise data are needed. This is necessitated by the fact that T_0 is obtained by a lengthy extrapolation from data obtained at high temperature. (What happens at low temperature is that the viscosities of the ionic liquids rise so much that stirring becomes impossible, and therefore inordinately long waiting times are needed for uniform temperatures to be achieved.) In the laboratory, high precision data were obtained by using an experimental apparatus that minimized systematic and random errors, and which allowed large data sets to be collected at high temperatures. In addition, a novel curve-fitting procedure was developed that not only converged on the global minimum of residuals, but also produced reliable estimates of the errors in derived parameter values.

Because the curve-fitting of the VTF equation to experimental data is a three-parameter fit, it is computationally intensive. A further problem is that conventional curve-fitting programs (such as the downhill simplex algorithm) do not readily furnish estimates of errors in the final fitted parameters. To overcome both of these problems, it was convenient to hold one variable (T_0) constant at a "trial value", and then carry out a global optimization of the other two variables using the Pearson product-moment correlation coefficient R. A particular advantage of this approach is that the Pearson product-moment correlation coefficient is invariant to changes in location and scale of the two variables, and hence responds only to the shape of the fitted curve rather than its scaling. Furthermore, the fitting process can be carried out for different trial values of T_0 until graphs of the form shown in ***Figure 6.11*** are obtained.

In ***Figure 6.11***, the vertical axis measures the precision of the best possible fit of the VTF function at each trial value of T_0 as measured by the formula $|\log_{10}(1-R^2)|$, where R is the correlation coefficient. This latter formula simply counts the "number-of-nines" appearing in the correlation coefficient R. The very pleasing result is a leptokurtic curve with a sharp maximum, centred on the global best estimate of T_0. At the same time, the width of the peak near the maximum provides an estimate of the error in the T_0 value.

Once the values of A, B, and T_0 have been determined, the corresponding VTF function can be computed and superimposed back onto the experimental data to provide a visual check of the goodness-of-fit.

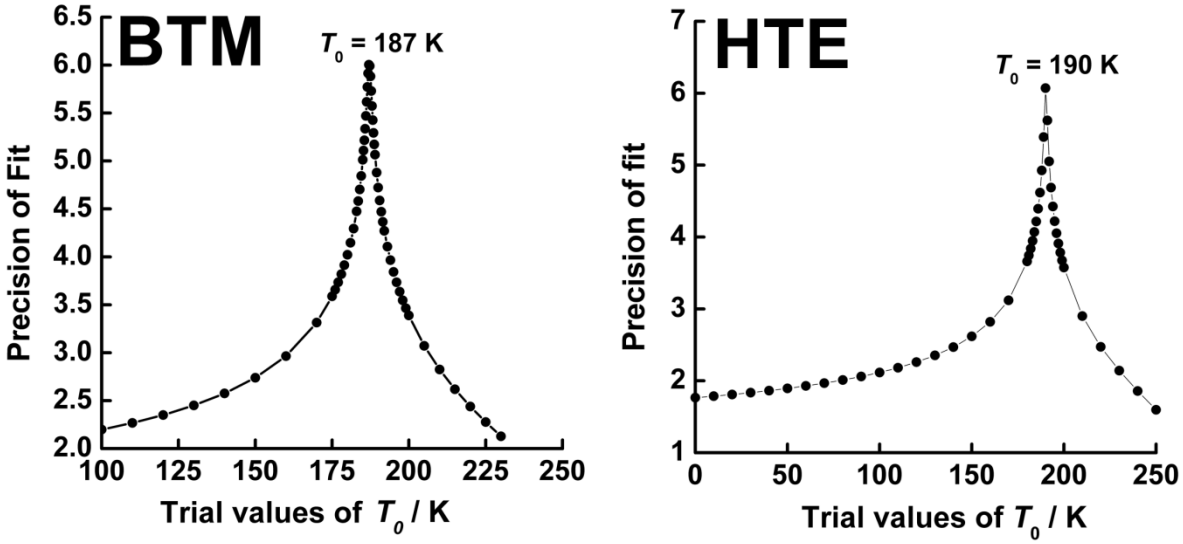

Figure 6.11 – A plot of precision-of-fit versus trial values of T_0 (100 K to 250 K) for the heating cycles of butyltrimethylammonium bis(trifluorormethylsulfonyl)imide (BTM) and hexyltriethyl-ammonium bis(trifluorormethylsulfonyl)imide (HTE) over the temperature range 20 ºC to 190 ºC (293.15 K to 463.15 K). The T_0 value that produces the most precise fit is labelled.

6.4 – Results

The global optimum fits of the VTF function to the conductivity data measured for the ionic liquids BTM and HTE are shown in ***Figure 6.12*** over the temperature range 20 ºC to 190 ºC.

An example of the residuals are shown in ***Figure 6.13***. It is possible to observe both random and systematic errors in the experimental data. The random errors appear as high frequency noise, while the systematic errors appear as low frequency "wiggles". Given the high precision of the conductivity measurements, it is suspected that the systematic errors arise from errors in the manufacturer's calibration of the temperature output of the temperature probe, which is known to be based on the fitting of an 11*th* order polynomial to the measured voltage. Regardless of this assumption, the data confirm that the VTF relation holds within ±0.1 K over the temperature range 300 K to 450 K.

A summary of best-fit VTF parameters derived from experimental conductivity data for a series of ionic liquids is given in ***Table 6.1***. The estimated errors in the critical temperature T_0 are ±5 K. The exceptional accuracy of these results encouraged an explanation for the physical origin of T_0 to be sought.

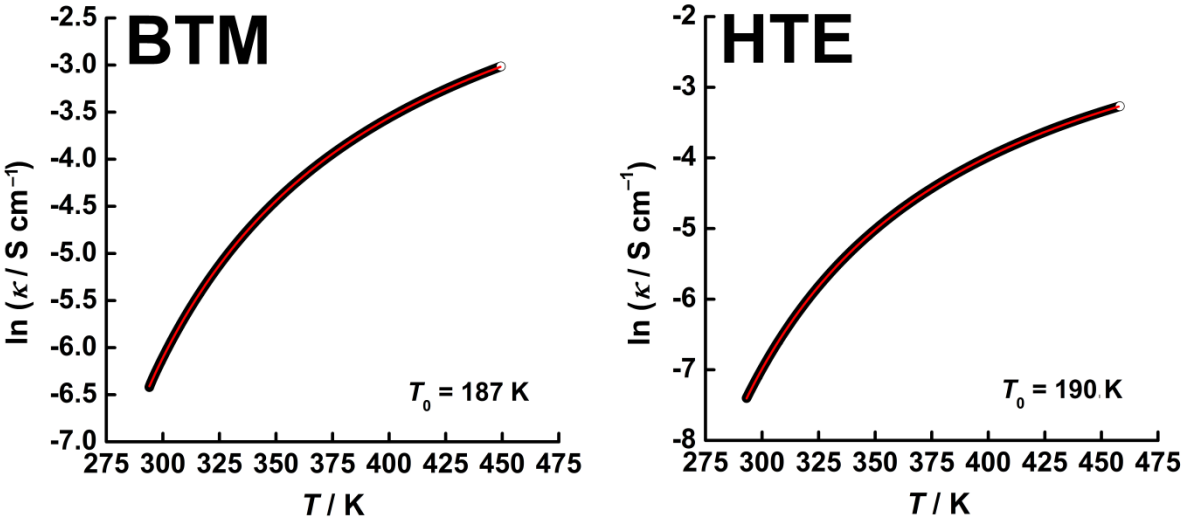

Figure 6.12 – Plots of ln conductivity (κ/S cm^{-1}) versus temperature, T/K for the heating cycles of butyltrimethylammonium bis(trifluorormethylsulfonyl)imide (BTM) and hexyltriethylammonium bis(trifluoromethylsulfonyl)imide (HTE) over the temperature range 20 ºC to 190 ºC (293.15 K to 463.15 K). The T_0 value with the most precise fit is labelled. The black line is the experimental data and the red line is the best fit (~40,000 data points).

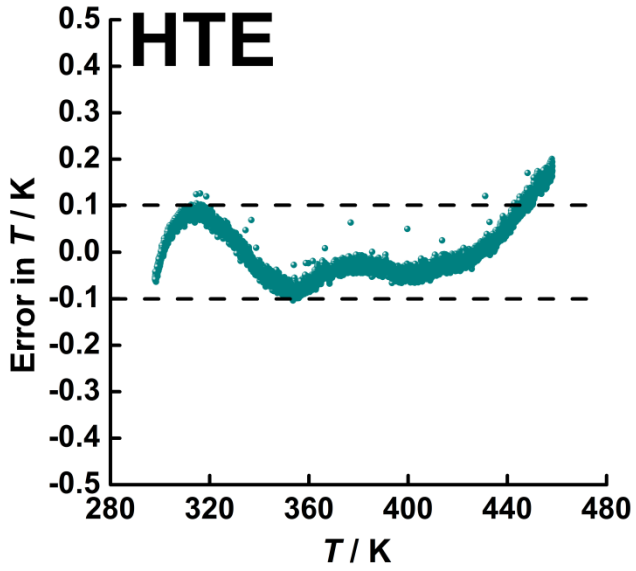

Figure 6.13 – Residual error in the fitting of the VTF equation to experimental data for HTE, expressed as error in temperature. The data reveal that the VTF relation holds within ±0.1 K over the range 300 K to 450 K.

Table 6.1 – A summary of best-fit VTF parameters derived from experimental conductivity data for a series of ionic liquids.

Ionic Liquid	*A*	*B*	T_0 / *K*	R^2	*Precision of fit*
Butyltrimethylammonium bis(trifluoromethylsulfonyl)imide	–0.68	634.1	187	0.99999903	6.01
Hexyltriethylammonium bis(trifluoromethylsulfonyl)imide	–1.09	652.8	190	0.99999915	6.07
1-Ethyl-3-methylimidazolium methanesulfonate	–6.61	547.1	198	0.99998020	5.30
Tetrabutylammonium bis(trifluoromethylsulfonyl)imide	–6.07	649.8	218	0.99999496	4.60
1-Butyl-3-methylimidazolium tetrafluoroborate	–6.98	651.7	183	0.99997476	4.57

It was strongly suspected from the present work, and the work of others, that each T_0 might correspond to the glass transition temperature T_g of the corresponding ionic liquid[20]. To confirm this hypothesis, comparison needed to be made with high precision measurements of the glass transition temperature obtained by thermal analysis. Two methods were used, differential scanning calorimetry (DSC) and spontaneous heating following shock cooling. A full discussion of the latter thermal method and DSC thermograms are deferred to ***Appendix 6C***, and ***Appendix 6D*** respectively but key results are summarised in ***Table 6.2***. It can be seen that the electrochemically-determined T_0 values and the thermally-determined T_g values are in very satisfactory agreement.

Table 6.2 – A summary of T_g values obtained by thermal analysis.

Ionic Liquid	T_g / *K*			
	VTF method	*DSC method*	*Shock cooling method*	*Literature*
BTM	187±5	192±5	185±10	199[21]
HTE	190±5	188±5	195±10	192[22]

Referring back to ***Equation 6.33***, the conductivity κ/(S m^{-1}) can be written in the form

$$\kappa \approx \kappa_{\infty} \exp\left(\frac{N}{2}\,\frac{T_g}{T_g - T}\right)$$

Equation 6.33

where N is the number of new degrees of freedom that are created by the detachment of the mobile species from the glass matrix, and κ_∞ is the limiting conductivity at infinitely high temperature.

This suggests that a plot of $\ln(\kappa) - \ln(\kappa_\infty)$ *versus* $T_g/(T - T_g)$ will be a straight line with a slope of N/2 and an intercept at the origin. This is shown to be true for HTE and BTM in ***Figure 6.14*** and for 1-ethyl-3-methylimidazolium methanesulfonate (MS), tetrabutyl-ammonium bis(trifluoromethylsulfonyl)imide (TBA), and 1-butyl-3-methyl-imidazolium tetrafluoroborate (TFB) in ***Figure 6.15***.

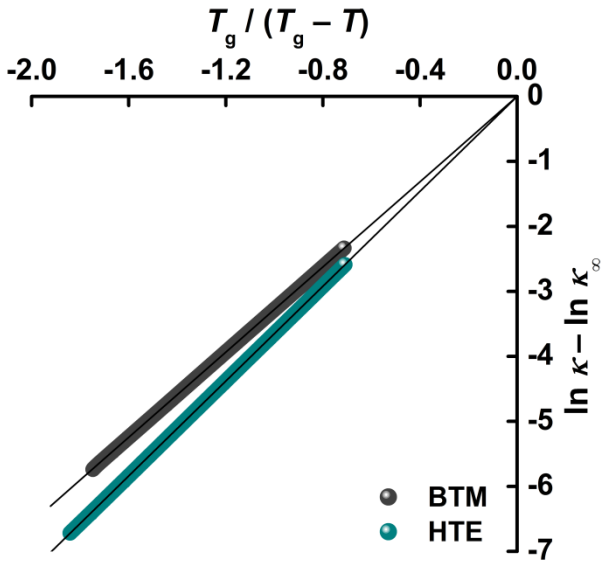

Figure 6.14 – Plot of ln κ – ln κ_∞ versus $T_g/(T_g–T)$ for butyltrimethylammonium bis(trifluoro-methylsulfonyl)imide (BTM) and hexyltriethylammonium bis(trifluoromethylsuylfonyl)imide (HTE) Approx. 40,000 data points per plot.

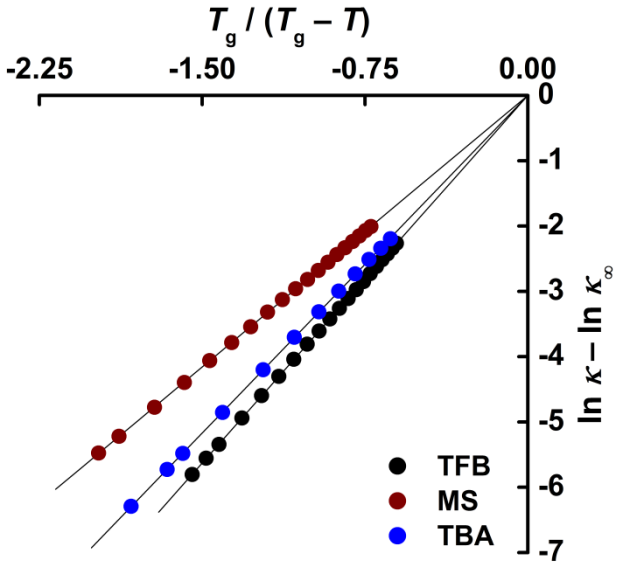

Figure 6.15 – Plot of ln κ – ln κ_∞ versus $T_g/(T_g–T)$ for 1-ethyl-3-methylimidazolium methanesulfonate (MS), tetrabutylammonium bis(trifluoromethylsulfonyl)imide (TBA), and 1-butyl-3-methylimidazolium tetrafluoroborate (TFB). 10-20 data points per plot.

Table 6.3 – A summary of the N and N/2 and values obtained for BTM and HTE via VTF analysis.

Ionic Liquid	**Gradient** (*N*/2)	**N**
Butyltrimethylammonium bis(trifluoromethylsulfonyl)imide	3.27	6.54
Hexyltriethylammonium bis(trifluoromethylsulfonyl)imide	3.65	7.30
1-Ethyl-3-methylimidazolium methanesulfonate	2.92	5.85
Tetrabutylammonium bis(trifluoromethylsulfonyl)imide	2.98	5.82
1-Butyl-3-methylimidazolium tetrafluoroborate	3.57	7.14

6.5 – Conclusion

In this chapter, the Vogel-Tammann-Fulcher equation has been derived from classical thermodynamics. In doing so, the unknown constants *A*, *B*, and T_0 have been identified for the first time. It is suggested that the constant T_0, which is the critical temperature for the onset of bulk conductivity, coincides with the glass transition temperature T_g. To confirm this hypothesis, a series of high-precision conductivity experiments were carried out and

estimates of T_0 were compared with estimates of T_g obtained by thermal analysis. These were found to coincide within $\pm$5 K. Thus, it is certain that the conducting species in ionic liquids are trapped in the glassy state until the glass transition temperature is exceeded. An immediate corollary is that the best conducting ionic liquids are those having the lowest glass transition temperatures.

As is well known, the fitting of the Vogel-Tammann-Fulcher equation to conductivity data is very tolerant to errors in the unknown constants *A*, *B*, and T_0. This feature makes the fitting process very precise, but amplifies the experimental errors if the equation is inverted to obtain estimates of *A*, *B*, and T_0. Mathematicians refer to this type of inverse problem as "ill-posed". The only rigorous way to overcome it is to obtain experimental data of very high accuracy. To achieve this, a single-frequency AC impedance technique (the Wayne-Kerr Precision Component Analyser method) was used to measure the conductivity, and a platinum resistance thermometer was used to measure the temperature. In each experiment, more than 40,000 data points were acquired over very wide temperature ranges (typically >100 K) over forty-eight hours of measurement. The resulting errors in T_0 were less than $\pm$5 K. This method therefore provides a new way of measuring the glass transition temperature of an ionic liquid without measuring its viscosity.

6.6 – References

[1] Vogel, H. *Physicalische Zeitschrift*, 22: 645-646 (1921).

[2] Tammann, G. & Hesse, W. *Die Abhängigkeit der Viscosistat von der Temperatur bei unterkühlten Flüssigkeiten*. Zeitschrift für anorganische und allgemeine Chemie, 156: 245-257 (1926).

[3] Fulcher, G. S. *Analysis of recent measurements of the viscosity of glass*. Journal of the American Ceramic Society, 8(12): 339-355 (1925).

[4] Atkins, P. W. & De Paula, J. *Atkins' Physical Chemistry*, 8, Oxford: Oxford University Press, Chapter 3: The Second Law, pp81 (2006).

[5] Marcelin, R. *Contribution à l'Étude de la Cinétique Physico-Chimique*. Annals of Physics (Paris) 3: 120-231 (1915).

[6] Eyring H. *The Activated Complex in Chemical Reactions*. Journal of Chemical Physics, 3: 107-115 (1935).

[7] Evans, M. G. & Polanyi, M. *Some Applications of the Transition State Method to the Calculation of Reaction Velocities, Especially in Solution*. Transactions of the Faraday Society, 31:875-894 (1935).

[8] Wigner, E. *The Transition State Method*. Transactions of the Faraday Society, 34: 29-41 (1938).

[9] Vila, J., Ginés, J. P., Pico, J. M., Franjo, C., Jiménez, E, Varela, L. M. & Cabeza, O. *Temperature dependence of the electrical conductivity in EMIM-based ionic liquids: evidence of Vogel-Tammann-Fulcher behaviour*. Fluid Phase Equilibria, 242: 141-146 (2006).

[10] Cohen, M. H. & Turnbull, D. *Metastability of amorphous structures*. Nature, 203: 964 (1964).

[11] Adam, G. & Gibbs, J. H. *On the temperature dependence of cooperative relaxation properties in glass forming liquids.* Journal of Physical Chemistry, 43: 139-146 (1965).

[12] Hammond, G. S. *A correlation of reaction rates*. Journal of the American Chemical Society, 77: 334-338 (1955).

[13] Angell, C. A., in Rubi, J-M. & Pérez-Vicente, C. Lecture notes in physics, vol. 492, complex behaviour of glassy systems, Springer, Berlin (1997).

[14] Greet, R. J. & Turnbull, D. *Glass Transitions in o-terphenyl*. Journal of Chemical Physics, 46: 1243-1251 (1967).

[15] Debenedetti, P. G. & Stillinger, F. H. Supercooled liquids and the glass transition. Nature, 6825: 259-267 (2001).

[16] Robinson, R. A. & Stokes, R. H., *Electrolyte Solutions*, Appendix 6.3: 2nd Edition (Revised), Butterworths, London, pp466 (1965).

[17] Barrosse-Antle, L. E., Bond, A. M., Compton, R. G., O'Mahony, A. M. Rogers, E. I. & Silvester, D. S. *Voltammetry in room temperature ionic liquids. Comparisons and contrasts with conventional electrochemical solvents*. Chemistry, An Asian Journal, 5: 202-230 (2010).

[18] Zhang, Z., Yang, Li., Luo, S., Tian, M., Tachibana. & Kimijima, K. *Ionic liquids based on aliphatic tetraalkylammonium cations and TFSI anion as potential electrolytes*. Journal of Power Sources, 167: 217-222 (2007).

[19] Jarosik, A., Krajewski, R., Lewandowski, A. & Radzimski, P. *Conductivity of ionic liquids in mixtures.* Journal of Molecular Liquids, 123: 43–50 (2006).

[20] Galiński, M., Lewandowski. A. & Stępniak. I. *Ionic liquids as electrolytes*. Electrochimica Acta, 51: 5567-5580 (2006).

[21] Tokuda, H., Tsuzuki, S., Hasan, S., Hayamizu, K. & Watanabe, M. *How Ionic Are Room-Temperature Ionic Liquids? An indicator of the Physiochemical Properties*. Journal of Physical Chemistry B, 110: 19593-19600 (2006).

[22] Sun, J., Forsyth, M. & MacFarlane, D. R. *Room-Temperature Molten Salts Based on the Quaternary Ammonium Ion*. Journal of Physical Chemistry B, 102: 8858-8864 (1998).

Chapter 7 – Development of a Conductivity Probe for Low Sample Volumes

7.1 – Introduction

In ***Chapter 6***, measurements of conductivity *versus* temperature were reported for a series of ionic liquids. These conductivity measurements were obtained using a commercial conductivity probe (027-013, Jenway) and required a large sample volume (10 ml). However, the high cost of ionic liquids meant that an alternative method of measuring their conductivity in smaller volumes (<2 ml) was desirable. In this section, a new design for a miniature conductivity probe is described. The purpose of the probe is to measure the conductivity of a single droplet of ionic liquid at room temperature, and possibly at elevated temperatures ($T \geq$ 100 ºC).

7.2 – Designing a low volume conductivity probe

When designing a conductivity probe to operate in low volumes of ionic liquid, there are two important criteria that need to be met.

1. The electrode material must have low impedance
2. The electrodes must have fixed geometry

7.2.1 – Selection of low impedance electrode material

Table 7.1 presents a list of common electrode materials along with their conductivities at 20 °C[1]. For the miniature probes, gold was chosen as the base electrode material. This is because, although silver and copper are more conducting than gold, gold is more inert. Silver and copper both tarnish in air, and they also exhibit undesirable redox electrochemistry in ionic liquids at low positive potentials (< 0.8 V *vs.* SCE, 25 ºC[2]). Additionally, pure gold is ductile and can therefore tolerate mechanical stresses caused by thermal shock, which is desirable when considering its use in a high temperature conductivity probe.

Table 7.1 – Conductivity and resistance values for some common electrode materials at 20 °C.

Electrode Material	Conductivity κ / 10^2 Ω^{-1} cm^{-1}	Resistivity ρ / μΩ cm
Silver	6520	1.6
Copper	5880	1.7
Gold	**4170**	**2.4**
Iridium	1890	5.3
Platinum	940	10.6
Lead	500	20
Mercury	100	98
Highly Oriented Pyrolytic Graphite	20	500
Graphite (isotropic)	7	1400
Carbon Fiber	6	1600
Glassy Carbon	2	5000

7.2.2 – Design of fixed electrode geometry

When measuring the conductivity of a solution, it is important that the measuring electrodes are a fixed distance apart. This ensures that the conductivity of the same volume of solution is measured each time, and the cell constant remains unchanged. The design that was developed for the miniature conductivity probe is shown in ***Figure 7.1***. It consists of two interdigitated gold electrodes screen printed onto an inert, thermally stable alumina substrate (22 mm x 7 mm x 1 mm). The gold bands are 200 μm thick and spaced 200 μm apart. The manufacturer was DropSens, Asturias, Spain (DRP-SCA-AU). In use, a layer of platinum black is coated on top of the gold surface.

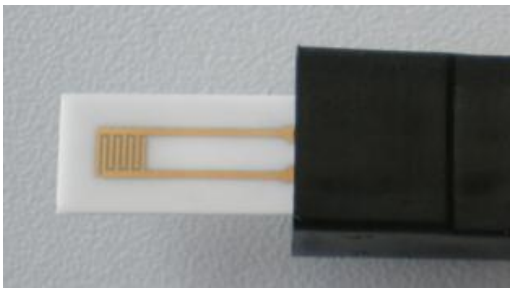

Figure 7.1 – Interdigitated gold electrode used as a substrate for miniature electrode. (DRP-SCA-AU, DropSens, Asturias, Spain).

7.3 – Platinisation of electrodes

7.3.1 – Theory

In a traditional two electrode conductivity cell, an alternating current is passed between two electrodes, and the resulting voltage is recorded. The aim is to measure *only* the resistance of the solution (R_{sol}), ***Figure 7.2***. To ensure accuracy, the impedance of the electrodes (Z_{el}) must be rendered negligible in comparison to the resistance of the solution. If this is not the case then R_{sol} and Z_{el} will both contribute to the output.

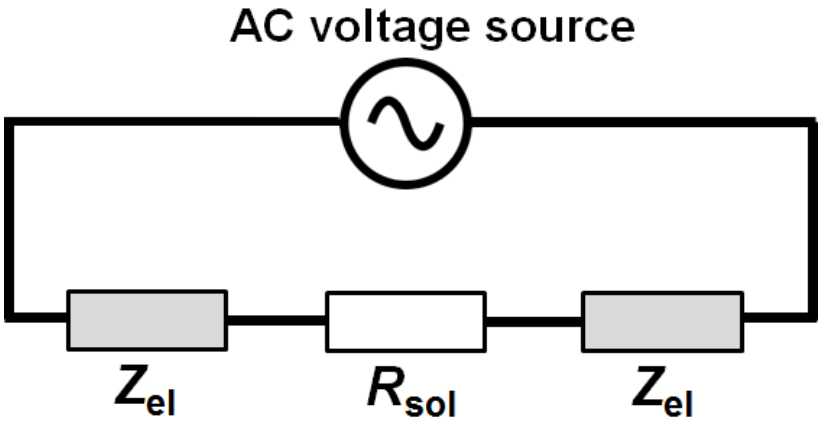

Figure 7.2 – Equivalent circuit of a two-electrode conductivity cell.

A well-established method for decreasing the impedance of electrodes is "platinisation"[2]. Platinised electrodes are often used in conductivity cells[3]. In the platinisation process, high surface area platinum black is electrochemically deposited onto the surfaces of test electrodes, to decrease their interfacial impedance. Platinum black is a fine powder that is porous on the micrometer and nanometer scales[4]. The porous structure traps light of visible wavelengths (0.4 μm to 0.8 μm), producing a black velvet appearance to the eye, even though the platinum is inherently reflective. Platinisation is an effective way of decreasing the interfacial impedance of an electrode because the process increases its surface area, and hence increases its capacitance. The relation between the interfacial impedance and the capacitance is given by ***Equation 7.1***.

$$Z_c = \frac{1}{j\ \omega\ C}$$

Equation 7.1

Here, Z_c is the interfacial impedance, C is the interfacial capacitance (F), j is the square root of minus one, and $\omega = 2\pi f$ is the angular frequency of the applied potential (radians s^{-1}).

Surprisingly, there is no "standard" platinising solution for the deposition of platinum black. Many different recipes have been presented in the literature, a few of which are tabulated in ***Table 7.2***.

Table 7.2 – Selected platinising solutions.

Platinising solution	Conditions	Reference
21 mM (1%) platinum chloride	Passing of current for several minutes	[5]
62 mM (3%) platinum chloride and 0.53 mM (0.2 %) lead acetate	Using a rheostat for slow gas evolution. Current stopped when electrodes go black	[6]
41 mM (2%) platinum chloride and 0.00053 M (0.2 %) lead acetate	Current reversed every 0.5 min for 10 min	[7]
1 part chloroplatinic acid to 0.008 parts lead acetate to 30 parts of water	4 V between platinum working electrodes 30 mA cm^{-2} current density at the cathode	[8]

Some of the recipes include lead acetate to supress hydrogen evolution, while others do not. There is also a wide diversity of deposition conditions and film thicknesses. In the present work, a platinising solution developed by Bates[9] and recommended by Ives and Hills[10] was arbitrarily selected. This consisted of a lead-free 2% w/w chloroplatinic acid (H_2PtCl_6) solution in 2 M HCl. Alternatively, a 2% w/w potassium hexachloroplatinate (K_2PtCl_6) solution in 2 M HCl was used instead. In the laboratory, no conclusive evidence was found that supported the claim that platinising solutions containing lead were more effective.

Preparation of platinising solution

In a 50 ml volumetric flask K_2PtCl_6 (1.19 g, 49 mM) was added to 9.82 ml of HCl (32%), and made up with de-ionized water. The resulting solution was heated to 90 °C on a hot plate, and sonicated until the orange/yellow K_2PtCl_6 solid had fully dissolved. Some K_2PtCl_6 did re-

precipitate upon cooling, but this was easily removed by decantation. The supernatant solution was used for platinisation.

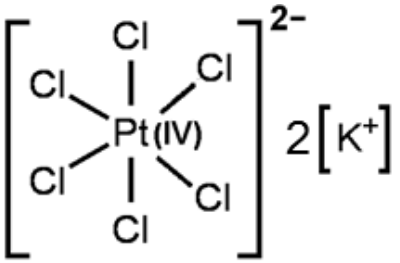

Figure 7.3 – Structural formula of potassium hexachloroplatinate.

Mechanism of deposition of platinum black

The mechanism by which platinum black is electrodeposited from chloroplatinic acid solutions is poorly understood, but two reaction pathways have been suggested by Feltham and Spiro[3].

Pathway (1)

$$[Pt^{IV}Cl_6]^{2-} + 2e^- \rightleftharpoons [Pt^{II}Cl_4]^{2-} + 2Cl^- \qquad \textbf{Equation 7.2}$$

$$Pt^{II}Cl_4]^{2-} + 2e^- \rightleftharpoons Pt^0 + 4Cl^- \qquad \textbf{Equation 7.3}$$

Pathway (2)

$$[Pt^{IV}Cl_6]^{2-} + 4e^- \rightleftharpoons Pt^0 + 6Cl^- \qquad \textbf{Equation 7.4}$$

However, these are very difficult to distinguish experimentally. Overall, the literature suggests that the deposition reaction is kinetically slow due to the difficulty of breaking the Pt–Cl bonds[3].

7.3.2 – Initial studies: platinum black deposition onto macroelectrodes

Due the high cost of prototype interdigitated gold electrodes, initial studies were carried out using less expensive macroelectrodes. These studies were typically performed on gold or platinum discs (d = 1.6 mm, BASi). These electrodes were robust and could be re-polished many times.

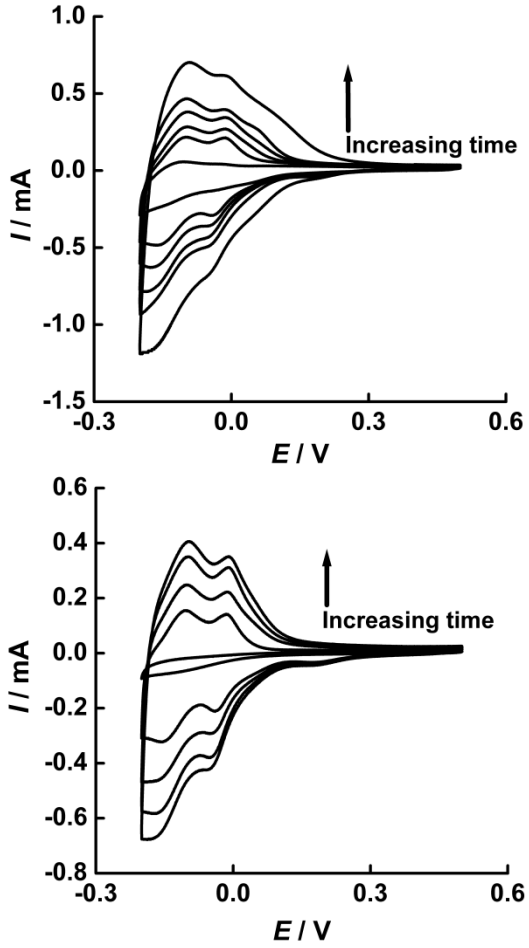

Figure 7.4 – Cyclic voltammetry of (top) a platinum disc electrode (d = 2 mm, BASi), and (bottom) a gold disc electrode (d = 1.6 mm, BASi) during the deposition of platinum black. The deposition solution was 2% K_2PtCl_6 in 2 M HCl, and the deposition potential was –0.2 V. Shown are cyclic voltammograms recorded after 0 min, 5 min, 10 min, 15 min, 20 min and 25 min of deposition. In each case the potential was cycled at a scan rate of 200 mV s^{-1}. The counter electrode was Pt gauze (A = 4.0 cm^2). Note the large increase in surface area as deposition time progresses.

Figure 7.4 shows the increase in voltammetric current as a function of deposition time of platinum black on gold and platinum electrodes. The electrodeposition was performed by

holding the electrode potential at +0.5 V *vs.* SCE for 10 s before each cycle between –0.2 and +0.5 V. After three cycles the potential was then held at –0.2 V for five minutes to allow platinum black to deposit. After five minutes, the potential was again cycled three times with the third cycle recorded. This process was repeated until the platinum had been deposited for $t \geq 20$ min.

The growth of the hydrogen adsorption and desorption peaks in both cases indicated that the surface area of the working electrode was increasing with time, and that the platinisation solution of Bates[9] was effective on both platinum and gold disc electrodes. Hence, it was concluded that this method might be suitable for the deposition of platinum black onto the interdigitated gold electrodes. This latter result is shown in ***Figure 7.5***.

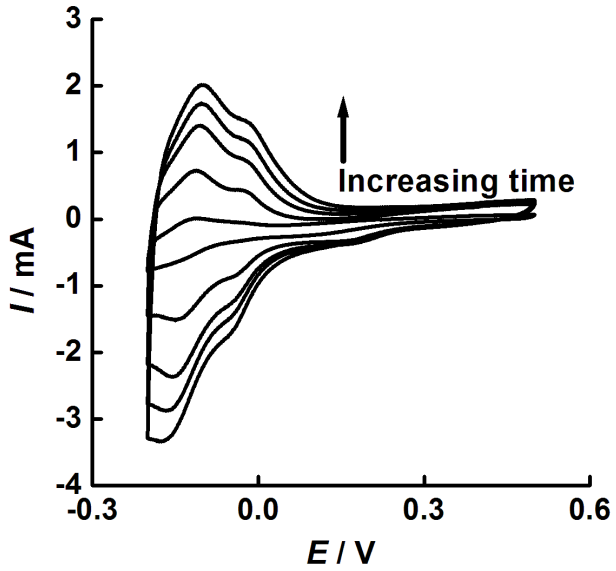

Figure 7.5 – Cyclic voltammograms of an interdigitated gold electrode (DropSens) during the deposition of platinum black. The deposition solution was 2% K_2PtCl_6 in 2 M HCl, and the deposition potential was –0.2 V. Shown are the voltammograms after 0 min, 5 min, 10 min, 15 min and 20 min. In each case the potential was cycled at a scan rate of 200 mV s^{-1}. The counter electrode was Pt gauze ($A = 4.0$ cm^2).

It can be seen that the deposition of platinum black onto the interdigitated gold electrodes was successful, evidenced by the growth of the hydrogen adsorption and desorption peaks around –0.1 V. By calculating the area under the peaks, it was shown that the surface area of the electrode had increased by a factor of eight during the deposition process. Although this

was significant, an even higher surface area was needed to ensure that the impedance of the electrodes was negligible when used in the conductivity cell. Hence, for a practical device, more platinum black needed to be deposited. There were two options (1) increasing the time of deposition and (2) increasing the rate of deposition. For these further studies, a platinum wire electrode was initially used, due to the fact that it could be flame treated to give a reproducible surface each time. This was important for direct comparisons between different deposition conditions. Later on, the platinum wire was substituted by a gold wire prior to transferring the technology to the interdigitated gold electrodes.

The cleanliness of a platinum surface can be assessed by recording its voltammetry in sulphuric acid (0.5 M). This is because a classic well-known shape is observed for this voltammetry, as shown in ***Figure 7.6***, which, if observed, confirms that the platinum surface is clean.

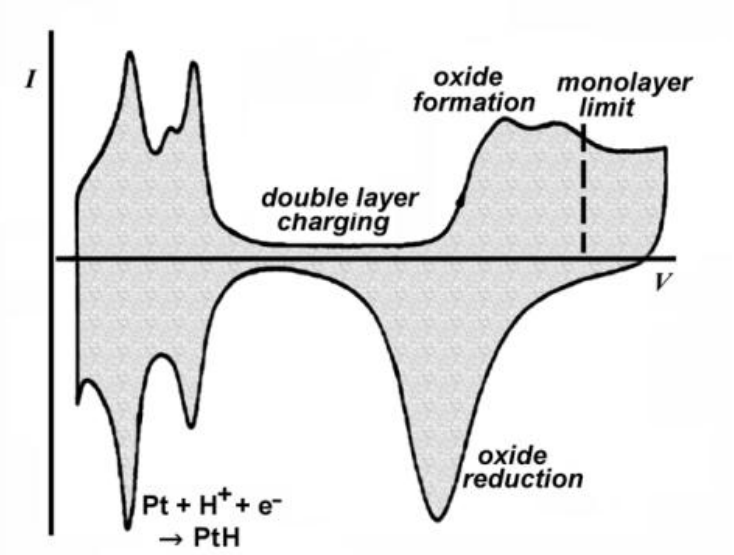

Figure 7.6 – Classic cyclic voltammogram of platinum in 0.5 M sulfuric acid (25 mV s^{-1}). Image derived from Conway, B. E. & Angerstein-Kozlowska[11].

The main features of the classic platinum voltammetry in sulphuric acid voltammetry are:

- Oxide formation at +0.7 V *vs.* SCE on the positive-going scan and oxide reduction on the negative-going scan.

- Two reversible hydrogen adsorption peaks between –0.2 V and 0 V on the negative-going scan.

The presence of two hydrogen adsorption peaks indicates the presence of two different crystal faces on the flame-annealed electrode surface, namely platinum(100) and platinum(111). The presence of a third anodic peak has also been reported by Conway *et al*.[11-12], shown in ***Figure 7.6***. The onset of hydrogen evolution is indicated by a very sharp increase in current at –0.25 *vs.* SCE (not shown). The voltammetric response for the flame-treated platinum wire electrode (A = 0.15 cm^2) is shown in ***Figure 7.7***.

The platinum wire was held in a methane flame for a minimum of 20 s, until the platinum glowed orange. This allowed a reproducible electrode surface to be obtained for extensive deposition testing. The wire was then allowed to cool before immersion in to the 0.5 M sulfuric acid solution. The electrode potential was held at –0.2 V *vs.* SCE for 10 s before being cycled from –0.2 V to +1.2 V. Nitrogen was bubbled through the solution for 10 minutes prior to starting the voltammetry. The 10th cycle was recorded each time.

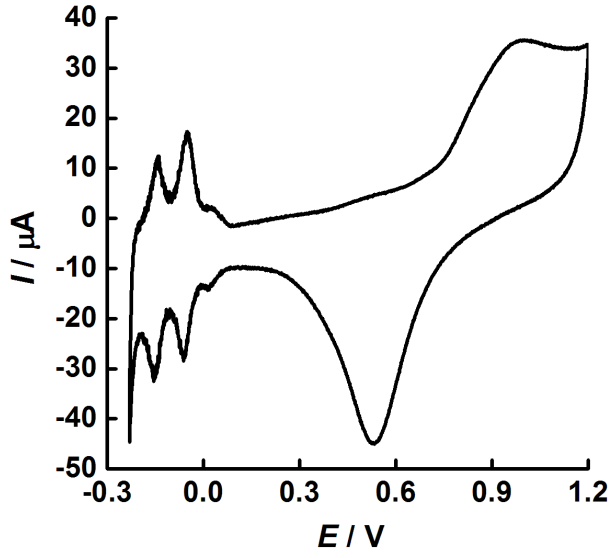

Figure 7.7 – Voltammogram of flame treated platinum wire (A = 0.15 cm^2) in 0.5 M H_2S0_4. The potential was held at –0.2 V vs. SCE for 10 s before being cycled from –0.2 V to + 1.2 V at a scan rate of 200 mV s^{-1}. The counter electrode was Pt gauze (A = 4.0 cm^2). Nitrogen was bubbled through the solution for 10 minutes prior to starting cyclic voltammetry. Shown above is the 10th cycle. The hydrogen peak charge was calculated to be 3.6 µC.

All the classic features can be observed following the flame treatment of platinum wire, shown in ***Figure 7.7***, indicating a successful method has been developed for reproducing the electrode surface. The process of optimising platinum black deposition on wire electrodes could now be investigated.

7.3.3 – Optimisation studies: platinum black deposition onto platinum and gold wire electrodes

Platinum wire

An example of a voltammogram obtained for platinum wire in the 2% K_2PtCl_6 in 2 M HCl platinising solution is given in ***Figure 7.8***.

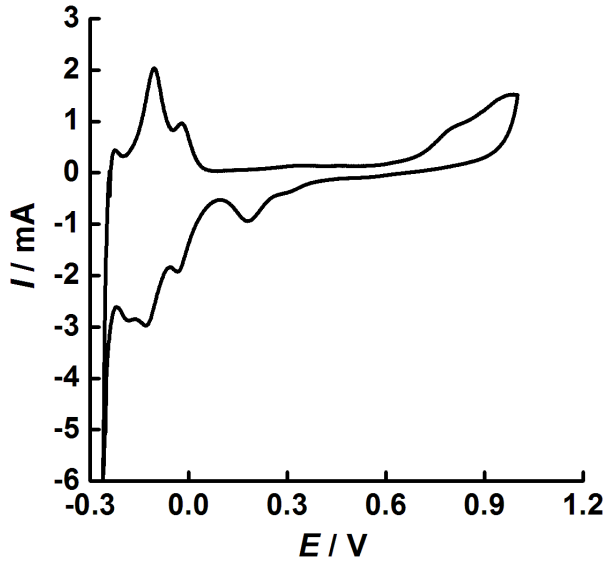

Figure 7.8 – Voltammetry of platinum wire (0.15 cm^2) in a solution of 2% K_2PtCl_6 in 2 M HCl. The potential was held at –0.2 V vs. SCE for 10 s before being cycled from –0.25 V to + 1.0 V, at a scan rate of 200 mV s^{-1}. The counter electrode was Pt gauze (A = 4.0 cm^2). Nitrogen was bubbled through the solution for 10 min prior to start. Shown above is the 10th cycle.

In order to try to increase the amount of platinum black that was deposited onto the surface of the electrode, it was decided to try platinising electrodes at more negative potentials than previously trialled (e.g. −0.4 V rather than −0.2 V). The idea behind this was that higher current values could be achieved and hence a higher rate of deposition would be achieved.

Platinum wire (A = 0.15 cm^2) was immersed into the deposition solution. The potential was held at +0.2 V *vs*. SCE for 10 s before being cycled from +0.2 V to –0.4 V to +0.2 V. After three cycles the potential was held at –0.4 V for ten minutes, before continuing to cycle for three more cycles and the subsequent voltammogram was recorded. This was repeated six times until t = 60 min. The result is shown in ***Figure 7.9***.

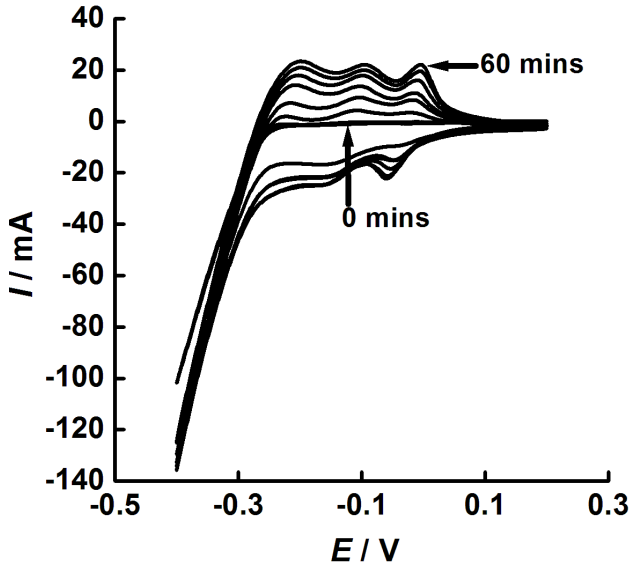

Figure 7.9 – Voltammograms of platinum wire (0.15 cm^2) in a solution of 2% K_2PtCl_6 in 2 M HCl. The potential was held at +0.2 V vs. SCE for 10 s before being cycled from –0.4 V to +0.2 V, at a scan rate of 200 mV s^{-1}. The counter electrode was Pt gauze (A = 4.0 cm^2). After the third cycle (labelled '0 mins') the potential was held at –0.4 V for 10 minutes. After 10 minutes, the cycle was continued for three more cycles and the third one was recorded. This process was repeated six times until t = 60 minutes. The surface area of the platinised gold following 60 minutes of platinum black deposition was 62.1 cm^2 (14.3 mC).

After sixty minutes of platinum black deposition at –0.4 V, the surface area of the electrode was calculated by integrating the charge under the hydrogen desorption peaks (in this case 14.3 mC) and dividing by 230 μC cm^{-2} (which is the known charge density value for a full monolayer of adsorbed hydrogen on polycrystalline platinum[13]). The surface area had increased substantially, from 0.15 cm^2 to 62.2 cm^2, an 414 fold increase. To see if more surface area could be deposited at an even more negative potential, the potential was held at –0.6 V for 60 minutes. The results are shown in ***Figure 7.10***.

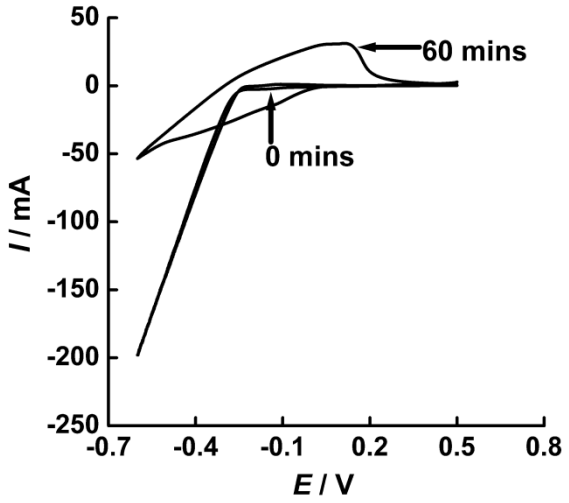

Figure 7.10 – Voltammetry of platinum wire (0.15 cm^2) in a solution of 2% K_2PtCl_6 in 2 M HCl. The potential was held at +0.2 V vs. SCE for 10 s before being cycled from –0.6V to +0.6 V, at a scan rate of 200 $mV\ s^{-1}$ for three cycles. The third cycle is labelled as '0 mins'. After the third cycle, the potential was held at –0.6 V for 60 minutes, before continuing to cycle for 3 more cycles. The final cycle was recorded and is labelled '60 mins'. The surface area of the platinised platinum following 60 minutes of platinum black deposition was 122 cm^2 (28.1 mC). The counter electrode was Pt gauze (A = 4.0 cm^2).

In ***Figure 7.10***, it is observed that the deposition of platinum black at –0.6 V is more effective than the deposition of platinum black at –0.4 V, evidenced by the larger surface area of platinum black deposited onto the surface of the platinum wire (122 cm^2 *vs.* 62.1 cm^2 previously). This suggested that a high rate of platinum black deposition correlates with a high surface area.

Gold wire

Having successfully demonstrated the importance of a high rate of platinum black deposition on platinum wire, the method was then transferred to gold wire. Hills and Ives stated that "platinum black is said to adhere more firmly to gold than platinum"[14], which was encouraging. The gold wire (E401-3, Agar Scientific Ltd, d = 0.2 mm) could not be flame treated due to it having a much lower melting point than platinum (1064 °C[15] *vs.* 1767 °C respectively[15]). As a result, instead of flame treatment, the gold wire was rinsed in a 50:50 nitric acid and water mixture prior to voltammetry. (Note: a*qua regia* was another option but

it was found to dissolve the gold wire.) The voltammetry of gold wire in the platinising solution is shown in ***Figures 7.11*** and deposition of platinum black at –0.6 V (60 mins) is shown in ***Figure 7.12.***

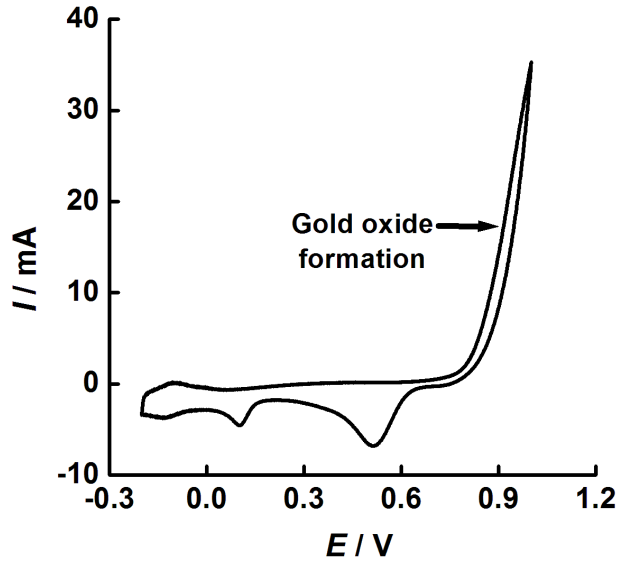

Figure 7.11 – Voltammogram of gold wire (0.11 cm^2) in a solution of 2% K_2PtCl_6 in 2 M HCl. The potential was held at –0.2 V vs. SCE for 10 s before being cycled from –0.2 V to + 1.0 V to –0.2 V, at a scan rate of 200 mV s^{-1}. The counter electrode was a Pt gauze (A = 4.0 cm^2). Shown above is the 10th scan.

The surface area of the gold wire following 60 minutes deposition at –0.6 V was 361 cm^2. This was much greater (3300 fold) than the initial surface area of the initial gold wire, 0.11 cm^2, proving that platinisation was highly successful. A photograph of the gold wire after 60 minutes platinisation in 2% K_2PtCl_6 in 2 M HCl is shown, ***Figure 7.13***. Further deposition resulted in poor adhesion, such that the deposit started to fall off the electrode surface.

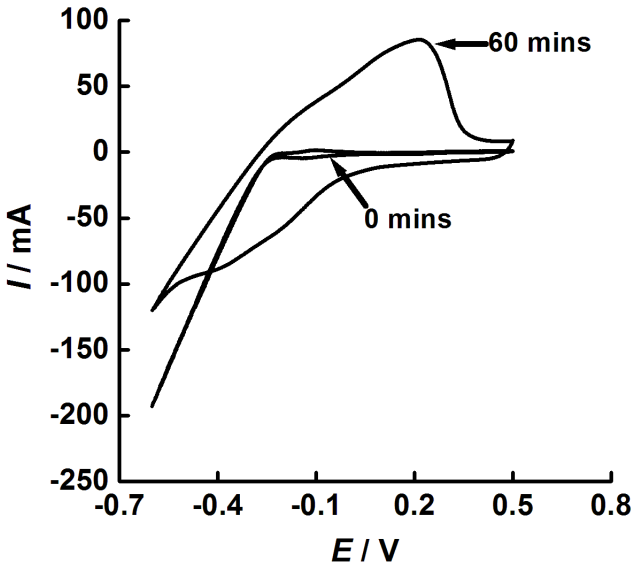

Figure 7.12 – Voltammetry of gold wire (0.11 cm^2) in a solution of 2% K_2PtCl_6 in 2 M HCl. The potential was held at –0.2 V vs. SCE for 10 s before being cycled from –0.6 V to +0.6 V, at a scan rate of 200 mV s^{-1} for three cycles. The third cycle is labelled as '0 mins'. After the third cycle, the potential was held at –0.6 V for 60 minutes, before continuing to cycle for 3 more cycles. The final cycle was recorded and is labelled '60 mins'. The surface area of the platinised gold following 60 minutes of platinum black deposition was 361 cm^2. The counter electrode was Pt gauze (A = 4.0 cm^2).

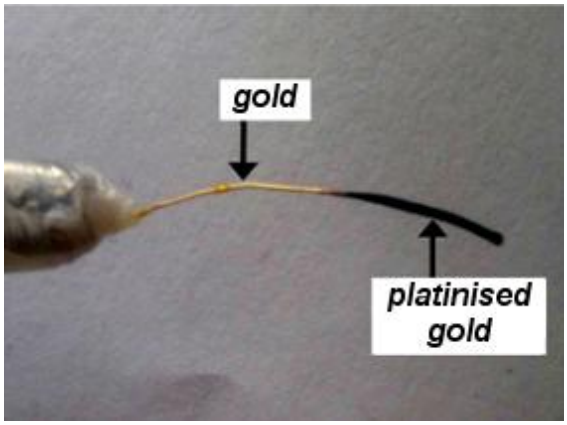

Figure 7.13 – A photograph showing gold wire after the deposition of platinum black.

7.3.4 – Final studies: platinum black deposition onto interdigitated gold electrodes

The voltammetry of the as-received interdigitated gold electrodes in the platinising solution is shown in ***Figure 7.14 and Figure 7.15***. Reasssuringly, it demonstrates similar voltammetric

behaviour to the previously tested gold wire. The nucleation of bulk gold oxide was observed whenever the applied potential exceeded the reversible potential of bulk gold oxide, *circa.* +0.7 V *vs.* Ag|AgCl, and is shown in ***Figure 7.14 (left)***. Increasing the potential beyond the reversible potential caused the appearance of classical nucleation/growth kinetics, as evidenced by the appearance of a distinct voltammetric loop in the first scan of ***Figure 7.14 (left)***. During the second scan, the loop was less prominent due the presence of nucleation sites remaining from the first scan. No nucleation was observed when scanning the potential between –0.2 V and +0.7 V, as shown in ***Figure 7.14 (right)***. Decreasing the potential to more negative values caused the onset of both hydrogen evolution and platinum black deposition. This can be seen in ***Figure 7.15***.

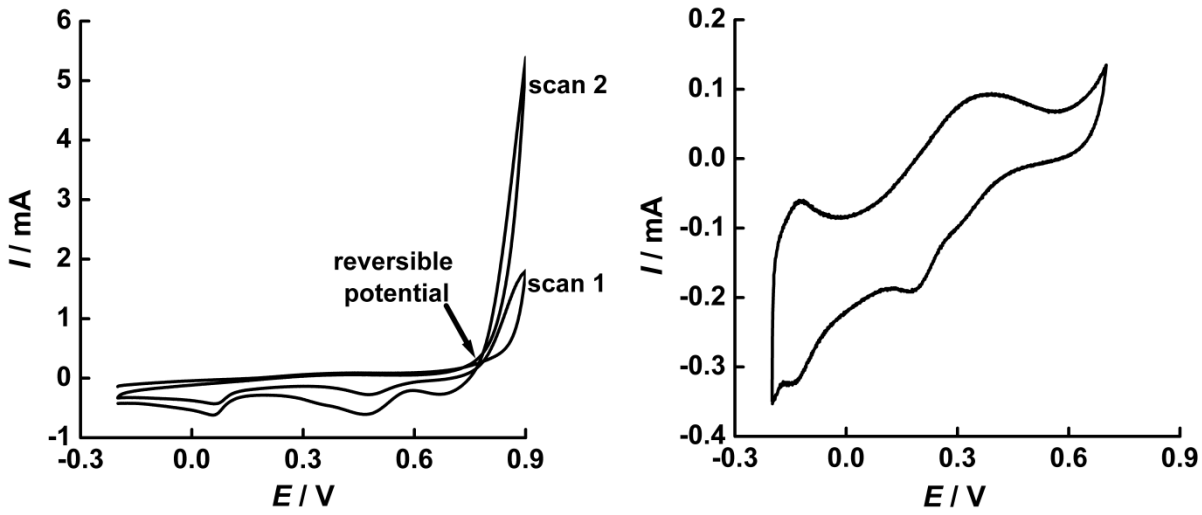

Figure 7.14 – Voltammetry of the interdigitated gold electrodes in a solution of 2% K_2PtCl_6 in 2 M HCl. The potential was held at –0.2 V vs. SCE for 10 s before being cycled from –0.2 V to + 0.9 V to –0.2 V(left) and –0.2 V to + 0.7 V to –0.2 V (right), at a scan rate of 200 mV s^{-1}. The counter electrode was Pt gauze (A = 4.0 cm^2). Shown above (left) are the first and second scans which show evidence of nucleation. The reversible potential of bulk gold oxide formation is +0.787 V.

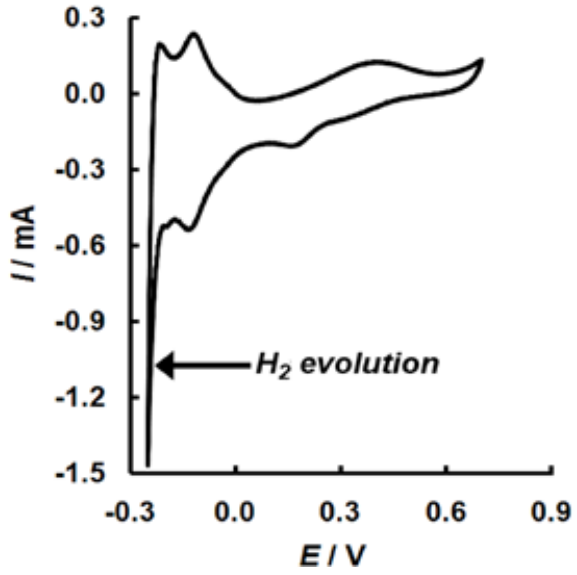

Figure 7.15 −Voltammetry of an interdigitated gold electrodes in a solution of 2% K_2PtCl_6 in 2 M HCl. The potential was held at –0.2 V vs. SCE for 10 s before being cycled from –0.2 V to + 0.7 V to –0.2 V, at a scan rate of 200 mV s^{-1}. The counter electrode was Pt gauze (A = 4.0 cm^2). Shown above is the 10th scan. Scans 1 to 10 were reproducible. This voltammogram shows the onset of hydrogen evolution on gold at –0.25 V.

The deposition technique for platinum black developed on the gold wire (60 minutes at −0.6 V) was tried on the interdigitated gold electrode but proved to be too effective! It was found that the platinum black grew so well that the interdigitated gold fingers were short circuited. Additionally, the presence of *IR* drop meant that the rate of platinisation could not be controlled for a given potential. To counter this problem, it was decided that the platinum should be deposited galvanostically rather than potentiostatically. After considerable experimental work, a standard method was established. The interdigitated gold electrodes were immersed into the platinising solution (2% K_2PtCl_6 in 2 M HCl) and the potential was cycled at a scan rate of 200 mV s^{-1} between +0.6 V and –0.4 V for three cycles. After the third cycle the current was then maintained galvanostatically at 20 mA (15 min) to allow the platinum black to deposit. The platinised electrodes were then removed from the cell, washed with deionised water and acetonitrile, and dried.

A voltammogram illustrating the success of the final method is given in ***Figure 7.16***. By integrating the area under the hydrogen adsoption/desorption peaks, the charge was calculated to be 2.7 mC (11.8 cm^2), approximately twenty five times greater than the charge before platinisation (0.1 mC, 0.435 cm^2). This means that the impedance of the electrode has

been decreased by a factor of twenty five, enough to ensure that the conductivity of the solution can be accurately measured. A photograph of a platinised interdigitated gold (PIG) electrode is shown in ***Figure 7.17***.

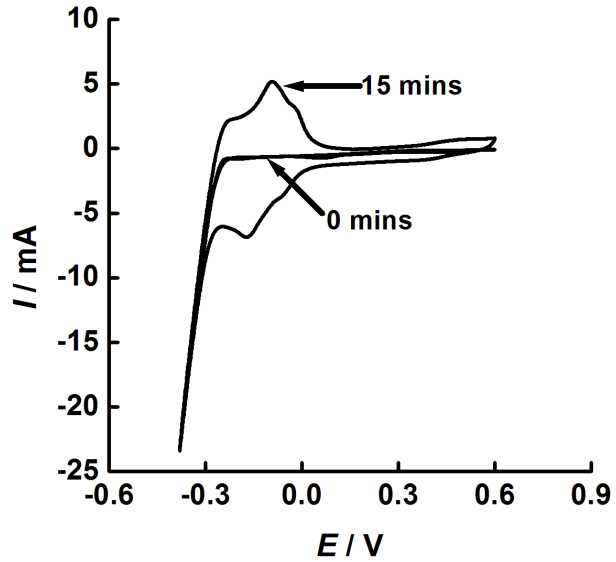

Figure 7.16 – Voltammetry of a platinised interdigitated array electrode in a solution of 2% K_2PtCl_6 in 2 M HCl. The potential was held at +0.6 V vs. SCE for 10 s before being cycled from +0.6 V to –0.4 V to +0.6 V, at a scan rate of 200 mV s^{-1}. The counter electrode was Pt gauze (A = 4.0 cm^2). After three cycles, the current was maintained galvanostatically at 20 mA (15 min), before removing the electrodes from the cell. The final cycle, after the 15 minute deposition is labelled as "15 mins". The accessible area increased by a factor of twenty five following platinisation (2.7 mC, 11.8 cm^2 compared with 0.1 mC, 0.435 cm^2)

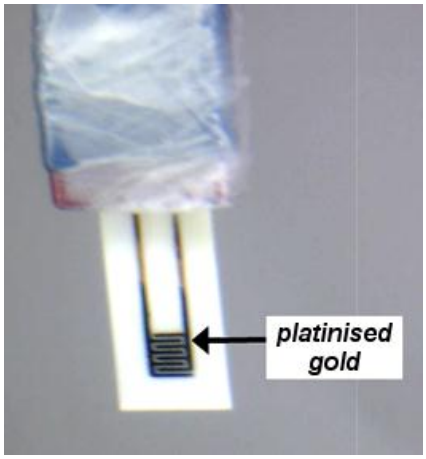

Figure 7.17 – The final product: a platinised interdigitated gold electrode.

SEM images of the finished electrodes were recorded and some of these images are presented in ***Figure 7.18***, ***Figure 7.19***, and ***Figure 7.20***. Because the alumina substrate was insulating it had to be coated with a very thin (nanometer) film of gold/palladium alloy prior to imaging to prevent electrostatic charging. This treatment is invisible at the magnification used. Further SEM images obtained for the early platinisation work on wire electrodes are shown in ***Appendix 7A***.

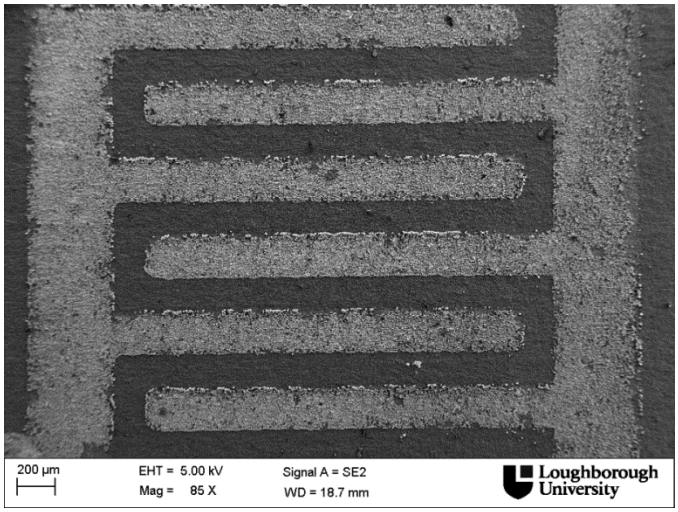

Figure 7.18 – An SEM image of an interdigitated gold electrode after platinisation (20 mA, 15 min). The scale bar is 200 µm. The lighter area is platinum black

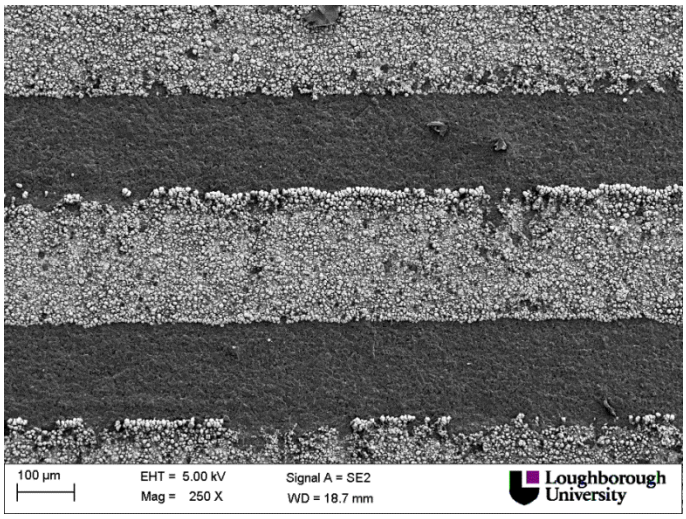

Figure 7.19 – An SEM image of an interdigitated gold electrode after platinisation (20 mA, 15 min). The scale bar is 100 µm. The lighter area is platinum black.

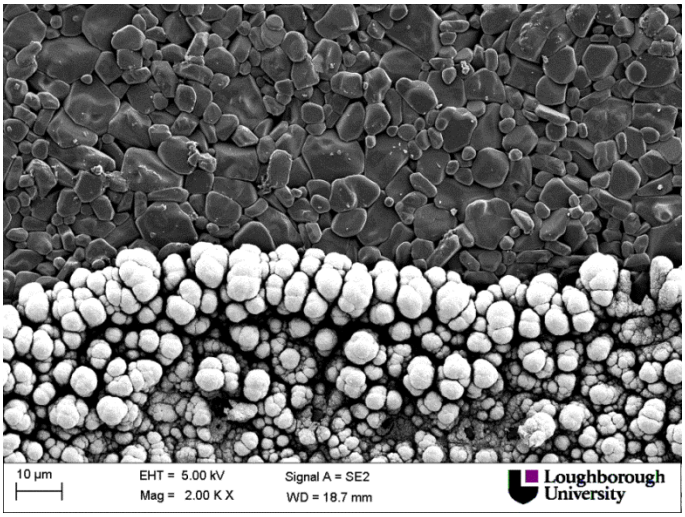

Figure 7.20 −A close-up of an interdigitated gold electrode after 15 min platinisation at 20 mA. The scale bar is 10 µm. Some enhanced deposition of platinum black is visible at the boundary. The lighter area is platinum black

7.4 – Conductivity measurements of ionic liquids using the new probe

As mentioned earlier, a big disadvantage of using a commercial conductivity probe for measuring the conductivity of an expensive solvent is that a large sample volume is required. To solve this problem, the feasibility of using the PIG electrodes to measure the conductivity of small droplets of ionic liquids (<2 ml) was investigated.

For droplet measurements, the PIG electrode was clamped in a horizontal position and a single droplet of ionic liquid was pipetted onto its surface as shown in ***Figure 7.21 (top)***. The volume of the droplet was sufficient to cover all of the array. Alternatively, the PIG electrode could be immersed into a test tube containing approximately 2 ml of ionic liquid. A temperature probe (Pt100) was placed as close to the electrode as possible, and temperature was logged every two seconds using a P755-log digital thermometer *via* a USB interface ***Figure 7.21 (bottom)***. Capacitance, impedance and phase angle values were also recorded every two seconds using a Wayne-Kerr Precision Component Analyser (6430 A) connected to the PIG electrode *via* a GPIB interface. Temperature, and the aforementioned parameters were logged for $t \geq 1$ h (1800 data points), and averaged to minimise random noise. The cell constant for the platinised interdigitated gold electrode was calculated to be 0.983 cm^{-1} (for method see ***section 6.3.3***), and the optimum frequency for measurements was determined to be 10 kHz (for method see ***section 6.3.4***). The supporting graphs are found in ***Appendix 7B***.

The ionic liquids measured were hexyltriethylammonium bis(trifluoromethylsulfonyl)imide (HTE) and butyltrimethylammonium bis(trifluoromethylsulfonyl)imide (BTM). This was because high precision conductivity data had already been recorded for these two ionic liquids using a macroscopic conductivity probe (027-013, Jenway) in ***Chapter 6*** and these data could be used for comparison to assess the performance of the PIG electrode.

Figure 7.21 – A photograph illustrating the set-up for measuring the conductivity of an ionic liquid in a single droplet (top) and a small sample volume (bottom) using a PIG electrode.

Table 7.3 provides a summary of the conductivity values and other measured parameters. Note that all values are an average of the data collected over one hour. Literature values are also provided for reference. It can be seen that the conductivity values measured with the PIG electrodes correspond closely with those measured using a commercial conductivity probe. Resistance and stray capacitance values were also similar. In part, this is due to the fact that the cell constants are similar in the two cases (0.983 cm^{-1} *vs.* 1.014 cm^{-1} respectively).

However, it is also testimony to the effectiveness of the platinisation process. The results are also consistent with literature data. The source of some minor discrepancies is unknown, but may be connected with poor temperature control by other workers.

Table 7.3 – Experimental results showing data obtained using a platinised interdigitated gold electrode and a single droplet of BTM and HTE ionic liquid, as well as comparison data obtained by other methods. Here κ (mS cm^{-1}) is the conductivity, R (Ω) is the resistance, T (°C) is the temperature, θ (°) is the phase angle, and C_2 (nF) is the stray capacitance. All experimental values are an average of data collected over 1 h (1800 data points).

	Hexyltriethylammonium bis(trifluoromethylsulfonyl)imide (HTE)			
	PIG droplet	**PIG (< 2ml)**	**Jenway (> 10 ml)**	**Literature**
***T* / ºC**	25.08	25.13	25.05	25
κ / mS cm^{-1}	0.89	0.89	0.83	0.67[16]
***R* / kΩ**	1.1	1.11	1.22	–
C_2 / nF	297	315	562	–
θ / º	2.8	2.62	1.33	–
	Butyltrimethylammonium bis(trifluoromethylsulfonyl)imide (BTM)			
	PIG (droplet)	**PIG (< 2 ml)**	**Jenway (> 10 ml)**	**Literature**
***T* / ºC**	24.97	25.03	25.07	25
κ / mS cm^{-1}	2.02	1.92	2.13	1.72[17] 2.1[18]
***R* / kΩ**	0.48	0.53	0.47	–
C_2 / nF	676	590	2260	–
θ / º	2.79	2.94	0.84	–

7.5 –Temperature dependence of conductivity using the new probe

After demonstrating that the miniature PIG electrodes were able to measure conductivity in ionic liquids (with values comparable to those of a commercial conductivity probe), it was decided to investigate whether they could also be used to determine the dependence of conductivity on temperature. The same experimental conditions were used as described in ***section 6.3.2***. The only difference was that, here, the conductivity probe was the newly developed PIG electrode, and so a smaller volume of ionic liquid was required (< 2 ml). The temperature range of measurements was 25 °C to 100 °C (293 K to 373 K). As a newly platinised interdigitated gold electrode was used for these measurements, the cell constant had to be recalculated. It was found to be 0.749 cm^{-1}. Once data had been collected, the glass transition temperature was estimated *via* the Vogel-Tammann-Fulcher equation. The ionic liquid was hexyltriethylammonium bis(trifluoromethylsulfonyl)imide (HTE). The

conductivity *vs*. temperature profile is given in ***Figure 7.22***, the trial-and-error fit is given in ***Figure 7.23*** and the global optimum fit of the VTF function over the temperature range 20 °C to 100 °C (293 K to 373 K) is shown in ***Figure 7.24***. The T_0 value was 193 K.

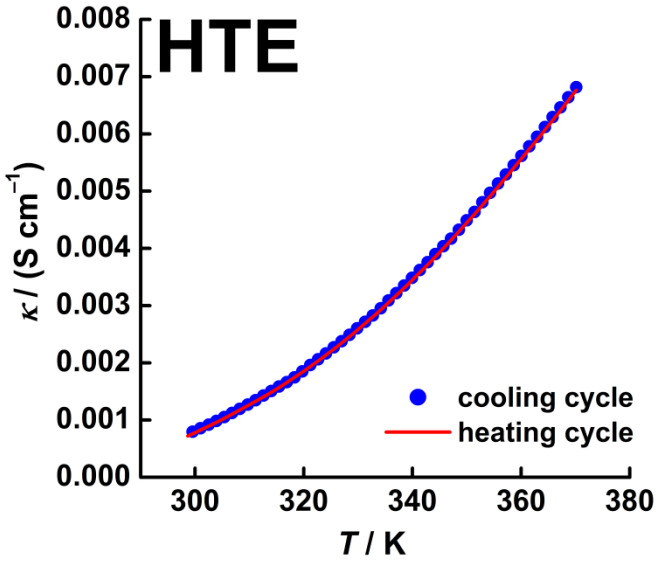

Figure 7.22 – A plot of conductivity (S cm^{-1}) vs. temperature (K) for the heating (red) and cooling (blue) cycles of a miniature PIG electrode in hexyltriethylammonium bis(trifluoromethylsulfonyl)imide over the temperature range (293 K to 373 K). Ramp speed was 0.1 °C min^{-1}. The overlapping plots show that there is no thermal hysteresis. Note for clarity, only 50 points from the cooling cycle have been displayed.

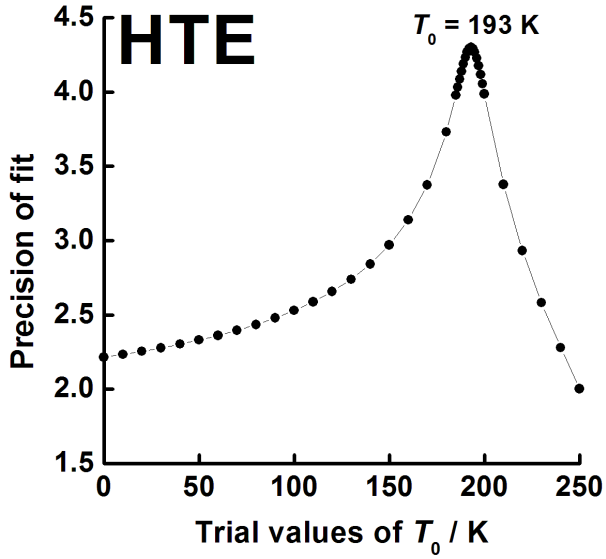

Figure 7.23 – A plot of precision-of-fit vs. trial values of T_0 (0 K to 250 K), for the heating cycles of a miniature PIG electrode in hexyltriethylammonium bis(trifluoromethylsulfonyl)imide. The T_0 with the most precise fit (R^2 = 0.99995) is labelled.

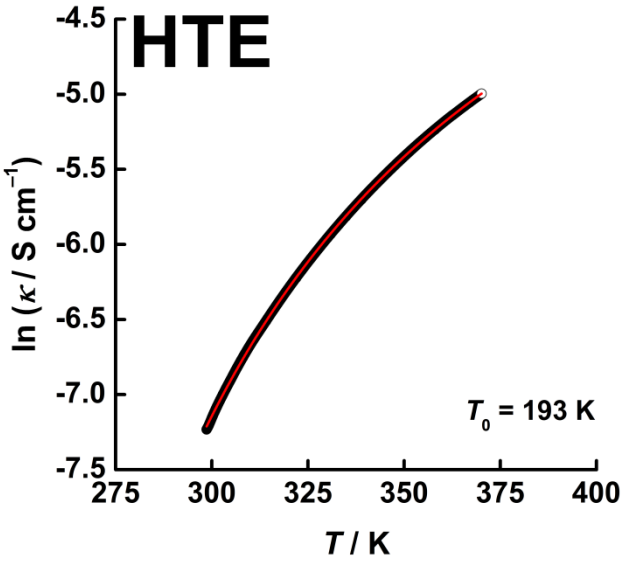

Figure 7.24 – A plot of ln κ (S cm^{-1}) vs. T (K) for the heating cycles of a PIG electrode in hexyltriethylammonium bis(trifluoromethylsulfonyl)imide over the temperature range 293 K to 373 K. Experimental data (black), best fit (red). R^2 = 0.99995.

It can be seen from ***Table 7.4*** that the T_0 value obtained using the interdigitated probe is in strong agreement (±3 K) with the value obtained for the commercial conductivity probe (027-013, Jenway). However, the precision-of-fit is reduced. The difference is more than likely due to the fact that the conductivity data recorded using the commercial conductivity probe were collected over a larger temperature range so a more accurate fit was possible.

Table 7.4 – Summary of T_0 values obtained by trial-and-error fitting to conductivity data obtained in hexyltriethylammonium bis(trifluoromethylsulfonyl)imide with a platinised interdigitated gold electrode and a commercial conductivity probe.

	Hexyltriethylammonium bis(trifluoromethylsulfonyl)imide			
	Interdigitated probe		**Commercial probe**	
	T_0 / K	***R^2***	***T_0 / K***	***R^2***
Trial-and-error method	193	0.99995	190	0.9999992

7.6 – Conclusion

A new conductivity probe for measuring the conductivity of a low sample volume of ionic liquid has been developed. The conductivity probe consists of two platinised gold electrodes arranged in a fixed interdigitated geometry, backed onto an alumina substrate. Considerable effort was expended on the development and optimisation of the platinum deposition process, which was important for minimising the impedance of the electrodes. The final deposition technique was 20 mA for 15 min on an electrode area of 0.435 cm^2 in 2% K_2PtCl_6 in 2 M HCl. The interfacial impedance decreased by a factor of twenty five. The success of the final deposition technique was confirmed by cyclic voltammetry and SEM imaging.

The ability of the platinised interdigitated electrodes (PIG electrodes) to measure the conductivity of a single droplet of ionic liquid was tested and confirmed by comparing results with those obtained using a commercial apparatus. The two test ionic liquids were hexyltriethylammonium bis(trifluoromethylsulfonyl)imide and butyltrimethylammonium bis(trifluoromethylsulfonyl)imide. Their conductivities were measured to be 0.89 mS cm^{-1} and 2.02 mS cm^{-1} using the PIG electrode, and 0.83 mS cm^{-1} and 2.13 mS cm^{-1} using the commercial apparatus, respectively.

The PIG electrode was also able to measure the relationship between temperature and conductivity (20 to 100 ºC) in a small sample volume (< 2ml) of hexyltriethylammonium bis(trifluoromethylsulfonyl)imide. The derived glass transition temperature (193 K) corresponded closely with that obtained using the commercial apparatus (190 K).

7.7 – References

[1] Deutscher, R. L. & Fletcher, S. *Nucleation on active sites. Part IV. Invention of electronic method of counting the number of crystals as a function of time; and the discovery of the nucleation rate dispersion*. Journal of Electroanalytical Chemistry, 239: 705-739 (2010).

[2] Rieger, P. H. *Electrochemistry*, 2nd Edition, Chapman & Hall, USA, pp438-448 (1994).

[3] Feltham, A. M. & Spiro, M. *Platinised platinum electrodes*. Chemical Reviews, 71: 177-193 (1971).

[4] Mills, A. *Porous Platinum Morphologies: Platinised, Sponge and Black.* Platinum Metals Review, 51: 52 (2007).

[5] Daniels, F., Matthews, J. H., Williams, J. W., Bender, P. & Alberty, R. A. *Experimental Physical Chemistry*, 5th Edition, McGraw-Hill: New York, pp177 (1956).

[6] Shoemaker, D. P. & Garland, C. W. *Experiments in Physical Chemistry*. McGraw-Hill: New York, Chapter 10, pp444 (1962).

[7] Findlay, A. & Kitchener, J. A. *Practical Physical Chemistry*. 8th Edition, Green and Co: London, pp206 (1954).

[8] Kurlbaum, F. & Lummer, O. Deutsche Physikalische Gesellschaft zu Berlin, 14: 56 (1985).

[9] Bates, R. G. *Determination of pH*, Wiley: New York, pp242 (1964).

[10] Hills, G. J. & Ives, D. J .G. *The Hydrogen-Calomel Cell*. Journal of the Chemical Society**,** 305-310 (1951).

[11] Conway, B. E. & Angerstein-Kozlowska, H. *Electrochemical Study of Multiple-State Adsorption in Monolayers*. Accounts of Chemical Research, 14: 49-56 (1981).

[12] Frelink, T., Visscher, W. & Van Veen, J. A. R. The third anodic hydrogen peak on platinum; surface hydrogen adsorption. Electrochemica Acta, 40**:** 545-549 (1995).

[13] Gileadi, E. *Physical Electrochemistry: Fundamentals, Techniques, Applications*. Wiley-VCH: Weinheim, Germany, pp172 (2011).

[14] Ives, D. J .G. & Janz, G. J. *Reference Electrodes, Theory and Practice*, Academic Press: New York & London, pp107 (1961).

[15] Lide, D. R (Editor). *Handbook of Chemistry and Physics*. 81st Edition. CRC Press: Boca Raton, Florida, USA, in *Melting, Boiling, and Critical Temperature of the Elements*, 4-124 (2000-2001).

[16] Sun, J., McFarlane, D. R. & Forsyth, M. *Synthesis and Properties of Ambient Temperature Molten Salts Based on the Quaternary Ammonium Ion*. Ionics, 3: 356-362 (1997).

[17]http://www.carlroth.com/catalogue/catalogue.do?favOid=000000080003c7e500020023&act=showBookmark&lang=en-com&market=COM (last accessed 15th March 2013).

[18] Tokuda, H., Tsuzuki, S. Susan, M. A. B. H, Hayamizu, K. & Watanabe, M. *How Ionic Are Room-Temperature Ionic Liquids? An Indicator of the Physicochemical Properties*. Journal of Physical Chemistry B, 39: 19593–19600 (2006).

Chapter 8 – Interfacial Capacitance of Porous Electrodes

8.1 – Equivalent circuits

A well-known method of analysing complex electrochemical systems is to model them using *equivalent circuits*. An equivalent circuit is a theoretical construct that generates the same output as a real system under a given set of conditions. Unfortunately, different standards for the "given set of conditions" have arisen in different disciplines, creating some subtle differences of interpretation between electrical engineers and electrochemists.

In electrical engineering, the phrase "equivalent circuit" generally refers to a simple series or parallel combination of two components (such as a resistor and a capacitor) that duplicates the response of a real system at a single specified frequency. An example is shown in ***Figure 8.1***. In this case, there is no requirement that the equivalent circuit should match the amplitude and phase shift of the real system at any other frequency.

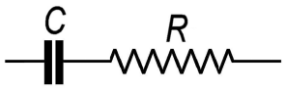

Figure 8.1 – An example of an "engineering" equivalent circuit. At each frequency, the quasi-capacitance and quasi-resistance values are adjusted to match the phase shifts of a real system.

Experimentally, the matching of a two-component equivalent circuit to a real system at one frequency is readily carried out by means of a "Wien bridge". This is a type of bridge circuit that was developed by Max Wien in 1891[1], and which allows the experimenter to treat *C* and *R* as fitting parameters.

In electrochemistry, the phrase "equivalent circuit" has a different meaning. It generally refers to a large multi-component network that duplicates the response of a real system over a wide range of frequencies. Although there is no restriction on the size of such networks, electrochemists generally apply Occam's Razor[2], and so do not insert more model components than there are physical phenomena to be explained. In the engineering case, it is

understood that the notional values of the model components may vary with frequency; but in the electrochemical case this is strictly forbidden.

The existence of two different approaches to equivalent circuits naturally raises questions of authenticity about the model components and their values. Consider, for example, a complicated real system having a true physical capacitance embedded somewhere inside it. An explicit formula for this latter quantity is always derivable by Gauss's law, which states that the stored charge Q is equal to the integral of the normal component of the local electric field $\vec{E}$ (a vector) over the area $\vec{A}$, multiplied by the local permittivity ε.

$$Q = \oint \varepsilon \vec{E} \cdot d\vec{A}$$

Equation 8.1

Accordingly, the ratio $Q/V = C_{\text{real}}$ is the true parameter of interest, which for a flat interface of thickness *d* takes the form

$$C_{\text{real}} = \frac{\varepsilon A}{d}$$

Equation 8.2

However, only a proper electrochemical equivalent circuit will successfully identify this quantity. An engineering equivalent circuit will fail to do so, because it contains a *fictional* capacitance (hereafter referred to as a *quasi*-capacitance) whose sole purpose is to match the phase shifts of the real system (see ***Figure 8.1***). Thus, the engineering quasi-capacitance is not necessarily real. Indeed, for the equivalent circuit shown in ***Figure 8.1*** it is simply the mathematical quantity

$$C_{\text{quasi}}(\omega) = \frac{1}{j\omega(\tilde{Z} - R)}$$

Equation 8.3

where $\tilde{Z}$ is the complex impedance of the real system, and R is the value of the resistor in the equivalent circuit. Note that, unlike the real physical capacitance, the quasi-capacitance derived from a simple "engineering" equivalent circuit may be (usually is) frequency dependent. This unphysical result arises because the quasi-capacitance is compelled to follow

the response of the system as a whole, not just the response of the isolated capacitor. Consequently,

$$C_{\text{quasi}}(\omega) \neq \frac{\varepsilon A}{d}$$

Equation 8.4

As a result of these considerations, literature plots of "capacitance" versus "surface area" should be treated with considerable scepticism unless the authors have defined exactly what they mean by "capacitance" and have also demonstrated that this same "capacitance" is not frequency dependent.

It is clear from the above discussion that two different approaches to "equivalent circuits" are in common use, and these generate two different values of "capacitance" for the same real system. On one hand, there is a two-component ("engineering") equivalent circuit that generates a frequency-dependent quasi-capacitance whose properties may sometimes violate common sense. And on the other hand, there is a multiple-component ("electrochemical") equivalent circuit that generates a frequency-independent true capacitance whose properties are well-behaved. It is particularly unfortunate that, in the scientific literature, authors do not always specify which approach is being used. For example, the capacitance derived by measuring the baseline hysteresis of voltammograms is nearly always a quasi-capacitance, yet this is rarely (if ever) mentioned to the reader. Similar considerations apply to capacitance measurements carried out by bridge methods.

8.2 – Equivalent circuit of carbon supercapacitors

In commercial supercapacitors, porous electrodes are used to increase the rates of interfacial charging between electron-conducting solids and ion-conducting solutions. However, increasing the surface area of any solid at fixed volume means decreasing the average diameter of its pores, leading to increased pore impedance. Therefore, when designing supercapacitors, an important consideration is the trade-off between the total capacitance of the interface and the electrical impedance of the pores.

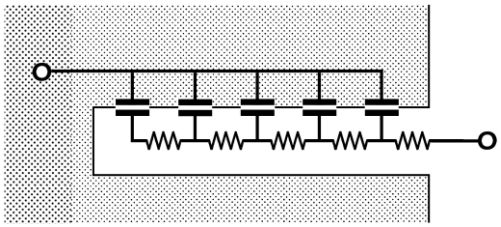

Figure 8.2 – The standard finite ladder network model of a single pore (transmission line model).The resistors and capacitors may all have different values.

The impedance of a single pore, in the case of an interface that is blocking to charge transfer, has been very widely studied. The standard model is a finite ladder network (transmission line) as shown in ***Figure 8.2***. In the scientific literature, this "single pore model" has been successfully applied to the charge/discharge behaviour of a range of homogeneous materials, including conducting polymer electrodes[3], dye-sensitized solar cells[4], and numerous corrosion systems[5].

Despite its great utility in the modelling of homogeneous phases, the single pore model fails in the case of highly heterogeneous materials (such as activated carbons) because the latter contain multitudes of pores of different lengths and diameters, all acting in parallel. Although this random arrangement of pores is easy to picture, its behaviour is very difficult to capture in a model, and so it has become a severe obstacle to the development of improved theory.

In 1994 Fletcher[6] published a series of tables of degenerate electrical networks for use in the equivalent circuit analysis of electrochemical systems. (Electrical networks are said to be degenerate if they exhibit identical total impedances at all frequencies.) Among the results presented by Fletcher was the one shown in ***Figure 8.3***.

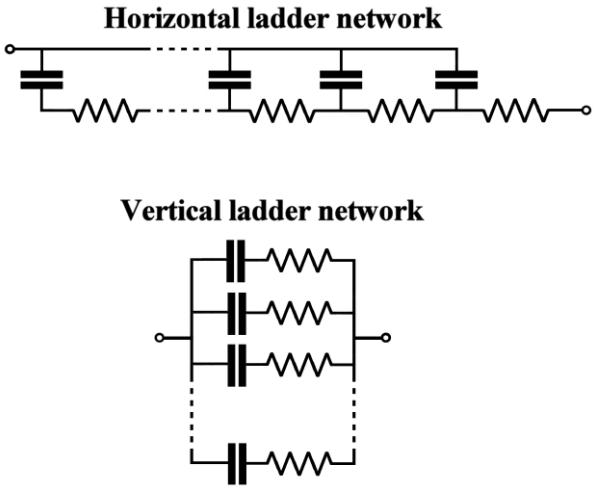

Figure 8.3 – A horizontal ladder network and its vertical equivalent[6]. The resistors and capacitors may have very wide ranges of different values.

Fletcher's result is of special interest in the present work because it shows that any conceivable arrangement of horizontal ladder networks wired in parallel is necessarily degenerate with a simple vertical ladder network. In other words, the vertical ladder network can be regarded as a *Universal Equivalent Circuit* for conducting porous solids such as activated carbon. Based on this novel insight, a high-precision equivalent circuit of an assembled symmetric supercapacitor can readily be devised, and this is shown in ***Figure 8.4***. It consists of a vertical ladder network of *RC*-series components, each of which has a different time constant from the others, and a solitary *RC*-parallel network (on the right-hand side of the diagram) which represents the resistance of the bulk of solution shunted by the dielectric polarization of the solution.

At this point, the reader must be cautioned against over-simplistic interpretation of the model shown in ***Figure 8.4***. It is certainly true that each capacitor is related to the capacitance of a patch of pore wall, and each resistor is related to the resistance of a length of pore channel, but the relationship is not necessarily one-to-one with the real physical values. More precisely, the proposed equivalent circuit is degenerate with another equivalent circuit (a random set of finite-length transmission lines in parallel) which *does* have a one-to-one correspondence with real physical values. Note that the vertical ladder network cannot extend to infinity because it is not possible to have infinite capacitance in a finite space. (It is, however, possible for some of the charging processes to occur arbitrarily slowly due to the high resistance of some of the pathways.)

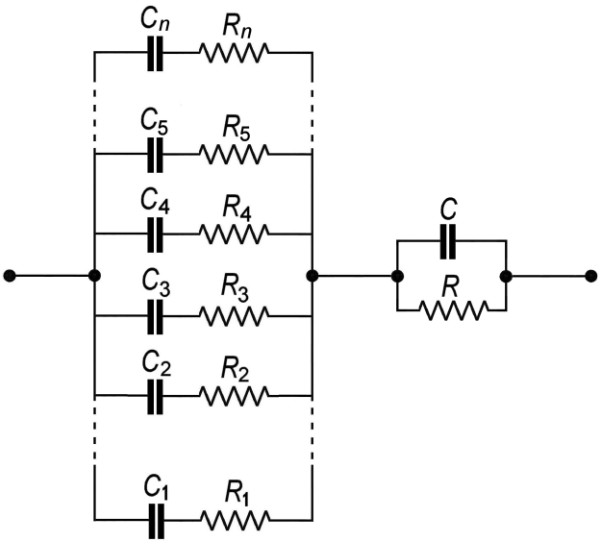

Figure 8.4 – Equivalent circuit of a symmetric supercapacitor for the case of activated carbon electrodes. It consists of the Universal Equivalent Circuit for a conducting porous solid (left) plus a simple RC-parallel network for the bulk of solution (right).

In supercapacitor devices, the resistance of solid carbon is generally insignificant compared with the resistance of liquid-filled pores, so it is the pores that control the *RC* time constants in the system. For example, the conductivity of basal plane graphite is about 3×10^3 S cm^{-1} at 25 °C, that of turbostratic graphite (glassy carbon) is about 0.6×10^3 S cm^{-1}, and the conductivity of activated carbon is about 0.06×10^3 S cm^{-1}. By comparison, the conductivity of a typical room-temperature ionic liquid such as BTM (butyltrimethylammonium bis(trifluoromethylsulfonyl)imide) is only 2.1×10^{-3} S cm^{-1}. Hence the pores containing ionic liquid are more resistive than the pore walls by a factor of 30,000 or so.

In most practical supercapacitors (whether aqueous, organic, or ionic liquid) the solitary *RC*-parallel network on the right-hand side of ***Figure 8.4*** dominates the impedance response at high frequencies (>10 kHz, say) whereas the vertical ladder network dominates the impedance response at low frequencies. In the latter case, a complex mixture of responses is observed because the time constants of the "rungs" of the ladder network are typically distributed over logarithmic timescales, from milliseconds to minutes. The origins of this distribution are mysterious, but possible explanations include the presence of bottleneck pores that have a range of different "access resistances", the existence of molecular-scale

heterogeneities (both chemical and physical) at the electrode surface, and the occurrence of anomalous diffusion/migration processes within nanopores.

In a few supercapacitors, a crude linear segment is observed in the complex plane of impedance at a fixed angle to the real axis. The general idea is illustrated in ***Figure 8.5***. In such cases, over the range of frequencies corresponding to the segment, the finite ladder network is indistinguishable from a well-known infinite ladder network known as a "constant phase element" (CPE). The mathematical form of the impedance of this element is given by:

$$Z = \frac{1}{T(j\omega)^p}$$

Equation 8.5

where Z is the complex impedance, ω is the radial frequency, and $j = \sqrt{-1}$. The terms T and p are constants. The corresponding phase angle is $-(90p)$ degrees, as observed. In the majority of cases, however, no linear segment is observed in the complex plane of impedance, and this approximation fails.

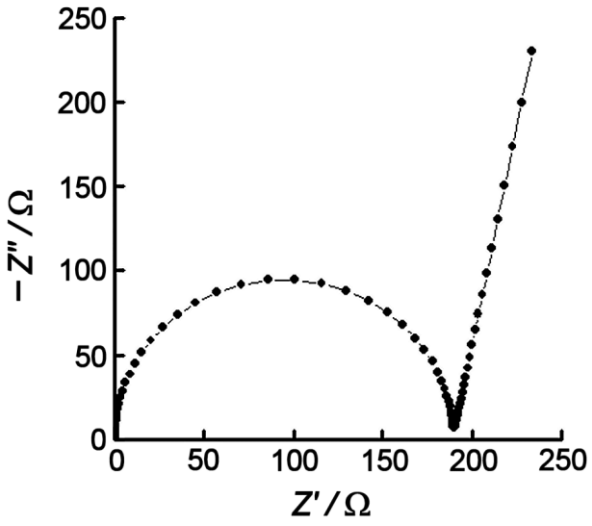

Figure 8.5 – Complex plane impedance plot of a model circuit consisting of a CPE in series with an RC-parallel network. Frequency range 100 Hz to 1 GHz, CPE-T = 1.1 × 10^{-5} F, CPE-P = 0.87, R = 190 Ω and C = 9.4 × 10^{-10} F.

Interestingly, when subjected to an electrical perturbation, the finite ladder network behaves differently at short and long times. At short times (high frequencies) no voltage develops across the capacitors, and the ladder network behaves as *n* resistors in parallel. But at long times (low frequencies) a voltage does develop across the capacitors, and the system behaves as a single, total capacitance of value

$$C_{\text{real}} = \sum_{1}^{\infty} C_1 + C_2 + C_3 + \cdots$$

Equation 8.6

This is the largest value of capacitance that can be measured on a supercapacitor, and tends to be the one quoted by manufacturers. Naturally it should not be mistaken for the value of quasi-capacitance that is actually available on a given time scale (and which is always smaller than C_{real}).

8.3 – Quasi-capacitance and the distribution of capacitive states

The presence of a vertical ladder network in an electrochemical equivalent circuit signifies the existence of a distribution of time-constants in the real system. ***Figure 8.6*** shows what a finite ladder network looks like when the "rungs" of the ladder are ordered in terms of their time constants $\tau_1 < \tau_2 < \tau_3$ ... As time progresses, the capacitors charge sequentially from bottom to top. Hereafter, this phenomenon is referred to as *asynchronous charging*.

Asynchronous charging creates the illusion that the electrode capacitance is larger at longer times (i.e. larger at smaller scan rates) as illustrated in ***Figure 8.7*** and ***Figure 8.8***. In impedance measurements it also makes the quasi-capacitance appear larger at lower frequencies (***Figure 8.9***). Strictly speaking, none of these effects is real, because the quasi-capacitance is not the real capacitance. However, on any given timescale, it is only the quasi-capacitance that can be measured, and it is only the quasi-capacitance that can do useful work.

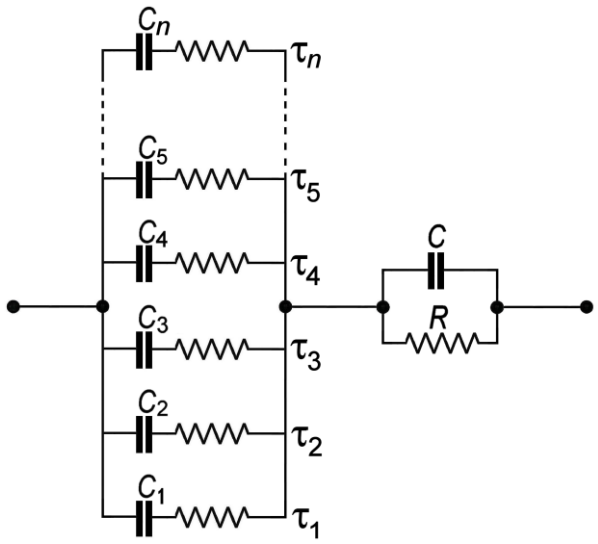

Figure 8.6 – The finite ladder network of a symmetric supercapacitor, arranged according to the sequence of time-constants $\tau_1 < \tau_2 < \tau_3$ ... The capacitors charge up in the sequence C_1, C_2, C_3..., creating the illusion that the electrode capacitance is larger at smaller scan rates.

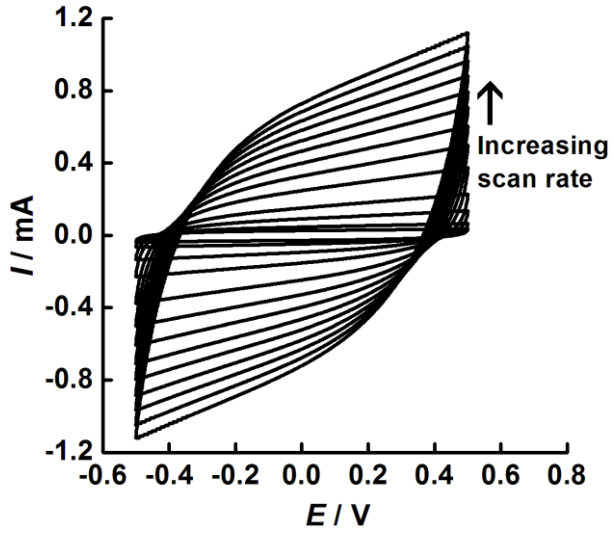

Figure 8.7 – Cyclic voltammograms of an ionic liquid-based supercapacitor. Electrodes: Activated carbon (100 µm x 1 cm^2). Solvent: Butyltrimethylammonium bis(trifluoromethylsulfonyl)imide. Temperature: 25 ºC. Scan rates: 1, 2, 5, 10, 20, 30, 40, 50, 60, 70, 80, 90, and 100 mV s^{-1}.

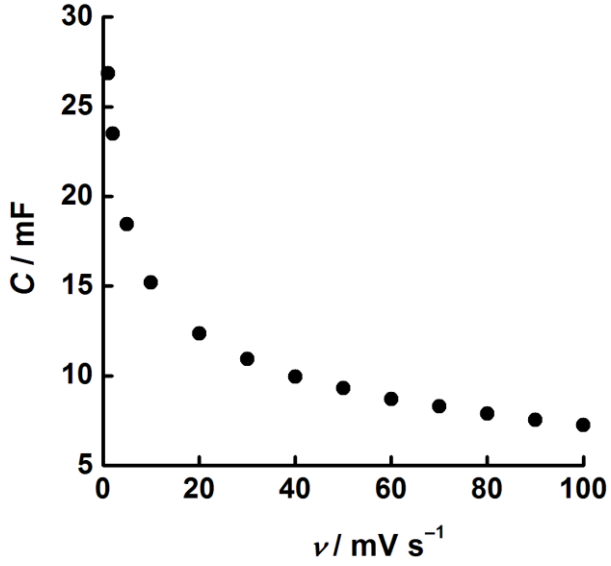

Figure 8.8 – The dependence of the quasi-capacitance (mF) on the scan rate (mV s^{-1}) for an ionic liquid-based supercapacitor, assuming a single RC-series model circuit. Electrodes: Activated carbon (100µm × 1cm^2). Solvent: Butyltrimethylammonium bis(trifluoromethylsulfonyl)imide. Temperature: 25 ºC. Scan rates: 1, 2, 5, 10, 20, 30, 40, 50, 60, 70, 80, 90, and 100 mV s^{-1}.

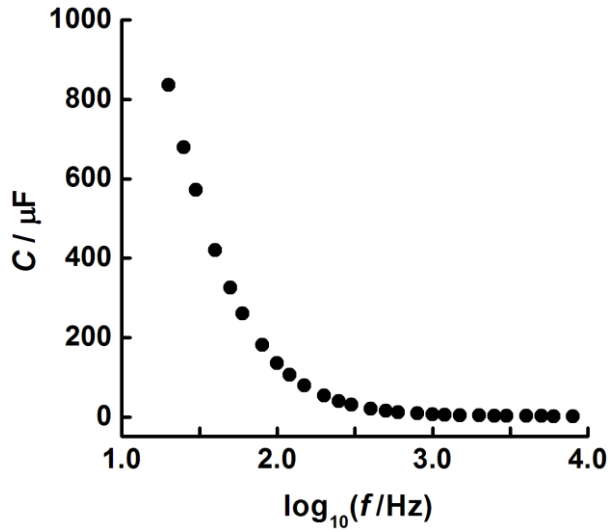

Figure 8.9 – The dependence of the quasi-capacitance (µF) on log_{10} (frequency/Hz) for an ionic liquid-based supercapacitor, assuming a single RC-series model circuit. Electrodes: Activated carbon (100µm × 1cm^2). Solvent: Butyltrimethylammonium bis(trifluoromethylsulfonyl)imide. Temperature: 25 ºC. Amplitude: 100 mV. Data recorded using a Wayne-Kerr Precision Component Analyser 6430 A.

Finally, the existence of asynchronous charging also explains why quasi-capacitance is larger at higher temperatures (***Figure 8.10***). Since real capacitance can only become smaller at higher temperature (because the temperature coefficient of the dielectric constant is always negative) the widely observed increase in capacitance has struck many researchers as anomalous. However, the effect is now explained by focussing on the decrease in resistance as the temperature is raised. This causes the distributed *RC* time constants to decrease, and thus causes the number of capacitors that can charge in a fixed period of time to *increase*.

As noted elsewhere in this thesis, the temperature variation of ionic resistivity is very large in ionic liquids, because of the non-linearity of the Vogel-Tammann-Fulcher relation. For example, the resistivity of BTM (butyltrimethylammonium bis(trifluoromethylsulfonyl)imide) decreases from 476 Ω cm at 25 ºC to 17.5 Ω cm at 200 ºC, a factor of nearly thirty. This precipitous fall causes a dramatic lowering of the *RC* time constants inside the electrodes, and hence a doubling of the quasi-capacitance.

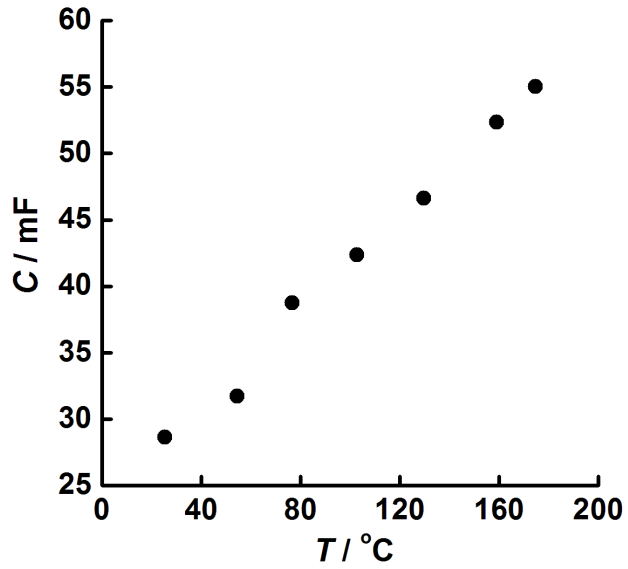

Figure 8.10 – The dependence of the measured capacitance (quasi-capacitance) on the temperature for an ionic liquid-based supercapacitor, assuming a single RC-series model circuit. Electrodes: Activated carbon (100µm × 1cm^2). Solvent: Butyltrimethylammonium bis(trifluoromethyl-sulfonyl)imide. Voltammograms recorded at approximately 25 ºC intervals from 25 ºC to 200 ºC at 20 mV s^{-1}.

8.4 – Conclusion

From the present work it is clear that a deeper understanding of nanopore geometry and its influence on both capacitance and resistance will be essential to the future development of supercapacitors. The historical neglect of pore resistance as a design parameter must certainly be overcome, since this markedly influences the quasi-capacitance. In this regard, the new Universal Equivalent Circuit for conducting porous solids should play an important role.

8.5 – References

[1] Wien, M. *Messung der Inductionsconstanten mit dem "optischen Telephon"* (Measurement of Inductive Constants with the "Optical Telephone"). Annalen der Physik, 280: 689-712 (1891).

[2] Heather, M. & McIntosh, M. *Stanford Encyclopedia of Philosophy*. Stanford University, Stanford, CA (2005).

[3] Fletcher, S. *Contribution to the theory of conducting-polymer electrodes in electrolyte solutions*. Journal of the Chemical Society, Faraday Transactions, 89: 311-320 (1993).

[4] Bisquert, J. *Theory of the Impedance of Electron Diffusion and Recombination in a Thin Layer*. Journal of Physical Chemistry B, 106: 325-333 (2002).

[5] Macdonald, D, D. *Why electrochemical impedance spectroscopy is the ultimate tool in mechanistic analysis*, Electrochemical Society Transactions, 19: 55-79 (2009).

[6] Fletcher, S. *Tables of Degenerate Electrical Networks for Use in the Equivalent Circuit Analysis of Electrochemical Systems*. Journal of the Electrochemical Society, 141: 1823-1826 (1994).

Chapter 9 – High Temperature Supercapacitors

9.1 – Introduction

At the present time, an important industrial goal is the development of new energy storage technologies for next-generation oilfield tools, in particular for down-hole applications. However, the storage and transmission of energy to operate such tools is hampered by the harsh environment. Temperatures greater than 220 °C can be encountered down-hole, and temperatures less than 25 ^{o}C can be encountered at start-up, so a high degree of tolerance to thermal extremes is required. In theory, supercapacitors offer an attractive option for high temperature usage due to their ability to deliver energy rapidly during periods of high power demand. In practice, however, very few tests have actually been carried out in the laboratory. In the present work, the feasibility of manufacturing high temperature supercapacitors that can operate at temperatures from 25 ^{o}C up to 220 ^{o}C has been demonstrated.

A supercapacitor consists of the following major components; two electrodes, an electrolyte, a separator, a cell body, and a cell sealant. For the task at hand, all of these had to be manufactured from thermally stable materials. In this chapter, the materials chosen for each component are discussed, along with methods for mitigating any problems.

9.2 – Materials for high temperature supercapacitors

9.2.1 – The electrolyte

The electrolyte is one of the main factors determining the electrical behaviour of a supercapacitor[1]. In general, the desired characteristics of a supercapacitor electrolyte are a large cell voltage to maximise energy storage and power output, good conductivity to allow fast charging/discharging, low cost for mass production, and low vapour pressure for safety. However, when designing a supercapacitor to operate at temperatures greater than two hundred degrees, the chemical stability of the electrolyte is paramount. Consequently, neither aqueous nor organic solvents are suitable for high temperature devices. Ionic liquids, on the other hand, have a range of suitable properties which include thermal stability, negligible vapour pressure, acceptable ionic conductivity (1-10 mS cm^{-1} at room temperature)[2] and

large voltage stability windows (> 4 V)[3]. They also have a wide liquid range, often >300 °C[3], which allows them to avoid phase transitions.

Due to the high importance of maintaining chemical stability at high temperature, the thermal analysis of a series of ionic liquids with different anion and cation pairings was performed by DSC (Q-1000, TA Instruments). A summary of the degradation onset temperatures is given in ***Table 9.1***. Plots of heat flow (W g^{-1}) *vs.* temperature (ºC) for all of the ionic liquids analysed are given in ***Appendix 9A***.

Table 9.1 – Thermal degradation temperatures of selected ionic liquids.

Ionic Liquid	Degradation onset temperature / ºC
Tetramethylammonium bis(trifluoromethylsulfonyl)imide (TMA)	426
1-Butyl-1-methylpyrrolidinium bis(trifluoromethylsulfonyl)imide (BMPY)	391
1-Ethyl-3-methylimidazolium triflate (EMIM TF)	374
Butyltrimethylammonium bis(trifluoromethylsulfonyl)imide (BTM TFSI)	371
Tetraethylammonium bis(trifluoromethylsulfonyl)imide (TEA)	362
Tetrapropylammonium bis(trifluoromethylsulfonyl)imide (TPA)	354
Tetrabutylammonium bis(trifluoromethylsulfonyl)imide	351
Hexyltriethylammonium bis(trifluoromethylsulfonyl)imide (HTE TFSI)	346
Tetrabutylphosphonium tetrafluoroborate	326
1-Butyl-3-methylimidazolium tetrafluoroborate (EMIM TFB)	325
1-Ethyl-3-methylimidazolium methanesulfonate (EMIM MS)	324
Tetrabutylammonium hexafluorophosphate (TBA)	248

It is evident from ***Table 9.1*** that all of the ionic liquids listed were thermally stable above 220 ºC. The most stable of all was tetramethylammonium bis(trifluoromethylsulfonyl)imide, but unfortunately this compound did not melt until 133 °C[4] which made it useless for a supercapacitor operating at room temperature. By contrast, butyltrimethylammonium bis(trifluoromethylsulfonyl)imide (BTM TFSI), and hexyltriethylammonium bis(trifluoro-methylsulfonyl)imide (HTE TFSI) both had melting points less than 25 ºC[5-6].

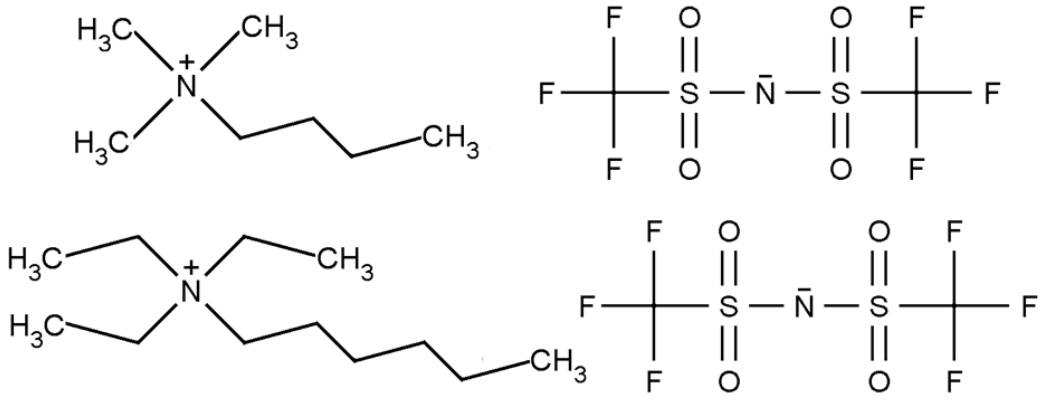

Figure 9.1 – Structural formulas of butyltrimethylammonium bistrifluoromethylsulfonyl)imide BTM TFSI (top) and hexyltriethylammonium bis(trifluoromethylsulfonyl)imide HTE TFSI (bottom).

The physical properties of BTM TFSI and HTE TFSI are given in ***Table 9.2***, and plots showing their thermal and electrochemical stabilities are given in ***Figures 9.2*** and ***9.3***. As noted in ***Chapter 4***, quaternary ammonium cations with long alkyl chains are able to resist electron tunnelling and also had wide voltage windows. In ***Chapter 6***, conductivity measurements showed that BTM TFSI was approximately three times more conducting than HTE TFSI at 25 °C, most likely due to its smaller cation size.

Table 9.2 – Physical properties of butyltrimethylammonium bis(trifluoromethylsulfonyl)imide and hexyltriethylammonium bis(trifluoromethylsulfonyl)imide. Viscosity, conductivity and voltage stability values were recorded at 25 °C. ***(–) indicates information not available.***

	Butyltrimethylammonium bis(trifluoromethylsulfonyl)imide	
	Literature	**Measured**
Melting point / °C	+19[6]/+21[7]	11
Degradation temperature / °C	–	> 300
Glass transition temperature / °C	–74[6]	–83 (VTF) –78 (DSC)
Viscosity / mPa s	116[7]	–
Conductivity / mS cm^{-1}	1.4[7]	2.1
Voltage stability window / V	4[7]	> 4

	Hexyltriethylammonium bis(trifluoromethylsulfonyl)imide.	
	Literature	**Measured**
Melting point / °C	+20[5]	5
Degradation temperature / °C	–	> 300
Glass transition temperature / °C	–81[5]	–86 (VTF) –85 (DSC)
Viscosity / mPa s	167[4]	–
Conductivity / mS cm^{-1}	0.67[5]	0.83
Voltage stability window / V	<4.5[4]	> 5

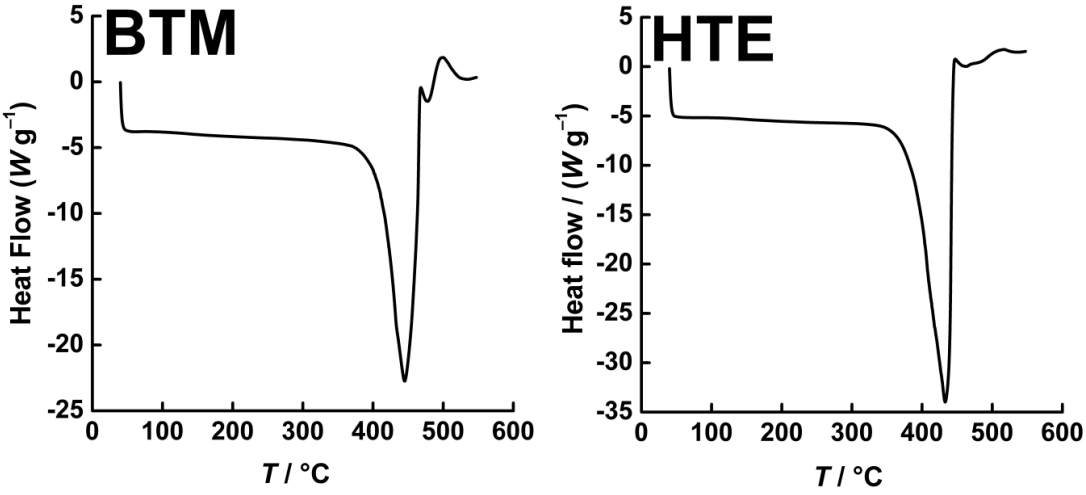

Figure 9.2 – Plots of heat flow (W g^{-1}) vs. temperature (ºC) for the ionic liquids butyltrimethylammonium bis(trifluoromethylsulfonyl)imide and hexyltriethylammonium bis(trifluoromethylsulfonyl)imide. The onset of thermal degradation occurs at ~370 ºC for BTM TFSI and ~346 ºC for HTE TFSI. Thermograms were recorded using a Q10 Differential Scanning Calorimeter (TA Instruments) under a nitrogen atmosphere (20 mL min^{-1}) from 40 ºC to 550 ºC at a rate of 10 ºC min^{-1}.

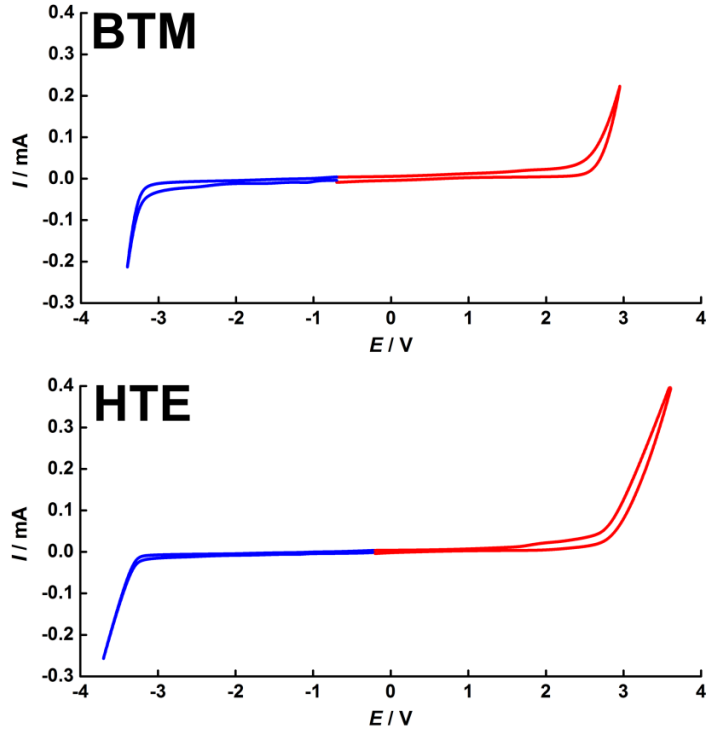

Figure 9.3 – Voltammograms showing the voltage stability windows of butyltrimethylammonium bis(trifluoromethylsulfonyl)imide (top) and hexyltriethylammonium bis(trifluoromethylsulfonyl)-imide (bottom). Cathodic and anodic scans were recorded separately. Scan rate was 100 mV s^{-1}. Working electrode was glassy carbon (d = 3.0 mm) press fitted in to a Teflon shroud, reference electrode was Ag|AgCl, and counter electrode was platinum gauze (A = 4.0 cm^2).

9.2.2 – Ionic liquid gels

Ionic liquids have low viscosity at high temperature (T > 220 ºC). In the event of device rupture, they can readily flow into areas where they are not wanted. To inhibit flow, fumed silica was trialled as a gelling agent. Fumed silica is an exceptionally pure form of silicon dioxide formed by flame hydrolysis of silicon tetrachloride at 1800 ºC[8].

$$SiCl_4 + 2H_2O \rightarrow SiO_2 + 4HCl \qquad \textbf{\textit{Equation 9.1}}$$

It is well known that paint can be gelled by the addition of fumed silica[8], however, there have only been a few scattered reports of ionic liquids being gelled in a similar way. Surprisingly, different authors have claimed to have successfully gelled ionic liquids using very different amounts of fumed silica, varying from 5% to as much as 50% by weight, and using silica particle sizes ranging from 7 nm to 100 μm[9-11]. In this study, it was found that fumed silica purchased from Sigma-Aldrich (S5130) having a primary particle size of 7 nm (BET > 350 $m^2\ g^{-1}$, m.p. 1600 ºC) was able to gel ionic liquids when added at the level of only 7.5% by weight. As a demonstration, ***Figure 9.4*** shows photographs taken after the addition of fumed silica to a commercial ionic liquid, triethylsulfonium bis(trifluoromethylsulfonyl)imide to create a free-standing gel. All ionic liquids tested including hexyltriethylammonium bis(trifluoromethylsulfonyl)imide and butyltrimethylammonium bis(trifluoromethylsulfonyl)imide exhibited the same behaviour. Thermal studies of ionic liquid gels showed that all gels were stable in a nitrogen atmosphere up to 250 ºC and those not containing sulfur were also stable in air (18 h).

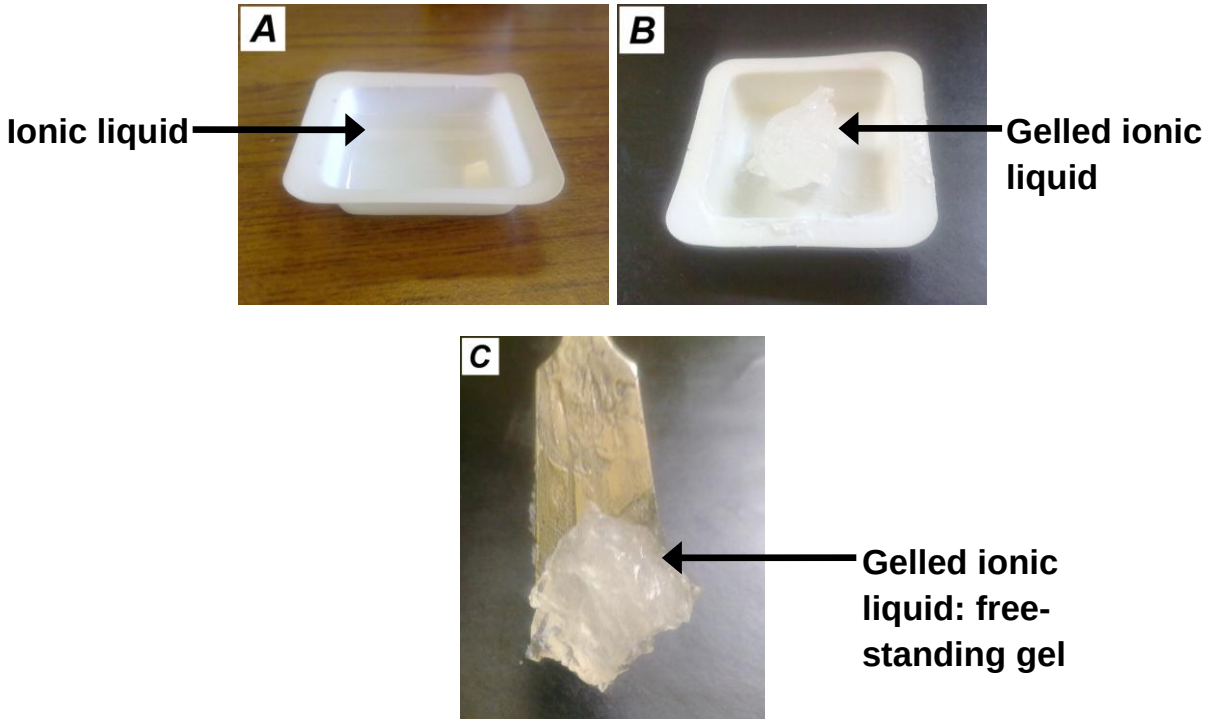

Figure 9.4 – Photographs of triethylsulfonium bis(trifluoromethylsulfonyl)imide in (A) liquid form, (B) gelled form, and (C) as a free-standing gel. The gelling agent was fumed silica (S5130, 7.5% w/w).

Voltammetry of ionic liquid gels

After perfecting a method for preparing stable gels of ionic liquids, the electrochemical responses of the gels were examined voltammetrically and compared with their un-gelled counterparts. Ferrocene (10 mM) was added as a redox-active test reagent, and its voltammetry was recorded at baseline (no gel), and after the addition of 7.5% w/w and 15% w/w silica. The experimental set-up is shown in ***Figure 9.5*** and the results are shown in ***Figure 9.6***.

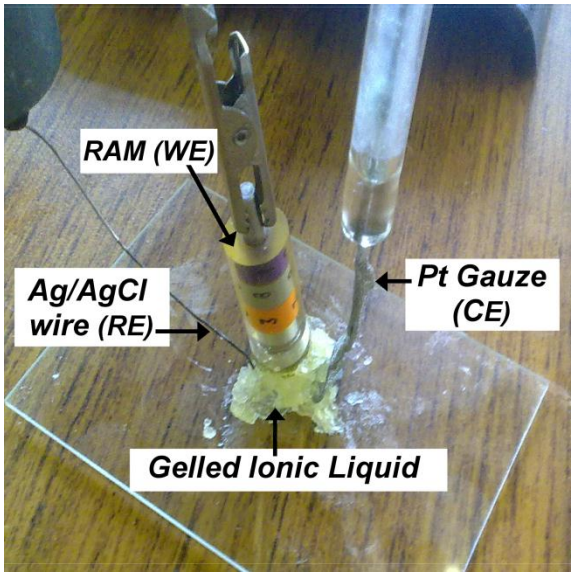

Figure 9.5 – Set-up for recording the cyclic voltammetry of a gelled ionic liquid using a RAM™ working electrode.

It can be seen from ***Figure 9.6*** that a small decrease in the voltammetric limiting current was observed as the amount of fumed silica in the gel was increased. However, the decrease was roughly in proportion to the volume fraction of silica dispersed in the ionic liquid. This indicates that the internal diffusion of ions is not being inhibited by the silica particles, other than in proportion to the volume fraction unoccupied by silica. The same effect was found for both the hydrophilic and hydrophobic fumed silica gels on both the glassy carbon and the RAM electrodes, suggesting that it is a general property of ionic-liquid/fumed silica gels. Most importantly, these results show that ionic liquids can maintain their electrolyte performance even when immobilised in the liquid phase. They also retain the same glass transition temperature, as determined by low temperature DSC.

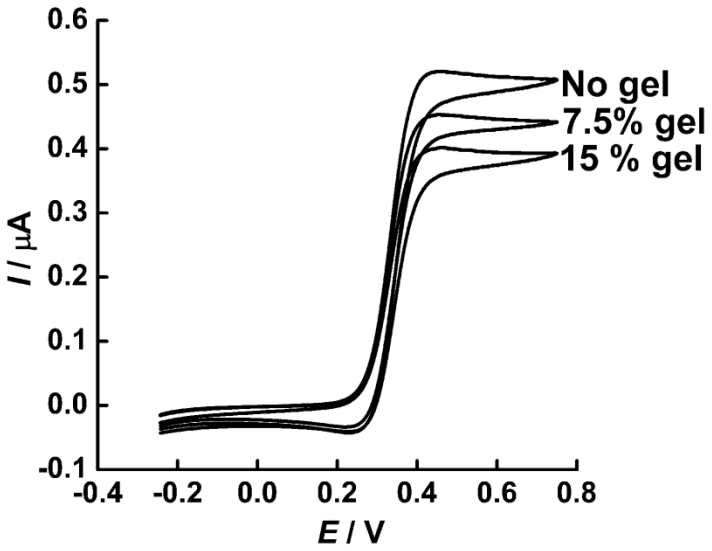

Figure 9.6 – The voltammetry of ferrocene (10 mM) in triethylsulfonium bis(trifluoro-methylsulfonyl)imide, before and after gelling the ionic liquid with hydrophilic fumed silica nanoparticles (S5130). The voltammetry was recorded using a RAM™ electrode (770 carbon microdisks, each of 7 μm diameter). The counter electrode was platinum gauze (A = 4.0 cm^2). The potential was cycled from –0.25 V to +0.75 V to –0.25 V at 20 mV s^{-1} at 25 °C following 30 seconds conditioning at –0.25 V vs. Ag\|AgCl. Shown above are the first scans. For each scan 3277 data points were collected and smoothed using a 21-point moving average to diminish mains interference.

9.2.3 – The separator

In supercapacitor design, the role of the separator is to prevent electronic contact between the two electrodes, whilst allowing ionic current to flow between them. When sourcing a separator material for use in a high temperature supercapacitor ($T \geq 220$ ºC) the following properties were sought; high thermal stability, high mechanical strength, chemical inertness, high porosity (to avoid osmotic effects) and low ohmic resistance to ion migration. According to ***Equation 9.2***, the ohmic resistance is proportional to the separator thickness and inversely proportional to its geometric area. Hence, it is generally advantageous, in terms of decreasing electrical resistance, to use a thin separator with a large geometric area.

$$R = \frac{\rho l}{A}$$

Equation 9.2

Here, R is the electrical resistance through the separator (Ω), l is the thickness of the separator (m), A is the geometric area of the separator (m^2), and ρ is the electrical resistivity of the separator (Ω·m). A short list of candidate materials is given in ***Table 9.3***.

Table 9.3 – Candidate separator materials for high temperature use.

	Material	Supplier
1	Schlumberger glass fibre	Schlumberger (Stonehouse, UK)
2	Glass fibre (VP35)	The Glass Company (Leicestershire, UK)
3	Filter paper (FB59015, QL100)	Fisher Scientific (Leicestershire, UK)
4	Fibreglass cloth	Unknown supplier
5	Fibreglass mat	Unknown supplier

To investigate which of the five candidate materials had the lowest ohmic resistance, an experiment was carried out using the cell set-up shown in ***Figure 9.7***. Twelve layers of each separator material (each 15 mm × 15 mm) were wetted with ionic liquid and sandwiched between two conducting stainless steel plates using bulldog clips for consistent pressure. A layer of Kapton (500 HN) was used between the stainless steel plates and the metal bulldog clips for electrical insulation. Silver coated copper wires (with insulating Teflon sheaths) were soldered to the outside of the stainless steel plates, and connected to a Wayne Kerr Precision Component Analyser. Impedance values were then recorded over the frequency range 20 Hz to 500 kHz (100 mV AC). Impedance plot for the five separator materials are given in ***Figure 9.8***.

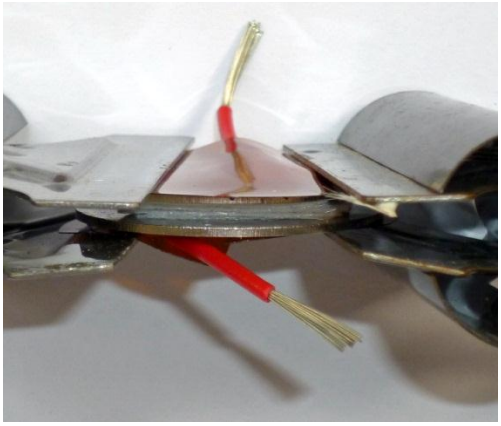

Figure 9.7 – Photograph of the test cell used for measuring the electrical resistance of separator materials.

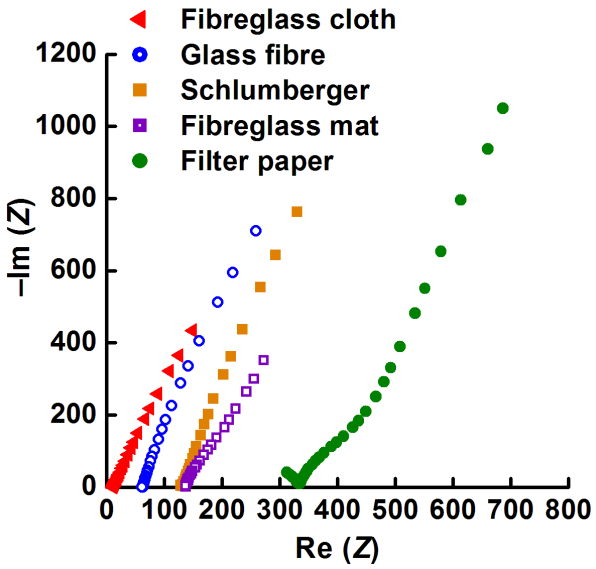

Figure 9.8 – Impedance plots in the complex plane for the five candidate separator materials (labelled). Twelve layers of separator material, each 15 × 15 mm, were wetted with HTE TFSI and sandwiched between two stainless steel plates. Impedance measurements were then recorded over the frequency range 20 Hz to 500 kHz at 100 mV AC.

It can be inferred from the impedance plots that fibreglass cloth had the lowest absolute ohmic resistance. However, it was not mechanically robust enough for industrial supercapacitor use and so was discarded. To make a rational comparison between the remaining four materials, the resistivity ρ / Ω·mm was calculated in each case. The results are presented in ***Table 9.4***. It can be seen that the glass fibre (VP35) had the lowest resistivity and thus it was decided that this was the most suitable choice for a separator material.

Table 9.4 – Physical parameters of candidate separator materials at 10 kHz. Resistance derived from the high frequency intercept with the real axis of impedance.

Material	R_{1layer} / Ω	A / mm^2	l / mm	ρ / Ω·mm
Schlumberger glass fibre	11	225	0.53	4670
Glass fibre (VP35)	5.2	225	0.315	3714
Filter paper (FB59015, QL100)	28.0	225	0.255	24706
Fibreglass cloth	1.0	225	0.04	5625
Fibreglass matt	11.3	225	0.295	8619

One minor problem with VP35 glass fibre was that it contained a binder, and the manufacturer was unwilling to reveal its chemical identity. Binders are common components in glass fibre products, as exemplified by the high resolution images of the VP35 glass fibre (***Figure 9.10***) and the Schlumberger glass fibre (***Appendix 9B***). It was therefore important to cross-check that the binder was chemically and thermally stable under the experimental conditions. Accordingly, DSC analysis was performed and the thermal profiles of the glass fibre materials were recorded both in air and in nitrogen (20 mL min^{-1}) from 40 ºC to 550 ºC at a heating rate of 10 ºC min^{-1}. The resulting DSC thermograms are shown in ***Figure 9.9***. It can clearly be seen that the glass fibre binder is stable at temperatures below 250 ºC. (Comparison with literature data suggests that the binder might be a nitrile rubber.)

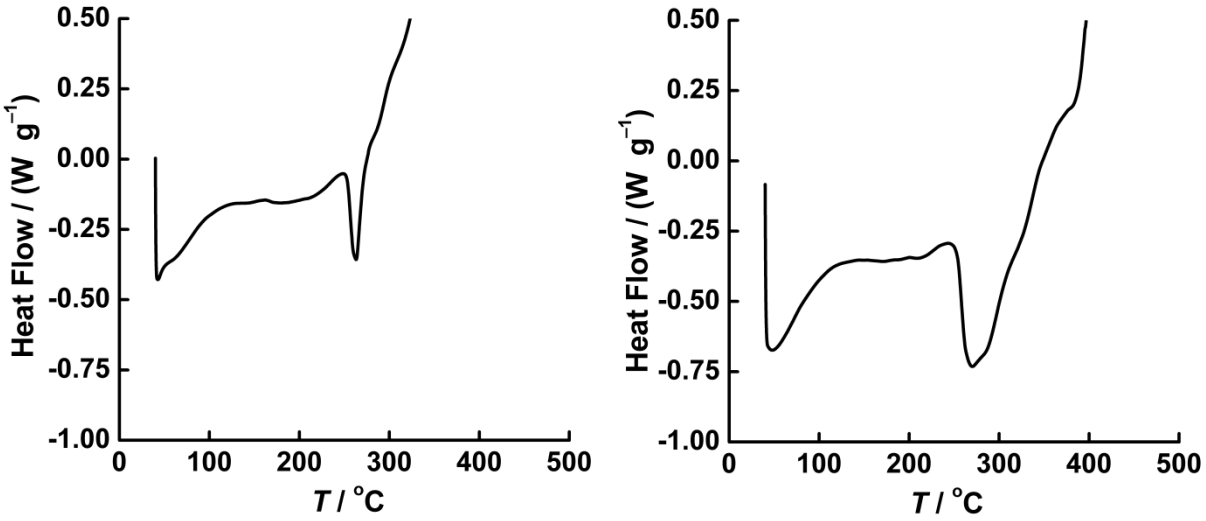

Figure 9.9 – Plots of heat flow (W g^{-1}) vs. temperature (°C) showing the thermal stability of the unknown binder in glass fibre VP35 in air (left) and nitrogen (right), 20 mL min^{-1}. In both cases, the samples were heated using a Q10 Differential Scanning Calorimeter (TA Instruments) from 40 ºC to 550 ºC at a rate of 10 ºC min^{-1}.

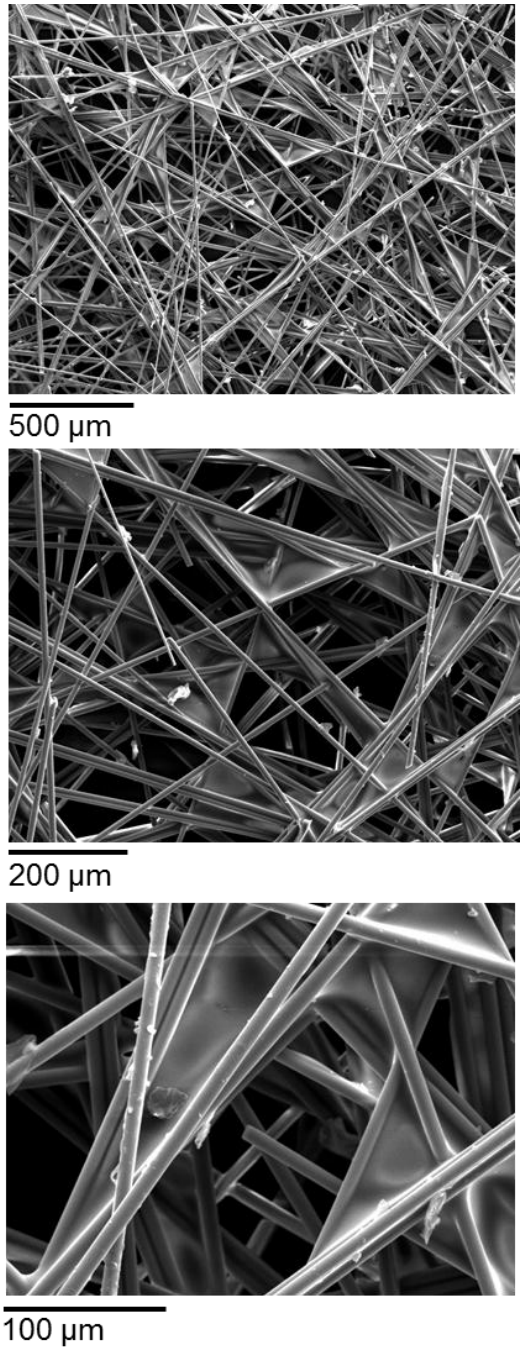

Figure 9.10 – SEM images of the VP35 glass fibre separator (The Glass Company, Leicester) obtained using a using a Carl Zeiss (Leo) 1530 VP FEGSEM.

SEM images of the other candidate separator materials are given in ***Appendix 9B***.

9.2.4 – The cell body

One of the main material challenges of the present work was to identify a robust material for the cell body. The material needed to be flexible, thermally stable ($T \geq 220$ ºC), and suitable for screen printing. Glass was briefly investigated in early work but was rejected due to its brittleness. Further searches were carried out and eventually a commercial polymer material, Kapton 500 HN (125 µm) was found. Kapton is a tough, aromatic heterocyclic polyimide film containing an "excellent balance of physical, chemical, electrical and mechanical properties over a wide temperature range, particularly at high temperatures"[12]. Some important properties of Kapton 500 HN are summarised in ***Table 9.5***. The HN class of Kapton was chosen because it was advertised as being a suitable substrate for screen printing, having high tensile strength, and was stable well above the desirable operating temperature for the superercapacitor. The structure of Kapton (poly(4,4'-oxydiphenylene-pyromellitimide)) is given in ***Figure 9.11***.

Kapton is synthesized by polymerizing an aromatic dianhydride and an aromatic diamine. It has excellent chemical resistance; there are no known organic solvents for the film. Kapton does not melt or burn in air. These outstanding properties of Kapton permit it to be used at both high and low temperatures where other organic polymeric materials are not suitable.

Table 9.5 – The physical properties of Kapton 500 HN (125 µm).

Property	Typical value
Melting point	none
Working temperature range	–26 ºC to 40 ºC
Tensile strength	231 MPa (2 ºC) 139 MPa (20 ºC)
Density	1.42 g ml^{-1}
Coefficient of expansion	17 ppm/ºC (30-10 ºC) 32 ppm/ºC (100-20 ºC)
Dielectric strength	3900 V mil^{-1}
Volume resistivity	1×10^{17} Ω.cm
Chemical resistance	>95 % (tensile retained)

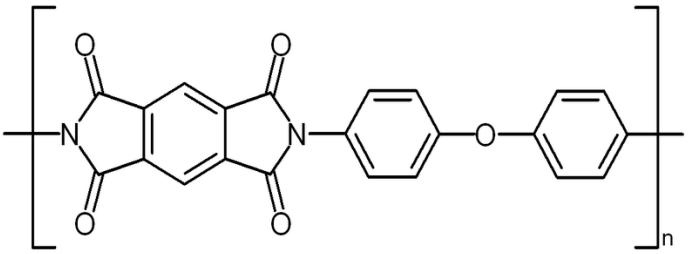

Figure 9.11 – Structural formula of poly(4,4'-oxydiphenylene-pyromellitimide (Kapton).

9.2.5 – The sealant

The role of a cell sealant is to produce a permanent seal which prevents both the electrolyte leaking out, and unwanted substances leaking in. Besides temperature stability, other desirable properties include adhesive strength, flexibility, and ease of application. Based on these properties, a range of commercial sealants was purchased that included oven glue and low melting point glass frit. None of these materials survived initial testing. A photograph of the cracking and charring of low temperature glass frit (flux 23901, Johnson Matthey Colour Technologies, Stoke on Trent, UK) at 250 ºC and 550 ºC is given in ***Figure 9.12***.

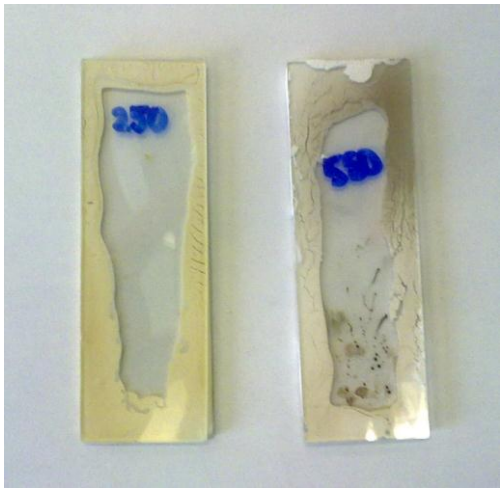

Figure 9.12 – Heat test of glass frit (flux 23901, Johnson-Matthey) after one hour at 250 ºC (left) and one hour at 550 ºC (right).

The breakthrough for a sealant material came whilst exploring the Kapton literature. A product manufactured by DuPont (Kapton K6339) was identified having an adhesive silicone

backing and a thermally stability up to 250 ºC. This was exceptionally good for sealing screen printed supercapacitor devices as it could be applied as a tape. The physical properties of Kapton 6339 are supplied in ***Table 9.6***.

Table 9.6 – The physical properties of Kapton 6339 silicone tape supplied by DuPont.

Property	Typical value
Thickness	0.085 mm
Peel strength	2.8 N cm^{-1}
Tensile strength	80 N cm^{-1}
Dielectric Strength	9000 V m^{-1}

9.2.6 – The electrodes

The total capacitance of a supercapacitor is determined by the porosity of its electrodes. For a high temperature supercapacitor ($T \geq 220$ ºC), other important features include high thermal stability, high conductivity, good wettability, low cost, and capability of mass scale-up. Accordingly, activated carbon was a natural choice.

DLC Supra 30 activated carbon (Norit) is especially suitable as electrode material in supercapacitors. Its narrow particle size distribution makes it highly suitable for printing thin carbon layers, and its large internal surface area, formed by large micropores and small mesopores, confers a high capacitance and low resistance. Consequently, this brand of activated carbon was chosen for the present work.

Once DLC Supra 30 had been identified, a suitable binder also needed to be sourced. Poly(1,1-difluoroethylene) often called poly(vinylene fluoride) (PVDF) had previously been used as a binder for DLC supra 30 carbon in low temperature proof-of-concept devices. However, its literature melting point, 157-170 ºC (MSDS, 3M), seemed to indicate that it would not function at high temperatures. Remarkably, however, electrodes maintained their mechanical integrity beyond 220 °C.

DSC thermograms of PVDF are shown in ***Figure 9.13***. An endotherm can be seen at 167 °C which corresponds to the melting point quoted in the literature. However, above this temperature the PVDF is chemically stable for another 200 °C.

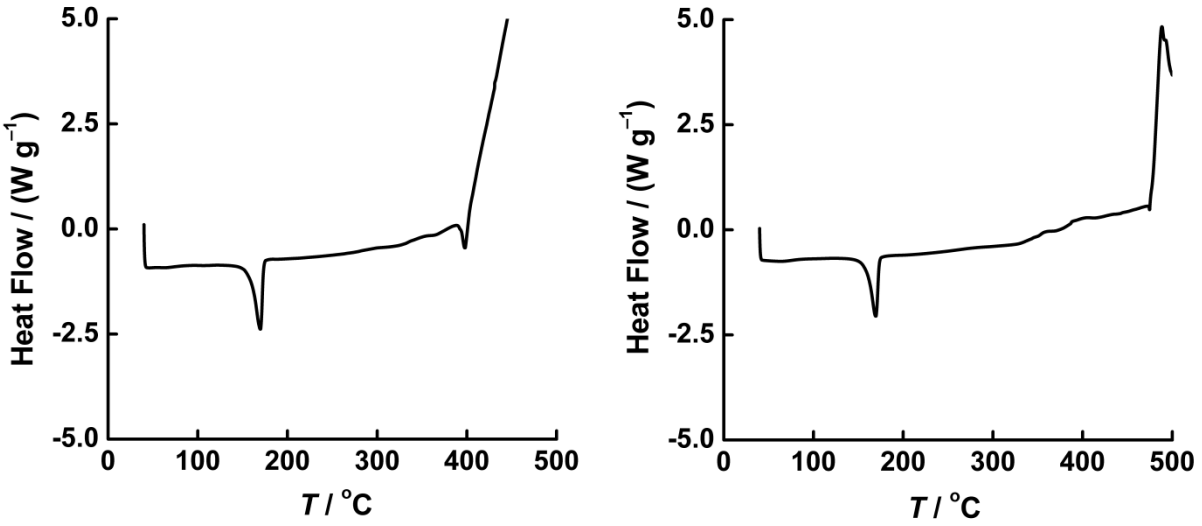

Figure 9.13 – A plot of heat flow (W g^{-1}) vs. temperature (ºC) for PVDF powder in air (left), and nitrogen (right). Gas flow 20 mL min^{-1}. DSC thermograms were recorded using a Q-1000 Differential Scanning Calorimeter (TA Instruments) from 40 ºC to 550 ºC at a heating rate of 10 ºC min^{-1}.

9.2.7 – The screen printing ink

The composition of the screen printing ink has the greatest influence on the success or failure of a finished electrode, due to the large number of ink-related variables. Some of these variables include viscosity, tack, surface tension, carbon particle size, speed of solvent evaporation, and temperature.

The basic composition of any screen printing ink is a mixture of solid particles, binder and solvent. Solvent properties are very important because the solvent must fulfil the following requirements: (1) it must dissolve the binder, (2) it must produce an ink with an appropriate spreadability, (3) it must produce an ink that does not dry out during printing, (4) it must be completely removable by evaporation, (5) it must not introduce impurities or chemically react with other components, and (6) it must have low toxicity. Candidate solvents that dissolve PVDF included propylene carbonate, DMSO, NMP, γ-butyrolactone, cyclohexanone, and dimethylacetamide. DMSO was eliminated immediately on account of its toxicity, and γ-butyrolactone, cyclohexanone, and dimethylacetamide were eliminated due to their high vapour pressure. Propylene carbonate was therefore chosen as the safest option. It also yielded screen printed activated carbon electrodes of high reproducibility.

The printing ink that was developed was prepared *via* the following method. In an agate pot, PVDF powder (0.3 g, 15% wt%) was dissolved in a small amount of propylene carbonate (~3 ml). Next, activated carbon powder (1.7 g, DLC Supra 30, Norit) was added into the mix, followed by a further 2-3 drops of propylene carbonate. The mixture was then ball milled with three agate balls, at 400 rpm for 2 min. The consistency of the ink was briefly inspected and the process was repeated until a smooth consistency suitable for printing was achieved. Total ball milling time was typically 12 minutes.

9.3 – Manufacturing method for high temperature supercapacitors

9.3.1 – Printing of high temperature electrodes

The final electrode design consisted of three layers, namely (1) a silver layer, to provide a low resistance pathway for current, (2) a smooth carbon layer, to mask the redox electrochemistry that would be exhibited by any exposed silver, and (3) an activated carbon layer, to provide a large specific surface area for maximum capacitance. The smooth carbon had a significantly lower surface area than the activated carbon so it did not significantly contribute to the measured capacitance.

The electrodes for high temperature supercapacitors were printed using a Dek 65 manual screen printer, assembled as shown in ***Figure 9.14***. The adopted strip design was based on previous work by Dr Nicholas J Van Dijk (private communication).

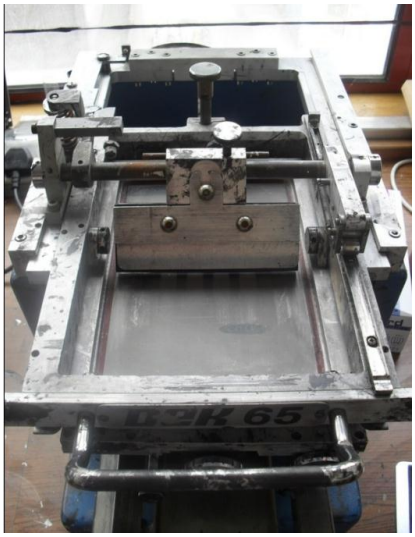

Figure 9.14 – The Dek 65 screen printer.

A 12 mm × 73 mm silver conducting layer (E-1660-136, Ercon) was first printed onto a 100 mm × 100 mm square of substrate material (500 HN, Kapton) and oven cured for 1 h (130 °C). Next, a 14 mm × 75 mm layer of smooth carbon ink (CHSN8032, SunTronic) was screen printed on top of the silver layer. This intermediate layer was cured for 1 h (25 °C) before being place in an oven for 5 h (130 °C). Finally, the activated carbon ink was screen printed on top of the smooth carbon layer and oven cured for 1 h (130 ºC) to form the completed electrode.

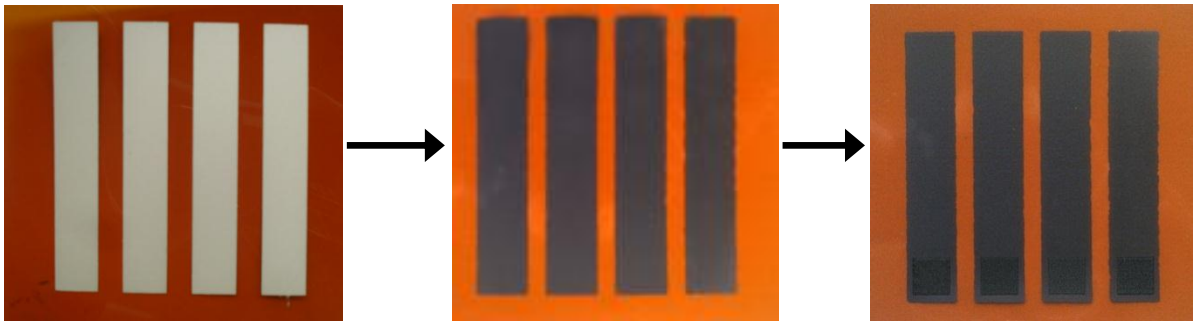

Figure 9.15 – Photographs of screen printed electrodes. Silver conducting layer (left), smooth carbon intermediate layer (middle), and activated carbon layer (right).

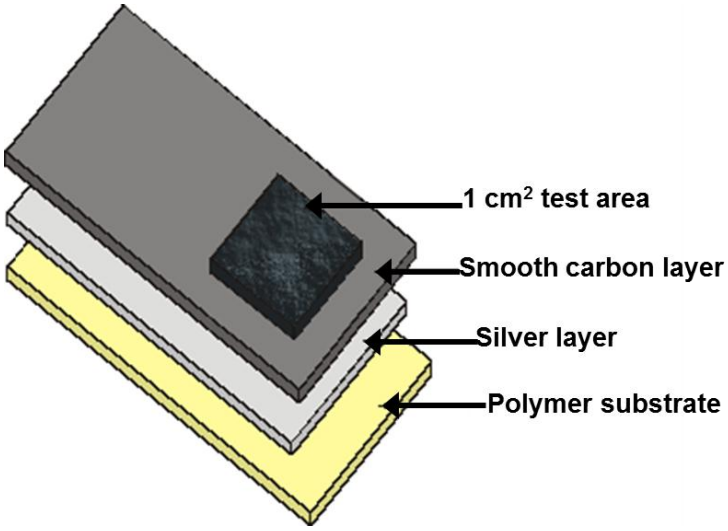

Figure 9.16– A Schematic illustrating the layered electrode design.

9.3.2 – Assembly of high temperature supercapacitors

For each supercapacitor, two individual electrodes were cut from the printed sheets and backed onto Kapton tape (6339, DuPont). The activated carbon squares on both electrodes were then wetted with a small drop of ionic liquid before a thin layer of ionic liquid gel was applied on top. Next, the glass fibre separator (VP35, The Glass Comany) was placed over the activated carbon, and insulating Kapton tape (6339, DuPont) was placed over the smooth carbon areas. Finally, the supercapacitor was sealed by aligning the two electrodes in parallel, facing each other, and pressing the adhesive tape together securely.

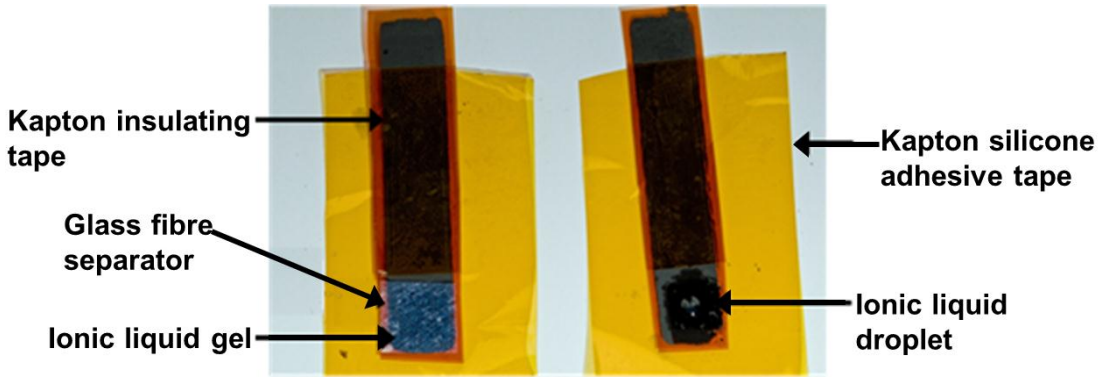

Figure 9.17 – A photograph illustrating the two supercapacitor electrodes during cell assembly.

Finally, in order to provide a highly conducting pathway from the supercapacitor to the potentiostat, an small area (2 mm^2) of the smooth carbon layer was removed from the top of each electrodes with superfine wet and dry paper (170-2975, Farnell) to expose the low resistance silver current collector below. Conducting copper tape (542-5369, RS, Corby) was then adhered to the silver. The fully assembled supercapacitor can be seen in ***Figure 9.18***.

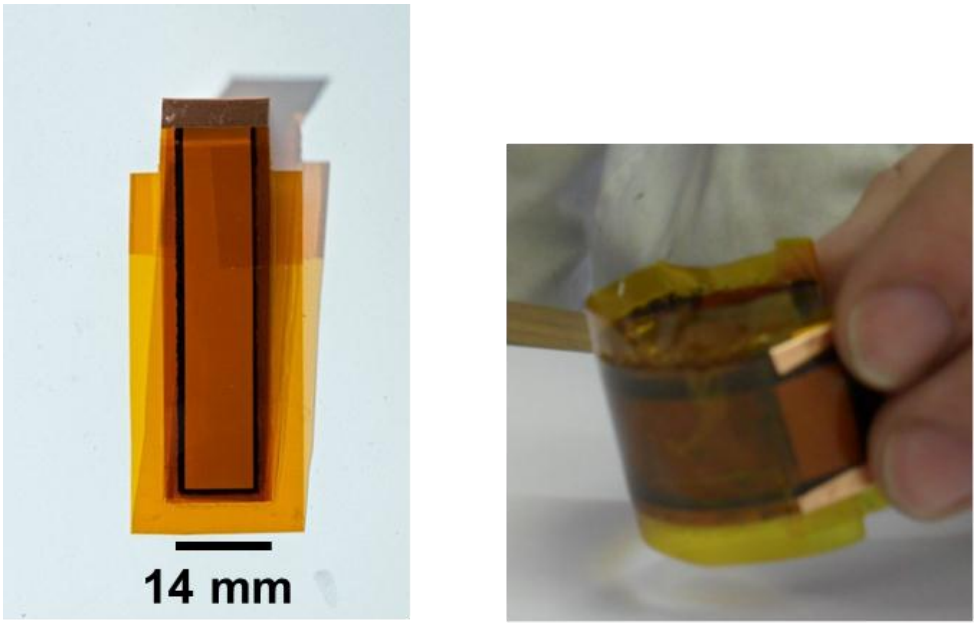

Figure 9.18 – A photograph of an assembled high temperature supercapacitor. The photograph on the right shows the flexibility of the supercapacitors.

All high temperature testing on the finished products was carried out in a horizontal tube furnace. To allow the supercapacitors to operate in the centre of the furnace, PTFE coated wires were soldered to the copper tape *via* a Pb/Sn/Ag solder (556-503, RS, 296-301 ºC). The wires were cut to a length that allowed the exposed ends to be outside the furnace so that a potentiostat could be attached to them.

9.4 – Characterisation of supercapacitors

Once the new supercapacitors had been assembled, experiments were carried out to compare their performance at room temperature (25 ºC) and at high temperature (220 ºC). Butyltrimethylammonium bis(trifluoromethylsulfonyl)imide was chosen as the ionic liquid for initial testing due its wide voltage stability window and acceptable conductivity. Hexyltriethyltrimethylammonium bis(trifluoromethylsulfonyl)imide was also used in more advanced stages of testing.

9.4.1 – Voltammetric stability tests

For the first experiment, a supercapacitor was cycled voltammetrically one hundred times at 25 ºC followed by a further one hundred times at 220 ºC, at a fixed potential window (1 V) and scan rate (5 mV s^{-1}). The results are shown in ***Figure 9.19***. The method used to calculate capacitance can be found in ***Appendix 9C***. It can be seen that the supercapacitors performed successfully at both room temperature and high temperature, even after one hundred cycles (11 h). Indeed, the results indicate that the measured capacitance was greater at high temperature. At 220 ºC the measured capacitance was approximately 20 mF greater than at 25 ºC.

An increase in measured capacitance with increasing temperature has been noted previously in the scientific literature[13-15] although there is no generally accepted explanation for the behaviour. One hypothesis is that ion association decreases with temperature allowing more ions to be adsorbed at the electrode surface[13,16], but this seems unlikely. Another hypothesis is that temperature decreases the viscosity of ionic liquids and thus increases the transport rate of ions. However, there is no indication that the charge/discharge process is under diffusion control. (A better explanation based on a decrease in electrical resistance is suggested elsewhere in this thesis.)

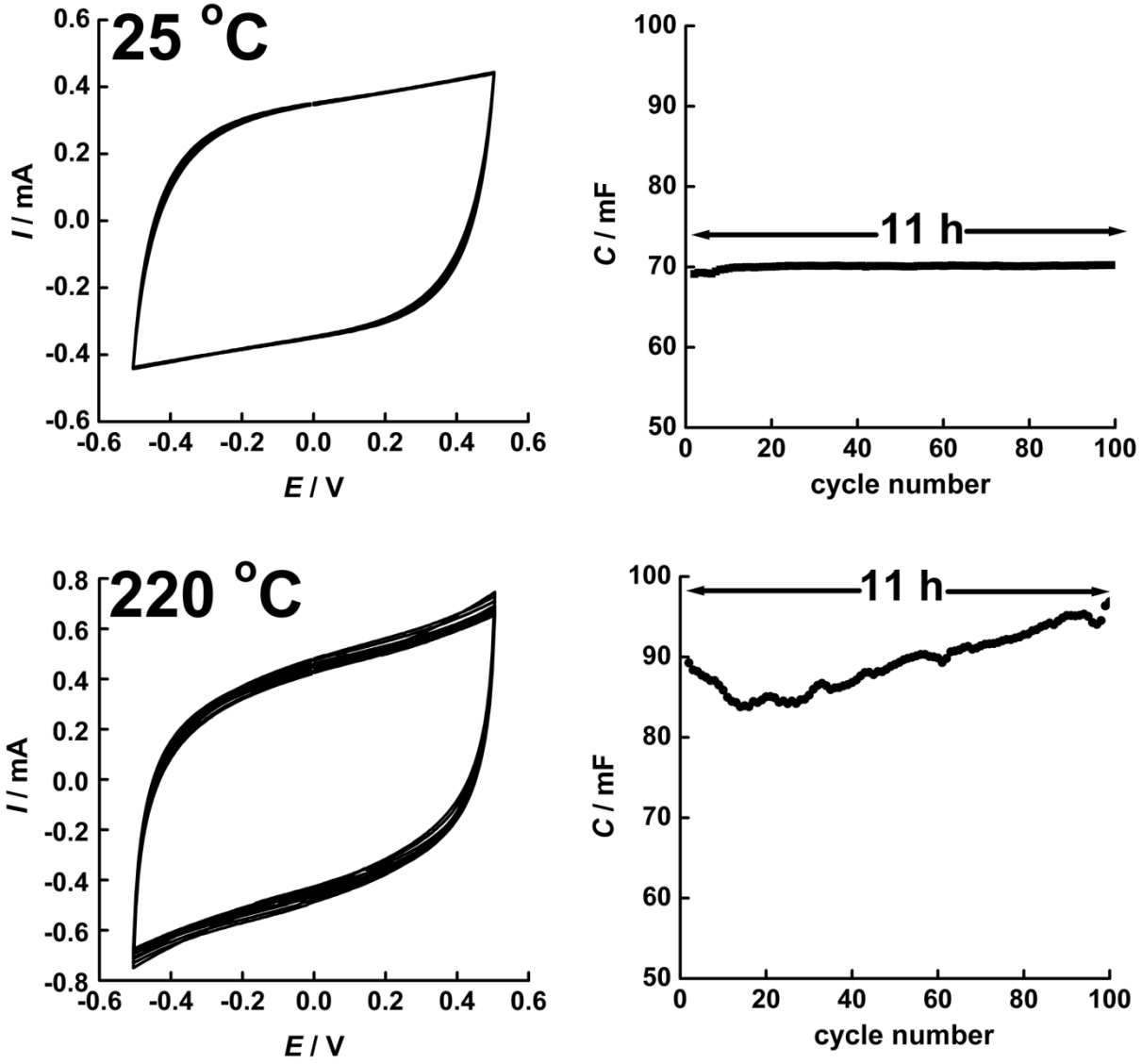

Figure 9.19 – Voltammetric stability tests for screen printed activated carbon supercapacitors at 25 ºC (top) and at 220 ºC (bottom). The electrolyte was butyltrimethylammonium bis(trifluoro-methylsulfonyl)imide. Voltammograms recorded every 10 cycles (left), and measured capacitance vs. cycle number (right). Scan rate 5 mV s^{-1}.

9.4.2 – The effect of temperature on measured capacitance

Following the discovery that the measured capacitance of supercapacitors was increasing with temperature, an experiment was set up to confirm this counter-intuitive relationship. A supercapacitor was assembled by the standard method and its voltammetry was recorded at 25 ºC. The same supercapacitor was then put into a tube furnace and the voltammetry was recorded at 25 ºC, 50 ºC, 100 ºC, 150 ºC, and 200 ºC. Once the furnace had reached each

programmed temperature, the supercapacitor was given forty five minutes to thermally equilibrate before its voltammetric response was recorded. The results are presented in ***Figure 9.20*** and a plot of measured capacitance *vs*. temperature is given in ***Figure 9.21***. Once again it can be seen that the measured capacitance increased with increasing temperature, which was advantageous in terms of energy storage, but puzzling in terms of theoretical understanding! From 50 ºC to 200 ºC the measured capacitance roughly doubled (58.8 mF to 105.68 mF).

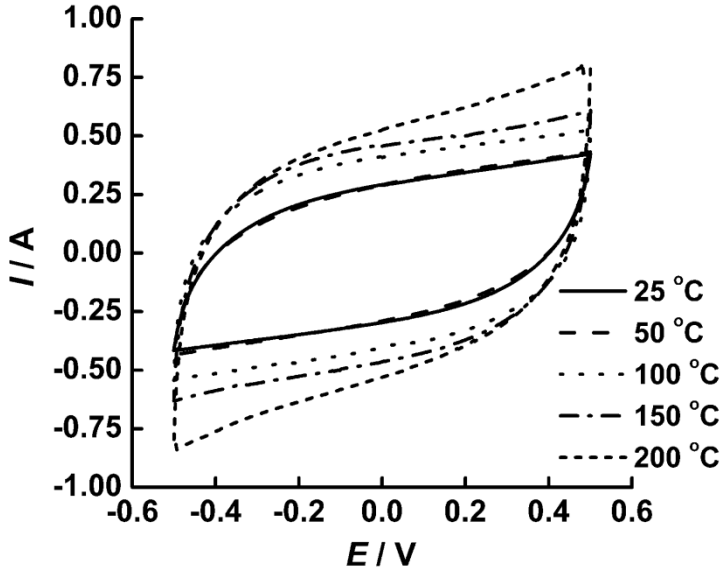

Figure 9.20 – Cyclic voltammograms for screen printed supercapacitors at temperatures of 25 ºC, 50 ºC, 100 ºC, 150 ºC, and 200 ºC. Forty five minutes was allowed for thermal equilibrium to be achieved at each temperature. The potential was held at 0.0 V for 10 s before being cycled from 0.0 V to +0.5 V to –0.5 V to 0.0 V, at 5 mV s^{-1}. The electrolyte was butyltrimethylammonium bis(trifluoromethylsulfonyl)imide. Shown above are the 2nd cycles.

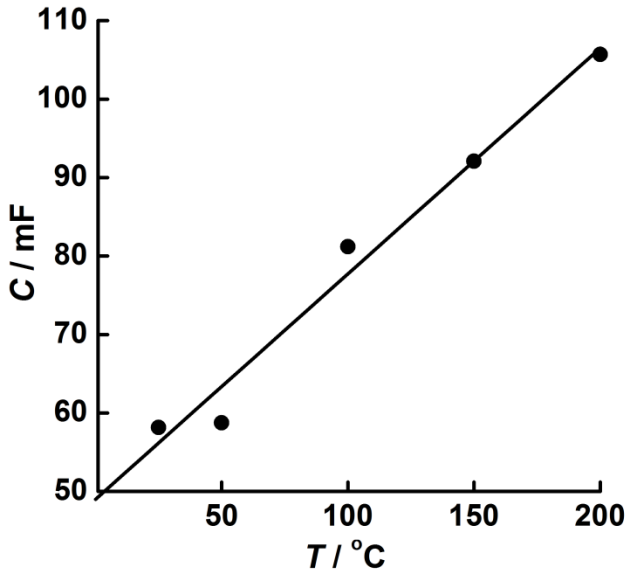

Figure 9.21 – Measured capacitance (mF) vs. temperature (ºC) for an activated carbon screen printed supercapacitor at temperatures of 25, 50, 100, 150, and 200 ºC. The electrolyte was butyltrimethylammonium bis(trifluoromethylsulfonyl)imide. Line of best fit displayed.

9.4.3 – Voltage stability windows

One of the remarkable properties of ionic liquids is their wide voltage stability windows. These are of great significance in supercapacitor performance because the amount of stored energy is proportional to the square of the applied voltage. The voltage stability windows of BTM TFSI (> 4 V) and HTE TFSI (> 5 V) were reported in ***Chapter 4***. However, the voltage stability windows that could be achieved at high temperature were unknown. To determine these, a series of experiments were performed on gelled ionic liquids at 25 ºC and 220 ºC.

Given the destructive nature of the high temperature stability tests, four separate supercapacitors were assembled, two with gelled BTM TFSI as the electrolyte and two with gelled HTE TFSI as the electrolyte. Both room temperature and high temperature tests were carried out in a tube furnace for better temperature control. For each supercapacitor, voltammetry was initially recorded over a 1 V range. The voltage range was then systematically increased in 0.5 V increments until solvent decomposition was observed. At that point the experiment was terminated. The scan rate in all cases was 10 mV s^{-1}. Recorded voltammograms are shown in ***Figure 9.22***. It can be seen that the voltage stability windows of both ionic liquids diminished at high temperature, due to the acceleration of the

electrochemical decomposition reactions. Nevertheless, the remaining voltage stability windows were still considerably larger than those of aqueous supercapacitors (1.2 V) at 25 ºC.

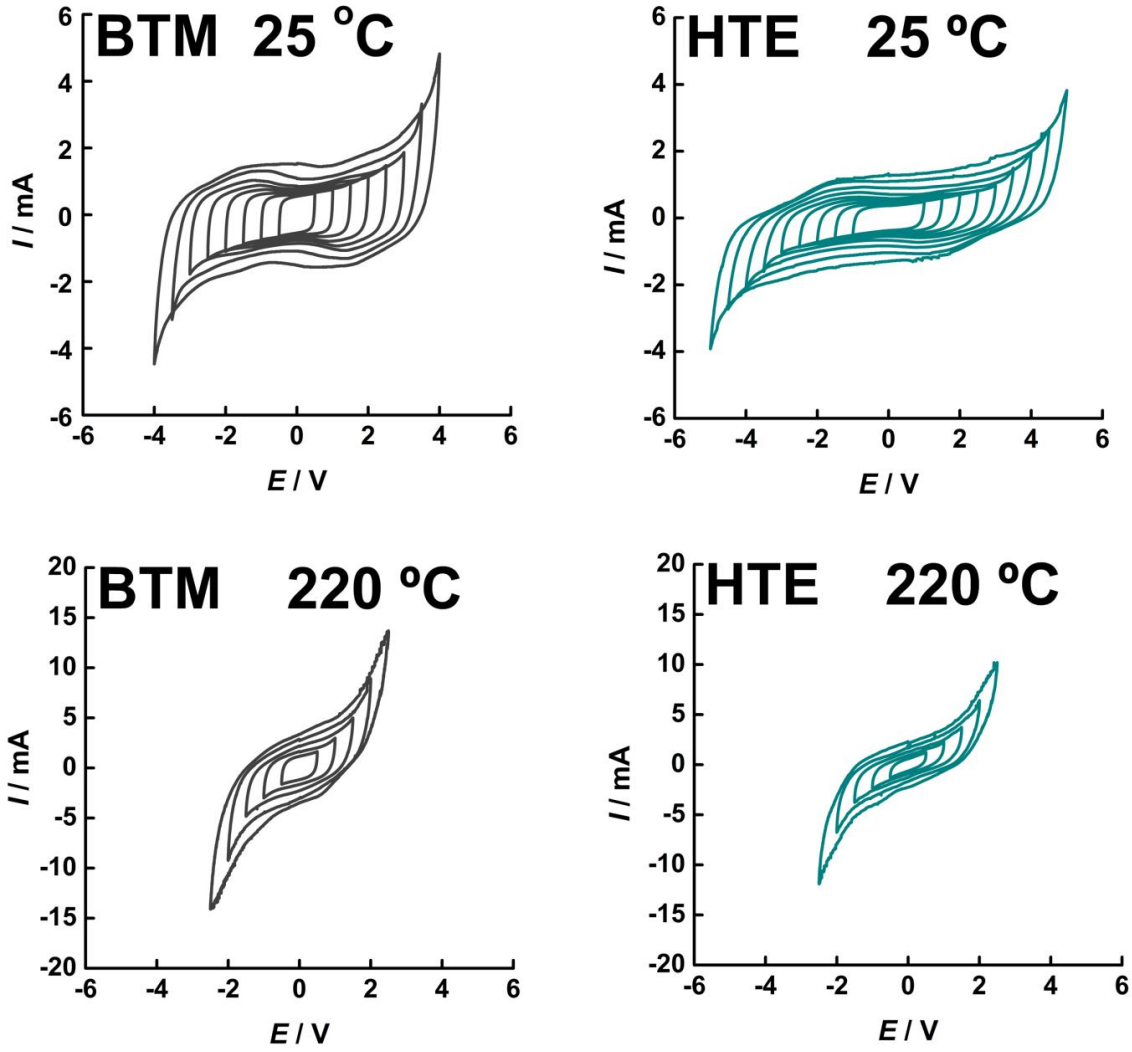

Figure 9.22 – The electrochemical stability windows of ionic liquid-based supercapacitors. (Left) butyltrimethylammonium bis(trifluoromethylsulfonyl)imide and (right) hexyltriethyl-ammonium bis(trifluoromethylsulfonyl)imide at 25 ºC (top) and 220 ºC (bottom). The scan rate for all voltammograms was 10 mV s^{-1}. (Note that the voltage stability windows of paired supercapacitor electrodes are twice those of individual electrodes.)

9.4.4 – Long-term stability at 220 ºC

As already noted in ***Section 9.4.1***, BTM TFSI supercapacitors are able to maintain their capacitive behaviour for 11 h at 220 ºC under continuous cycling. Nevertheless, for a practical device in the field, even longer times are required (time scale of weeks), so 'long-term' thermal testing was also undertaken. For this, four BTM TFSI supercapacitors, labelled A, B, C, and D were assembled and continuously maintained in a tube furnace at 220 ºC. Voltammetry was recorded every twenty four hours over a period of two weeks. The results are shown in ***Figure 9.24***. Pleasingly, even after 336 h (2 weeks) at 220 ºC, the performance of the supercapacitor was maintained. In fact, the trend in capacitance over time showed a slight increase. For supercapacitor B, two small peaks were observed in the voltammetry after 240 h, suggesting the presence of faradaic processes, but these did not damage the overall performance. The corresponding results for the HTE TFSI electrolyte are shown in ***Figure 9.25***. In this case, the voltammetry remained clean even after 360 h cycling.

Finally, the time evolution of the cyclic voltammetry of HTE TFSI supercapacitors was examined over an 8 V range at 25 ºC (8 V) and over a 4 V range at 220 ºC. The results are shown in ***Figure 9.26*** and ***Figure 9.27***. The successful operation of the supercapacitors is evident throughout.

Figure 9.23 – The tube furnace used for testing the long term stability of screen printed supercapacitors.

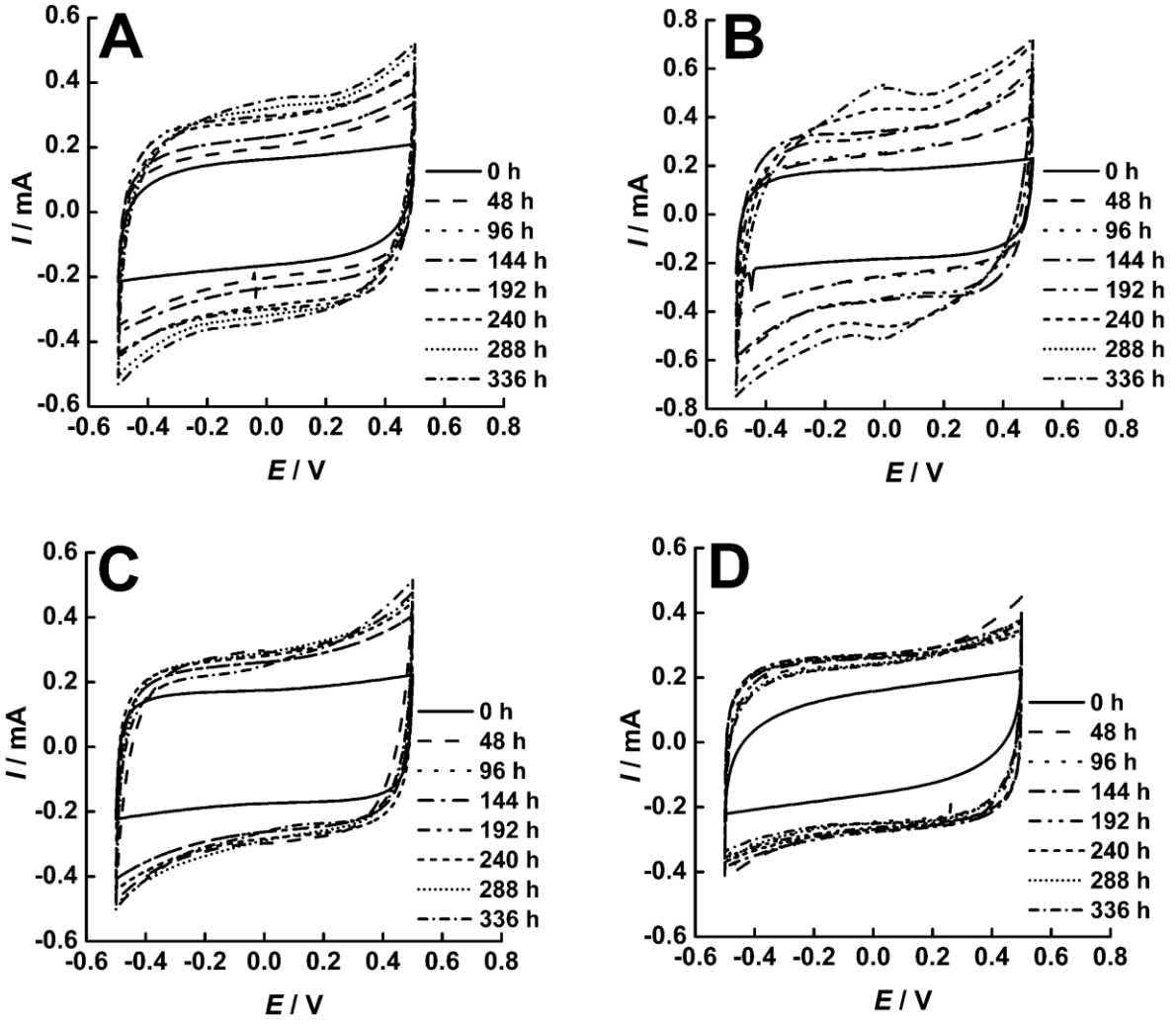

Figure 9.24 – Cyclic voltammograms at 220 ºC for four notionally identical supercapacitors containing gelled BTM TFSI. The devices were conditioned at 0.0 V (10 s) before being cycled at a scan rate of 5 mV s^{-1}.

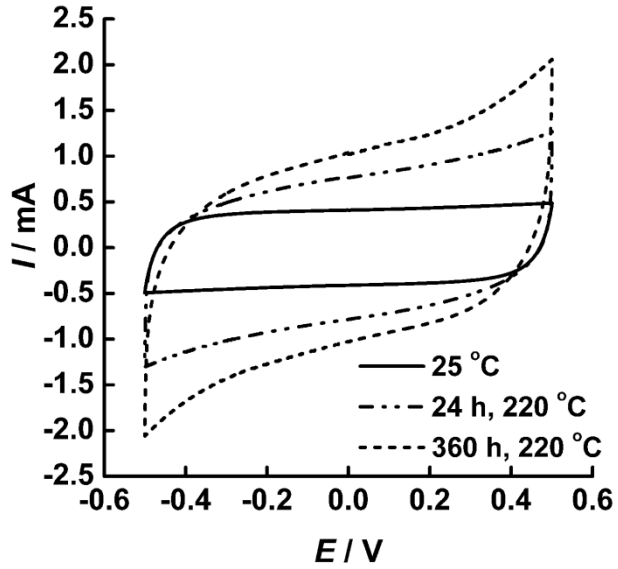

Figure 9.25 – Cyclic voltammograms at 220 ºC for a supercapacitor containing gelled HTE TFSI. The device was conditioned at 0.0 V (10 s) before being cycled at a scan rate of 5 mV s^{-1}.

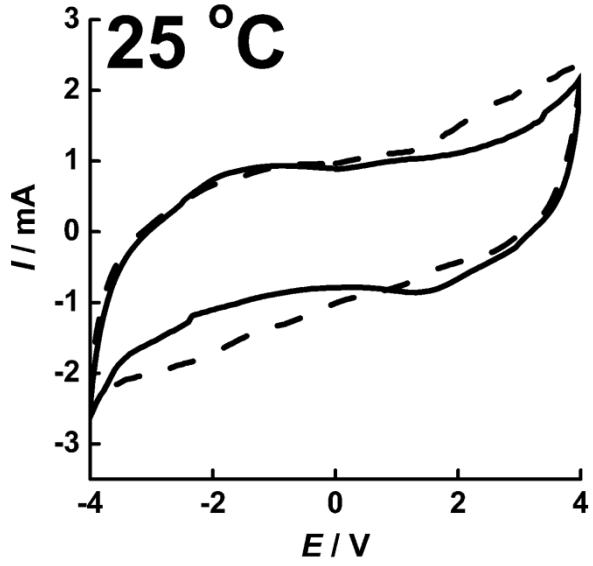

Figure 9.26 – Cyclic voltammograms for an HTE TFSI supercapacitor after 1 cycle (solid line) and 100 cycles (dotted line) at 25 ºC. The scan rate was 5 mV s^{-1}.

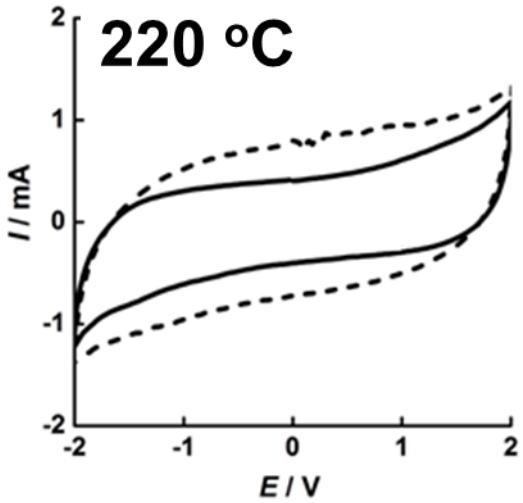

Figure 9.27 – Cyclic voltammograms for an HTE TFSI supercapacitor after 1 cycle (solid line) and 100 cycles (dotted line) at 220 ºC. The scan rate was 5 mV s^{-1}.

9.4.5 – Voltage relaxation measurements

Voltage relaxation manifests as a decrease in the potential difference between the supercapacitor terminals when the supercapacitor is disconnected after brief charging. The voltage relaxation phenomenon is well documented, and is commonly attributed to self-discharge. However, an alternative interpretation suggested by the present work is that voltage relaxation is a manifestation of the distribution of time constants inside the activated carbon electrodes.

Voltage relaxation measurements were carried out to see how the relaxation was affected by temperature. For this purpose, a supercapacitor was assembled using gelled hexyltriethyl-ammonium bis(trifluoromethylsulfonyl)imide, and then charged to 2 V (5 minutes) using a power supply. After the specified voltage was attained, the device was switched to open circuit and its voltage was monitored against time using a data logger (8SP, 2 samples per second) and Chart software (*version* 4.0, both PowerLab, AD Instruments, UK). After recording the voltage relaxation profile at 25 °C, the supercapacitor was then heated to 220 °C using a horizontal tube furnace and the voltage relaxation profile was re-recorded. The voltage relaxation curves were then analysed using a dispersive kinetic model, based on the Lévy distribution, to yield a mean time constant, see ***Appendix 9D***.

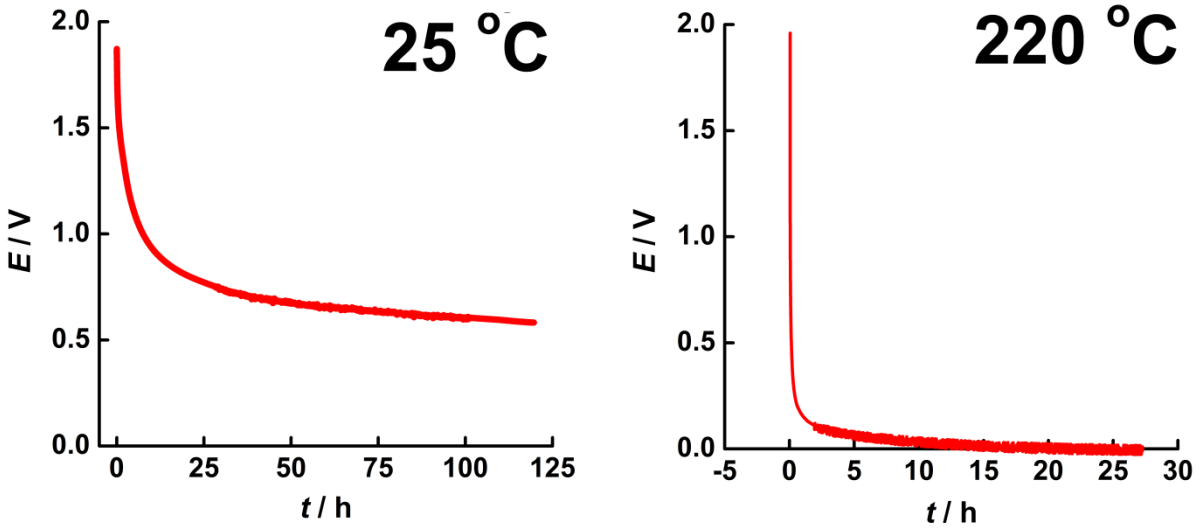

Figure 9.28 – The cell potential (V) vs time (s) for a HTE TFSI supercapacitor at open circuit following charging at 2 V. (Left) 5 mins at 25 °C, and (right) 5 mins at 220 °C.

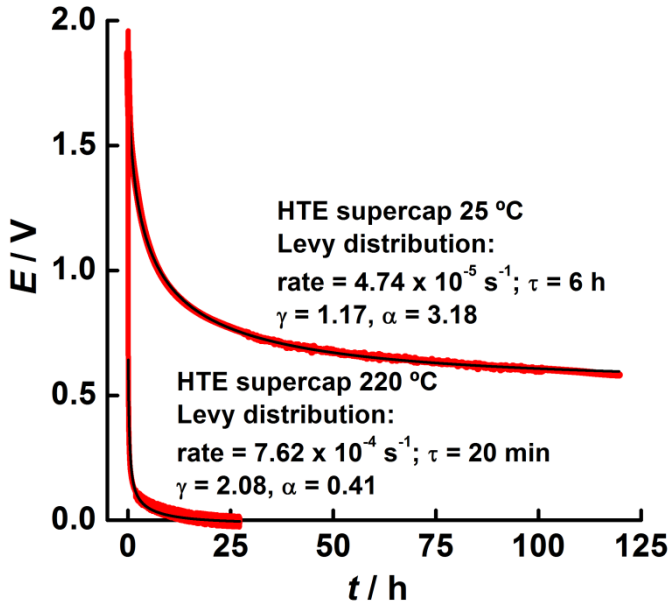

Figure 9.29 – Voltage relaxation curves for a HTE TFSI supercapacitor at open circuit (red lines), fitted using the Lévy distribution (black lines). The supercapacitor was charged at 2 V (5 mins). Top curve recorded at 25 °C, bottom curve recorded at 220 °C. Note: γ and α are numerical factors that characterise the shape of the probability density function of the Lévy distribution. For a symmetric probability density function, increasing α causes the tails of the distribution to disappear, while increasing γ flattens the centre of the distribution.

It can be seen from ***Figure 9.29***, that the voltage relaxation is much faster at 220 °C than at 25 °C. The corresponding rates are 7.62×10^{-4} s^{-1} and 4.74×10^{-5} s^{-1}. For the room temperature supercapacitor, the voltage relaxation is initially fast, dropping to 1/*e* (37%) of its original charge in 6 h. However, in the following 100 h, the voltage relaxation stabilises. This is precisely the response to be expected if the activated carbon electrodes exhibit a very wide range of time constants, as discussed in ***Chapter 8.*** At higher temperature, the smaller fitted α value and the larger fitted γ value reflect a systematic shift in contributions from the centre of the rate distribution to the tails. This implies that some pores that are inactive at room temperature are becoming active at high temperature. Most likely, this is caused by a decrease in internal pore resistance and a decrease in electrolyte viscosity. Such an interpretation is consistent with literature studies relating the Lévy distribution to surface morphology[17][18].

9.5 – Scale up of supercapacitor technology

9.5.1 – The effect of activated carbon thickness on capacitance

Throughout the present work, many small test devices were successfully demonstrated in the laboratory. However, scale-up was needed for working devices in the field. Although the screen printed electrodes typically yielded capacitance values of 30-50 mF cm^{-2}, much larger capacitances were needed for down-hole telemetry. With this aim in view, experiments were initiated to decide whether the capacitance could be enhanced in a controlled way by screen printing multiple activated carbon layers. Overall, twenty supercapacitors were assembled. Six had one layer of screen-printed activated carbon, six had two layers, six had three layers, and the final two supercapacitors had thick painted layers of activated carbon. Before applying each layer, the previous layer was thoroughly dried in an oven for 1 h (130 ºC) to remove any remaining propylene carbonate solvent. To ensure that painted layers were exactly 1 cm^2, the end of an optical cuvette with a path length of 1 cm was attached to the smooth carbon, and ink was applied inside the square (see ***Figure 9.30*** (right)) Photographs of the screen-printed electrodes before assembly into supercapacitors are shown in ***Figure 9.30*** (left). The resulting voltammograms are shown in ***Figure 9.31***.

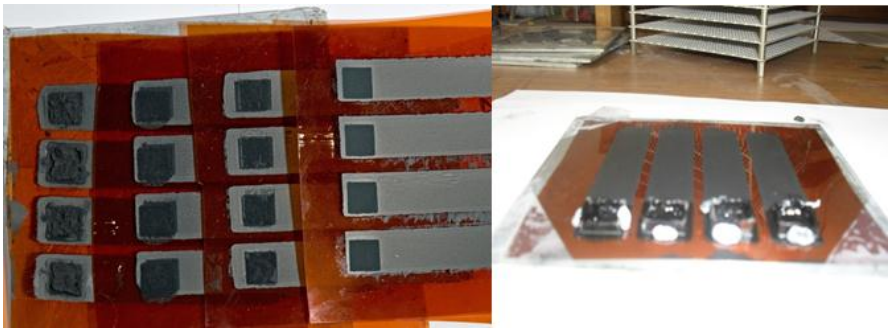

Figure 9.30 – A photograph of screen printed electrodes with (from right to left) one layer, two layers, three layers and a manual layer of activated carbon ink (left), and a photograph of the method used for applying manual layer of 1 cm ^{2} activated carbon (right).

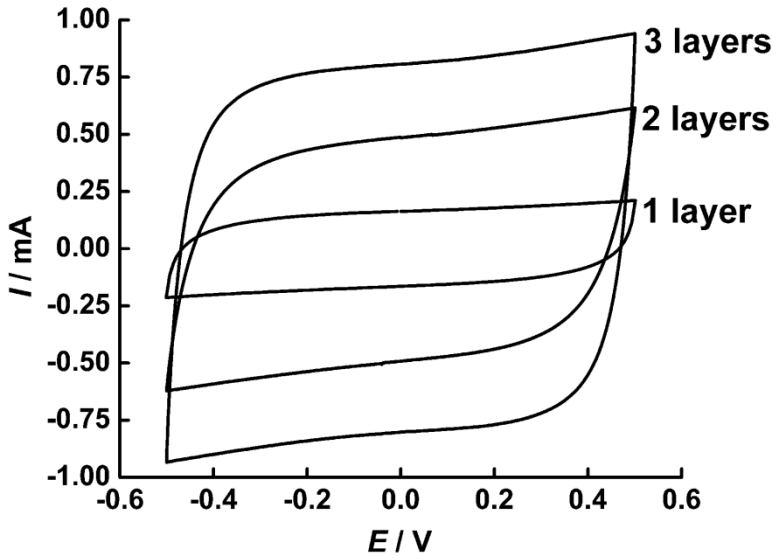

Figure 9.31 – Voltammograms of screen printed supercapacitors with 1 layer, 2 layers and 3 layers of activated carbon. The potential was conditioned at 0.0 V (10 s) before being cycled from 0.0 V to 0.5 V to –0.5 V to 0.0 V at a scan rate of 5 mV s^{-1}(2 ºC). The ionic liquid was butyltrimethyl-ammonium bis(trifluoromethylsulfonyl)imide.

It can be seen that the measured capacitance increases linearly with the number of deposited layers of activated carbon. This implies that the ionic liquid is successfully wetting the full surface area of each of the deposited activated carbon layers. Each layer is contributing approximately 50 mF under the stated conditions. Based on this figure, it can be estimated that the painted layer corresponds to approximately four layers of screen printed activated carbon. This result is reassuring and implies that the technology is scalable.

9.5.2 – Development of prototype large scale supercapacitor

After a provisional patent for the high temperature supercapacitor design had been granted, further work in collaboration with Dr Iain Kirkpatrick (Loughborough University) resulted in the construction of a large prototype device. The prototype design was the same as the original strip design, except that the supercapacitor was 20 × 20 cm (previously 14 mm × 75 mm), the device was sealed with epoxy (previously polyimide tape), and aluminium foil was used in the place of silver ink to provide a more flexible current pathway. The supercapacitor containing aluminium foil also had approximately half the electrical resistance of the supercapacitor containing silver ink. Photographs showing the 20 × 20 cm supercapacitor at various stages of construction are shown in ***Figure 9.32*** and the final design in ***Figure 9.33***.

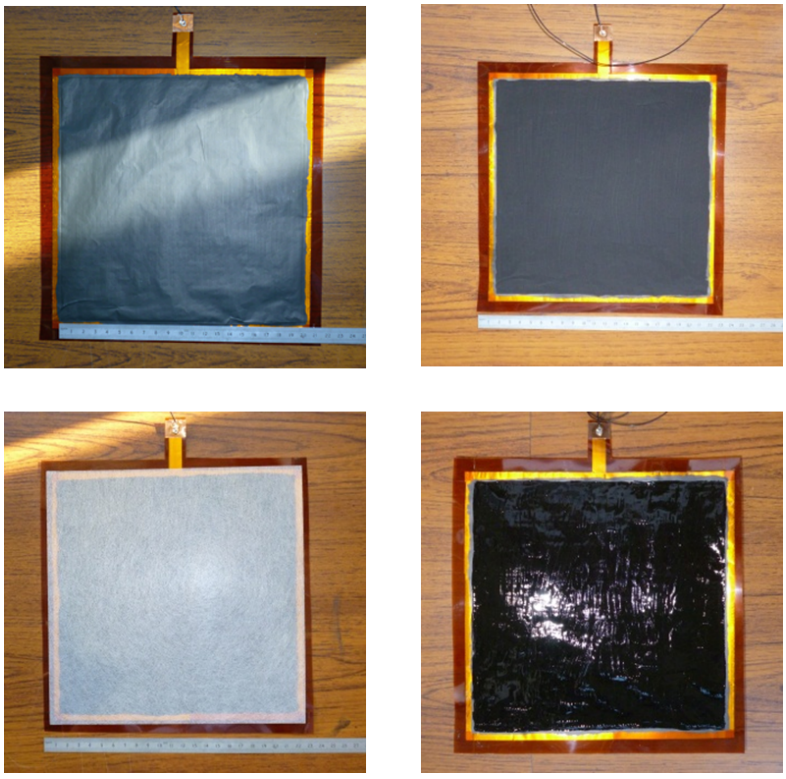

Figure 9.32 – Photographs showing stages of the large scale supercapacitor construction (20 × 20 cm). Top left: smooth carbon layer, top right: activated carbon, bottom left: separator and bottom right: ionic liquid gel.

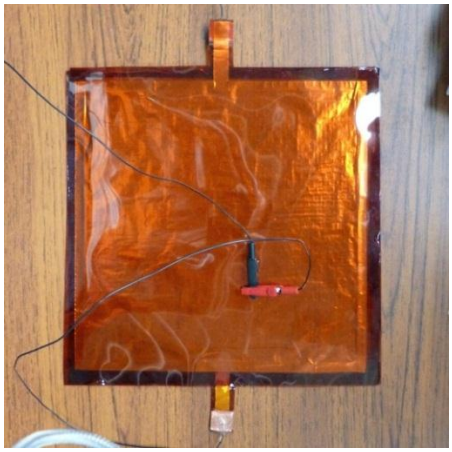

Figure 9.33 – A Photograph showing a fully assembled large scale supercapacitor.

A cyclic voltammogram of the prototype large-scale supercapacitor is shown in ***Figure 9.34***. The measured capacitance is approximately 20 F, which is consistent with linear scale-up from the 1 cm^2 device.

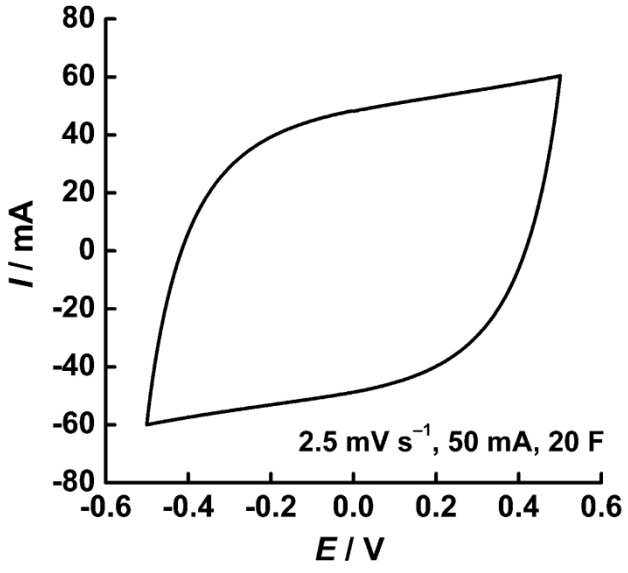

Figure 9.34 – Cyclic voltammogram of prototype large-scale supercapacitor (20 cm × 20 cm). Scan rate was 2.5 mV s^{-1} and measured capacitance was 20 F. The ionic liquid was butyltrimethylammonium bis(trifluoromethylsulfonyl)imide.

The power performance of the prototype large-scale supercapacitor was measured using a 9 V D.C. electric motor (LEGO). The supercapacitor was charged for five minutes at a number of cell voltages and the running time of the motor was measured. The results are shown in ***Figure 9.35***. A linear relation between cell potential and running time is evident. When fully charged, the supercapacitor was capable of running the D.C. motor for one hour.

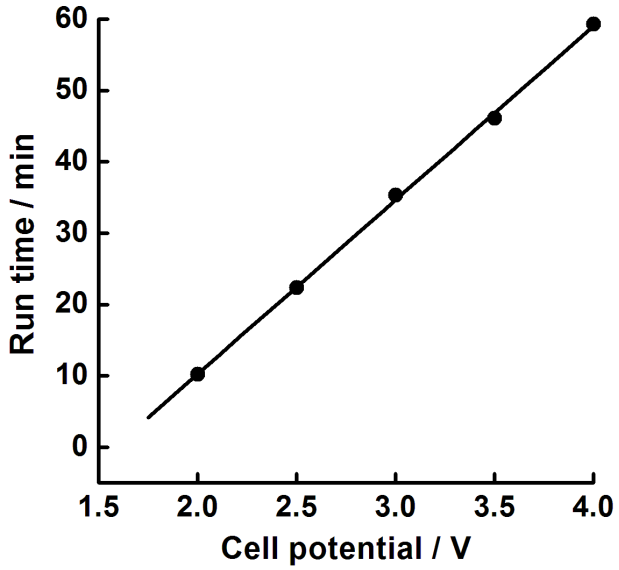

Figure 9.35 – Running time (min) of a 9 V D.C. electric motor, as a function of supercapacitor cell potential. The electrolyte was butyltrimethylammonium bis(trifluoromethylsulfonyl)imide. The line of best fit for the data is displayed.

9.6 – Conclusion

A prototype supercapacitor, made from temperature resistant materials ($T \geq 220$ °C) with a measured capacitance of 20 F has been successfully manufactured. The device consists of a three layer electrode design (aluminium, smooth carbon and activated carbon), a polyimide cell body, a sealant, a glass fibre separator, and an ionic liquid electrolyte. The chosen ionic liquids for high temperature electrolytes were asymmetric tetraalkylammonium bis(trifluoromethylsulfonyl)imides. Extensive testing has confirmed that this technology can power real-world devices (such as a 9 V motor for 1 h following only 5 minutes charging at 4 V). Further testing has also revealed that the supercapacitors perform better at high temperature. A provisional patent has been filed with the US provisional patent office (No. IS12.2724-US-

PSP) for the use of this technology as a "thermally stable supercapacitor for application in hostile environments such as oil and gas wells."

9.7 – References

[1] Conway, B. E. *Electrochemical Supercapacitors. Scientific Fundamentals and Technological Applications*. Kluwer academic / Plenum publishers, New York. Chapter 11, pp335-375 (1999).

[2] Suarez, P. A. Z., Consorti, C. S., de Souza, R. F., Dupont. J. & Goncąlves, R. S. *Electrochemical behaviour of vitreous glass carbon and platinum electrodes in the ionic liquid 1-n-butyl-3-methylimidazolium trifluoroacetate.* Journal of the Brazilian Chemical Society, 13: pp 106-109 (2002).

[3] Izmailova, M. Y., Rychagov, Y., Den'shchikoc, K. K., Vol'fkovich, Y. M., Lozinskaya, E. I. & Shaplov, A. S. *Electrochemical Supercapacitor with Electrolyte Based on an Ionic Liquid.* Russian Journal of Electrochemistry, 48: 1014-1015 (2009).

[4] Sun, J., Forsyth, M. & MacFarlane, D. R. *Room-temperature molten salts based on the quaternary ammonium ion.* Journal of Physical Chemistry B, 102: 8858–8864 (1998).

[5] Sun, J., MacFarlane, D. R. & Forsyth, M. *Synthesis and Properties of Ambient Temperature Molten Salts Based on the Quaternary Ammonium Ion*. Ionics, 3: 356-361 (1997).

[6] Tokuda, H., Tsuzuki, S., Hasan, M. A. B., Hayamizu, S. K & Watanabe, M. J. *How Ionic are Room-Temperature Ionic Liquids? An Indicator of the Physichemical Properties*. Journal of Physical Chemistry B, 110: 19593–19600 (2006).

[7] Sun, J., MacFarlane, D. R. Golding, , J. & Forsyth, M. *Highly conducting salts based on Imide ion*. Electrochimica Acta, 45:1271 (2000).

[8]http://www.sigmaaldrich.com/etc/medialib/docs/Aldrich/Product_Information_Sheet/s5130pis.Par.0001.File.tmp/s5130pis.pdf (last accessed 22nd March 2013)

[9] Wang, P., Zakeeruddin, S. M., Comte, P., Exnar. I. & Grätzel, M. *Gelation of Ionic Liquid-Based Electrolytes with Silica Nanoparticles for Quasi-Solid-State Dye-Sensitized Solar Cells*, Journal of the American Chemical Society. 125: 1166-1167 (2003).

[10] Shimano, S., Zhou, H. & Honma, I. *Preparation of Nanohybrid Solid-State Electrolytes with Liquid-like Mobilities by Solidifying Ionic Liquids with Silica Particles*. Journal of Materials Chemistry, 19: 5216-5221 (2007).

[11] Vioux, A., Viau, L., Volland, S. & Bideau, J. L. *Use of ionic liquids in sol-gel; ionogels and applications*. Comptes Rendu Chimie, 13: 242-255 (2010).

[12] http://www2.dupont.com /Kapton/en_US/ (last accesed 20th September 2012).

[13] Lockett, V., Sedev, R., Ralston J., Horne, M., Rodopoulos. *Differential Capacitance of the Electrical Double Layer in Imidazolium-Based Ionic Liquids: Influence of Potential, Cation Size, and Temperature*. Journal of Physical Chemistry C, 112: 7486-7495 (2008).

[14] Masarapu, C, Zeng, H. F., Hung, K. H. & Wei, B. *Effect of temperature on the capacitance of carbon nanotube supercapacitors*. Acs Nano 3, 8: 2199-2206 (2009).

[15] Fernando, S., Gomes, C., Figueiredo, M., Costa, R., Martins, A. & Pereira, C. M. *The electrical double layer at the* [BMIM][PF6] *ionic liquid/electrode interface–Effect of temperature on the differential capacitance*. Journal of Electroanalytical Chemistry 622(2): 153-160 (2008).

[16] Holovko, M., Kapko, V., Henderson, D., Boda, D. *On the influence of ionic association on the capacitance of an electrical double layer*. Chemical Physics Letter, 341: 363-368 (2001).

[17] Worrall, D. R., Williams, S. L & Ganguly, T. *Ion-electron recombination on silica gel surfaces: experiment and modelling*. Photochemical & Photobiological Sciences, 5: 844–849 (2006).

[18] Stoudt, M. & Hubbard, J. *Analysis of deformation-induced surface morphologies in steel sheet*. Acta Materialia, 53: 4293–4304 (2005).

Chapter 10 – Conclusions and Suggestions for Future Work

The primary objective of this research program was to determine the feasibility of manufacturing an ionic liquid-based supercapacitor that could operate at temperatures up to 220 ^{o}C. A secondary objective was to determine the compatibility of ionic liquids with other cell components (e.g. current collectors) at high temperature and, if required, consider means of mitigating any problems. Both objectives were successfully achieved and original contributions have been made to electrochemical theory, experimental practise, and materials science.

The final supercapacitor design combined multiple components, such as high surface area activated carbon electrodes, a gelled ionic liquid electrolyte, a polyimide substrate, a glass fibre separator, and a silicone sealant. The resulting device was demonstrated to be stable for a minimum of three weeks at 220 ^{o}C. Remarkably, the capacitance was found to increase with increasing temperature, but at the cost of a decreased voltage stability window. As designed, individual cells were scalable, and had a measured capacitance directly proportional to the working electrode area. The largest prototype supercapacitor assembled was 20 × 20 cm and exhibited a capacitance of 20 F. The capacitance density was therefore 50 mF cm^{-2}.

In order to enhance the power density and energy density of supercapacitors, novel ionic liquids were developed which had enhanced voltage stability windows. In particular, quantum tunnelling theory was applied to the problem, and this revealed that butyltrimethylammonium bis(trifluoromethylsulfonyl)imide (BTM TFSI) and hexyltriethyl-ammonium bis(trifluoromethylsulfonyl)imide (HTE TFSI) were near-ideal electrolytes. These had voltage stability windows greater than 5 V at room temperature, and were chemically stable up to 350 ºC. This discovery forms the basis of a provisional patent application in the US Patent Office. Additionally, both ionic liquids could be gelled by fumed silica, thereby enhancing safety without compromising conductivity or capacitance.

High surface area carbon electrodes were successfully produced through the development of a screen printing technique. A number of activated carbon inks were developed through the optimisation of particle size, polymer binder, and solvent. The final composition had a

median particle size of 10 μm, a poly(vinylene fluoride) (PVDF) polymer binder, and a propylene carbonate solvent. This combination produced electrodes that were flexible, mechanically robust, and highly reproducible.

On an industrial scale, the presence of impurities might generate unwanted faradaic reactions that would decrease the working life of a supercapacitor. Therefore, a passivation technique was developed to forestall this problem. This involved the *in situ* electropolymerisation of bisphenol monomers and related compounds. The resulting films had a nanometer thickness and were stable up to 150 ºC. A patent for this process is also being considered.

A high precision (r^2 > 0.999 999) method for measuring the temperature dependence of conductivity was developed involving an AC impedance bridge technique. Highly reproducible data were acquired by employing ultra-slow temperature ramps (0.1 ºC min^{-1}) over a wide temperature range 20-195 ºC to eliminate thermal hysteresis. Data were recorded at a high sample rate (1 s^{-1}) and stored in computer memory. The results established that the temperature dependence of conductivity followed the Vogel-Tammann-Fulcher relation. The coincidence of the conductivity onset temperature with the glass transition temperature suggested a new theory of the glass transition. This latter led to the *ab initio* derivation of the Vogel-Tammann-Fulcher relation and implied that the activation energy for the onset of conduction was simply the Gibbs energy needed to detach the mobile species from the immobile matrix.

Overall, the present work has opened up several new lines of enquiry which could be usefully pursued in future work. Firstly, quantum theory could be used to extend the voltage stability window of ionic liquid anions. (So far, only cations have been investigated.) Secondly, it would be of interest to determine the extent and mechanism of the thermal degradation of ionic liquids at high temperature. In the present work, ionic liquids have been briefly heated to 350 ºC without any problems, but their long term stability remains an open question. Thirdly, it would be of some industrial interest to identify redox couples that could be cycled under supercapacitor conditions. These would provide improved capacitance, and might also form the basis of a new class of redox flow cell. Finally, many different types of activated carbon could be screened to minimise the problem of asynchronous charging. An activated carbon having a uniform pore size distribution would be ideal in this regard.

Appendices

Appendix 5A – Passivation kinetics of electrode blocking films

Preliminary data exploring the passivation kinetics of glassy carbon and a RAM electrode with poly(bisphenol A) is given in ***Figure 5A.1*** and ***5A.2.*** It can be seen that 50 s is sufficient time to guarantee that the residual current is less than 1 μA at all potential steps below 2 V. It can also readily be seen that the rate of reaction diminishes as a function of t^{-1}. This is an exceptionally unusual time dependence and may warrant further studies.

Glassy carbon macroelectrode

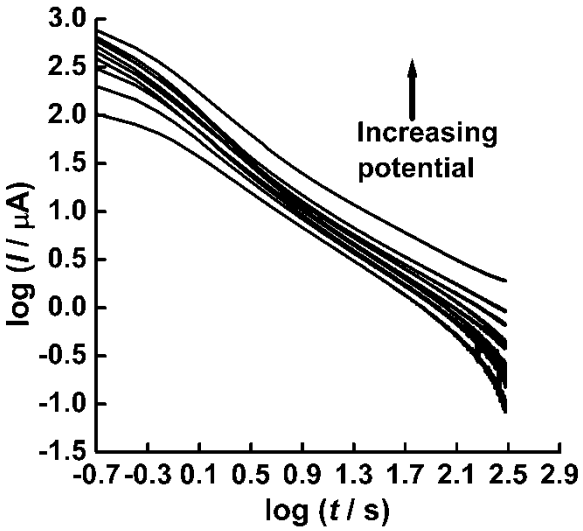

Figure 5A.1 – Kinetic analysis of the electrode passivation of a macro-glassy carbon electrode (d = 3.0 mm) in a solution of bisphenol A (saturated). The poly(bisphenol A) film was grown for 1000 s in a solution of butyltrimethylammonium bis(trifluoromethylsulfonyl)imide saturated with bisphenol A. The potential was held at –0.5 V (10 s) vs. Ag\|AgCl before being stepped to various potentials (1.2 to 2.0 V in 100 mV increments) and the current was monitored. The graph has been cut off at log t = 2.5 (350 s) to remove noise. The counter electrode was platinum gauze (A = 4.0 cm^2).

Table 5A.1 – A table of stepping potentials and the resulting gradients measured from a graph of log (I / μA) vs. log (t / s) for the passivation of a macro-carbon electrode with bisphenol A.

Potential / V	Gradient
1.2	*–0.89*
1.3	*–0.96*
1.4	*–0.96*
1.5	*–0.95*
1.6	*–0.96*
1.7	*–1.03*
1.8	*–0.96*
1.9	*–0.94*
2.0	*–1.01*

Array of carbon micro-electrodes

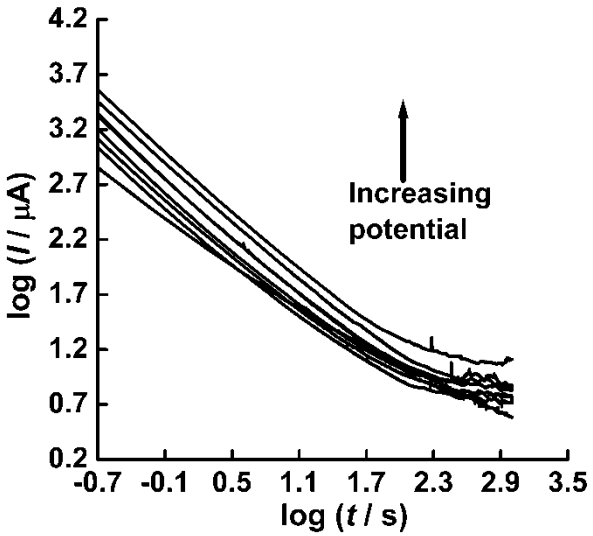

Figure 5A.2 – Kinetic analysis of the electrode passivation of a micro-electrode array (RAM electrode) in a solution of bisphenol A (saturated). The poly(bisphenol A) film was grown for 1000 s in a solution of butyltrimethylammonium bis(trifluoromethylsulfonyl)imide saturated with bisphenol A. The potential was held at –0.5 V (10 s) vs. Ag\|AgCl before being stepped to various potentials (1.2 to 2.0 V in 100 mV increments) and the current was monitored. The graph has been cut off at log t = 2.5 (350 s) to remove noise. The counter electrode was platinum gauze (A = 4.0 cm^2).

Table 5A.2 – A table of stepping potentials and the resulting gradients measured from a graph of log (I / μA) vs. log (t / s) for the passivation of a micro-electrode array (RAM electrode) with bisphenol A.

Potential / V	Gradient
1.2	*–*
1.3	*–*
1.4	*–0.83*
1.5	*–0.85*
1.6	*–0.86*
1.7	*–0.88*
1.8	*–0.88*
1.9	*–0.89*
2.0	*–0.88*

Appendix 6A – Preliminary work: temperature ramp *versus* temperature step

In order to obtain high precision conductivity measurements it was apparent that the temperature would need to be carefully controlled. However, there was uncertaincy as to whether a continuous temperature ramp or a step-and-hold ramp would the most suitable method. As a result, work was undertaken to optimise both methods. Once completed, conductivity data collected using the optimum continuous (0.1 ºC min^{-1}), and step-and-hold (step time for 5 ºC = 15 minutes, hold time = 1 h) temperature ramps were compared by calculating T_0 values**.** It can be seen from ***Figure 6A.1***, that there was no significant difference between the T_0 values extracted for the two different methods (221 K *vs* 224 K). Therefore, simply due to the fact that the ramp method was easier to implement and outputted data was easier to analyse, the continuous ramp was chosen.

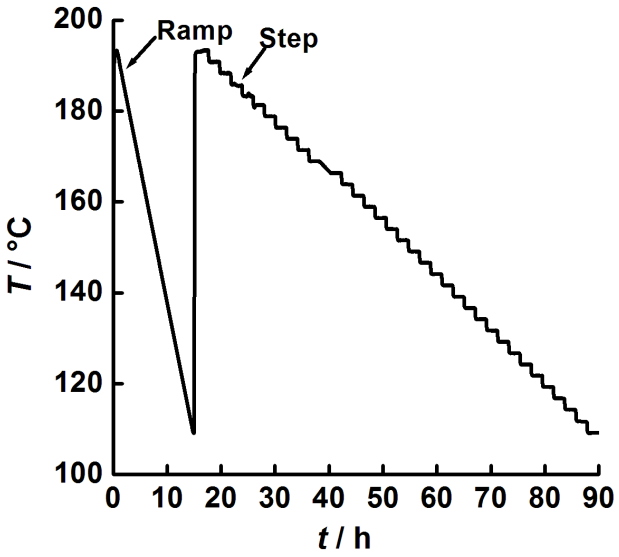

Figure 6A.1 – Temperature versus time profile for a temperature ramp (0.1 ºC min^{-1}), and a temperature step (step time: 15 minutes, hold time: 1 h, 5 ºC intervals), as labelled. Data points were recorded every 2 s from 378 K to 468 K, approximately 27,000 data points.

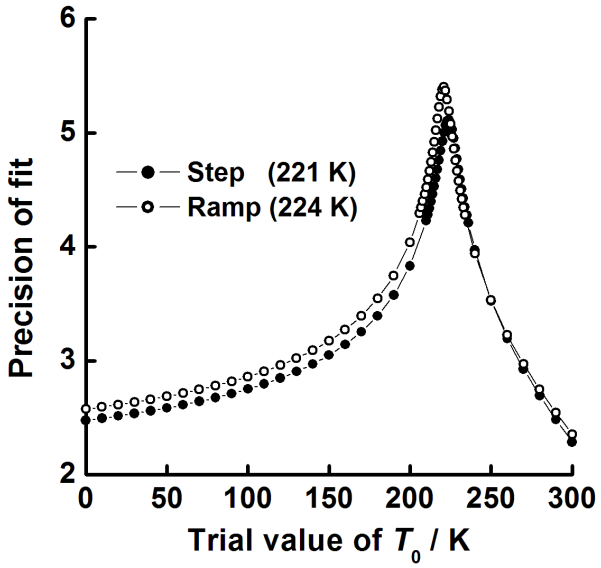

Figure 6A.2 – Graph showing similarity between T_0 values obtained by trial-and-error fitting of data obtained by a ramp (0.1 ℃ min^{-1}) and step method (15 minutes, hold time: 1 h, 5 ℃ intervals) to the VTF equation. Step = 221 K, ramp = 224 K.

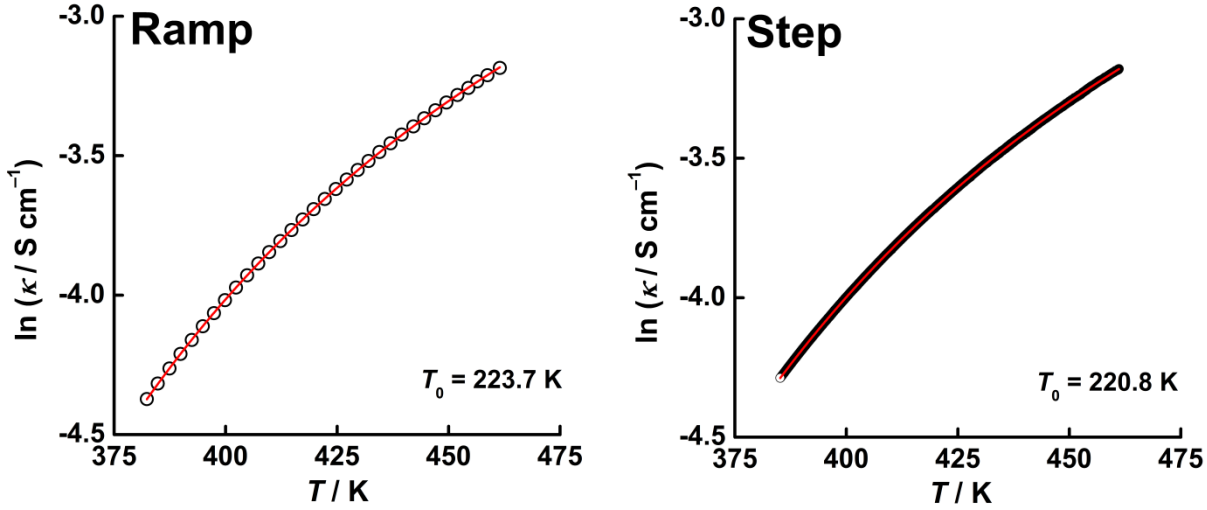

Figure 6A.3 – Graph showing similarity between T_0 values obtained using non-linear curve fitting function and a simplex algorithm for data obtained by left: a ramp (0.1 ℃ min^{-1}) and right: a step method (15 minutes, hold time: 1 h, 5 ℃ intervals). Step = 224 K, ramp = 220 K.

Appendix 6B – Preliminary work: Determination of optimum frequency for conductivity measurements

Table 6B.1 summarizes the frequency values where the minimum phase angle was observed for a range of ionic liquids. Supporting graphs are presented in ***Figures 6B.1 to 6B.12.*** 10 kHz was chosen as the measurement frequency for all ionic liquids for consistency and to allow direct comparison of results.

Table 6B.1 – Optimum frequencies for exploring the relationship between conductivity and temperature in ionic liquids.

Ionic Liquid	Optimum Frequency / kHz
Butyltrimethylammonium bis(trifluoromethylsulfonyl)imide	**10**
Hexyltriethylammonium bis(trifluoromethylsulfonyl)imide	**3**
1-Ethyl-3-methylimidazolium methanesulfonate	**1**
1-Butyl-3-methylimidazolium tetrafluoroborate	**10**
Tetrabutylammonium bis(trifluoromethylsulfonyl)imide	**10**
Tetrabutylphosphonium tetrafluoroborate	**10**

Tetrabutylammonium bis(trifluoromethylsulfonyl)imide

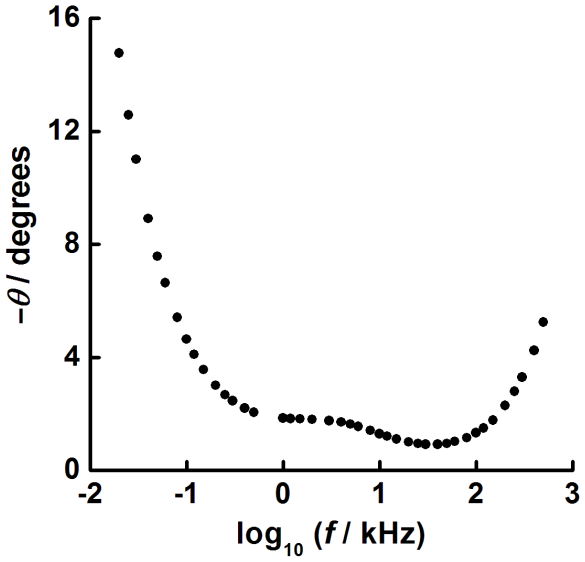

Figure 6B.1 – A plot of phase angle (degrees) versus log10 (frequency) for tetrabutylammonium bis(trifluoromethylsulfonyl)imide at 25 ºC. Data shown over a 20 Hz to 500 kHz frequency range and recorded using a Wayne-Kerr Precision Component Analyser (6430A). The minimum phase angle is at 10 kHz.

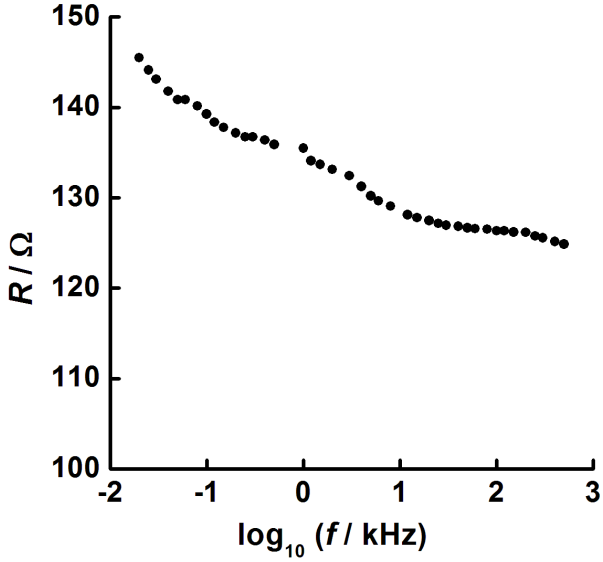

Figure 6B.2 – A plot of resistance (ohms) versus log_{10} (frequency) for tetrabutylammonium bis(trifluoromethylsulfonyl)imide at 25 ºC. Data shown over a 20 Hz to 500 kHz frequency range and recorded using a Wayne-Kerr Precision Component Analyser (6430A). The resistance is stable with frequency at 10 kHz.

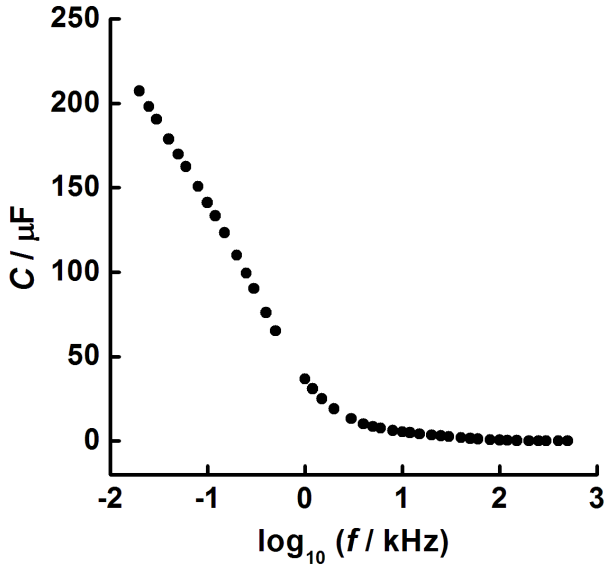

Figure 6B.3 – A plot of log_{10} frequency (kilohertz) versus capacitance (microfarads) for tetrabutylammonium bis(trifluoromethylsulfonyl)imide at 25°C. Data shown over a 20 Hz to 500 kHz frequency range and recorded using a Wayne-Kerr Precision Component Analyser (6430A).

Tetrabutylphosphonium tetrafluoroborate

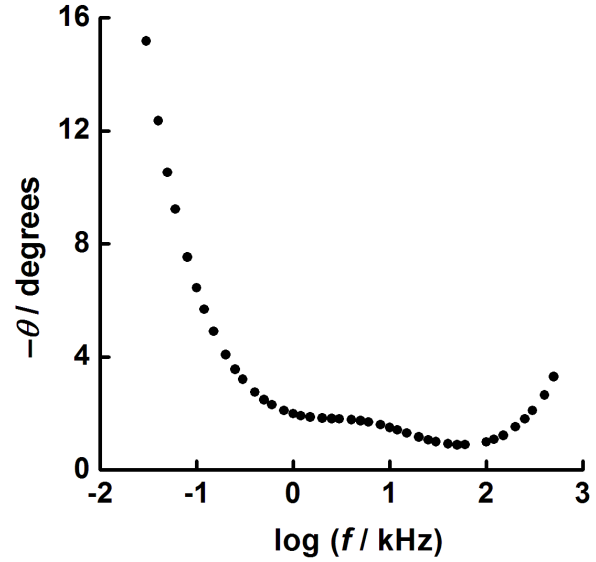

Figure 6B.4 –A plot of phase angle (degrees) versus log_{10} (frequency) for tetrabutylphosphonium tetrafluoroborate at 25 °C. Data shown over a 20 Hz to 500 kHz frequency range and recorded using a Wayne-Kerr Precision Component Analyser (6430A). The minimum phase angle is at 10 kHz.

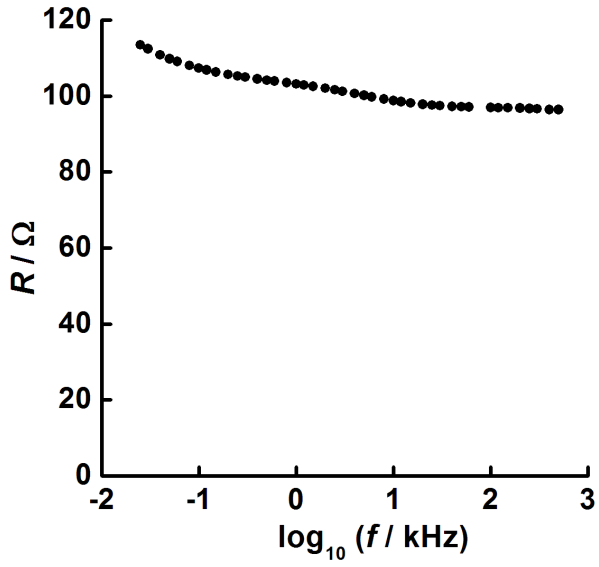

Figure 6B.5 – A plot of resistance (ohms) versus log_{10} (frequency) for tetrabutylphosphonium tetrafluoroborate at 25 ºC. Data shown over a 20 Hz to 500 kHz frequency range and recorded using a Wayne-Kerr Precision Component Analyser (6430A). The resistance is stable with frequency at 10 kHz.

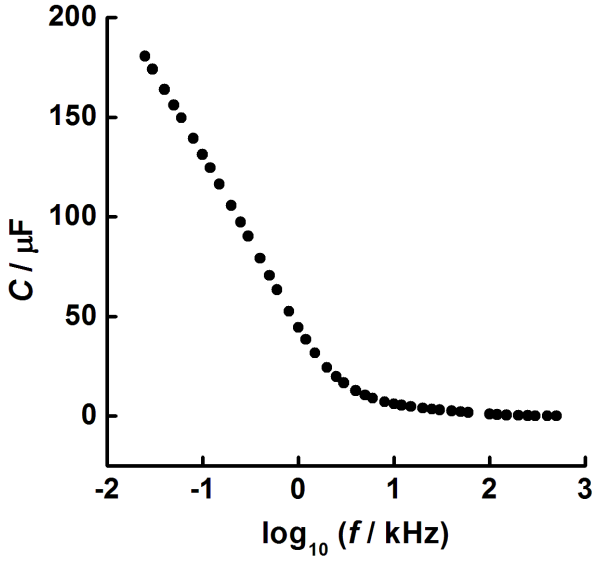

Figure 6B.6 – A plot of log_{10} frequency (kilohertz) versus capacitance (microfarads) for tetrabutylphosphonium tetrafluoroborate at 25 ºC. Data shown over a 20 Hz to 500 kHz frequency range and recorded using a Wayne-Kerr Precision Component Analyser (6430A).

1-Butyl-3-methylimidazolium tetrafluoroborate

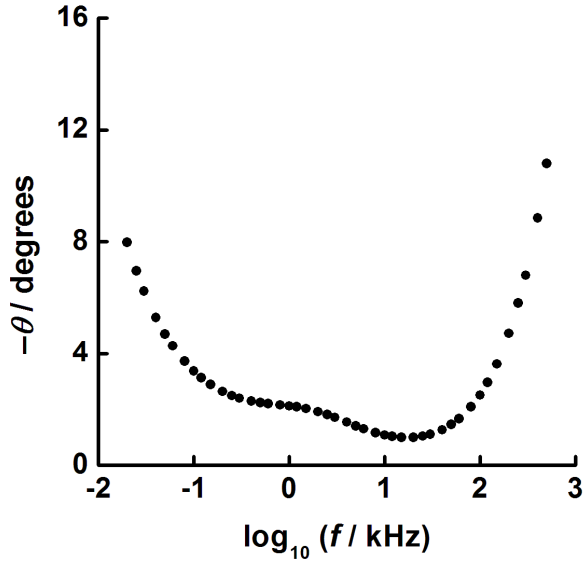

Figure 6B.7 – A plot of phase angle (degrees) versus log_{10} (frequency) for 1-butyl-3-methyl-imidazolium tetrafluoroborate at 25 ºC. Data shown over a 20 Hz to 500 kHz frequency range and recorded using a Wayne-Kerr Precision Component Analyser (6430A). The minimum phase angle is at 10 kHz.

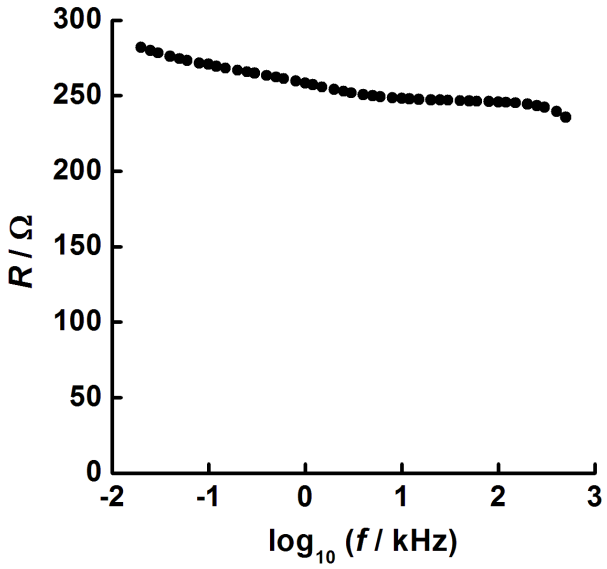

Figure 6B.8 – A plot of resistance (ohms) versus log_{10} (frequency) for tetrabutylphosphonium tetrafluoroborate at 25 ºC. Data shown over a 20 Hz to 500 kHz frequency range and recorded using a Wayne-Kerr Precision Component Analyser (6430A). The resistance is stable with frequency at 10 kHz.

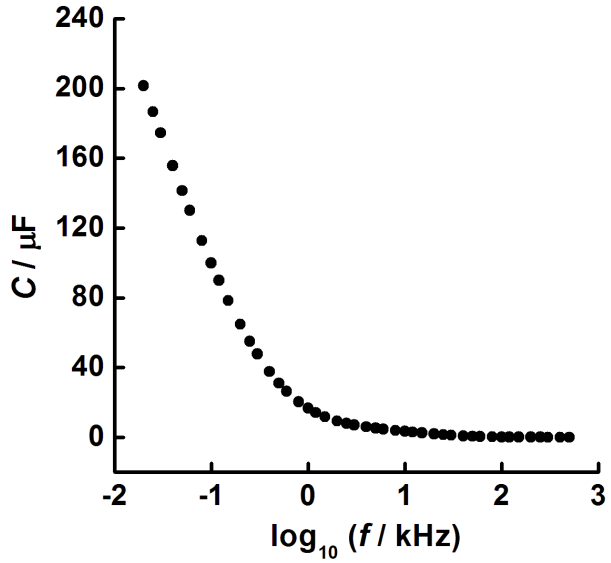

Figure 6B.9 – A plot of log_{10} frequency (kilohertz) vs. capacitance (microfarads) for 1-butyl-3-methylimidazolium tetrafluoroborate at 25 ºC. Data shown over a 20 Hz to 500 kHz frequency range and recorded using a Wayne-Kerr Precision Component Analyser (6430A).

Hexyltriethylammonium bis(trifluoromethylsulfonyl)imide

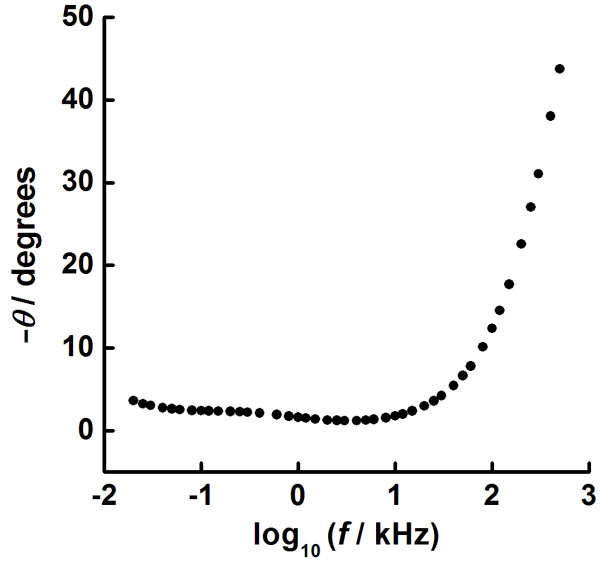

Figure 6B.10 – A plot of phase angle (degrees) versus log_{10} (frequency) for hexyltriethylammonium bis(trifluoromethylsulfonyl)imide at 25 ºC. Data shown over a 20 Hz to 500 kHz frequency range and recorded using a Wayne-Kerr Precision Component Analyser (6430A). The minimum phase angle is at 3 kHz.

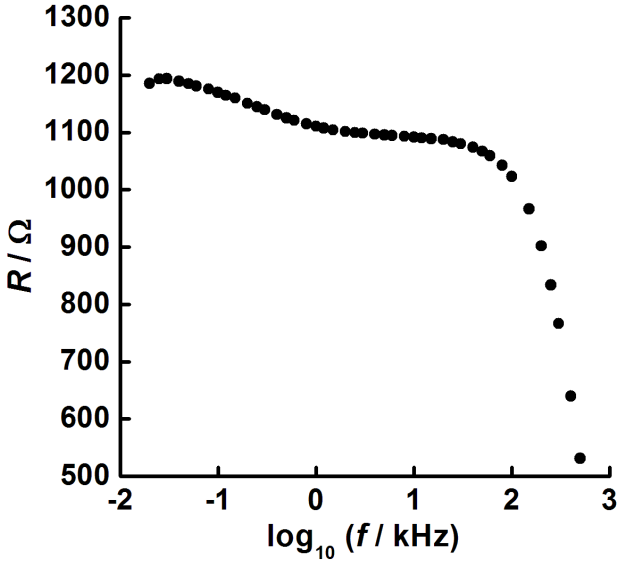

Figure 6B.11 – A plot of resistance (ohms) versus log_{10} (frequency) for hexyltriethylammonium bis(trifluoromethylsulfonyl)imide at 25 ºC. Data shown over a 20 Hz to 500 kHz frequency range and recorded using a Wayne-Kerr Precision Component Analyser (6430A). The resistance is stable with frequency at 3 kHz.

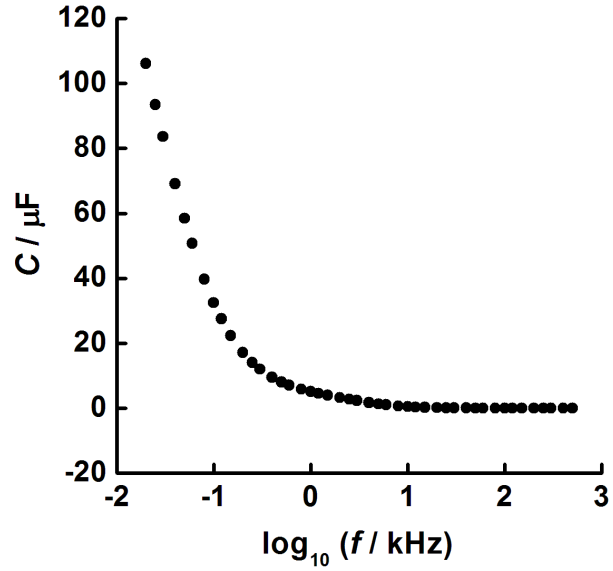

Figure 6B.12 – A plot of log_{10} frequency (kilohertz) versus capacitance (microfarads) for hexyltriethylammonium bis(trifluoromethylsulfonyl)imide at 25 ºC. Data shown over a 20 Hz to 500 kHz frequency range and recorded using a Wayne-Kerr Precision Component Analyser (6430A).

Appendix 6C – A new bench-top shock cooling method for measurement of T_g in ionic liquids

Here, a new bench-top 'shock cooling' method for measuring glass transition temperatures, as well as crystallisation temperatures. T_c, and melting point temperatures, T_m, in ionic liquids is presented. This method is advantageous in as much as it does not require the costly high-tech instrumentation needed for DSC measurements, and therefore, could be used as a cheap alternative where DSC is not available. ***Table 6.2*** shows the strong correlation between the numbers obtained via this method and the numbers recorded by DSC.

Prior to experiments, ionic liquids were heated to 130 ºC (24 h) to remove residual water, the same pre-treatment used prior to DSC analysis. The ionic liquid of choice was then poured into an insulated (expanded polystyrene) glass test tube and rapidly shock-cooled in liquid nitrogen to –196 ºC, (77 K), so that the ionic liquid went straight into the glassy state without crystallisation. The insulated test tube was then immediately placed into a thermos flask and allowed to warm to room temperature over a period of several hours. The temperature increase was measured over time using a temperature probe (Pt-100, Dostmann) immersed in the liquid, connected to a digital thermometer (P755-Log, Dostmann) with data logging capability. Temperature readings were recorded once every second. Since the temperature was measured over a relatively large range, from 77 K to 298 K, it was possible to identify T_c, and in some cases, T_m. The apparatus for the experiment can be seen in ***Figure 6C.1***.

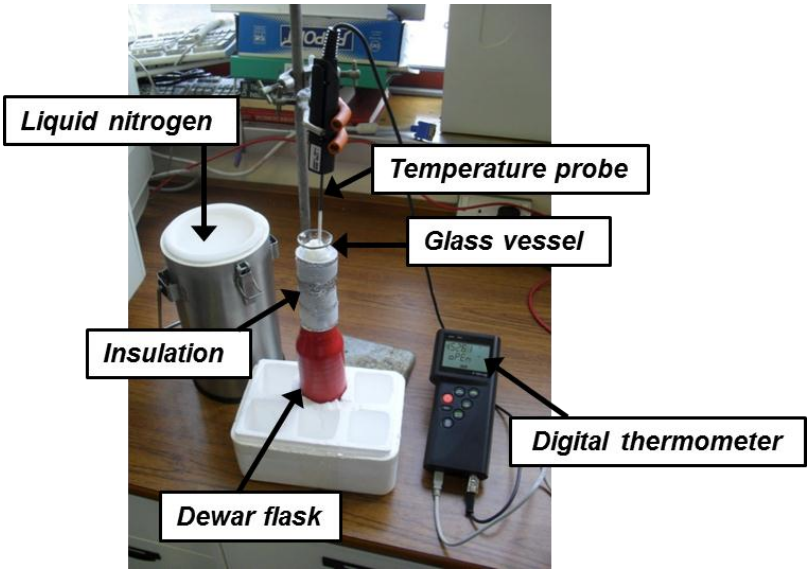

Figure 6C.1 – A photograph of the apparatus used for measuring phase transitions of ionic liquids by shock cooling method.

In order to extract T_m, T_c and T_g from the recorded thermal profile, the following method was applied. A 100 point adjacent smoothing average was applied to the temperature-time profile in order to minimise the effect of digitisation from the analogue to digital conversion employed by the digital thermometer. A transform, ***Equation 6C.1***, was then applied to the measured temperature data in order to reduce the curvature of the observed profile. By subtracting 300 from the temperature values (in K), and taking the reciprocal, a greater degree of straightening of the function is achieved at small values of *T*, given that room temperature (293 K) was the maximum achievable temperature in the system.

$$T^* = \frac{-1}{T - 300}$$

Equation 6C.1

The original temperature-time profile and the temperature-time profile achieved after applying the above transform can be seen in ***Figure 6C.2***.

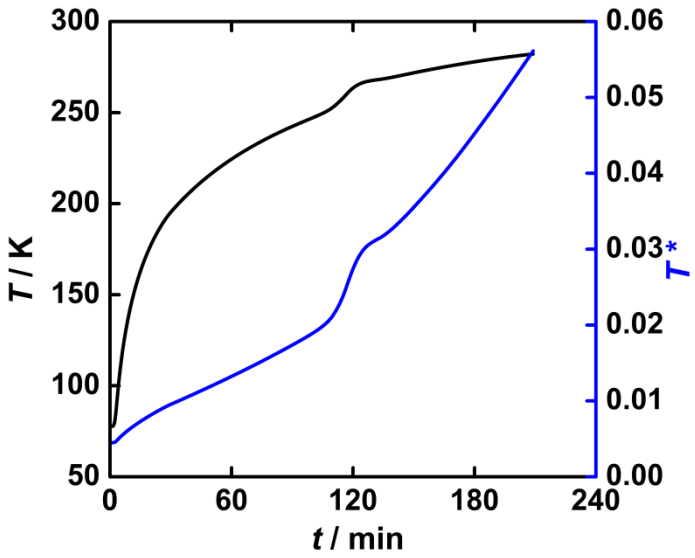

Figure 6C.2 – A plot of temperature (Kelvin), and T* versus time (minutes) for hexyltriethylammonium bis(trifluoromethylsulfonyl)imide. Blue line indicates T / K versus time (original data). Black line indicates T* versus time (following transform).

In order to extract the important features corresponding to phase changes, the transform *T** was differentiated with respect to time, to give *T*′* as shown in ***Figure 6C.3***. Positive changes are exothermic with negative changes being endothermic.

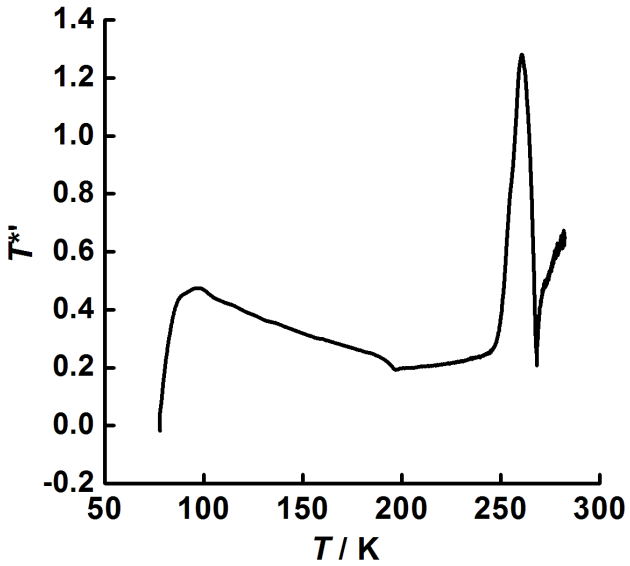

Figure 6C.3 – A plot of T*′ versus temperature (Kelvin) for hexyltriethylammonium bis(trifluoro-methylsulfonyl)imide.

In some cases, the first derivative was enough to be able to identify transition temperatures, however, when this was not the case, the data was differentiated again, termed T*″ to provide more obvious peaks for identifying transitions. The second derivative of the above data is given in ***Figure 6C.4***. The glass transition endotherm can be observed at –78.4 ºC (194.8K) and the crystallisation exotherm at –20.5 ºC (252.7 K). The observation of a phase change corresponding to the temperature of crystallisation during the warming cycle provides evidence that the ionic liquid goes straight into the glassy state (vitrifies) when subjected to rapid cooling, with no tendency to crystallise. Hence, when the ionic liquid is allowed to warm back up to room temperature the mobility of the ions increases, and at a given temperature, they are able to arrange themselves into an ordered solid, evidence by a sharp exotherm in the temperature profile for T_c. T_m cannot be identified in this profile as the melting point of the ionic liquids is beyond the final temperature recorded in this run.

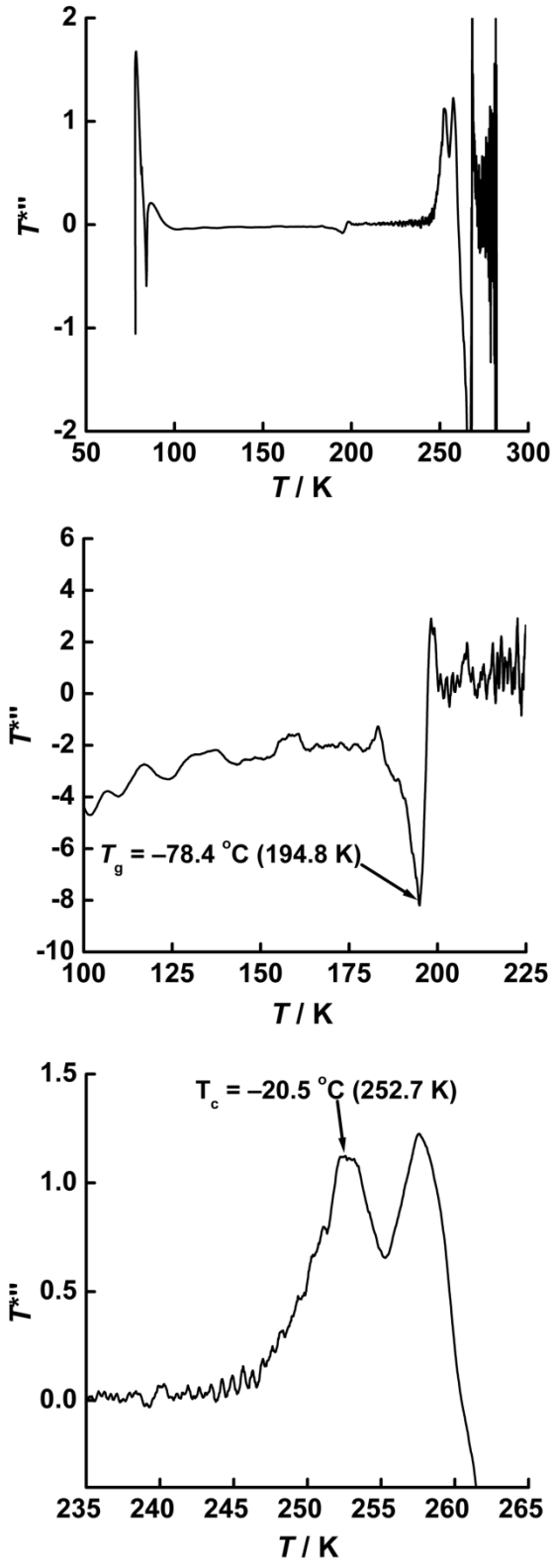

Figure 6C.4 – Plots of T*″ vs. temperature (Kelvin) for hexyltriethylammonium bis(trifluoromethyl-sulfonyl)imide. Top: over the full temperature range, middle: over the temperature range 100 K to 225 K, highlighting the glass transition temperature T_g, and bottom: over the temperature range 235 K to 265 K, highlighting the crystallisation temperature T_c. T_g is –78.4 ºC (194.8 K) and T_c is –20.5 ºC (252.7 K).

Appendix 6D – DSC thermograms of the glass transition region for BTM TFSI and HTE TFSI measured by DSC

In ***Table 6.2***, the glass transition temperatures of HTE and BTM are reported. ***Figure 6D.1*** shows the supporting DSC thermograms which from which the transition temperatures were obtained using Universal Analysis 2000 software (version 4.3, TA instruments).

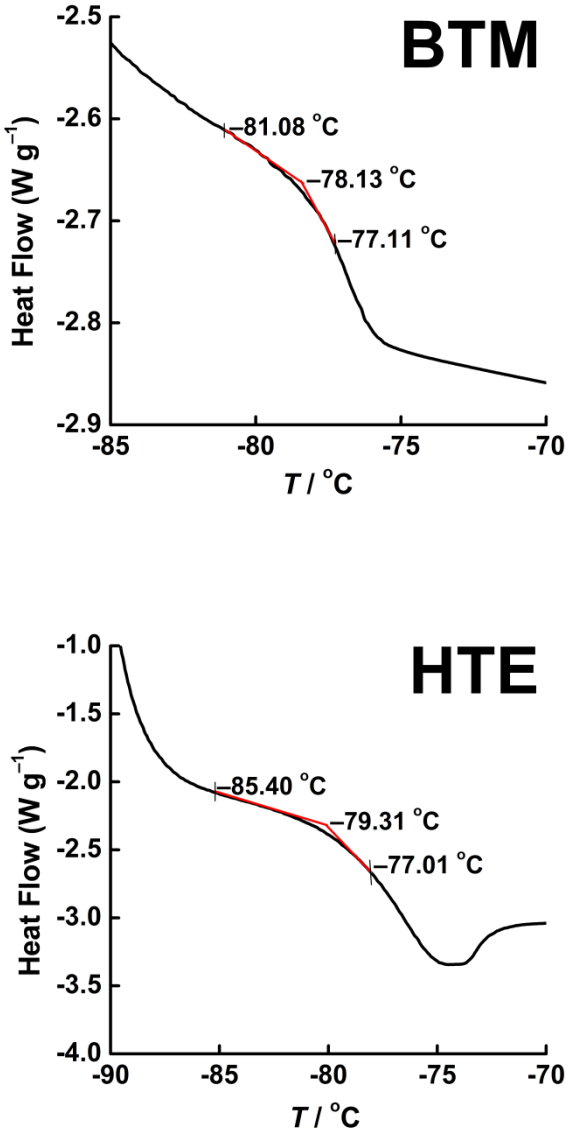

Figure 6D.1 – DSC curves showing the glass transition temperature (T_g / ℃) of BTM TFSI (top) and HTE TFSI (bottom). The curve shows T_1, the onset of T_g, and T_2, the midpoint of T_g (which is the intersect between the tangent and co-tangent) for both ionic liquids. For BTM, T_1 = –81.08 ℃ and T_2 = –78.13 ℃. For HTE, T_1 = –85.40 ℃ and T_2 = –79.31 ℃.

Appendix 6E – Supporting data for *Figure 6.15*

Before the automation of the data collection was feasible, data was manually collected for a variety of ionic liquids. Below plots of conductivity, capacitance, phase angle and resistance *versus* temperature are given for these measurements along with volcano plots displaying the T_0 values derived from the data.

Butyltrimethylammonium bis(trifluoromethylsulfonyl)imide

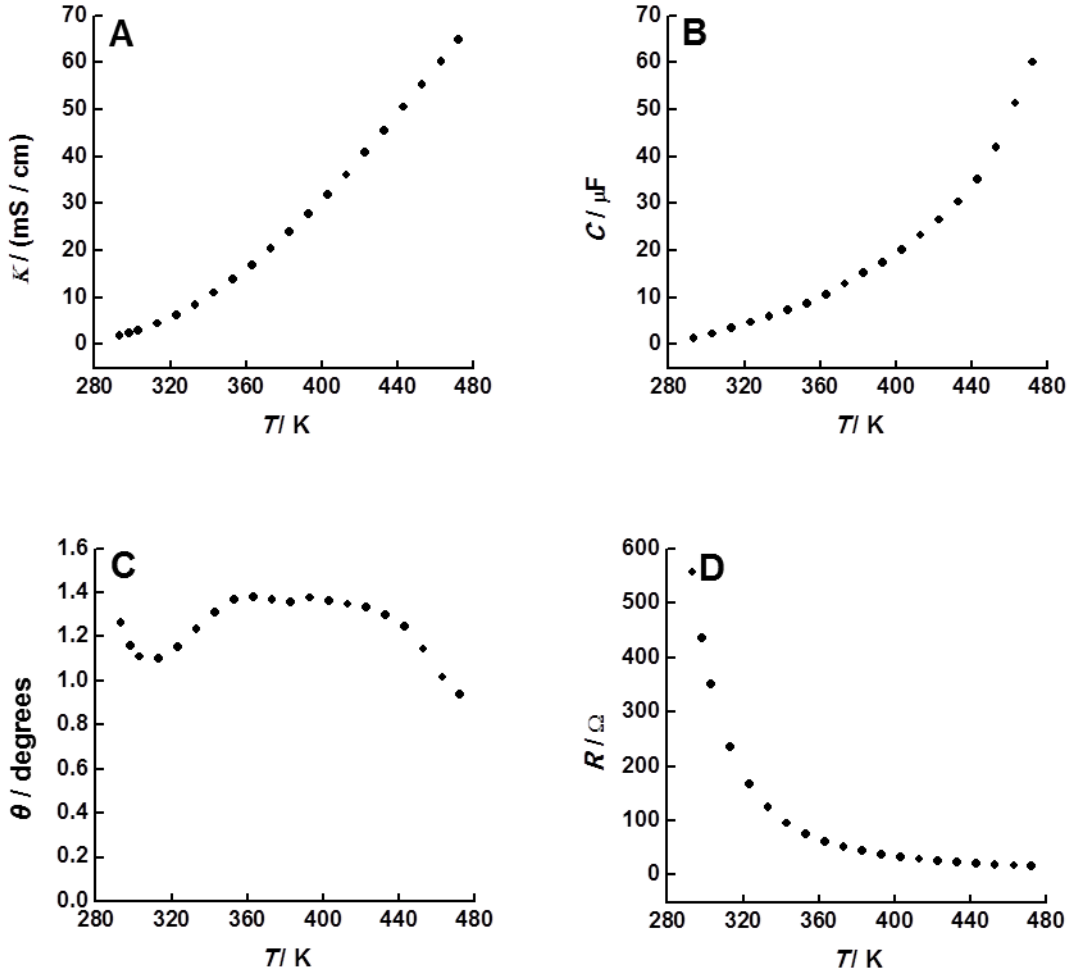

Figure 6E.1 – A plot of A. capacitance (microfarads) versus temperature (Kelvin) B. conductivity (millisiemens per centimetre) versus temperature (Kelvin) C. phase angle (degrees) versus temperature (Kelvin), and D. resistance (ohms) versus temperature (Kelvin) for butyltrimethylammonium bis(trifluoromethylsulfonyl)imide over a temperature range of 25 ºC to 199 ºC at 10 kHz. The data was collected for increasing and decreasing temperature runs to ensure there was no thermal hysteresis. Shown above are the data for the decreasing temperature run. At each temperature the apparatus was given 15 minutes to equilibrate thermally.

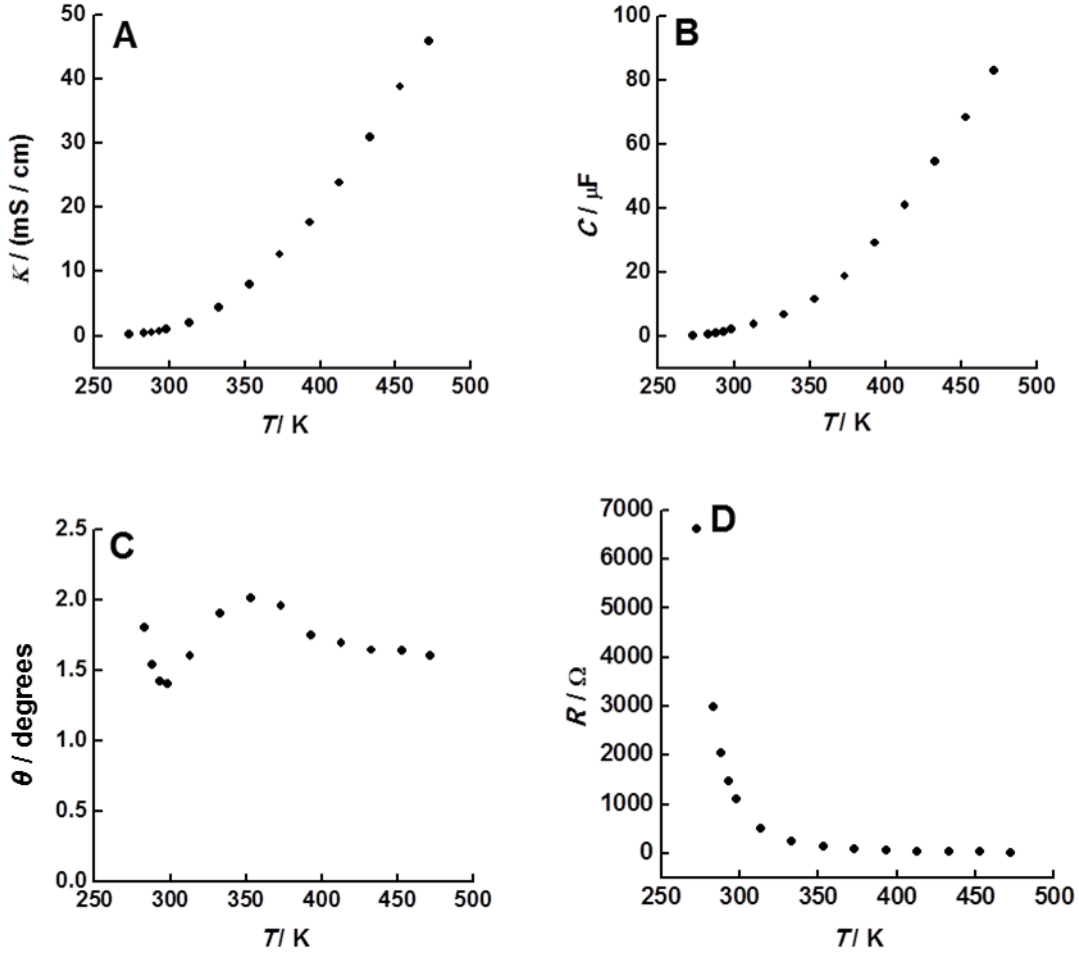

Figure 6E.2 – A plot of A. capacitance (microfarads) versus temperature (Kelvin) B. conductivity (millisiemens per centimetre) versus temperature (Kelvin) C. phase angle (degrees) versus temperature (Kelvin), and D. resistance (ohms) versus temperature (Kelvin) for hexyltriethylammonium bis(trifluoromethylsulfonyl)imide over a temperature range of 25 ºC to 199 ºC at 3kHz. The data was collected for increasing and decreasing temperature runs to ensure there was no thermal hysteresis. Shown above are the data for the decreasing temperature run. At each temperature the apparatus was given 15 minutes to equilibrate thermally.

1-Ethyl-3-methylimidazolium methanesulfonate

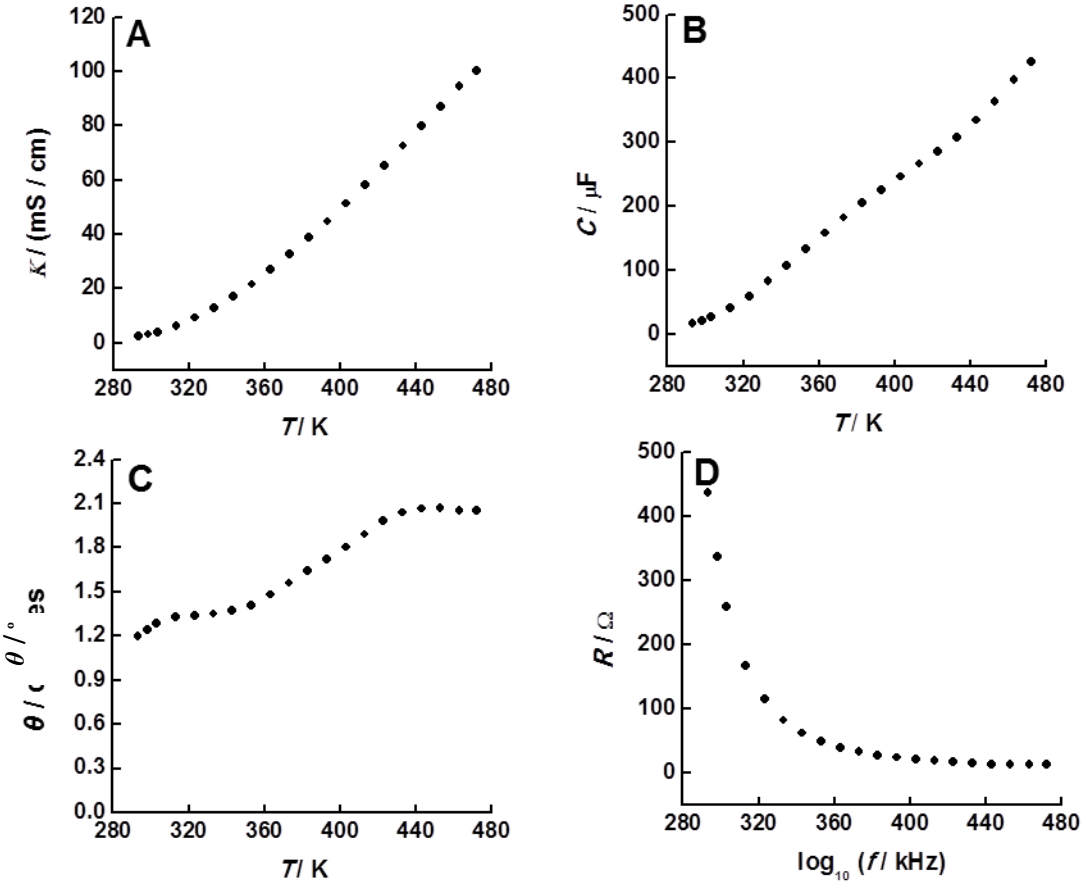

Figure 6E.3– A plot of A. capacitance (microfarads) versus temperature (Kelvin) B. conductivity (millisiemens per centimetre) versus temperature (Kelvin) C. phase angle (degrees) versus temperature (Kelvin), and D. resistance (ohms) versus temperature (Kelvin) for 1-ethyl-3-methylimidazolium methanesulfonate over a temperature range of 20 ºC to 199 ºC at 1 kHz. The data was collected for increasing and decreasing temperature runs to ensure there was no thermal hysteresis. Shown above are the data for the decreasing temperature run. At each temperature the apparatus was given 15 minutes to equilibrate thermally.

1-Butyl-3-methylimidazolium tetrafluoroborate

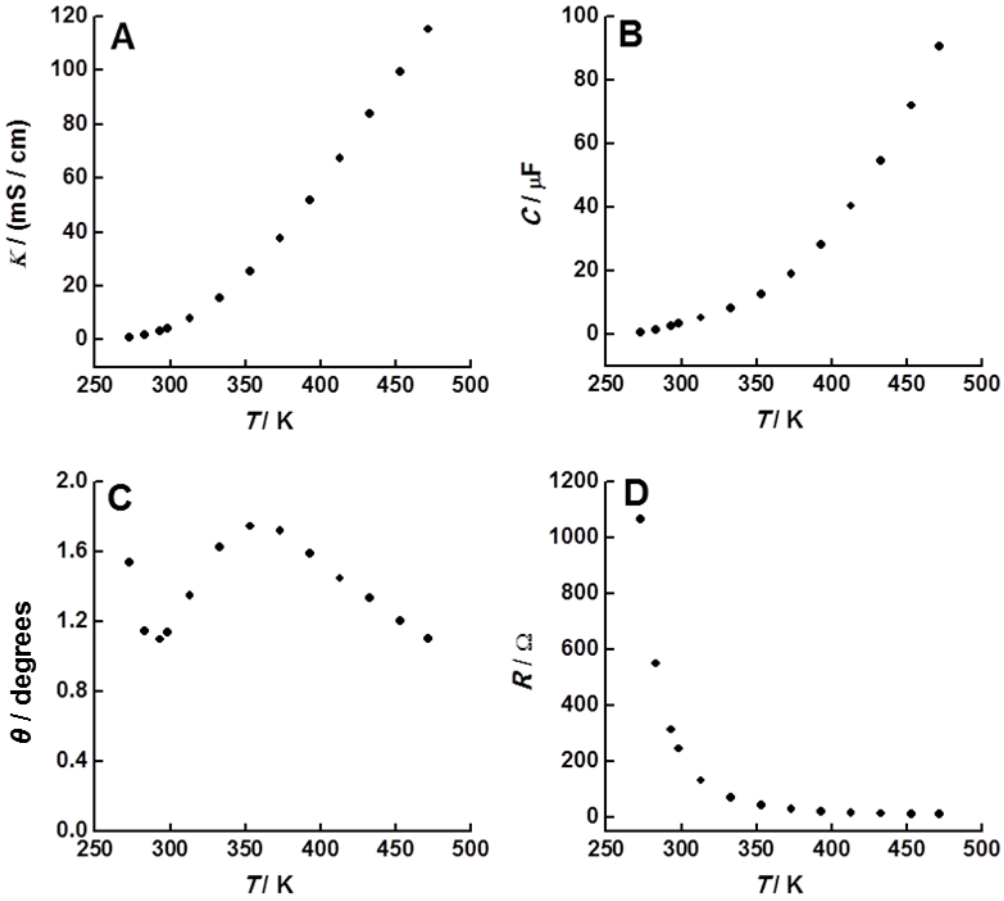

Figure 6E.4 – A plot of A. capacitance (microfarads) versus temperature (Kelvin) B. conductivity (millisiemens per centimetre) versus temperature (Kelvin) C. phase angle (degrees) versus temperature (Kelvin), and D. resistance (ohms) versus temperature (Kelvin) for 1-butyl-3-methylimidazolium tetrafluoroborate over a temperature range of 25 ºC to 199 ºC at 10 kHz. The data was collected for increasing and decreasing temperature runs to ensure there was no thermal hysteresis. Shown above are the data for the decreasing temperature run. At each temperature the apparatus was given 15 minutes to equilibrate thermally.

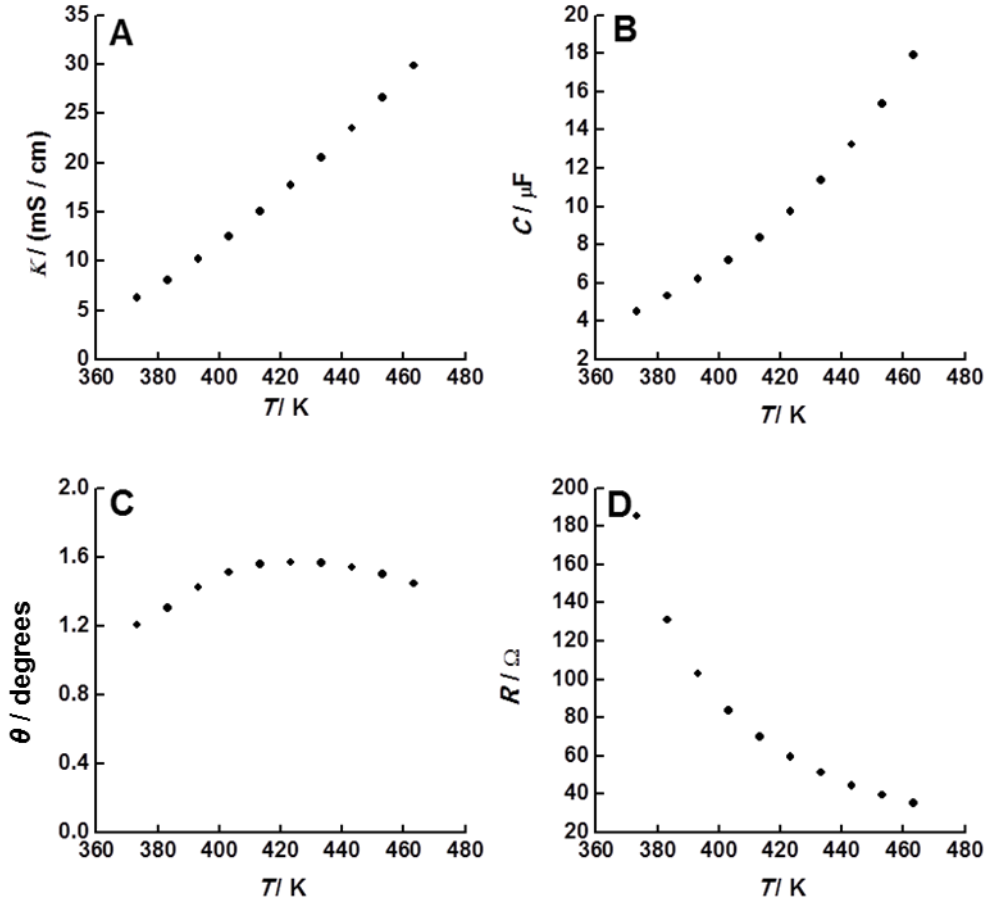

Figure 6E.5 – A plot of (A) capacitance (microfarads) versus temperature (Kelvin) and (B) conductivity (millisiemens per centimetre) versus temperature (Kelvin) C. phase angle (degrees) versus temperature (Kelvin), and D. resistance (ohms) versus temperature (Kelvin) for tetrabutylammonium bis(trifluoromethylsulfonyl)imide over a temperature range of 100 ºC to 190 ºC at 10 kHz. The data was collected for increasing and decreasing temperature runs to ensure there was no thermal hysteresis. Shown above are the data for the decreasing temperature run. At each temperature the apparatus was given 15 minutes to equilibrate thermally.

Tetrabutylphosphonium tetrafluoroborate

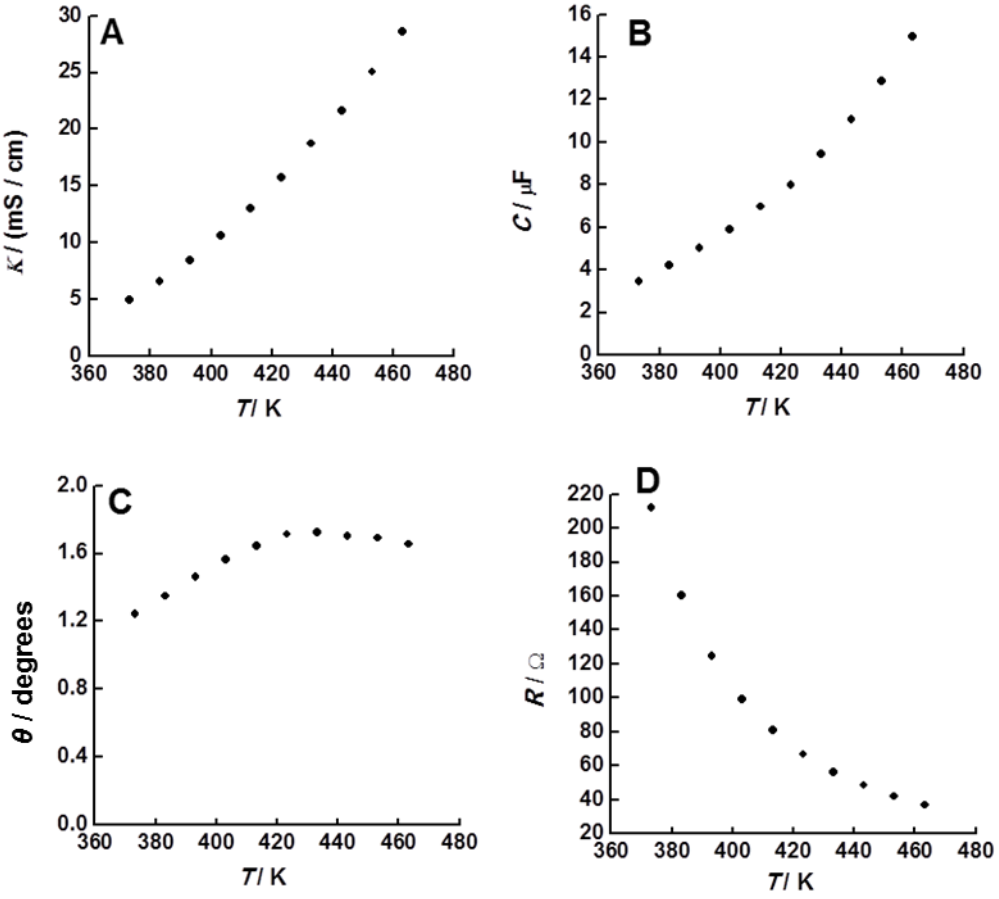

Figure 6E.6 – A plot of (A) capacitance (microfarads) versus temperature (Kelvin) and (B) conductivity (millisiemens per centimetre) versus temperature (Kelvin) C. phase angle (degrees) versus temperature (Kelvin), and D. resistance (ohms) versus temperature (Kelvin) for tetrabutylphosphonium tetrafluoroborate over a temperature range of 100 ºC to 190 ºC at 10 kHz. The data was collected for increasing and decreasing temperature runs to ensure there was no thermal hysteresis. Shown above are the data for the decreasing temperature run. At each temperature the apparatus was given 15 minutes to equilibrate thermally.

Determination of T_0

1-Ethyl-3-methylimidazolium methanesulfonate

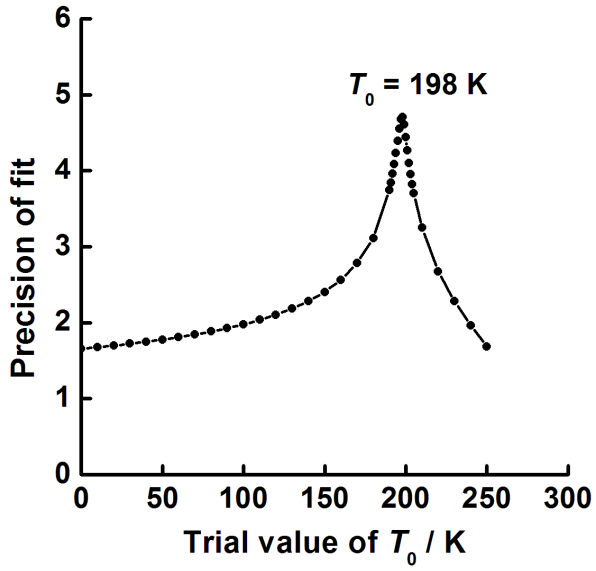

Figure 6E.7 – A plot of precision of fit versus trial values of T_0 (0 to 290 Kelvin) for 1-ethyl-3-methylimidazolium methanesulfonate. The T_0 value with the most precise fit is 198 K.

***Tetra**butylammonium bis(trifluoromethylsulfonyl)imide*

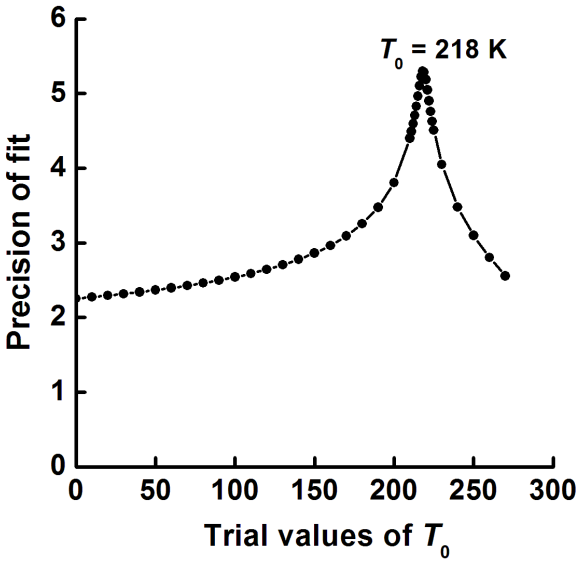

Figure 6E.8 – A plot of precision of fit versus trial values of T_0 (0 to 290 Kelvin) for tetrabutylammonium bis(trifluoromethylsulfonyl)imide. The T_0 value with the most precise fit is 218 K.

Butyltrimethylammonium bis(trifluoromethylsulfonyl)imide

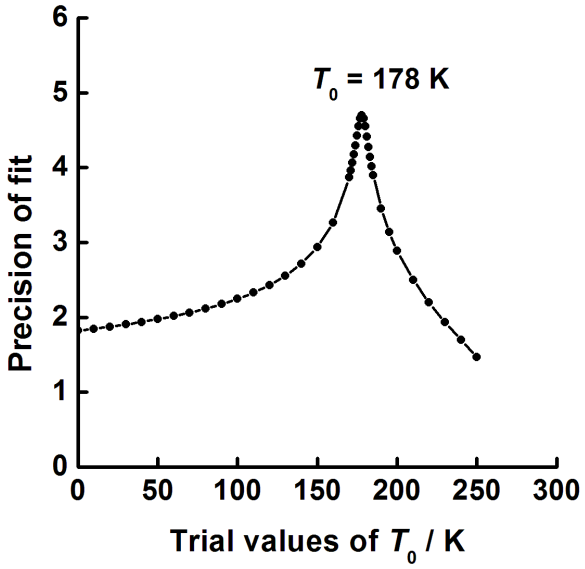

Figure 6E.9 – A plot of precision of fit versus trial values of T_0 (0 to 290 Kelvin) for Butyltrimethylammonium bis(trifluoromethylsulfonyl)imide. The T_0 value with the most precise fit is 178 K.

Hexyltriethylammonium bis(trifluoromethylsulfonyl)imide

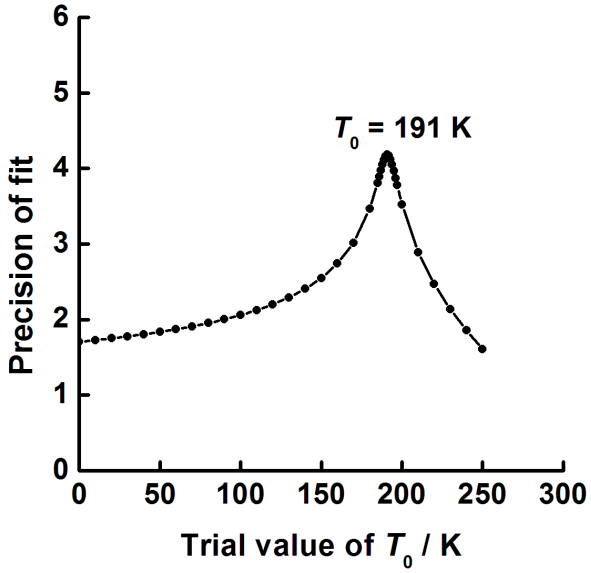

Figure 6E.10 – A plot of precision of fit versus trial values of T_0 (0 to 290 Kelvin) for hexyltriethyl-ammonium bis(trifluoromethylsulfonyl)imide. The T_0 value with the most precise fit is 191 K.

Tetrabutylphosphonium tetrafluoroborate

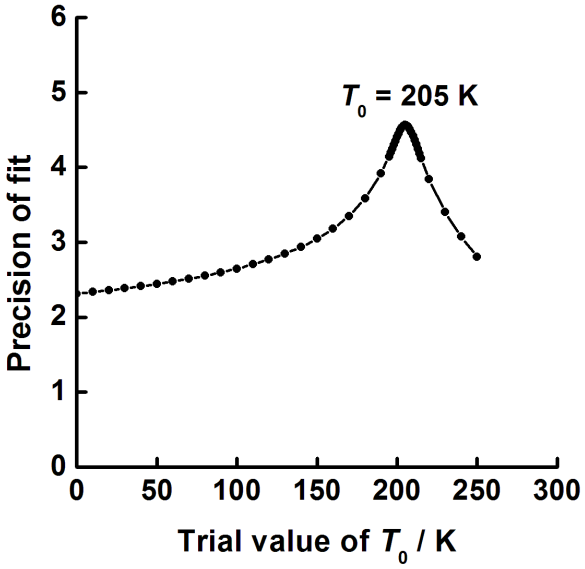

Figure 6E.11 – A plot of precision of fit versus trial values of T_0 (0 to 290 Kelvin) for tetrabutyl-phosphonium tetrafluoroborate. The T_0 value with the most precise fit is 205 K.

1-Butyl-3-methylimidazolium tetrafluoroborate

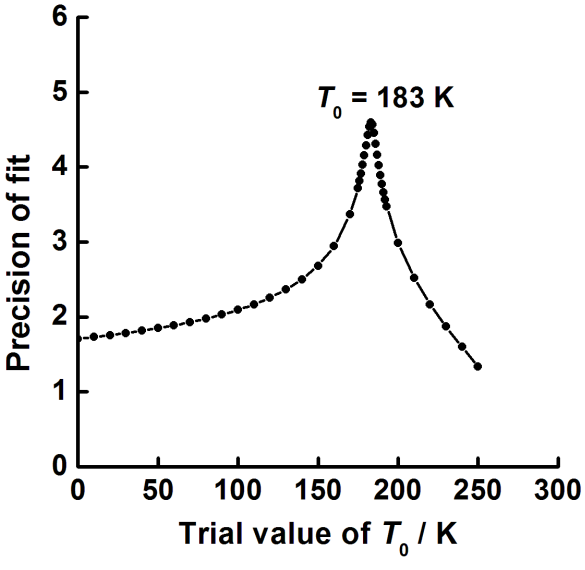

Figure 6E.12 – A plot of precision of fit versus trial values of T_0 (0 to 290 Kelvin) for 1-butyl-3-methyl-imidazolium tetrafluoroborate. The T_0 value with the most precise fit is 183 K.

Appendix 7A – SEM images of platinum black deposited to gold wire.

Figure 7A.1 shows SEM images of gold wire (E401-3, Agar Scientific Ltd) after platinum black deposition from a solution of 2% K_2PtCl_6 in 2 M HCl. The deposition conditions were as follows:

- 10 voltammetric cycles (–0.2 V to +0.9 V at 200 mV s^{-1}).
- 10 minutes (–0.38 V *vs.* SCE, 32 mA)
- 60 minutes (–0.35 V *vs.* SCE, 32 mA)

The evolving surface area of the platinum black deposit can be seen in ***Figure 7A.1***. A fractal growth pattern is observed.

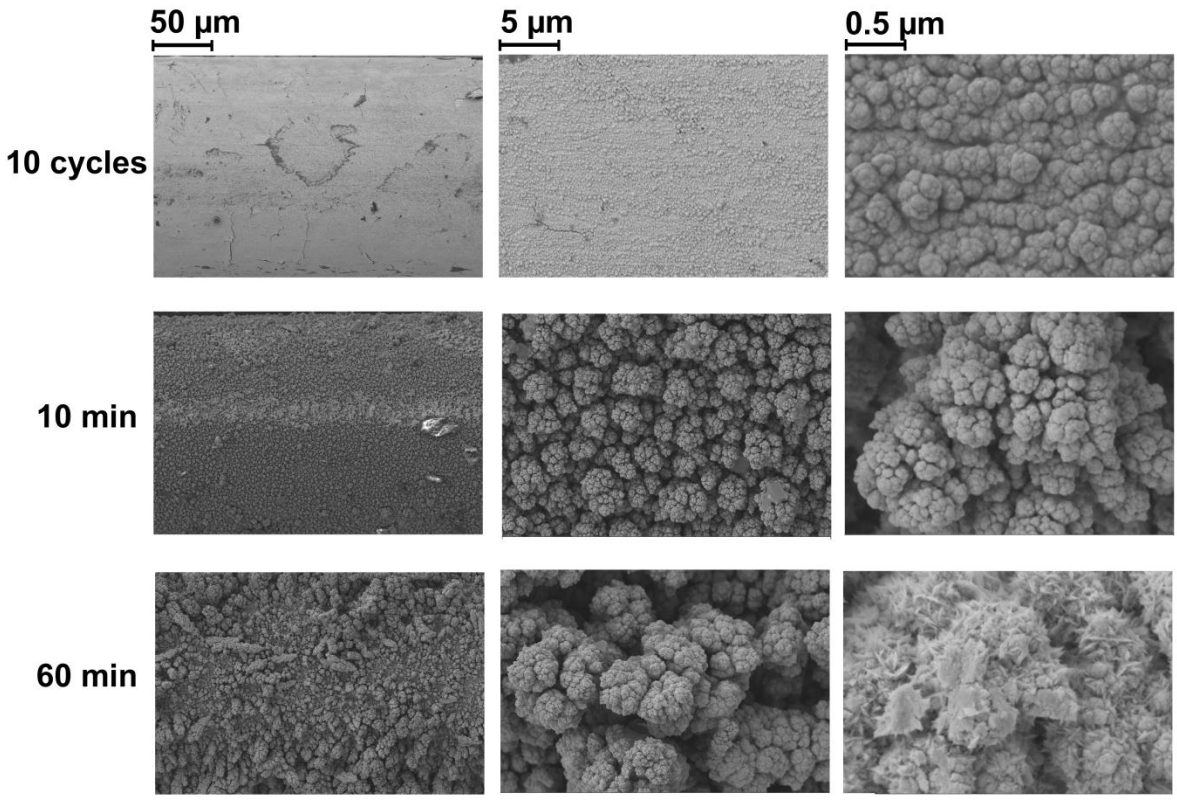

Figure 7A.1 – Morphogenesis of platinum black on a gold wire substrate as a function of deposition time for a gold wire (E401-3, Agar Scientific Ltd). Top: after 10 voltammetric cycles in 0.06 M chloroplatinate solution. Middle: after 10 minutes deposition at –0.38 V (32 mA) vs. SCE. Bottom: after 60 min deposition at –0.35 mV (33 mA) vs. SCE. Scale bars 50 µm, 5 µm, and 0.5 µm (as labelled).

Appendix 7B – Impedance plots

Figure 7B.1 shows impedance plots in the complex plane for a PIG electrode in hexyltriethylammonium bis(trifluoromethylsulfonyl)imide. It can be observed that the optimum measuring frequency is 10 kHz where the phase angle is only 2.85° and stray capacitance is no factor.

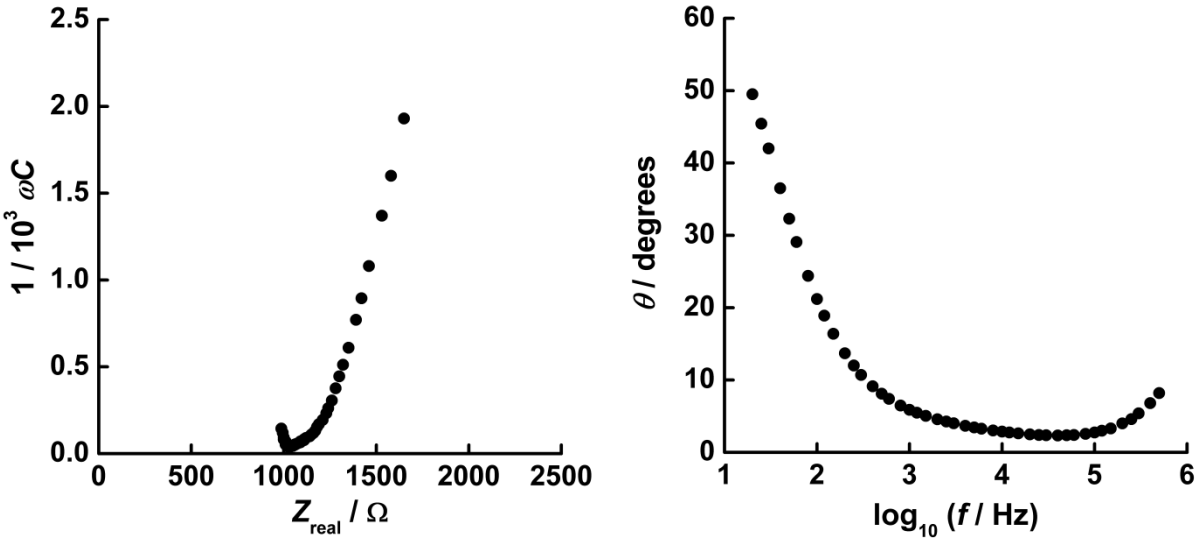

Figure 7B.1 – An impedance plot in the complex plane (left), and a plot of phase angle (°) vs. log_{10} frequency (kHz) (right) for HTE TFSI measured using a PIG electrode. Data shown over the frequency range 20 Hz to 500 kHz. Data recorded using a Wayne-Kerr Precision Component Analyser (6430 A). The phase angle at 10 kHz is 2.85°.

Appendix 7C – An unexpected side effect: the dissolution of the interdigitated gold electrode connectors at open circuit potential

An unexpected finding during the platinisation work with the interdigitated gold electrodes was that any exposed gold remaining after platinum black deposition was rapidly corroded away at open circuit potential. The oxidisation current was balanced by reduction of H^+ ions at the platinum black surface, and the gold was dissolved in the chloride solution. An example of a damaged electrode is shown in ***Figure 7C.1***. The corrosion of the gold ruins the current collector capability of the electrode and highlights the need for preventative measures. Short term, it was evident that the platinised gold needed to be removed from the platinising solution immediately upon completion of platinisation. Long term, a possible solution to the corrosion problem could be to passivate the finished product using the recently discovered poly(resveratrol) technique presented in ***Chapter 5***.

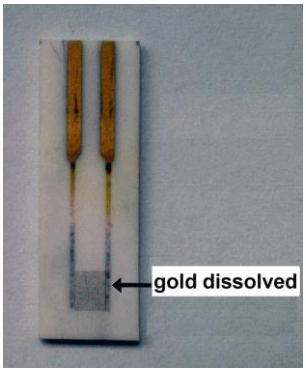

Figure 7C.1 – The effect of gold dissolution in chloride solution at open circuit (5 h).

9A – Thermal degradation temperatures of ionic liquids

The thermal degradation profiles of several ionic liquids are shown in ***Figures 9A.1*** to ***Figures 9A.11***.

Butyltrimethylammonium bis(trifluoromethylsulfonyl)imide

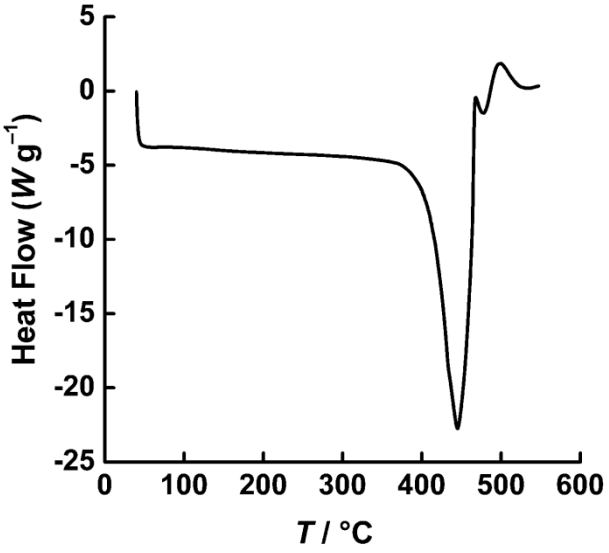

Figure 9A.1 – A plot of heat flow (W g^{-1}) vs. temperature (ºC) for the ionic liquid butyltrimethylammonium bis(trifluoromethylsulfonyl)imide. The onset of thermal degradation can be seen at ~371 ºC. Thermogram recorded using a Q-1000 Differential Scanning Calorimeter (TA Instruments) under a nitrogen atmosphere (20 mL min-1) from 40 ºC to 550 ºC at a rate of 10 ºC min^{-1}.

1-Ethyl-3-methylimidazolium methanesulfonate

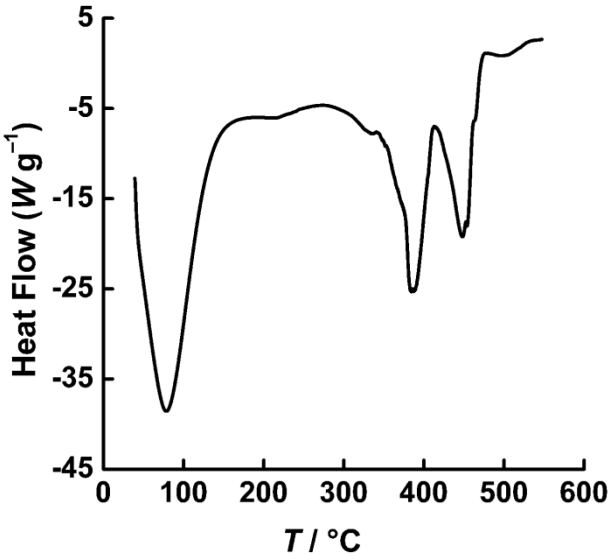

Figure 9A.2 – A plot of heat flow (W g^{-1}) vs. temperature (ºC) for the ionic liquid 1-ethyl-3-methylimidazolium methanesulfonate. The onset of thermal degradation can be seen at ~324 ºC. Thermogram recorded using a Q-1000 Differential Scanning Calorimeter (TA Instruments) under a nitrogen atmosphere (20 mL min-1) from 40 ºC to 550 ºC at a rate of 10 ºC min^{-1}.

1-Butyl-3-methylimidazolium tetrafluoroborate

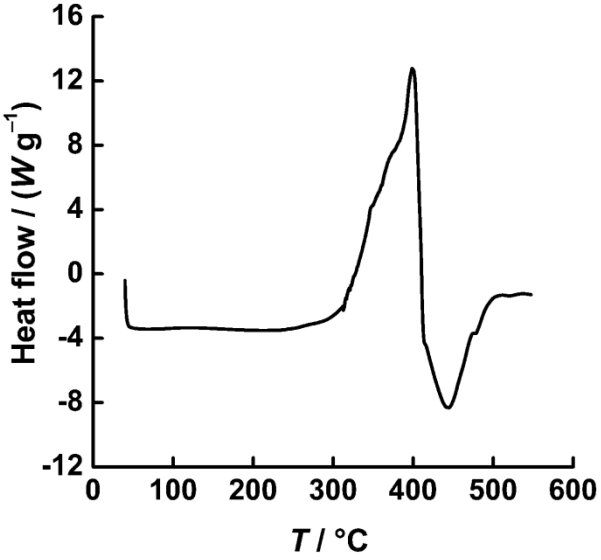

Figure 9A.3 – A plot of heat flow (W g^{-1}) vs. temperature (ºC) for the ionic liquid 1-butyl-3-methylimidazolium tetrafluoroborate. The onset of thermal degradation can be seen at ~325 ºC. Thermogram recorded using a Q-1000 Differential Scanning Calorimeter (TA Instruments) under a nitrogen atmosphere (20 mL min^{-1}) from 40 ºC to 550 ºC at a rate of 10 ºC min^{-1}.

Tetrabutylphosphonium tetrafluoroborate

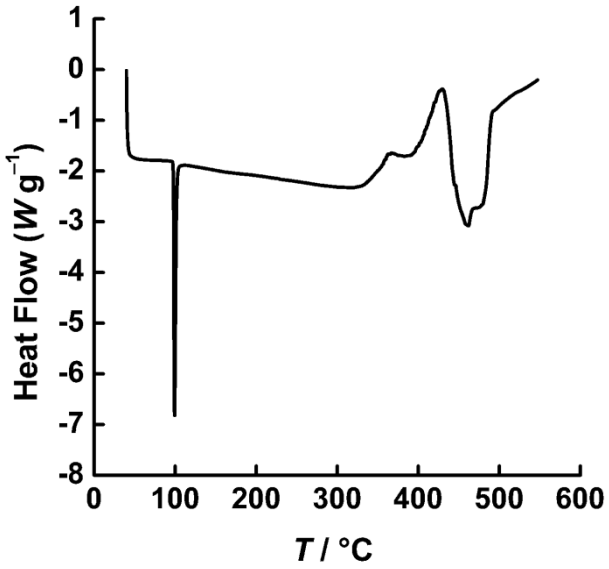

Figure 9A.4 – A plot of heat flow (W g^{-1}) vs. temperature (ºC) for the ionic liquid tetrabutylphosphonium tetrafluoroborate. The onset of thermal degradation can be seen at ~326 ºC. Thermogram recorded using a Q-1000 Differential Scanning Calorimeter (TA Instruments) under a nitrogen atmosphere (20 mL min^{-1}) from 40 ºC to 550 ºC at a rate of 10 ºC min^{-1}.

Tetramethylammonium bis(trifluoromethylsulfonyl)imide

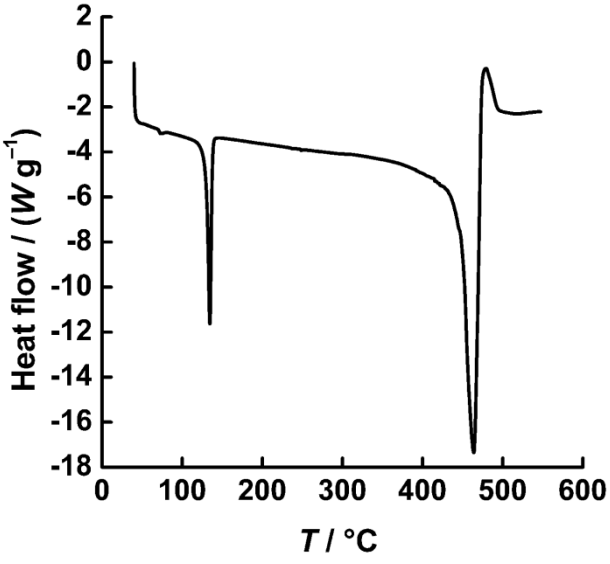

Figure 9A.5 – A plot of heat flow (W g^{-1}) vs. temperature (ºC) for the ionic liquid tetramethylammonium bis(trifluoromethylsulfonyl)imide. The onset of thermal degradation can be seen at ~426 ºC. Thermogram recorded using a Q-1000 Differential Scanning Calorimeter (TA Instruments) under a nitrogen atmosphere (20 mL min^{-1}) from 40 ºC to 550 ºC at a rate of 10 ºC min^{-1}.

Tetraethylammonium bis(trifluoromethylsulfonyl)imide

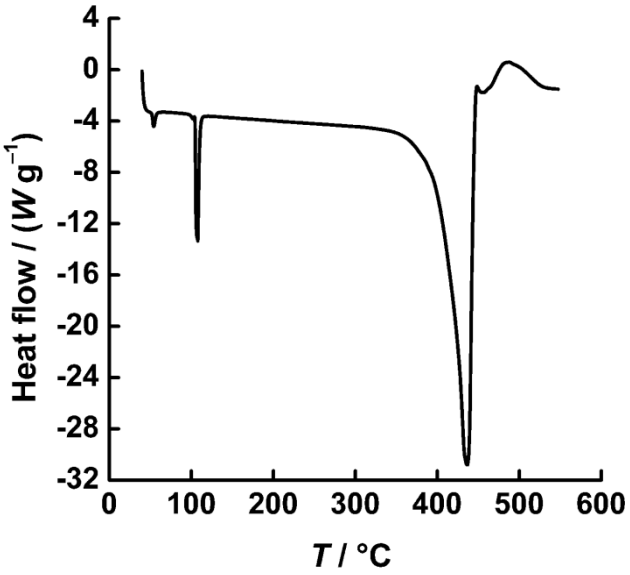

Figure 9A.6 – A plot of heat flow (W g^{-1}) vs. temperature (ºC) for the ionic liquid tetraethylammonium bis(trifluoromethylsulfonyl)imide. The onset of thermal degradation can be seen at ~362 ºC. Thermogram recorded using a Q-1000 Differential Scanning Calorimeter under a nitrogen atmosphere (20 mL min^{-1}) from 40 ºC to 550 ºC at a rate of 10 ºC min^{-1}.

Tetrapropylammonium bis(trifluoromethylsulfonyl)imide

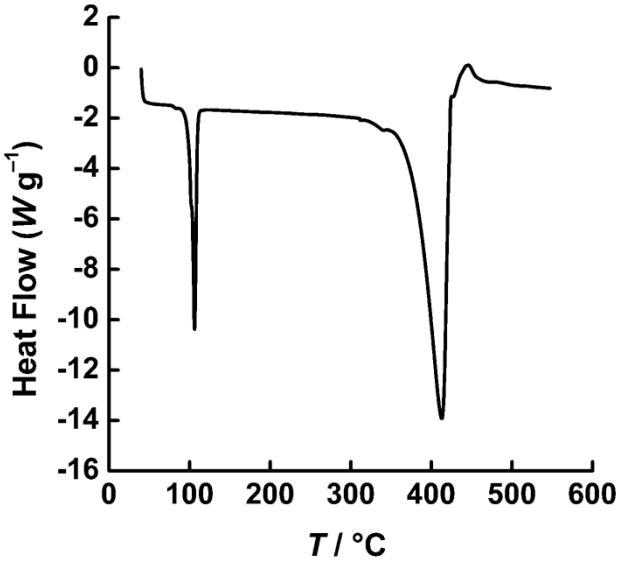

Figure 9A.7 – A plot of heat flow (W g^{-1}) vs. temperature (ºC) for the ionic liquid tetrapropylammonium bis(trifluoromethylsulfonyl)imide. The onset of thermal degradation can be seen at ~354 ºC. Thermogram recorded using a Q-1000 Differential Scanning Calorimeter (TA Instruments) under a nitrogen atmosphere (20 mL min^{-1}) from 40 ºC to 550 ºC at a rate of 10 ºC min^{-1}.

Tetrabutylammonium bis(trifluoromethylsulfonyl)imide

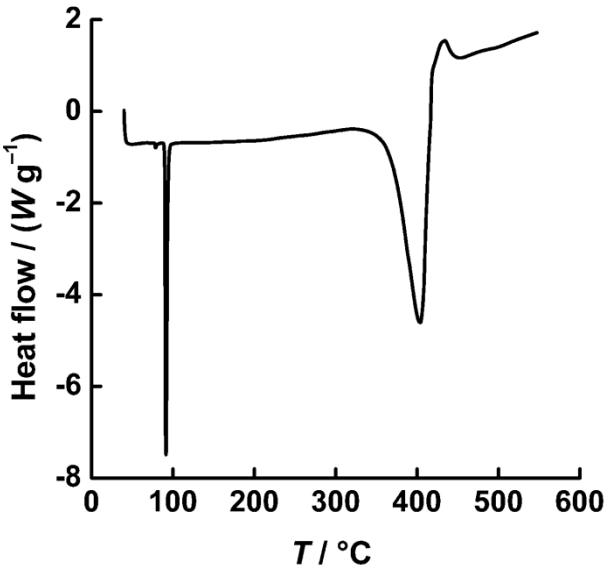

Figure 9A.8 – A plot of heat flow (W g^{-1}) vs. temperature (ºC) for the ionic liquid tetrabutylammonium bis(trifluoromethylsulfonyl)imide recorded using a Q-1000 Differential Scanning Calorimeter (TA Instruments) under a nitrogen atmosphere (20 mL min^{-1}) from 40 ºC to 550 ºC at a heating rate of 10 ºC min^{-1}. The onset of thermal degradation can be seen at ~351 ºC.

1-Ethyl-3-methylimidazolium triflate

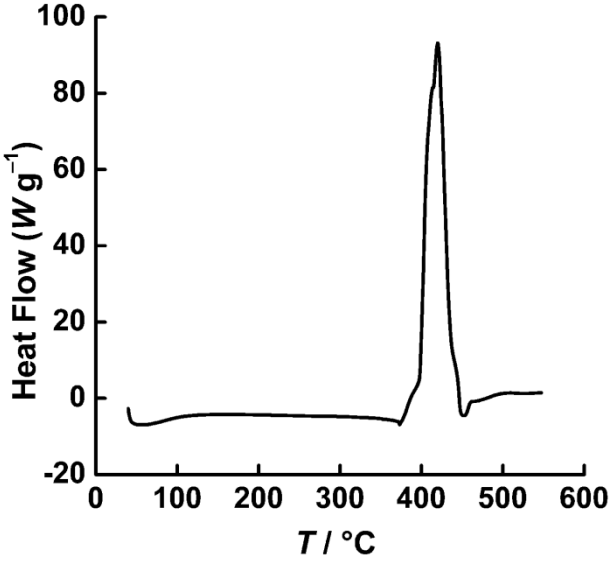

Figure 9A.9 – A plot of heat flow (W g^{-1}) vs. temperature (ºC) for the ionic liquid 1-ethyl-3-methylimidazolium triflate recorded using a Q-1000 Differential Scanning Calorimeter (TA Instruments) under a nitrogen atmosphere (20 mL min^{-1}) from 40 ºC to 550 ºC at a heating rate of 10 ºC min^{-1}. The onset of thermal degradation can be seen at ~374 ºC.

Tetrabutylammonium hexafluorophospate

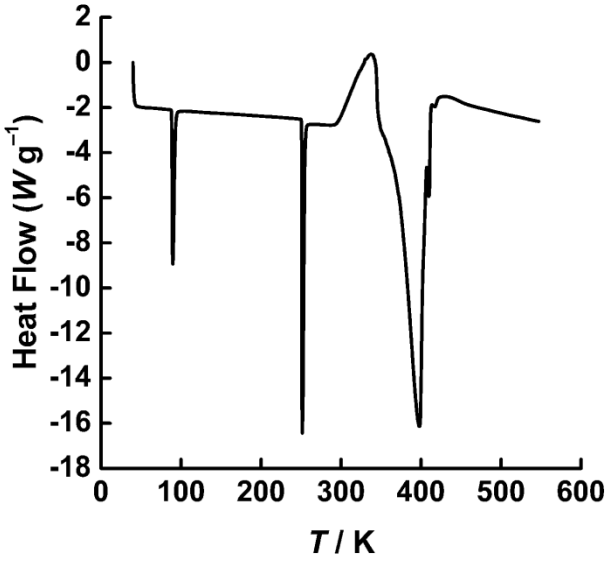

Figure 9A.10 – A plot of heat flow (W g^{-1}) vs. temperature (ºC) for the ionic liquid tetrabutylammonium hexafluorophospate recorded using a Q-1000 Differential Scanning Calorimeter (TA Instruments) under a nitrogen atmosphere (20 mL min^{-1}) from 40 ºC to 550 ºC at a heating rate of 10 ºC min^{-1}. The onset of thermal degradation can be seen at ~248 ºC.

1-Butyl-1-methylpyrrolidinium bis(trifluoromethylsulfonyl)imide

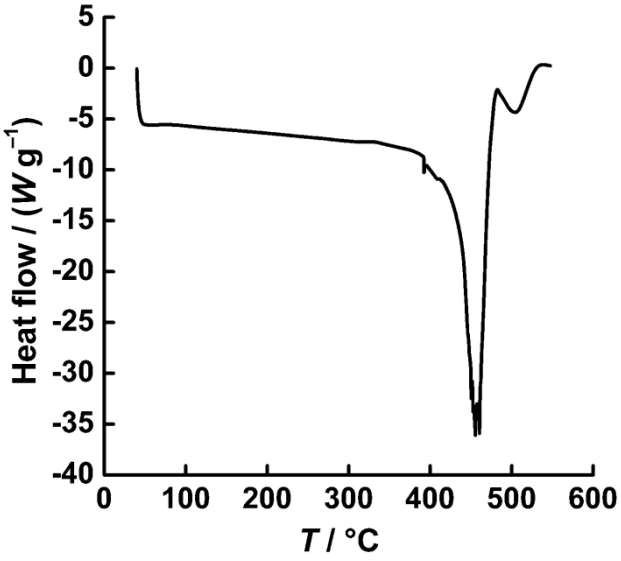

Figure 9A.11 – A plot of heat flow (W g^{-1}) vs. temperature (ºC) for the ionic liquid tetrabutylammonium hexafluorophospate recorded using a Q-1000 Differential Scanning Calorimeter (TA Instruments) under a nitrogen atmosphere (20 mL min^{-1}) from 40 ºC to 550 ºC at a heating rate of 10 ºC min^{-1}. The onset of thermal degradation can be seen at ~388 ºC.

9B – SEM images of candidate supercapacitor separator materials

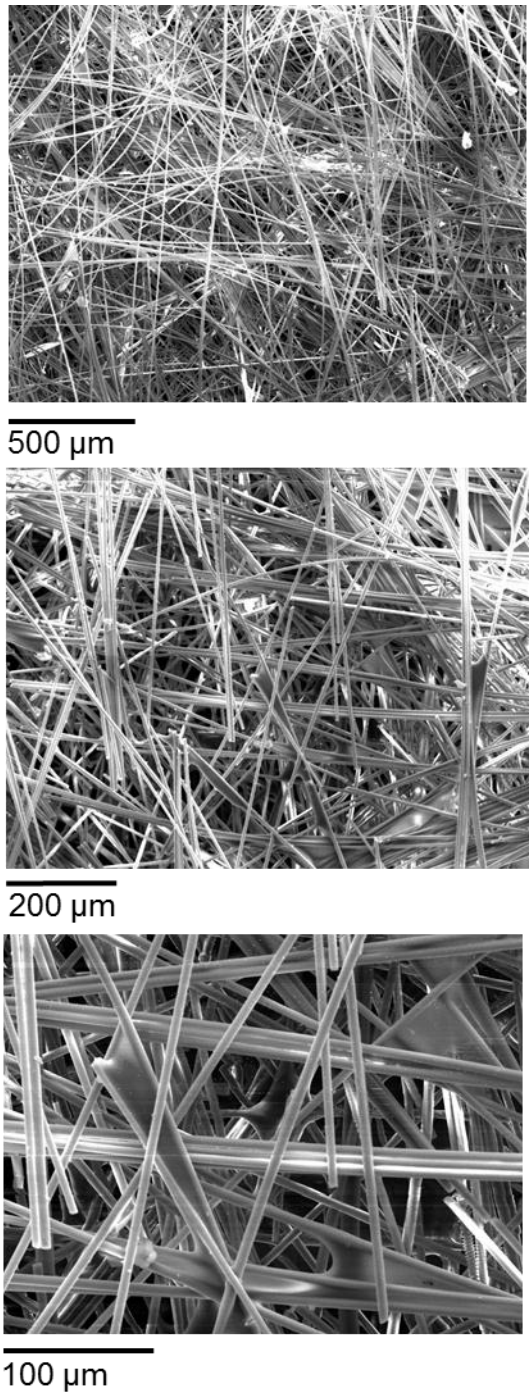

Figure 9B.1 – SEM images of the Schlumberger glass fibre separator obtained using a Carl Zeiss (Leo) 1530 VP FEGSEM. Scale bar is 500 µm (top), 200 µm (middle), and 100 µm (bottom).

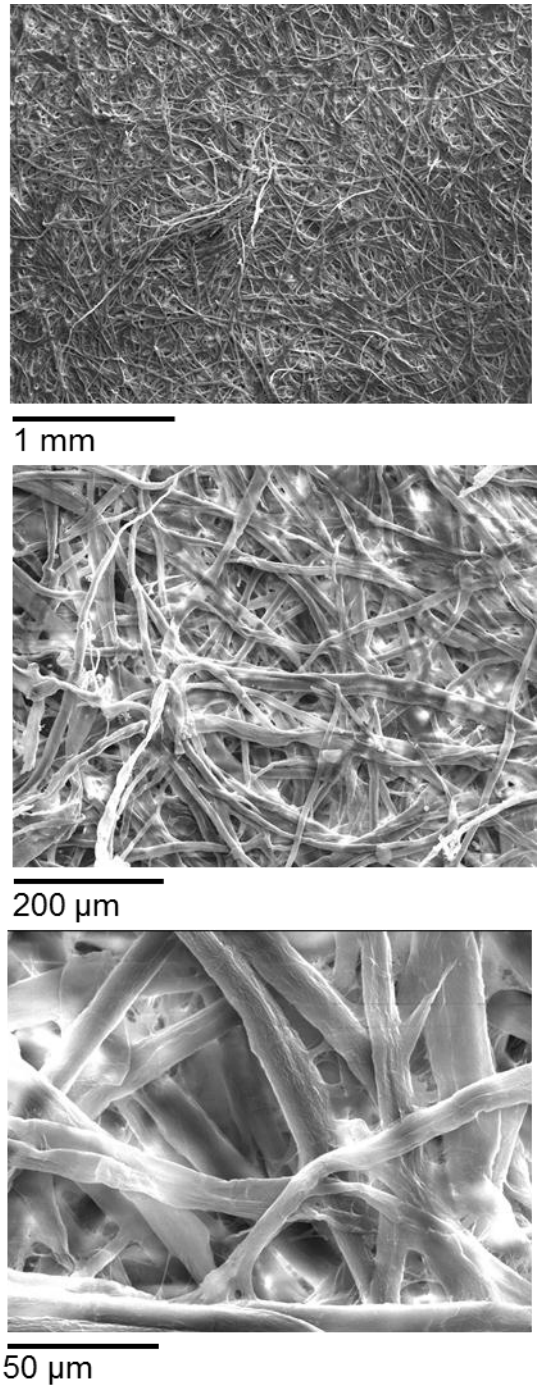

Figure 9B.2 – SEM images of the filter paper obtained using a Carl Zeiss (Leo) 1530 VP FEGSEM. Scale bar is 1 mm (top), 200 µm (middle), and 50 µm (bottom).

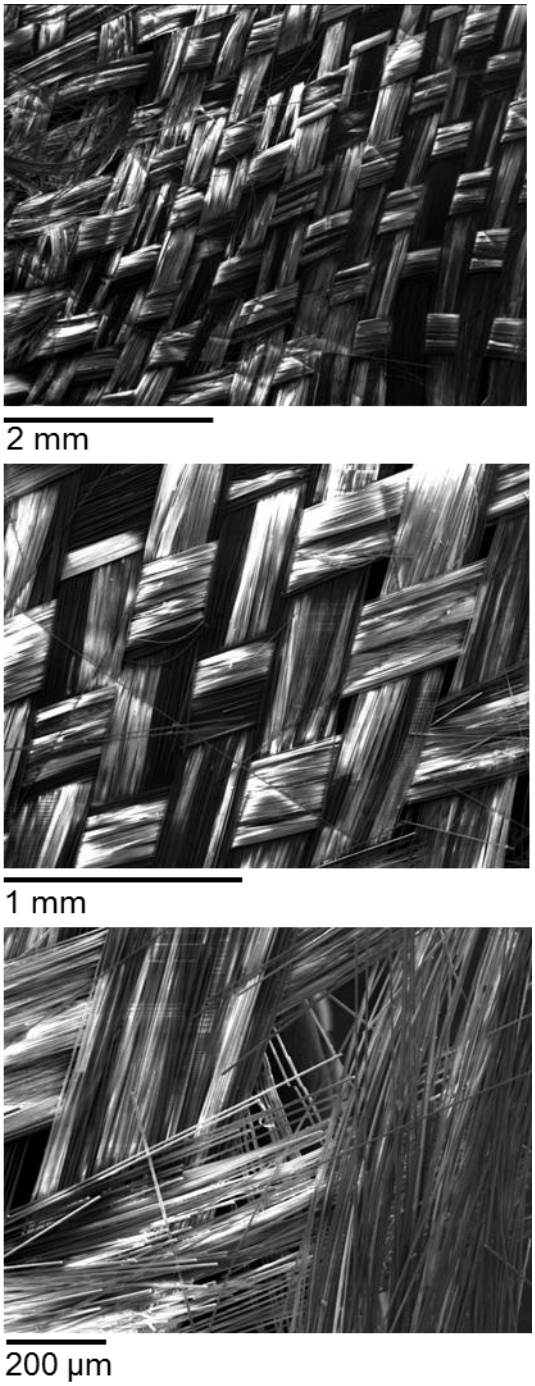

Figure 9B.3 – SEM images of fibreglass cloth obtained using a Carl Zeiss (Leo) 1530 VP FEGSEM. Scale bar is 2 mm (top), 1 mm (middle), and 200 µm (bottom).

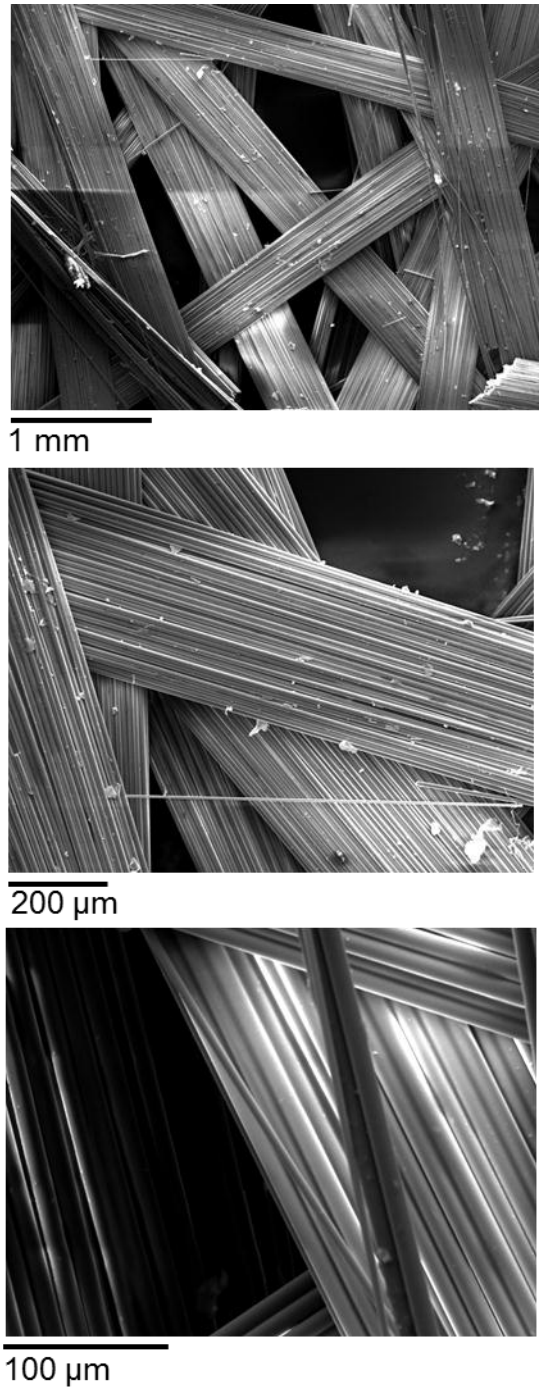

Figure 9B.4 – SEM images of fibreglass matt obtained using a Carl Zeiss (Leo) 1530 VP FEGSEM. Scale bar is 1 mm (top), 200 µm (middle), and 100 µm (bottom).

Appendix 9C – Method used for calculating measured capacitance in supercapacitors

The capacitance C (F) of a supercapacitor can be calculated by rearranging ***Equation 9C.1***:

$$I = C\,\frac{dE}{dt} \qquad \textit{Equation 9C.1}$$

where I is the current (A) and $\frac{dE}{dt}$ is the scan rate ν (V s^{-1}), giving:

$$C = \frac{I}{\nu} \qquad \textit{Equation 9C.2}$$

To cancel out any offset in the data, the current I is calculated as $\frac{2I}{2}$

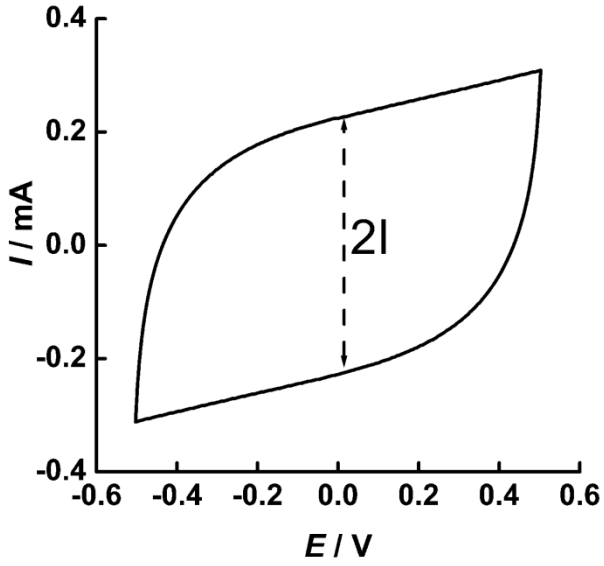

Figure 9C.1 – An illustration of the method used to calculate current values for screen printed supercapacitors.

9D – Method for calculating time constants of supercapacitors - a dispersive kinetic model

To extract mean rates, $\bar{k}$, from our voltage-time and capacitance-time plots, we have employed a Lévy probability density function of the form

$$P\left(k;\bar{k},\alpha,\gamma\right) = \frac{1}{\pi}\int_0^\infty \exp(-\gamma q^\alpha)\cos\left(\bar{k}q\right)\,\mathrm{d}q$$

Equation 9D.1

where *P* is the probability density, *k*-bar is the mean rate, and γ and α are numerical constants that change the shape of the distribution. The reciprocal of the mean rate gives *τ,* which is the *RC* time constant.

The Lévy distribution is a dispersive kinetic model and allows a distribution of rates to be accounted for. We have treated the voltage-time and capacitance-time data as having a distribution of time constants because the activated carbon has a wide variety of pore diameters and depths. Consequently, the mobile ions experience a wide range of environments. In this regard, the Lévy distribution enables a much better fit of data than narrower distributions such as the Gaussian.

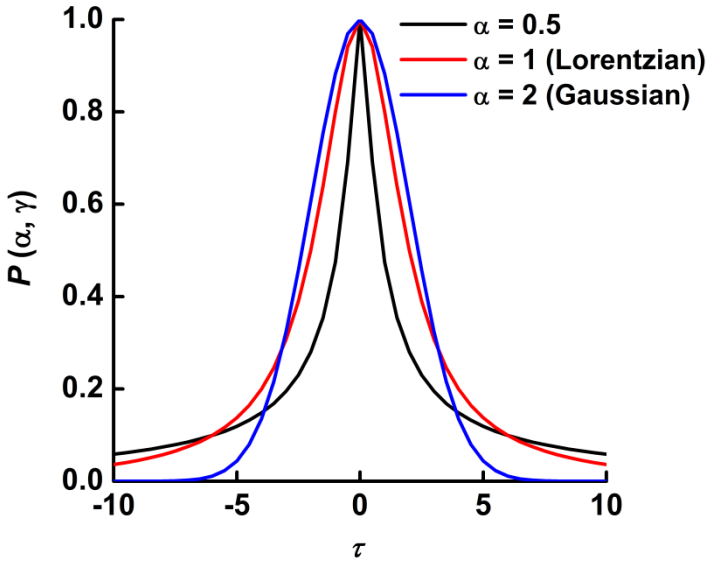

Figure 9D.1 – Comparison of Lévy and Gaussian distributions for various value of α.

It should be noted that many probability distributions lack analytical solutions, and in the case of the Lévy distribution solutions only exist when α = 1 or 2. These cases conform to the Lorentzian and Gaussian distributions, respectively. If the data were to exhibit simple exponential behaviour, the distribution width, α, would tend towards zero. This flexibility makes the Lévy distribution an attractive model. In addition it provides a consistent measure of α which may be compared directly between different supercapacitor devices or parameters such as temperature change. This parameter is expected to vary with surface morphology

Capacitance curves were recorded and sectioned into charging and discharging curves (*I vs. E*). The data was then converted to capacitance and time by dividing both axes by the scan rate. An example for a capacitance curve at 100 ºC (charging) is in ***Figure 9D.2***.

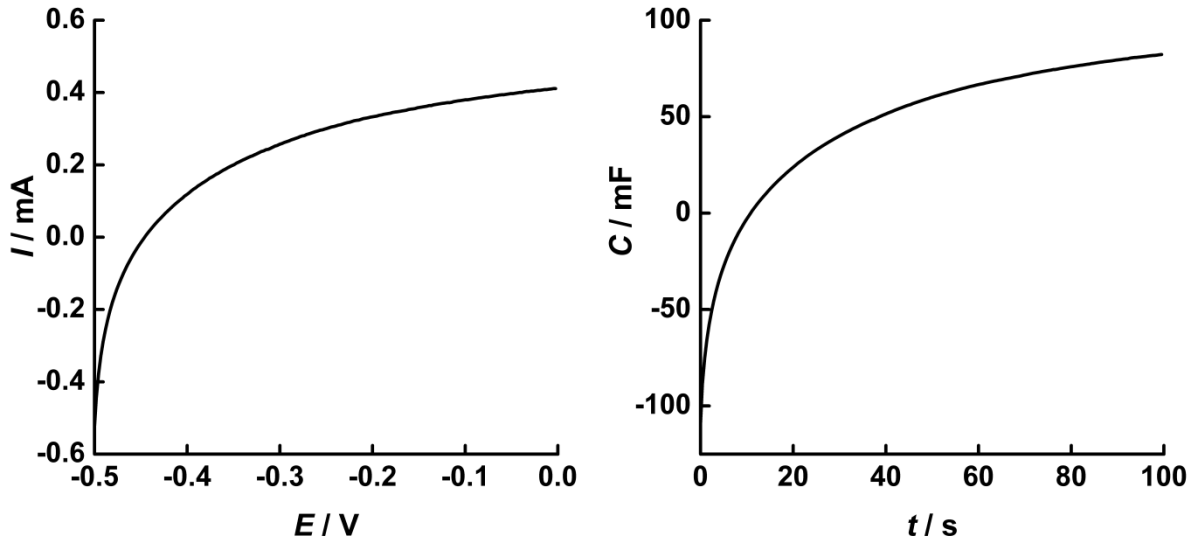

Figure 9D.2 – Graphs illustrating current (mA) vs. potential (V), and capacitance (mF) vs. time (s) data for the charging cycle of a screen printed supercapacitor at 100 ºC. The scan rate was 5 mV s^{-1}.

Capacitance *vs.* time data was then analysed by numerical integration using software written in-house[1][2] (in Microsoft Visual Basic*). The fit is a four-parameter fit (for rate, offset, α and γ) performed *via* a simplex algorithm. Initially some trial values for the offset are examined and selected based upon the value of χ^2, which is a correlation coefficient analogous to r^2 in linear regression. The smaller this value, the better the fit. The residuals are

also displayed. An example of a fitted decay for the data shown above is given in ***Figure 9D.3***.

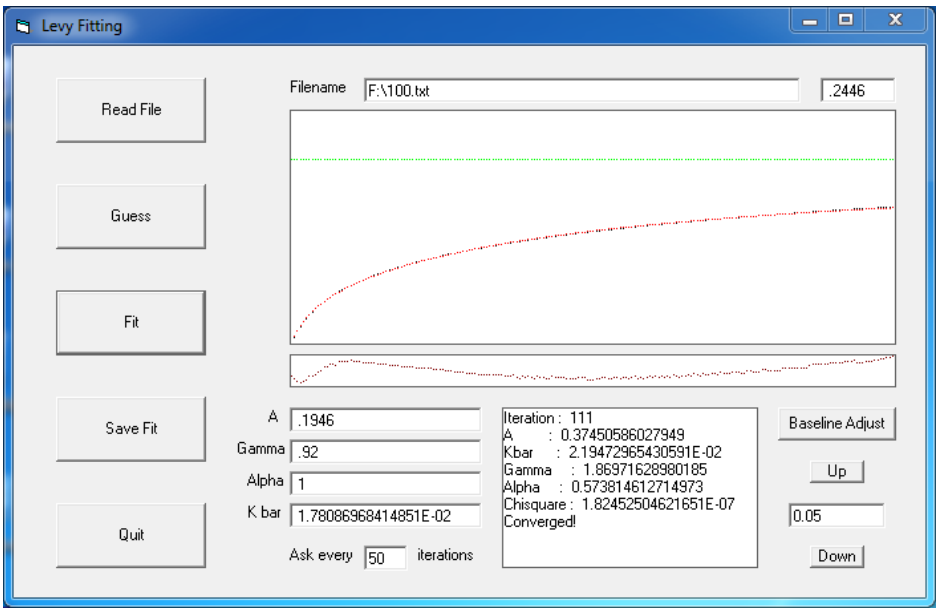

Figure 9D.3 – Four parameter fit for a Levy distribution of k. Values on the left are default initial guesses for the simplex algorithm and on the right the convergence output.

It can be seen that in this example an offset (baseline) of 50 mF was chosen based on χ^2. This is necessary due to the asymptotic behaviour of the data. The *RC* time constant is then obtained from $\tau = \frac{1}{k-bar}$. In this case τ = 46 s.

By saving the fitted function and laying it on top of the original data, the "goodness-of-fit" is clearly seen, ***Figure 9D.4***. A first order exponential fit of the data is shown in ***Figure 9D.5***, illustrating that the Lévy model is a much better fit in comparison.

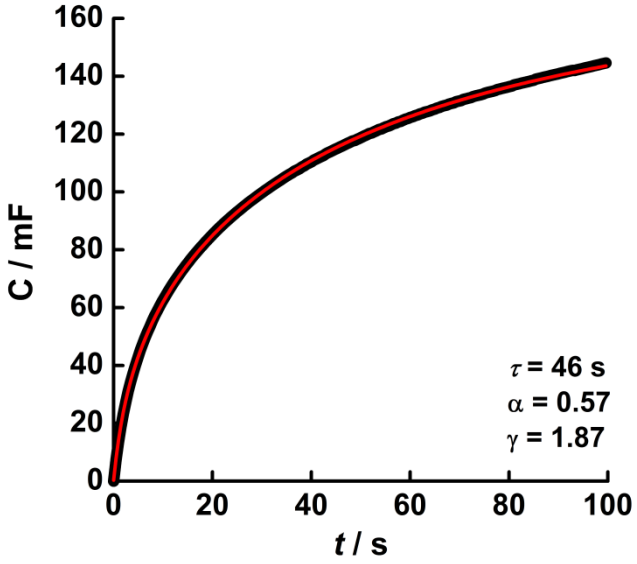

Figure 9D.4 – Plot of capacitance (mF) vs. time (s) showing fit for k using Lévy stable distribution.

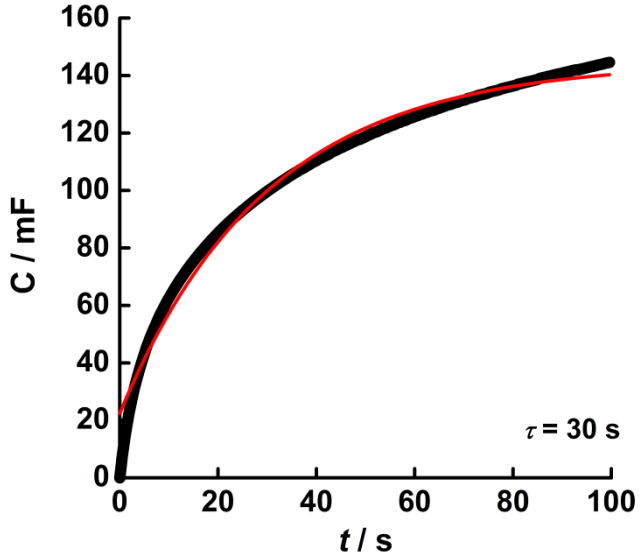

Figure 9D.5 – Plot of capacitance (mF) vs. time (s) showing fit for k using exponential fit.

* Software for performing numerical integration of distributed rates *via* simplex algorithm was originally developed by Dr David R. Worrall for analysis of photochemical electron transfer reactions in heterogeneous media, and later adapted for a Lévy stable distribution by Dr Iain Kirkpatrick.

Fitting of Lévy distributions to the charging process of a supercapacitor at increasing temperature.

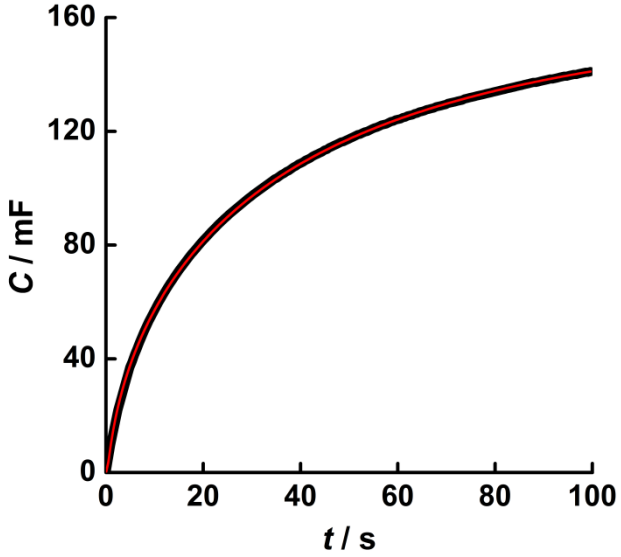

Figure 9D.6 – A graph of capacitance vs. time (black) and fit (red) using Lévy distribution for the charging cycle of a supercapacitor at 25 ^{o}C. $\alpha = 0.6$, $\gamma = 1.5$, $\tau = 38$ s.

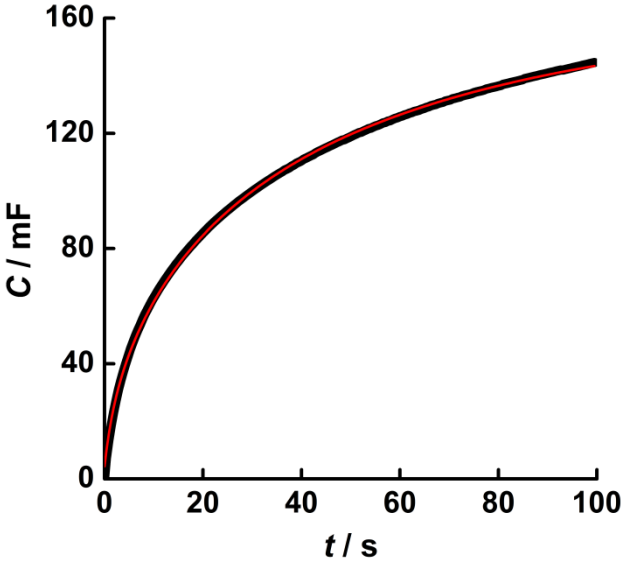

Figure 9D.7 – A graph of capacitance vs. time (black) and fit (red) using Lévy distribution for the charging cycle of a supercapacitor at 50 ^{o}C. $\alpha = 0.6$, $\gamma = 1.5$, $\tau = 41$ s.

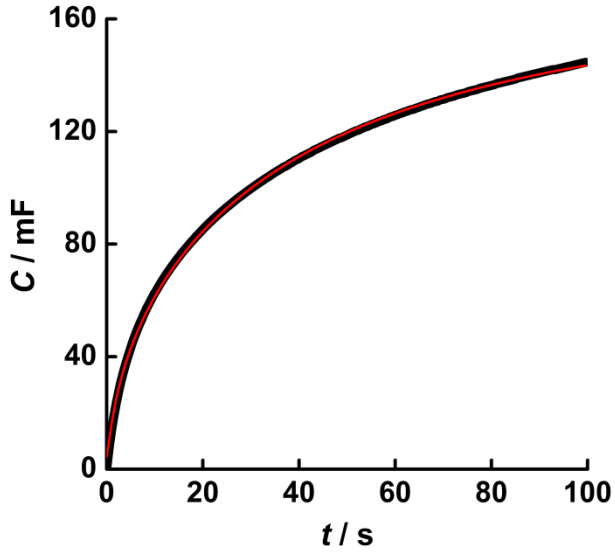

Figure 9D.8 – A graph of capacitance vs. time (black) and fit (red) using Lévy distribution for the charging cycle of a supercapacitor at 100 ^{o}C. $\alpha = 0.6$, $\gamma = 1.5$, $\tau = 41$ s.

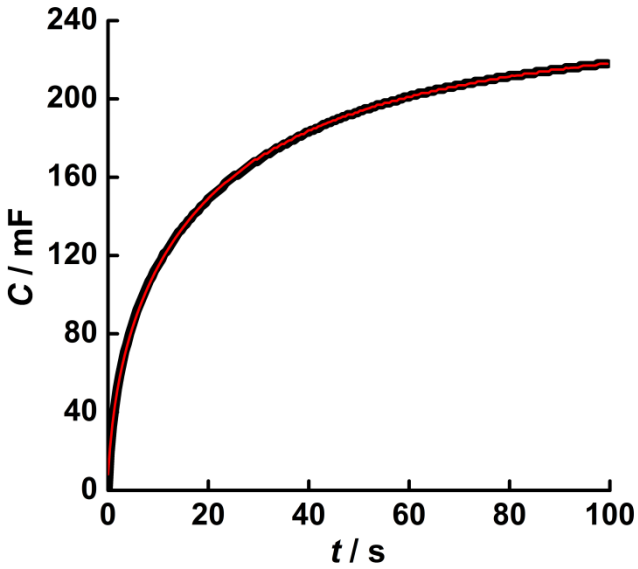

Figure 9D.9 – A graph of capacitance vs. time (black) and fit (red) using Lévy distribution for the charging cycle of a supercapacitor at 150 ^{o}C. $\alpha = 0.7$, $\gamma = 1.5$, $\tau = 25$ s.

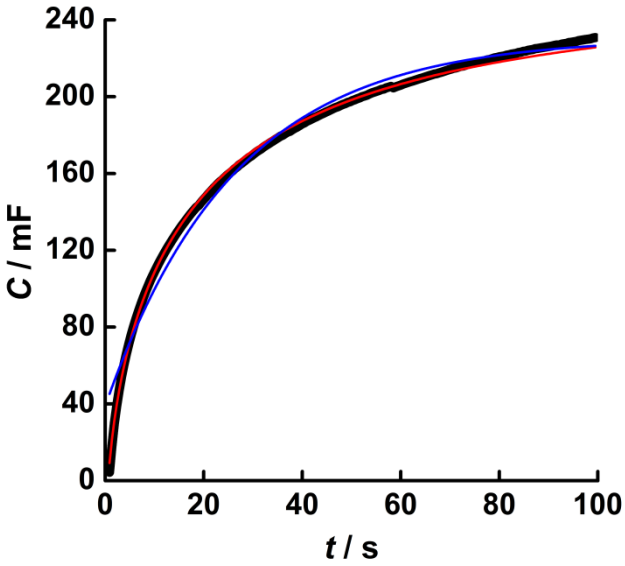

Figure 9D.10 – A graph of capacitance vs. time (black) and fit (red) using Lévy distribution for the charging cycle of a supercapacitor at 200 °C. α = 0.8, γ = 1.5, τ = 21 s. A single exponential fit has also been added (blue) to illustrate that the Levy distribution is the better fit.

References

[1] Worrall, D. R., Kirkpatrick, I. & Williams, S. L. *Bimolecular processes on silica gel surfaces: energetic factors in determining electron-transfer rates*. Journal of Photochemistry and Photobiology, 3: 63-70 (2004).

[2] Worrall, D. R., Kirkpatrick, I. & Williams, S. L. *Controlling factors in electron and energy transfer reactions on silica gel surfaces*, Journal of Photochemistry and Photobiology, 1: 896-901 (2002).

Appendix 9E – The development of self-indicating ionic liquids

The presence of water in ionic liquids damages the voltage window that is accessible to supercapacitors. (The voltage window of pure water is only 1.2 V). One method of drying ionic liquids is to add anhydrous "silica gel" (actually microporous monolithic beads of silica). Since it had already been found that fumed silica was a good gelling agent, it became apparent that the addition of self-indicating "silica gel" to the gelled ionic liquid would create a *self-indicating* ionic liquid.

Self-indicating silica gels are commercially available. They are typically solid beads containing a moisture-sensitive agent that changes colour in the presence of water. The microstructure of the solid beads is very different from the microstructure of fumed silica, however. The solid beads are micro-porous (800 m^2 g^{-1}) and contain cavities that allow large amounts of water to be absorbed. By contrast, fumed silica consists of chains of solid nanoparticles.

Micro-porous silica gel was purchased from Fisher Scientific UK Ltd (Loughborough, UK). It has a bead size in the range 2.5 mm to 6 mm and contains an orange additive that changes to pale yellow/colourless upon absorption of water (see ***Figure 9E.1***). It is robust and well suited to regeneration and re-use. However, the identity of the orange compound is unknown. It is suspected to be an iron compound, although other possibilities include methyl violet and phenolphalein. Further analysis is needed.

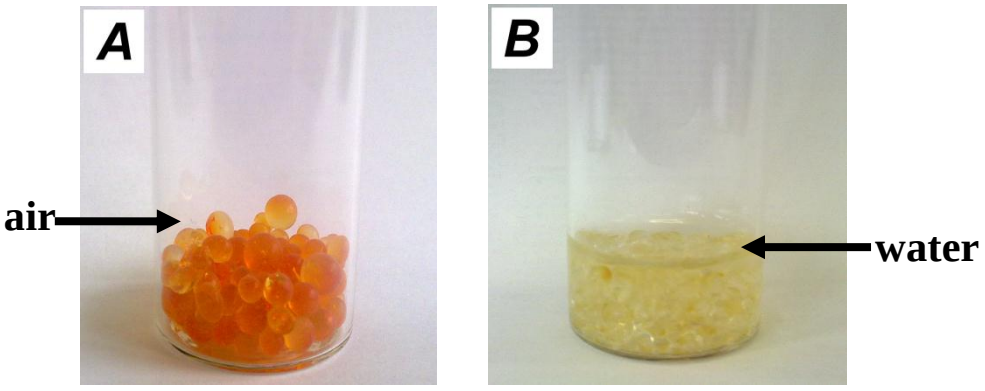

Figure 9E.1 – Photographs of self-indicating silica gel. (A) In air and (B) in water.

Appendix 9F – The removal of unknown colour impurities from ionic liquids

The existence of colour-forming impurities in ionic liquids is well-known in the literature but their identity is somewhat of a puzzle. While exploring the thermal stability of ionic liquid gels, it was observed that the ionic liquids were turning from colourless to orange-brown after prolonged temperature exposure at temperatures exceeding 200 ºC. However, it was established that by adding activated carbon to a discoloured ionic liquid after heat treatment, and filtering, the ionic liquid was readily restored to its clear state. This method would be a good way of purifying ionic liquids in future work. The discoloured beaker of butyltrimethylammonium bis(trifluoromethylsulfonyl)imide following heat treatment (18 h at 220 ºC) is shown in ***Figure 9F.1*** and the clear mixture resulting from the addition of activated carbon and filtration is shown in ***Figure 9F.2***.

Figure 9F.1 – Effect of long-term heat treatment on butyltrimethylammonium bis(trifluoromethyl-sulfonyl)imide liquid after 18 hours heating at 250 ºC in air.

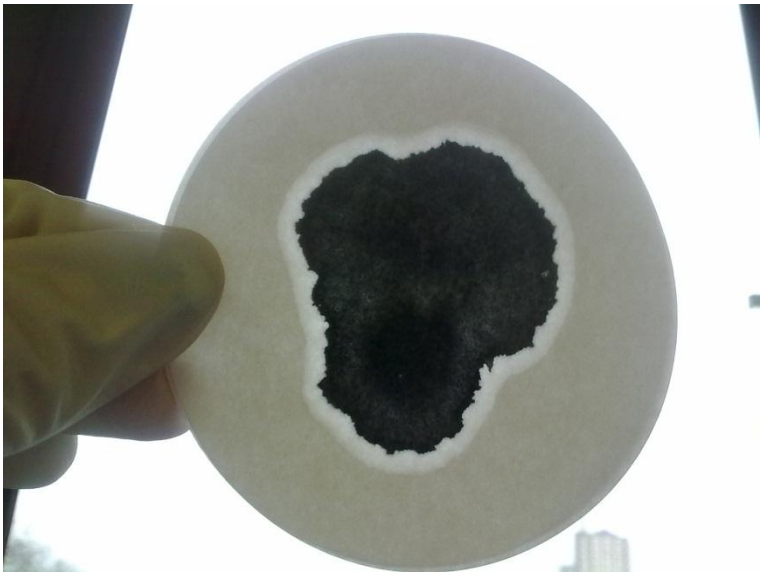

Figure 9F.2 – Coloured impurities are removed from ionic liquids by activated carbon. Here, butyltrimethylammonium bis(trifluoromethylsulfonyl) imide appears clear after added activated carbon and filtering the discoloured mix arising from 18 hours heating at 250 ºC in air.